Local THz Spectroscopy in the Condensed Phase: Femtosecond Stokes Shift of Molecular Probes

Dissertation

zur Erlangung des akademischen Grades
doctor rerum naturalium
(Dr. rer. nat.)
im Fach Physik
eingereicht an der

Mathematisch-Naturwissenschaftlichen Fakultät I
der Humboldt-Universität zu Berlin
Von

Mohsen Sajadi Hezaveh, M.Sc.

Präsident der Humboldt-Universität zu Berlin
Prof. Dr. Jan-Hendrik Olbertz

Dekan der Mathematisch-Naturwissenschaftlichen Fakultät I
Prof. Dr. Andreas Herrmann

Gutachter/innen: 1. Prof. Dr. Nikolaus Ernsting
2. Prof. Dr. Jürgen Rabe
3. Prof. Dr. Thomas Elsässer

Tag der mündlichen Prüfung: 31. 01. 2012

For Fatemeh

Abstract

Solvation dynamics of a solvatochromic molecular probe is discussed as a method to yield local IR-THz spectra of complex systems. After femtosecond excitation, the charge distribution of the probe is altered and, as a consequence, an electric field is generated. At this stage the solute acts as a light source with THz frequencies. Since by excitation the equilibrium of the system is perturbed, solvent molecules reorganize such that a new equilibrium is created in the excited state. This motion of solvent molecules can be seen (in an averaged form) by recording the Stokes shift of the fluorescence band. By an appropriate transformation of the time-resolved Stokes shift, a local IR-THz spectrum is obtained. The probe molecule therefore also acts as a detector. The advantage of such a "molecular spectrometer" is its locality, which becomes important when measurements are made in water. In this case, intense absorption by the solvent makes impossible the penetration of external THz beams deep into the sample.

To measure solvation dynamics, a broadband fluorescence up-conversion setup with acceptance bandwidth of ~11000 cm^{-1} was developed. With this spectrograph, transient fluorescence lineshapes, totally background free and with high S/N and time resolution (80 fs), can be measured. A Kerr shutter was also developed to extend the spectral window into the UV.

As a first methodical step, the solvation dynamics of 4-aminophthalimide (4AP) in methanol is measured and compared with predictions of simple continuum theory. Results show an accurate prediction even though strong contributions exist from hydrogen bonding.

Studies about the molecularity of solvation dynamics reveal that rotation of the molecular probe accelerates the spectral relaxation. Also we find that solvation dynamics depends on excitation energy in nonpolar and aprotic polar solvents. In these two groups of solvents, a "retro-" or blue shift in the tail of Stokes shift relaxation is observed when excess vibrational energy is given to the molecule upon optical excitation. The latter effect becomes important when the solvation dynamics

of a complex system, comprising compartments with different polarity, is measured. In this case the true spectral relaxation is only obtained when the molecular probe is excited at the red edge of the absorption band.

We conclude with studies of biological relevance. The first consists of N-Methyl-6-Quinolone (MQ) in two states, free in aqueous trehalose (0.5 M and 1 M), and also covalently bound to trehalose in water. For the former, the IR-THz spectra of the mixtures are obtained. For the latter, the thickness of a hydration layer around the trehalose moiety is estimated.

As a second and more complex biological system, the spectral relaxation of a molecular probe (Hoechst 33258) in the minor groove of DNA is measured. A modulation of the spectral relaxation with an oscillation is observed, which is attributed to in/out motion of the ligand and breathing of minor groove of DNA.

Zusammenfassung

In dieser Arbeit wird die Solvatationsdynamik einer solvatochromen molekularen Sonde diskutiert, und zwar als Methode für den Erhalt von lokalen IR-THz-Spektren von komplexen Systemen. Durch Femtosekundenanregung wird die Ladungsverteilung der Sonde verändert, und als Folge davon wird ein elektrisches Feld induziert. Zu diesem Zeitpunkt wirkt die im Lösungsmittel gelöste Sonde als Lichtquelle mit THz-Frequenzen. Da durch die Anregung das Gleichgewicht des Systems gestört wird, reorganisieren sich die Lösungsmittelmoleküle, sodass ein neues Gleichgewicht im angeregten Zustand entsteht. Die Bewegung der Lösungsmittelmoleküle ist (in gemittelter Form) als Stokes-Verschiebung des Fluoreszenz-Bandes beobachtbar. Durch eine geeignete Transformation der zeitaufgelösten Stokes-Verschiebung erhält man ein lokales IR-THz-Spektrum. Das Sondenmolekül wirkt daher auch als ein Detektor. Der Vorteil eines solchen "molekularen Spektrometers" ist sein mikroskopischer Aufenthaltsort, der u.a. sehr wichtig wird, wenn Messungen in Wasser durchgeführt werden: In diesem Fall macht eine intensive Absorption durch das Lösungsmittel das Eindringen von externen THz Strahlen tief in die Probe unmöglich.

Um die Solvatationsdynamik zu messen, wird ein Aufbau zur Messung von Breitband-Fluoreszenz mithilfe der sog. „up-conversion“ entwickelt; die Bandbreite beträgt ~ 11000 cm^{-1}. Mit diesem Spektrographen können transiente Fluoreszenz Linienformen, absolut hintergrundsfrei mit einem hohen S / N Verhältnis sowie mit hoher Zeitauflösung (80 fs), gemessen werden. Zudem wird ein Kerr-Schalter entwickelt, womit das spektrale Fenster in den UV-Bereich erweitert wird.

In einem ersten methodischen Schritt wird die Solvatationsdynamik von 4-Aminophthalimid (4AP) in Methanol gemessen und mit den Vorhersagen der einfachen Kontinuum-Theorie verglichen. Die Ergebnisse zeigen eine genaue Vorhersage, obwohl starke Beiträge aus Wasserstoffbrückenbindungen existieren.

Studien über die Molekularität der Solvatationsdynamik zeigen, dass die Rotation der molekularen Sonde die spektrale Relaxation beschleunigt. Es wird

beobachtet, wie die Solvatationsdynamik von der Anregungsenergie in unpolaren und aprotisch-polaren Lösungsmitteln abhängt. In diesen beiden Lösungsmittelgruppen wird eine "Retro-" oder Blauverschiebung im späten Teil der Stokes-Relaxation beobachtet, wenn überschüssige Schwingungsenergie an das Molekül durch optische Anregung abgegeben wird. Der letztere Effekt ist von Bedeutung, wenn die Solvatationsdynamik eines komplexen Systems, bestehend aus Bereichen mit unterschiedlicher Polarität, gemessen wird. In diesem Fall wird die wahre spektrale Relaxation nur gesehen, wenn die molekulare Sonde am roten Rand der Absorptionsbande angeregt wird.

Diese Arbeit wird mit zwei Studien über die biologische Relevanz der Forschungsergebnisse abgeschlossen. Die erste besteht aus der Untersuchung von N-Methyl-6-Chinolon (MQ) in zwei Zuständen, einmal frei in wässriger Trehalose Lösung (0,5 M und 1 M), und in wässrigem Medium kovalent an Trehalose gebunden. Für erstere wurden die IR-THz-Spektren der Mischungen erhalten. Für letztere wurde die Dicke einer Hydratationschicht um die Trehaloseeinheit geschätzt.

Als zweites und komplexeres biologisches System wird die spektrale Relaxation einer molekularen Sonde (Hoechst 33258) in der kleinen Furche der DNA gemessen. Es wird eine Modulation der spektralen Relaxation mit einer Schwingung beobachtet, die auf die auf/ab Bewegung des Liganden sowie auf die Atmung der kleinen Furche der DNA zurück geführt wird.

Table of contents

1 Introduction

Solvation dynamics of polar chromophores in polar liquids has been studied over the last decades to answer fundamental questions in solution chemistry. Most prominently the rate of charge transfer was examined.[1,2,3,4] By "solvation dynamics" one means the rate of polar solvent response to a suddenly created charge distribution in the chromophore. Experimentally this rate can be measured by recording the time-dependent Stokes shift (TDSS) of the fluorescence spectrum after femtosecond optical excitation. From the temporal evolution of the fluorescence band, *i.e.* the spectral relaxation, the dynamics of the surrounding can be extracted, provided that it is independent of the chromophore.

Besides helping to understand chemical reactions, solvation dynamics is being used with more complex systems than conventional solvents. Especially with biological systems one can observe the local dynamics at specific sites.[5,6,7,8,9,10,11] However the quantitative analysis of such data is not satisfactory at this stage. In this thesis a number of methodical steps is taken to make such solvation data accurate. The dynamics of the microscopic environment is explored quantitatively for two model biophysical systems.

1.1 TDSS recording methods

The methods typically used for solvation dynamics studies are time correlated single photon counting (TCSPC),[12] fluorescence up-conversion at single wavelengths,[13] Kerr gating,[14] and transient absorption.[15] They miss at least one of the following items: high time resolution, bandshape measurement, and background-free signals. In TCSPC the fluorescence at selected wavelengths is measured and the temporal evolution of the band is reconstructed with low time resolution (~15 ps). In single wavelength fluorescence up-conversion the time resolution is improved significantly (< 100 fs) but still the band shape must be reconstructed. Here reconstruction means using only a few time traces (~10) to cover the entire bandshape

(> 10000 cm^{-1}) from time-zero till time-infinity. With Kerr gating the full bandshape can be recorded with acceptable time resolution (~ 250 fs). However, since the gated signal and nanosecond fluorescence are spectrally identical, residual fluorescence in the gated signal is still a serious problem. Transient absorption measurements can be performed in a broad-band scheme with high time resolution (<100 fs), and it is intrinsically background free.[16] However the measured signal is a superposition of stimulated emission (SE), excited state absorption (ESA) and ground state bleach (BL). To obtain the temporal evolution of the emission band, the measured spectrum must be decomposed. In most cases ESA and SE can not be separated uniquely, and therefore the dynamics of emission band can only be estimated and is subject to systematic errors.

To overcome the above-mentioned difficulties, in this thesis a broadband up-conversion setup was developed which can measure fluorescence bandshapes at high time resolution (80 fs fwhm). The background has been essentially removed compared to the previous design. Biological samples can be measured because of new collection optics. Thus the S/N ratio of transient fluorescence has been improved significantly and the spectral range was extended. A progression of small systematic steps, both in methodical and in molecular directions, leads to the first observation of DNA breathing, by the emission of a ligand in the minor groove.

1.2 Solvation dynamics for local THz spectroscopy

Dynamical aspects of biological systems, and in particular of DNA, are of great interest. Many groups are developing novel methods to capture the structural dynamics of proteins,[7,8] DNA,[5,10] and other biological environments.[9] Electron and X-ray diffraction,[17] THz[18] and IR absorption,[19] and Raman spectroscopy[20] are among the methods, each with their own limitations, which are used to explore dynamical and structural information of biological systems.

The solvation dynamics of a solvatochromic molecule can also be used to measure the dynamics of a complex system. The probe molecule is attached to the system

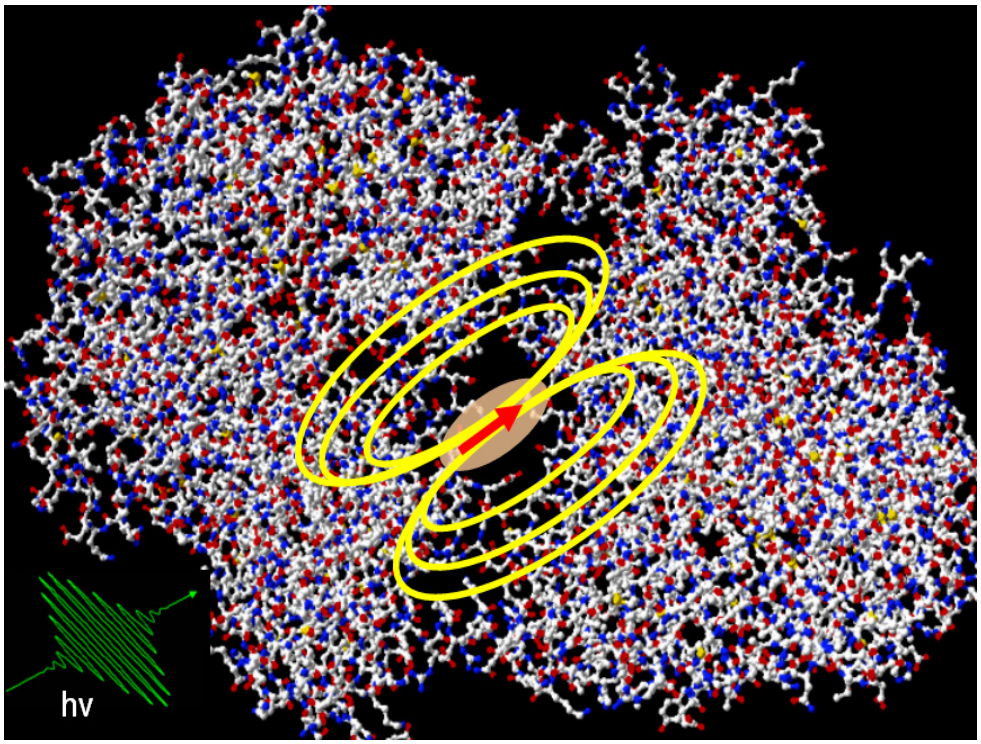

Fig. 1.1 A local IR-THz spectrometer in a complex system. Exciting a molecular probe with femtosecond pulses (green) generates an electric field (yellow) in the surrounding environment. The response of the medium is recorded through Stokes-shift measurements.

where it acts as a local spectrometer for the IR-THz region. In ideal cases the solvation relaxation can be fitted by the frequency-dependent dielectric permittivity $\varepsilon(\omega)$. This observation initiates the idea of a reverse process, to obtain the local dielectric permittivity of the surrounding environment. The main features of such measurements are its intrinsic broadness and locality. Fig. 1.1 depicts a schematic view of the whole idea. Here a newly created charge distribution or dipole moment in the probe, by femtosecond optical excitation, instantly generates an electric field in THz frequency range. In other words, the excited probe acts as a THz light source. Subsequently, nearby solvent molecules respond to this perturbation of the electric field, and thereby change the reaction field $\mathbf{R}(t)$ at the probe position. The temporal evolution of $\mathbf{R}$ contains important dynamical information about the system. The dynamics of the reaction field reflects the change of free energy in the system. The latter is measurable through recording the transient fluorescence of the molecular probe. Therefore the probe has a second role as detector. This method becomes particularly interesting when dynamical information at a specific position of a biological system is targeted. In another words, locality brings about an opportunity to

reach special regions in biological samples. Furthermore, with a single solvation relaxation measurement, one obtains broad permittivity dispersion, which usually needs complementary conventional methods to cover.

The present thesis starts with solvation dynamics in a simple environment, namely methanol. A full description of experimental procedures to record transient fluorescence with high time resolution is provided. Molecularity aspects of solvation dynamics are discussed and at the end two biological systems, trehalose solutions and DNA, are measured and new achievements are discussed.

The work is arranged as follows:

Chapter 2 presents a self-contained summary of the theoretical background which is needed to understand solvation dynamics. The chapter starts with a more general view and then details the ideas behind linear response. Different solvation dynamic theories also are discussed with regard to their advantages and disadvantages.

In *chapter 3* the experimental procedures are described which are used to measure the spectral relaxation of a solvatochromic probe. Broadband fluorescence up-conversion as the main method is discussed in quite some detail, including the various corrections which are needed to arrive at results which are photometrically reliable. The reproducibility of the set up is shown by comparing measurements, of same systems, which were recorded almost two years apart.

In *chapter 4* the solvation dynamics of 4-aminophthalimide (4AP) in methanol is reported, by broadband fluorescence up-conversion. Despite a known contribution from hydrogen bonding between solute and solvent molecules, it is shown that spectral relaxation follows dielectric relaxation of pure methanol exactly. The specific interactions of the system are not observed dynamically. Transient absorption spectra are also provided. They are decomposed into partial spectra due to bleach (BL), excited state absorption (ESA), and stimulated emission (SE). On the other hand, the temporal evolution of SE is known independently from up-conversion measurements.

In *chapter 5* molecularity aspects of solvation dynamics are discussed. It is shown that rotation of the probe accelerates the observed energy relaxation. Also a dependence on excitation energy is investigated. The latter reveals that the fluorescence band is red shifted by giving excess energy to the molecule, compared to red–edge excitation. This effect is observed in nonpolar and aprotic polar solvents.

In *chapter 6* a first biological sample is measured, and the reliability of our local spectrometer is tested in this way. Thus, the solvation dynamics of N-Methyl-6-Quinolone (MQ) in trehalose/water mixture is measured. By virtue of simple continuum theory, in a reverse process (ie. starting from the measured spectral relaxation) the local spectrum $\varepsilon(\omega)$ of the environment is obtained. Solvation dynamics of MQ which is covalently bound to trehalose also is measured. From the latter the thickness of the hydration layer around the trehalose moiety is estimated.

In *chapter 7* the solvation dynamics of the dye Hoechst 33258 bound in the minor groove of DNA is measured. The biopolymer is thus studied in water and also in ethylene glycol solutions. A modulation of the spectral relaxation is observed, and it is attributed to the breathing of DNA.

Finally an outlook is given in *chapter 8*.

2 Background

This chapter is intended to briefly review the theoretical basis of solvation dynamics process. To this end, linear response theory is discussed in more detail. Also the main theories which have been used so far to formulate solvation dynamics of a molecular probe are described. The review presented in this chapter should be useful for a short introduction to the field.

2.1 Light mater interaction (largely based on Ref. 21.)

Maxwell´s equations describe the spatial and temporal evolution of electric and magnetic fields

$$\nabla \cdot D = 0 \tag{2.1.a}$$

$$\nabla \cdot B = 0 \tag{2.1.b}$$

$$\nabla \times E = -\frac{\partial B}{\partial t} \tag{2.1.c}$$

$$\nabla \times H = \frac{\partial D}{\partial t} \tag{2.1.d}$$

In Eqs. 2.1 a nonmagnetic medium ($B = \mu_0 H$) with no free charges (in SI units) is assumed. Here displacement D is defined as

$$D = \varepsilon_0 E + P \tag{2.2}$$

where P is the electric dipole moment density, or polarization (*in SI*). For a transverse electric field ($\nabla \cdot E = 0$) a wave equation can be written as

$$\left(\nabla^2 - \frac{1}{c^2}\frac{\partial^2}{\partial t^2} \right) E(r,t) = \frac{1}{\varepsilon_0 c^2}\frac{\partial^2}{\partial t^2} P(r,t) \tag{2.3}$$

where c is the speed of light. Eq. (2.3) implies that the temporal and spatial variation of the electric field is determined by the time evolution of electric polarization, which is a property of the medium that the electric field propagates in. Therefore, obtaining the temporal evolution of polarization is a key parameter to solve the wave equation inside matter.

2.2 Temporal evolution of a system (largely based on Ref. 22.)

The statistical state of an ensemble may be described by density matrix ρ. The temporal evolution of ρ is given by the Liouville equation

$$\frac{d\rho}{dt} = \frac{1}{i\hbar}[H, \rho] \tag{2.4}$$

where H represents the total Hamiltonian of the system, including interaction with external fields and the environment.

To solve the Liouville equation, the total Hamiltonian is broken up into time independent and time dependent parts: $H(t)=H_0+H'(t)$. Starting from the Schrödinger equation, in an iterative approach one obtains the time dependent evolution of the density matrix

$$\begin{aligned}\rho(t) = \rho(t_0) + \sum_{n=1}^{\infty}\left(-\frac{i}{\hbar}\right)^n \int_{t_0}^{t} d\tau_n \int_{t_0}^{\tau_n} d\tau_{n-1} \cdots \int_{t_0}^{\tau_2} d\tau_1 \\ U_0(t,t_0)\cdot\left[H_I'(\tau_n),\left[H_I'(\tau_{n-1}),\cdots\left[H_I'(\tau_1),\rho(t_0)\right]\cdots\right]\right]\cdot U_0^{\dagger}(t,t_0)\end{aligned} \tag{2.5}$$

here $U_0(t,t_0) = e^{-\frac{i}{\hbar}H_0(t-t_0)}$ is a unitary operator that transfers operators between Interaction and Schrödinger pictures. Eq. (2.5) converges for a weak perturbation. In the case that the time dependent part of the Hamiltonian is described by interaction of an electric field and dipoles of the medium, the perturbative term is given by

$$H'(\mathrm{t}) = -\mu \cdot E(\mathrm{t}) \tag{2.6}$$

and the density matrix can be written as

$$\begin{aligned}\rho(t) = \rho(-\infty) + \sum_{n=1}^{\infty}\left(-\frac{i}{\hbar}\right)^n \int_{-\infty}^{t} d\tau_n \int_{-\infty}^{\tau_n} d\tau_{n-1} \cdots \int_{-\infty}^{\tau_2} d\tau_1 E(\tau_n)E(\tau_{n-1})\cdots E(\tau_1) \\ U_0(t,-\infty)\cdot\left[\mu_I(\tau_n),\left[\mu_I(\tau_{n-1}),\cdots\left[\mu_I(\tau_1),\rho(-\infty)\right]\cdots\right]\right]\cdot U_0^{\dagger}(t,-\infty)\end{aligned} \tag{2.7}$$

here μ_I is the dipole operator in the interaction picture. Using Eq. (2.7), the polarization can be calculated

$$P(t) = Tr(\mu\rho(t)) = \langle \mu\rho(t) \rangle . \tag{2.8}$$

Expanding $P(t)$ in a power series in the electric field one gets

$$P(t) = \sum_n \int_0^{\infty}\int_0^{\infty}\cdots\int_0^{\infty} dt_n dt_{n-1}\ldots dt_1 S^n(t_n,t_{n-1},\ldots,t_1)E^n(t,t_n,t_{n-1},\ldots,t_1) \tag{2.9}$$

where time−ordered electric fields E^n and response functions S^n are given as follow

$$E^n(t,t_n,t_{n-1},\ldots,t_1) = E(t-t_n)E(t-t_n-t_{n-1})\ldots E(t-t_n-t_{n-1}-\ldots t_1) \tag{2.10}$$

and

$$S^n(t_n,t_{n-1},\ldots,t_1) = \left(\frac{i}{\hbar}\right)^n Tr\left(\mu_I(t)\left[\mu_I(\tau_n),\left[\mu_I(\tau_{n-1}),\ldots\left[\mu_I(\tau_1),\rho(-\infty)\right]\ldots\right]\right]\right). \tag{2.11}$$

Non-linear as well as linear spectroscopies can be built based on the knowledge of response functions, for instance $S^1(t) = \langle \mu(t_1)\mu(0)\rho(-\infty)\rangle$ describes the absorption line shape. Experiments like pump–probe, photon echo and transient fluorescence are formulated by S^3, and transient stimulated Raman spectroscopy by S^5.

2.3 Solvent effect on optical dynamics

There are different methods, with various levels of sophistications, to describe the influence of a solvent on the stationary absorption and fluorescence spectra, and on the dynamics of a molecular system. Assume that a molecule in the gas phase is described by its Hamiltonian. For the molecule in a solvent bath, additional terms must be added which describe solute-solvent interactions. Here very briefly, Kubo and Brownian Oscillator Models, as two methods dealing with solvent effects on optical dynamics are reviewed.

2.3.1 Kubo's model (mostly based on Ref. 23.)

In Kubo's approach the effect of solvent is considered as a small fluctuation in the energy gap between ground and electronically excited states of a molecule. Therefore, ω as the frequency of this transition can be modulated by a time dependent fluctuating term

$\omega(t)=\omega_0+\Omega(t)$ *and* $\Omega(t)<<\omega_0$ (2.12)

here ω_0 is the mean frequency of transition and $\Omega(t)$ is a small fluctuating part with Gaussian probability distribution. Thus the total Hamiltonian is given by

$H_g=H_{0g}$; $H_e=H_{0e}+\hbar\Omega(t)$ (2.13)

here H_g and H_e are the total Hamiltonians for ground and excited electronic states, H_{0g} and H_{0e} are the same quantities *in vacuo* , and $\hbar\Omega(t)$ describes the solvent effect on the excited−state Hamiltonian.

Time evolution of transition dipole moment in the absence of solvent fluctuation can be given as follow[23]

$$\mu_{10}(t) = \left\langle 1 \middle| e^{\frac{i}{\hbar}Ht} \mu\, e^{-\frac{i}{\hbar}Ht} \middle| 0 \right\rangle = \mu_{10} e^{-\frac{i}{\hbar}(\varepsilon_1 - \varepsilon_0)} \Rightarrow \mu_{10}(t) = \mu_{10} e^{-i\omega t} \tag{2.14}$$

where ε_0 and ε_1 are the energies of the molecule in its ground and first excited state. For a molecule in solution, the transition frequency is time dependent and is represented by

$$\mu_{10}(t) = \mu_{10} e^{i\int_0^t \omega(t')dt'} . \tag{2.15}$$

Now linear response can be calculated

$$S^1(t) = \left\langle \mu(t)\mu(0) \right\rangle = \mu_0^2 e^{-i\omega t} \left\langle e^{-\int_0^t d\tau \Omega(\tau)} \right\rangle = \mu_0^2 e^{-i\omega t} \phi(t) . \tag{2.16}$$

Expanding this equation in power series of Ω(t) and changing the integral variables leads to[24]

$$\phi(t) = \exp\left[-\frac{1}{2}\int_0^t dt_1 dt_2 \left\langle \Omega(t_1)\Omega(t_2) \right\rangle \right] = \exp\left[- < \Omega^2 > \int_0^t dt'(t - t')C(t) \right] \tag{2.17}$$

where $C(t) = \left\langle \Omega(t)\Omega(0) \right\rangle$ is the time correlation of energy fluctuations. In deriving Eq. (2.17) the fact was used that the correlation refers to a stationary process, *i.e.* it depends only on time intervals (i.e $\left\langle \Omega(\tau + t)\Omega(\tau) \right\rangle = \left\langle \Omega(t)\Omega(0) \right\rangle$). Thus, according to the Wiener-Khintchine theorem, the power spectrum is given by[25]

$$\begin{aligned} I(\omega) = \frac{1}{2\pi}\int_{-\infty}^{\infty} \phi(t) e^{-i\omega t} dt = \frac{1}{2\pi}\int_{-\infty}^{\infty} dt \exp\left[-i\omega t - \Delta^2 \int_0^t (t - \tau)C(\tau)d\tau \right] = \\ = \frac{1}{2\pi}\int_{-\infty}^{\infty} dt e^{-i\omega t} e^{-gt} \end{aligned} \tag{2.18}$$

here $\Delta^2 = \left\langle \Omega^2 \right\rangle$ is a parameter which shows the magnitude of fluctuation and *C(τ)* determines the rate of frequency modulation. In the literature, usually $g(t) = - < \Omega^2 > \int_0^t dt'(t - t')C(t)$ is separately termed as line shape function.

In terms of optical transitions, Eqs. (2.18) implies that as a result of solvent effect, the line shape function is determined by the time correlation of the energy gap between ground and excited state.

2.3.2 Brownian oscillator model (mostly based on Ref. 26.)

As was shown in the previous section, in Kubo's approach the influence of solvent bath is regarded as a fluctuating part in the transition frequency between two energy levels. There is no provision in this model for spectral shifts. In a more advanced theory of Brownian Oscillators, the interaction of a molecular probe with the solvent bath is formulated by a set of nuclear modes. Each of the modes is displaced between ground and excited electronic states (thus providing for spectral shifts), and also experiences Brownian motion (providing for broadening, for example).[27,28,29,30,31] Connection between modes and solvent are made by a friction coefficient γ which in general is a time dependent parameter. Typically harmonic potential surfaces are assumed, with displacement in the excited state, as mentioned. Therefore vertical fluctuations in energy are mapped linearly onto coordinate q(t). Nuclear modes dynamics can be described by Langevin equation[27]

$$\ddot{q} + \gamma\dot{q} + \omega_0^{\,2} q = f(t) \tag{2.19}$$

where ω_0 is the characteristic frequency for nuclear motion. Random force f(t) and friction constant γ are related via fluctuation-dissipation theorem

$$\langle f(t) f(0) \rangle = \frac{\gamma}{k\,T}\delta(t)\,. \tag{2.20}$$

In this simple case the correlation function of the coordinate q(t) is given by[27]

$$C(t) = \langle q q(t) \rangle = \exp(-\gamma\ t/2)\left[\cos(\omega\ t) + \frac{\gamma}{2\omega}\sin(\omega\ t)\right] \text{ where}$$
$$\omega = \left[\omega_0^{\,2} - (\frac{\gamma}{2})^2\right]^{1/2}. \tag{2.21}$$

Eq. (2.21) is obtained with the assumption that random force f(t) is memoryless and its time correlation is described by a delta function. In more general cases, when the friction coefficient is time dependent (with memory), correlation functions are given by more complicated forms. Kubo's line shape can also be constructed from this

correlation function. If the solvent effect is removed (γ=0) then the correlation is purely oscillatory which describes nuclear coherent states.

2.4 Linear response formalism (largely based on Refs. 23 and 32.)

In this section the basic concepts of correlation functions and linear response functions, as doorways for understanding solvation dynamics, are reviewed.[25,33,32] Let us start with *Fermi's golden rule* in order to show that a correlation function is a familiar concept. For an ensemble of molecules perturbed by an external electric field the rate of energy loss of the radiation is given by[34]

$$\dot{\varepsilon} = \sum\sum \rho_i \hbar\omega_{fi} P_{f\leftarrow i} = \frac{\pi E_0^2}{2\hbar} \sum_i \sum_f \omega_{fi}(\rho_i - \rho_f) \left| \left\langle f \left| \hat{u}_0 \cdot \mu \right| i \right\rangle \right|^2 \delta(\omega_{if} - \omega) \tag{2.22}$$

here $P_{i\to f}$ is the probability of the transition from state *i* to *f,* μ is the dipole moment of the molecules, *E* is the external electric field, ρ_i is the probability of finding the system in state *i*, $\hat{u}_0$ is the unite vector in the direction of electric field and finally $\omega_{fi}=\omega_f-\omega_i$. After some manipulations, from the rate of energy loss, one obtains the absorption line shape

$$I(\omega) = \frac{1}{2\pi} \int_{-\infty}^{+\infty} dt\ e^{-i\omega t} \left\langle \mu \cdot \mu(t) \right\rangle . \tag{2.23}$$

This equation states that the absorption line shape is the Fourier transform of the autocorrelation of the dipole moments of the absorbing molecules. From here one can build a bridge between frequency–dependent stationary absorption and time resolved experiments.

Now let us consider the problem in more detail. Assume a system with Hamiltonian H_0. Applying a weak time–dependent external field *F*(t) to the system adds an additional term to the Hamiltonian

$$H^1 = -A.F(t), \tag{2.24}$$

here A is an interaction matrix while F(t) is a time-dependent scalar. The response of the system can be obtained by measuring a physical quantity of the system. If the perturbation is weak, linear response should deliver an accurate approximation. Now let us calculate the time evolution of the system by solving the Liouville equation (Eq.

(2.4)).[35] One may write ρ as the summation of unperturbed part plus small perturbed one ($\rho=\rho_0+\Delta\rho$) and obtain the time evolution of $\Delta\rho$ as[32]

$$\frac{d\Delta\rho}{dt} = -i\ell_0\Delta\rho - \frac{1}{i\hbar}[A,\rho]F(t) \tag{2.25}$$

where $-i\ell_0\Delta\rho = \frac{1}{i\hbar}[H,\Delta\rho]$ and $H=H_0+H^1$. Now by solving Eq. (2.25), $\Delta\rho$ can be obtained

$$\Delta\rho = -\frac{1}{i\hbar}\int_{-\infty}^{t} e^{i(t'-t)\ell_0}[A,\rho_0]F(t')\ dt'. \tag{2.26}$$

Using Eq. (2.26), the expectation value of a physical quantity B can be calculated

$$\langle B(t)\rangle = \langle B|\Delta\rho\rangle = Tr[B\Delta\rho(t)] = -\frac{1}{i\hbar}\int_{-\infty}^{t} Tr\{B(t-t')[A(t'),\rho_0(t')]\}F(t')\ dt' \tag{2.27}$$

here for simplicity we have assumed that the average of B in the absence of external field is zero. From Eq. (2.27) the response or after-effect function is defined

$$\phi(t) = \frac{1}{i\hbar}Tr\{\ [\rho_0,A]B(t)\} = \frac{1}{i\hbar}Tr\{\rho_0[A,B(t)]\} \tag{2.28}$$

where we have used the fact that trace is invariant under the permutations of the operators. Thus, the expectation value of B can be summarized as

$$\langle B(t)\rangle = \int_{-\infty}^{t}\phi(t-t')F(t')\ dt'. \tag{2.29}$$

Eq. (2.29) is the first order approximation of Eq. (2.9) when B is total polarization P and A is the polarization operator μ. Assuming a canonical distribution function for ρ and using the identity[32]

$$\begin{aligned}
[A,\exp(-\beta H)] &\equiv \exp(-\beta H)\int_0^{\beta} d\lambda \exp(H\lambda)[H,A]\exp(-H\lambda) \\
&= \frac{\hbar}{i}\exp(-\beta H)\int_0^{\beta} d\lambda \exp(H\lambda)\dot{A}\exp(-H\lambda) \\
&= \frac{\hbar}{i}\exp(-\beta H)\int_0^{\beta}\dot{A}(-i\hbar\lambda)\ d\lambda \\
&\Rightarrow [\rho,A] = \frac{\hbar}{i}\int_0^{\beta}\rho\ \dot{A}(-i\hbar\lambda)\ d\lambda = i\hbar\beta\rho\tilde{\dot{A}}
\end{aligned} \tag{2.30}$$

Eq. (2.28) can be recast in the following form

$$\phi(t) = \beta\ Tr\left[\rho_0 B(t)\tilde{\dot{A}}\right]. \tag{2.31}$$

The tilde describes the Kubo transfer as $\tilde{\dot{A}} = \frac{1}{\beta}\int_0^\beta e^{\lambda H_0}\dot{A}e^{-\lambda H_0}d\lambda$. Finally the response function is expressed in the following forms

$$\phi(t) = \frac{1}{i\hbar}Tr\{\rho_0[A, B(t)]\} = \beta\ Tr\left[\rho_0 B(t)\tilde{\dot{A}}\right]. \tag{2.32}$$

2.4.1 Debye relaxation (mostly based on Ref. 25.)

As the first example we consider the Debye relaxation of a system consist of N molecules with dipole moments μ and total polarization P=Nμ. The aim is to obtain the response of such system to an external electric field and calculate its susceptibility. The experiment is conceptually as follows: a capacitor, having dielectric with permittivity ε between its plates, is suddenly discharged. The external electric field performs a step-function change, and the polarization autocorrelation represents the response of the system. The total Hamiltonian of the system in the presence of external electric field is given by

$H=H_0 - P\cdot E(t)$. (2.33)

In frequency space the susceptibility of the system has the following relation with total polarization

$$P = \chi(\omega)E \qquad \text{and} \qquad \chi(\omega) = \int_0^\infty e^{-i\omega t}\phi(t)\ dt\,. \tag{2.34}$$

Referring to notations of linear response, polarization P stands for variables A and B in Eqs. (2.24) and (2.31). Since D=E+4πP (*in cgs*) and D=εE, susceptibility and permittivity are related

$$\varepsilon(\omega) = 1 + 4\pi\chi(\omega)\,. \tag{2.35}$$

For such system, the corresponding response function is given by

$$\phi(t) = \frac{1}{i\hbar}Tr\{\rho_0[P, P(t)]\} = \beta\ Tr\left[\rho_0 P(t)\tilde{\dot{P}}\right] \tag{2.36}$$

where dot stands, as usual, for the time-derivative of the variable. For a dilute ensemble, in which cross correlation between dipoles is negligible Eq. (2.36) can be written in a simpler form

$$\phi(t) = N\beta\left\langle \dot{\mu}(0)\mu(t)\right\rangle . \tag{2.37}$$

Since the response function is a stationary quantity and independent of the time origin, it can be shown that

$$\left\langle \dot{\mu}(0)\mu(t)\right\rangle = -\frac{d}{dt}\left\langle \mu(0)\mu(t)\right\rangle \tag{2.38}$$

Avoiding tedious task of solving equation of motions for each individual dipole in a dense system, one may assume a simple relaxation of the dipole autocorrelation to facilitate the calculations. In a Debye theory it is assumed that the dipole autocorrelation, due to collision between neighboring dipoles, decays exponentially with time constant τ_D

$$\left\langle \mu(0)\mu(t)\right\rangle = \mu_0 e^{\frac{-t}{\tau_D}} . \tag{2.39}$$

Exponential decay of dipole correlation leads to an interesting result. By taking time derivative of Eq. (2.39) one obtains the response function through Eqs. (2.38) and (2.37). Susceptibility can be calculated by taking Fourier Laplace transform of the response function (see Eq. (2.34))[25]

$$\chi(\omega) = \beta\mu_0^2\left(\frac{1}{1+\omega^2{\tau_D}^2} - \frac{i\omega\tau_D}{1+\omega^2{\tau_D}^2}\right). \tag{2.40}$$

finally using Eq. (2.35) Debye equations can be derived

$$\varepsilon'(\omega) - 1 = 4\pi\beta\mu_0^2\left(\frac{1}{1+\omega^2{\tau_D}^2}\right), \tag{2.41}$$

$$\varepsilon''(\omega) = 4\pi\beta\mu_0^2\left(\frac{\omega\tau_D}{1+\omega^2{\tau_D}^2}\right). \tag{2.42}$$

2.4.2 Pulse and step-function responses (mostly based on Ref. 23.)

It is interesting to consider the response of a system to two types of external forces. In the first case (Fig. 2.1a) a delta function field at time t_1 is exerted

$$F(t) = \delta(t - t_1) . \tag{2.43}$$

Placing Eq. (2.43) into the Eq. (2.29) and using definition of Heaviside function $\theta(t) = \int_{-\infty}^{t} dt' \delta(t') = \begin{cases} 1 & t > 0 \\ 0 & t < 0 \end{cases}$, one gets

$$\langle B(t) \rangle = \phi(t - t_1)\theta(t - t) \tag{2.44}$$

here for the sake of simplicity the instantaneous response has been omitted. If there is a correlation between variables *A* and *B* (see Eq. (2.32)) the response is not instantaneous and a part of it lags behind and response $\phi(t - t_1)$ reaches to zero at times after t_1.

In the second case (Fig. 2.1.b) we assume that a constant external field is suddenly switched off. Now a Heaviside function describes the external field

$$F(t) = \theta(t - t_1). \tag{2.45}$$

Substituting Eq. (2.45) into Eq. (2.29) delivers an interesting concept. In this case the averaged quantity (*B* in Eq. (2.29)) is related to the integral of the pulse response

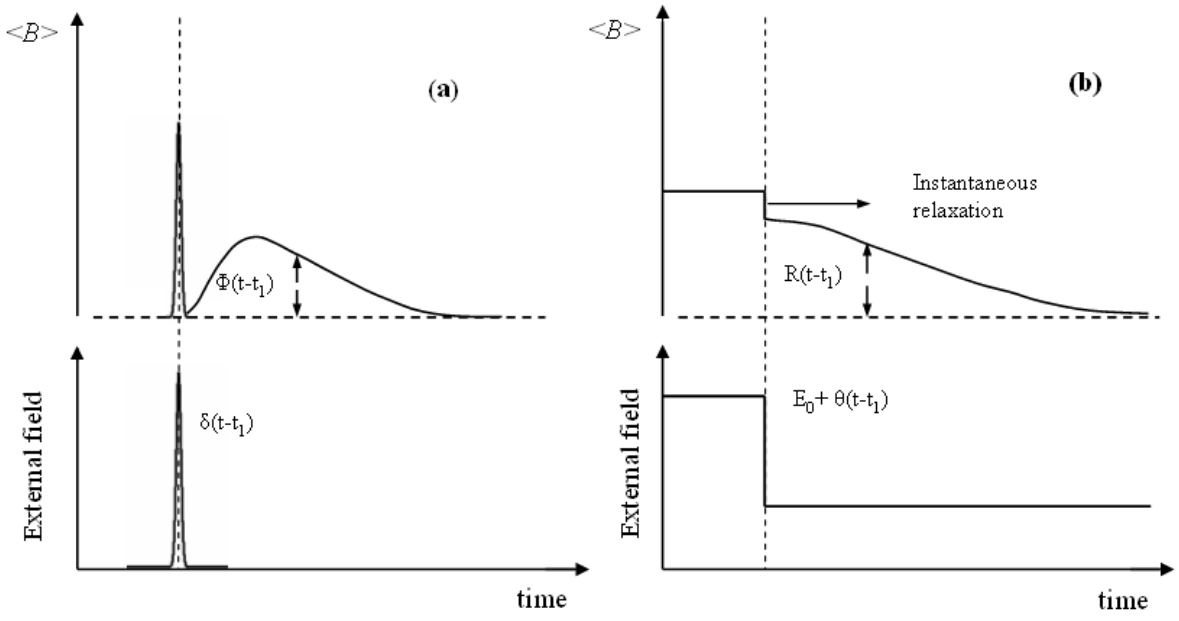

Fig. 2.1 Response of a system to the (a) delta function and (b) step-function types of external fields.[23]

$$R(t) = \int_t^\infty dt' \phi(t') \qquad \text{or} \qquad \phi(t) = -\frac{d}{dt} R(t) \tag{2.46}$$

here R(t) is termed relaxation function, whereas $\phi(t)$ is termed pulse response function. Eq. (2.46) implies that properties of a system can be obtained either from response or relaxation functions.

In frequency space one can introduce the susceptibility as the Fourier Laplace transform of the response function

$$\chi(\omega) = \int_0^\infty e^{-i\omega t} \phi(t) dt + const\,. \tag{2.47}$$

A constant contribution accounts for instantaneous response. Substituting the derivative of relaxation function in Eq. (2.47) yields

$$\chi(\omega) = const + R(0) + i\omega \int_0^\infty e^{-i\omega t} R(t) dt\,. \tag{2.48}$$

One can write Eq. (2.48) in another form[23]

$$\frac{\chi(\omega) - \chi(0)}{i\omega} = \int_0^\infty e^{-i\omega t} R(t) dt \tag{2.49}$$

where $const + R(0)$ are taken as zero component of susceptibility.

As a brief summary, if a system is perturbed by a weak external field F(t), following equations can be derived as a results of introducing a perturbative term in the total Hamiltonian, H^1=-$A.F$(t)

Linear response: $\left\langle B(t) \right\rangle = \int_0^t \phi(t-t') F(t')\ dt' \overset{Fourier\ \ Transfer}{\Leftrightarrow} \left\langle B_\omega \right\rangle = \chi_\omega F_\omega$

Response function: $\phi(t) = \frac{1}{i\hbar} Tr\{\rho_0 [A, B(t)]\} = \beta\, Tr\left[\rho_0 B(t) \dot{\tilde{A}}\right] = \beta \left\langle \dot{\tilde{A}} B(t) \right\rangle$

Relaxation function: $R(t) = \int_t^\infty dt' \phi(t') = \left\langle AB(t) \right\rangle$ or $\phi(t) = -\frac{d}{dt} R(t)$

2.5 Fluctuation dissipation theorem (based on Ref. 36.)

Fluctuation-dissipation theorem (FDT) -in virtue of only equilibrium information of a system- addresses the question how quickly a new equilibrium is achieved when a weak external field perturbs the system. In FDT, a relation between an equilibrium correlation function (i.e. light scattering) and linear response of a system to an external perturbation (i.e. polarization relaxation) is established. Therefore, the problem of solving a response in non-equilibrium state reduces to the equilibrium one.[36] Eq. (2.50) describes the relation that in FDT one needs to establish

$$\bar{S}_{AB}(t-t') = \langle A(t)B(t')\rangle \overset{?}{\Leftrightarrow} \frac{1}{2\hbar}\langle [A(t), B(t')]\rangle = \varphi_{AB}(t-t') \tag{2.50}$$

here $\bar{S}_{AB}(t-t')$ is the time correlation between operators *A* and *B* which is obtained according to the information of the system in equilibrium, and $\varphi_{AB}(\omega)$ is the response of the system observed in operator *B*. $\langle\cdots\rangle$ denotes the ensemble average. One may transfer Eq. (2.50) into the frequency domain and obtains following relations between *spectral densities* (Fourier transform of $\bar{S}_{AB}(t-t')$) with positive and negative arguments

$$\bar{S}_{BA}(-\omega)/\bar{S}_{AB}(\omega) = e^{-\beta\hbar\omega} \tag{2.51}$$

here $\bar{S}_{AB}(\omega)$ and $\bar{S}_{BA}(-\omega)$ (the spectra of cross-correlations between *A* and *B*) indicate creation and annihilation of excited state with energy difference, $\hbar\omega = \varepsilon_i - \varepsilon_f$ and density $e^{-\beta\hbar\omega}$. Response function also can be transferred in frequency domain and written in the following form

$$\chi''(\omega) = \frac{1}{2\hbar}\left[\bar{S}_{AB}(\omega) - \bar{S}_{BA}(\omega)\right] = \frac{1-e^{-\beta\hbar\omega}}{2\hbar}\bar{S}_{AB}(\omega) \tag{2.52}$$

here $\chi''(\omega)$ is the response function in frequency space. Introducing a symmetric form of spectral density $S_{AB}(\omega) = \frac{1}{2}\left[\bar{S}_{AB}(\omega) + \bar{S}_{BA}(\omega)\right] = \frac{1}{2}\bar{S}_{AB}(\omega)(1+e^{-\beta\hbar\omega})$ leads to the final result

$$S_{AB}(\omega) = \hbar\coth(\frac{\beta\hbar\omega}{2})\chi''_{AB}. \tag{2.53}$$

Symmetry consideration of the response function shows that $\chi''_{AB}(\omega)$ is the imaginary part of total susceptibility. In the classical limit where $\hbar \to 0$ Eq.(2.53) is simplified to

$$S_{AB}(\omega) = \frac{2}{\beta\omega}\chi''_{AB}(\omega). \tag{2.54}$$

Eqs. (2.53) and (2.54) imply that, relaxation function in non-equilibrium can be obtained only by calculating the correlation function of the physical quantities in equilibrium.

2.6 Energy relaxation-reaction field approach (mostly based on Ref. 37.)

A solute with surrounding solvent molecules, in a thermodynamically stable state, is termed a solvation system; the corresponding free energy is termed solvation energy. In the case of aqueous solutions, the term "hydration" is used instead of solvation.[38] Since solvation is central in chemistry, many studies have been devoted to understand its mechanism. Among them, transient spectroscopic studies of solvation allowed to observe the stabilization path of energy in real time. The solvent effect on spectral positions also can, more simply, be seen in stationary spectra. Both absorption and emission of a polar chromophore are affected by variations of the local environment and solvent polarity. Simplified versions of solute-solvent interaction are discussed with Onsager´s reaction field model.[39] In this model one assumes a spherical shape for the solute inside the solvent bath, with its dipole μ in the center. In this case the energy of the system is given by

$$E = -R.\mu, \quad \text{where} \quad R = \chi.\mu \text{ and } \chi = \frac{1}{a^3}\left(\frac{\varepsilon_0 - 1}{2\varepsilon_0 + 1} - \frac{n-1}{2n+1}\right) \tag{2.55}$$

here R is the reaction field calculated in the center of the spherical cavity,[37] χ is the susceptibility of reaction field and n is the refractive index of the solvent. In virtue of the Onsager model, a frequency shift between absorption and fluorescence of a polar molecular probe inside a polar solvent is given by the Lippert equation [40,41,42,43]

$$\Delta\nu = \langle\nu_{abs}\rangle - \langle\nu_{flu}\rangle = \frac{(\mu_1 - \mu_0)^2}{hca^3}\left[\frac{\varepsilon - 1}{2\varepsilon + 1} - \frac{n^2 - 1}{2n^2 + 1}\right] + const \tag{2.56}$$

here $\langle\nu_{abs}\rangle$ and $\langle\nu_{flu}\rangle$ are absorption and emission spectral positions, μ_0 and μ_1 are the dipole moments of the molecule in ground and excited states, c is the velocity of

light, *a* is the radius of the cavity where the molecule is located, and *h* is the Planck constant. The first term in the bracket accounts for the reorientation contribution of solvent molecules together with the correlated redistribution of the electrons, while the second term describes the instantaneous electronic contribution.[12] Both spectral positions are shifted compared to the gas phase, due to the solvent interaction.

2.7 Solvation dynamics

Solvation dynamics of a solvatochromic probe inside a solvent bath is shown schematically in Fig. 2.2. Before time zero solute and solvent molecules are energetically in equilibrium. After femtosecond excitation a new charge distribution is created and equilibrium state of the system is altered. Since femtosecond excitation is faster than any

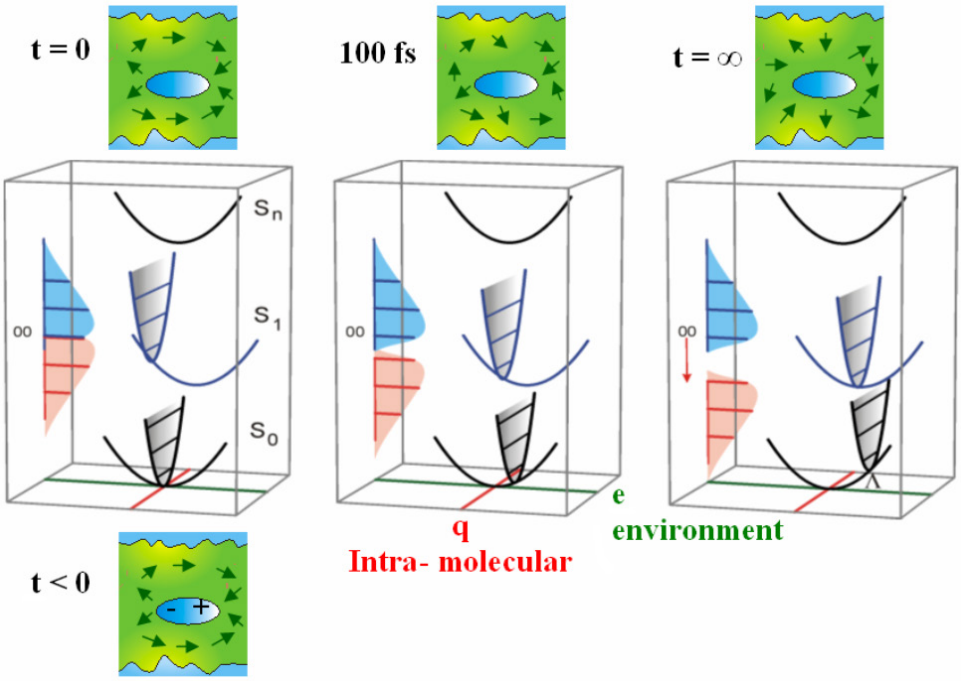

Fig. 2.2 Dynamic Stokes shift of a solvatochromic chromophore in a polar solvent. In the electronic ground state, the solvent environment is in equilibrium with the solute charge distribution. By femtosecond excitation the charge distribution of the molecule is changed, and a non-equilibrium state is created. Transient Stokes shift measurement maps the reorganization path of the solvent toward a new equilibrium. Here e and q represent environmental (=solvent) and intramolecular coordinates, respectively.

nuclear response (Frank Condon transition) a non-equilibrium state is created. Dipolar interactions (in the case of polar solute inside a polar solvent) between solute and solvent alter the free energy of the system. Response of the solvent to the perturbation originates from intrinsic motions of the solvent (libration, vibration, and reorientation) which prepare a new equilibrium in excited state. In other words, solvent reorganization prepares a new equilibrium for the system. The latter motion is mapped into the frequency domain, if one looks at the potential-energy difference between the two electronic states- Experimentally solvation dynamics is obtained through time-dependent Stokes shift (TDSS) measurement.

Using Onsager´s reaction field model one may describe the free energy of the system by electrostatic interaction between solute and solvent. Here we ignore solvent dispersion contributions to the free energy which for most polar solvents is relatively small. As was already mentioned, femtosecond excitation leaves the nuclear motions behind and no entropy alteration occurs in the transition, therefore the free energy can be described by solute-solvent electrostatic interactions.[44,45]

To facilitate the connection between experiment and theories, it is convenient to introduce a normalized energy relaxation function. Its dimensionless character helps to compare dynamics, irrespective of absolute energy values,

$$S_S(t) = \frac{\overline{E}(t) - \overline{E}(\infty)}{\overline{E}(0) - \overline{E}(\infty)} \tag{2.57}$$

here $\overline{E}(t)$ is the free energy of solvation at time t, $\overline{E}(0)$ and $\overline{E}(\infty)$ are the same quantities at time zero, and at a very late time ("infinite") when the system has reached equilibrium. Subscript S refers to solvation energy. As already mentioned, in transient fluorescence one measures the energy difference between ground and excited states $\Delta E_{el}(t)=E_e(t)-E_g(t)=h\nu(t)$, and the relaxation function is given by

$$S_F(t) = \frac{\nu(t) - \nu(\infty)}{\nu(0) - \nu(\infty)} \tag{2.58}$$

here $\nu(t)$, $\nu(0)$ and $\nu(\infty)$ are the transition frequencies between ground and excited state of the molecule in times t, zero, and infinity. In Eq. (2.58) the subscript F refers to transient fluorescence. $S_S=S_F$ is generally accepted if the contribution from intramolecular vibrational relaxation is small. Also it implies that solvation dynamics can be achieved via time resolved Stokes shift measurements.

To formulate the solvation energy relaxation we use the discussion in Sec.2.4.2. In solvation relaxation, a step-function change in charge distribution, after a short pulse excitation, is regarded as a source for creating an external field in the medium. For a well-chosen chromophore one may assume that the created charge distribution remains constant for a long period of time (at least, much longer than the solvent reorganization time). To simplify the problem, one may use Onsager model in which molecular probe is a point dipole in the center of a spherical cavity carved out of a medium with permittivity $\varepsilon(\omega)$. For such system solvation energy is given by

$$E(t) = -\mu(t) \cdot R(t) \qquad \text{and} \qquad \mu(t) = \mu_0 + \theta(t)(\mu_1 - \mu_0) \tag{2.59}$$

where $R(t)$ is the time dependent reaction field in the position of the dipole, created by surrounding dielectric, $\theta(t)$ is the Heaviside function, and μ_1 and μ_0 are the static dipole moments of the probe in the excited and ground states. Solvation dynamics is obtained via frequency dependent susceptibility of the reaction field[46]

$$\chi_R(\omega) = \frac{1}{a^3}\left(\frac{\varepsilon(\omega) - 1}{2\varepsilon(\omega) + n_c^2} - \frac{n^2 - 1}{2n^2 + n_c^2} \right) \tag{2.60}$$

here n_c , a refractive index of the cavity, is also added to the Glarum function. It is related to the polarizability of the solute α through Clausius-Mosotti equation[37]

$$\frac{\alpha}{r^3} = \frac{n_c - 1}{n_c + 2} \tag{2.610}$$

where r is the radius of the spherical cavity. Pulse response of the system is obtained by taking the inverse Fourier Laplace transform of the susceptibility

$$\Phi(t) = £^{-1}\{\chi(\omega)\}, \tag{2.62}$$

and its integration delivers the solvation relaxation

$$S(t) = \int_t^\infty \Phi(t')dt' . \tag{2.63}$$

Also one may use the compact formula given in Eq. (2.49) to obtain solvation relaxation[47]

$$S(t) = £^{-1}[\{\chi(\varepsilon(0)) - \chi(\varepsilon(i\omega))\}/(i\omega)] \tag{2.64}$$

2.8 Solvation dynamics models (based on Refs.1, 48, 49, 50.)

2.8.1 Homogenous Models

2.8.1.1 Simple continuum model

In this model, solute is assumed as a point dipole in the center of a spherical cavity immersed in solvent bath. Solvent is considered as a continuous dielectric medium surrounding the solute. In this simple approach dielectric of the solvent is presented only by a single Debye term $\varepsilon(\omega) = \varepsilon_\infty + \frac{\varepsilon_0 - \varepsilon_\infty}{1 + i\omega\tau_D}$. Using the susceptibility of reaction field (Eq. (2.60)) the solvation relaxation is obtained (see Eq. (2.64)) as

$$S(t) = \exp(-t/\tau_L). \tag{2.65}$$

The so-called "longitudinal relaxation time" τ_L which is a function of ε_0, ε_∞ and τ_D.[45,51,52,53,54] In case that solute resembles a point dipole, τ_L is expressed as

$$\tau_L = \left(\frac{2\varepsilon_\infty + 1}{2\varepsilon_0 + 1}\right)\tau_D, \tag{2.66a}$$

and for an ion as

$$\tau_L = \left(\varepsilon_\infty / \varepsilon_0\right)\ \tau_D. \tag{2.66b}$$

Experimental results from TDSS measurements shows that average time of solvation relaxation usually is placed between the prediction of simple continuum model and τ_D. However, as a simple model it is a useful guide. For methanol with ε_0=33.4, ε_∞=2, and τ_D=52 ps, τ_L is about 3 ps. This example shows that solvation relaxation is, typically, much faster than Debye relaxation. One may illustrate the solvation acceleration as follows.

To measure τ_D , the dielectric medium is placed between the plates of a charged capacitor. In perfect alignment all dipoles are parallel. In such a geometry the net torque exerted from neighboring dipoles has vanished (they are all compensated). Thus, after discharging the capacitor each dipole starts its rotational diffusion independently. In other words, in dielectric relaxation the Debye time τ_D may be though of as diffusive time constant of a single molecule. However in solvation relaxation the geometry is different. In a simple model all solvents dipoles are aligned around a sphere where the solute is located in its center. In such a configuration the net torque from neighboring dipoles is not zero, and unfavorable torque from other

solvent dipoles in addition to the electric field of the solute is exerted on each solvent molecule.[55] Now if the latter field is switched off (by optical excitation) each dipole can not diffuse independently and the rotation is accelerated by the fields from other dipoles. In other words, the cooperative nature of solvent molecular motion speeds up the energy relaxation process and also makes it more complex.

2.8.1.2 Mean spherical approximation (MSA)

In "Mean spherical approximation", in contrast to the simple continuum theory, a structured solvent is assumed around the solute. A dynamical version of this theory was introduced by Wolynes [46] and was further developed by Rips et al[56] and Nichols et al.[57] Here susceptibility of the reaction field is calculated for a system in which solvent molecules are hard spheres with specific size, surrounding a spherical cavity where the solute is a dipole or an ion at its center. As an improvement to the simple theories (see 2.8.1.1) the solute/solvent size ratio enters as a parameter in the calculated spectral relaxation[47,48,58] This model was successful to predict biexponential behavior of the solvation dynamics.[47,48]

2.8.1.3 Simple continuum with entire dielectric dispersion

This model is the extension of the simple dielectric approach (sec. 2.8.1.1), by extending the dielectric dispersion far beyond a single Debye term. Marcus and coworkers showed that solvation dynamics can be calculated quantitatively, by using entire spectrum $\varepsilon(\omega)$.[59] The authors successfully calculated water solvation in excellent agreement with experimental results.[60] Later Ernsting and coworkers corroborated the continuum model in more solvents.[61,62]

For practical calculations, it should be noted that Eq. (2.64) is rather inconvenient, as it requires an inverse Laplace transform of experimental (hence noisy) $\varepsilon(\omega)$ data. Numerically, it is more convenient to construct the spectral density $S(\omega)$ through FDT. Remember that one can connect the time resolved Stokes shift, as a non-equilibrium relaxation phenomenon, to the time correlation of equilibrium fliuctuation, namely of the energy gap between ground and excited state of the molecular probe[63]. We have

$$\delta\Delta E(t) = \Delta E(t) - \langle \Delta E \rangle \tag{2.67}$$

where $\Delta E(t)$ is the energy gap at time *t* and $\langle\ \rangle$ denote the ensemble average. The time correlation function of energy fluctuations is given by

$$C(t) = \frac{\langle \delta\Delta E(0)\delta\Delta E(t) \rangle}{\langle \delta\Delta E(0) \rangle^2}. \tag{2.68}$$

Within linear response approximation one may assume that equilibrium time correlation and non-equilibrium relaxation are equal, $S(t) \approx C(t)$, Therefore, based on FDT and using the susceptibility of the reaction field (Eq. (2.60), one may the construct spectral density

$$C(\nu) = \{1+\coth(h\nu/2\, k_B T)\}\, \chi''_R(\nu) \tag{2.69}$$

where $\chi''_R(\nu)$ is the imaginary part of susceptibility, T is the absolute temperature and k_B is Boltzmann constant. Solvation relaxation can be calculated as cosine transform of the spectral density

$$S(t) = \int_{-\infty}^{+\infty} C(\nu) \cos(2\pi\nu)\, d\nu\ . \tag{2.70}$$

2.8.2 Inhomogeneous models

In these approaches, permittivity of the solvent is assumed either as a function of distance between solute and solvation shell- $\varepsilon(r,\omega)$ - or as a function of wavevector- $\varepsilon(k,\omega)$. In the former, solvation relaxation is obtained via superposition of responses from different shells.[49,64] In the case of solvation relaxation of an ion, Castner et al obtained

$$S(t) = \sum_{k=1}^{n+1} a_k e^{-t/\tau_k} \text{ and } a_k = \left(\frac{1}{\varepsilon_\infty} - \frac{1}{\varepsilon_k}\right)\left(\frac{1}{r_{k-1}} - \frac{1}{r_k}\right) \text{ and } \tau_k = \left(\frac{\varepsilon_\infty}{\varepsilon_k}\right)\tau_D \tag{2.71}$$

where r_k is the radius of shell k with dielectric constants ε_∞ and ε_k.

Spatial heterogeneity of solvation response was proposed by Onsager. According to his so called “inverted snowball” (IS) conjecture, the first solvation shell relaxes slower compared to the shells far apart. Inspired from IS, a more accurate way

to include spatial heterogeneity is available by the $\varepsilon(k,\omega)$ approach. Similar to IS, a wavevector representation of the permittivity $\varepsilon(k,\omega)$ predicts that the solvation relaxation of large **k** components of permittivity are slower than small **k**. Since in dielectric measurements only the permittivity of medium for long wavelength (**k**→0) is determined, main drawback of inhomogeneous models is the lack of experimental **K** dependent permittivity data.[50,65,66,67,68]

2.9 Solvation mechanism

Most of the insights into the mechanism of solvation dynamics come from molecular dynamic (MD) simulations. One may divide total solvation relaxation roughly into three time intervals. In the first part a fast (Gaussian) relaxation is observed and later relaxation may be modulated by an oscillatory behavior which is damped very quickly. At the late time solvation dynamics is diffusive.

In some small solvents like acetonitrile[63] and water[69,70] the Gaussian response makes more than half of the total relaxation (about 70 % in acetonitrile). This relaxation is attributed to the ‘‘free-steaming’’ inertial motion of the solvent molecules where the intermolecular forces has no contribution.[63,71,72,73] (or can be neglected in practice). This motion lasts for a short period of time (typically < 100 fs). Before excitation, the velocity distribution of solvent molecules is given by Maxwell-Boltzmann statistic. Shortly after excitation, the solvent molecules still keep their initial velocities. In the case of water this initial motion is partly ascribed to the librational oscillation of single water molecules in their neighborhoods. Despite the fact that these inertial amplitudes are small, however, a large fraction of energy is relaxed in this time scale because a large number of solvent molecules participates.[74]

On an intermediate time scale an oscillatory behavior may be observed[61] which originates from coherent and collective vibrational and librational motions of solvent molecules. Finally, long time solvation relaxation is attributed to the diffusive, random-walk like motions of the solvent molecules, both in regard to orientation and spatial position.

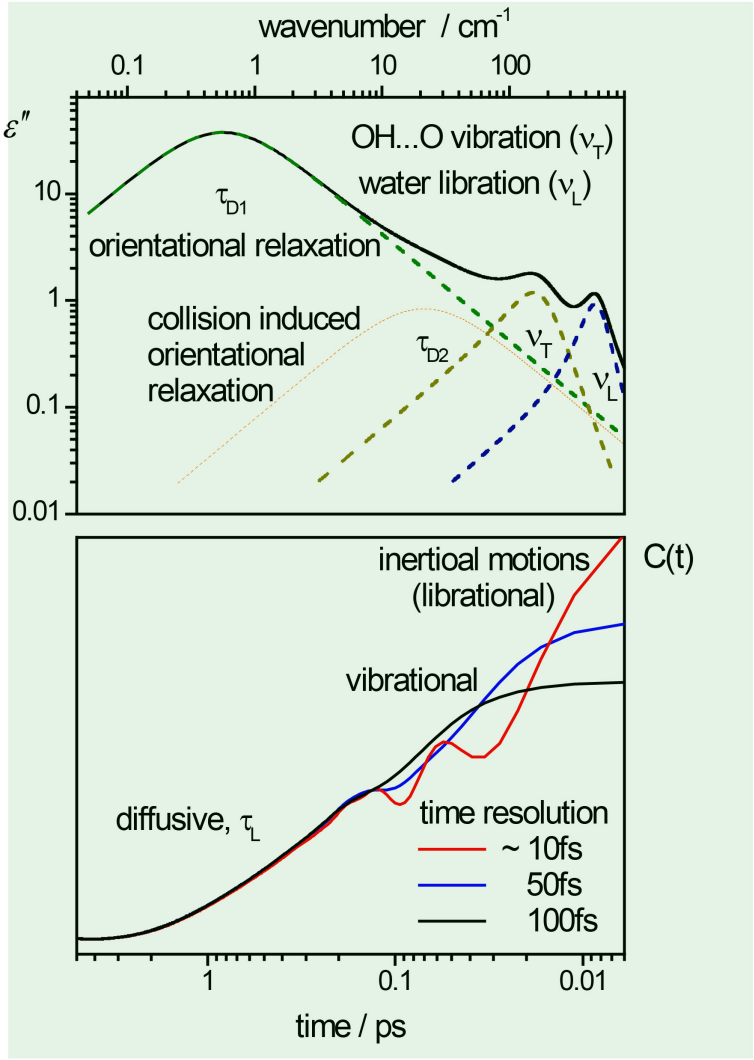

Fig. 2.3 Transient Stokes shift measurements reflect the dielectric response of the medium. Upper panel: The imaginary part of water permittivity, $\varepsilon''(\omega)$, is decomposed into two Debye terms and two resonance components. Lower panel: solvation relaxation S(t) maps the dielectric information in to the energy domain.

Fig. 2.3 summarizes the solvation relaxation mechanism, by comparing the solvation relaxation (bottom) simulated by water dielectric and imaginary part of permittivity (ε″) of water, up to few hundred wavenumber (upper). Here ε″ is decomposed into two Debye terms and two high frequency components. The Debye terms are interpreted as orientational relaxation and collision-induced orientational relaxation of water molecules. Two resonances, at 200 and 500 cm^{-1}, denote the OH…O vibrations and librational motions of water. Energy relaxation observed with different time resolution shows contributions from different motions of the solvent. In

other words, solvent molecular motion is mapped by the energy relaxation curve. By increasing the time resolution in TDSS measurements, ever more details of this motion can be observed.

3 Experimental Section

3.1 Stationary measurements

Stationary absorption spectra were obtained by a VARIAN CARY 300 spectrophotometer. Temperature dependent absorptions were also measured with this system. Stationary fluorescence spectra of samples at room temperature were measured with a SPEX FLUOROLOG-2 fluorometer. Temperature dependent fluorescence spectra were recorded with a SPECTRONICS INSTRUMENTS 8100 fluorometer. The measured raw spectra (count rates as function of wavelength) were converted into quantum distributions over wavelength, by comparison with the emission from a secondary standard lamp (LSP035-Hg(Ar), LOT-ORIEL)

3.2 Femtosecond laser system (partly based on Ref. 75.)

Studying dynamical processes in chemistry, physics and biology requires ultra-short laser pulses. The broad bandwidth and high intensity of such pulses is also needed in telecommunications and metrology. For both reasons the femtosecond laser field developed dizzyingly over the last decades. The Titanium-doped sapphire crystal Ti: Al_2O_3 (Ti:sa) is most frequently used as active medium because of its broad gain bandwidth (more than 400 nm centered around 800 nm).

Increasing the intensity of the laser beam in the Ti:sa crystal changes its refractive index, which is known as the Kerr effect. This effect causes broadening of the spectral bandwidth of laser light, according to the self-phase modulation (SPM) mechanism in which the phase of the light field is modified by a time-dependent term. Spectral broadening is the main reason for generating short pulses in mode locked lasers. Besides spectral broadening, the Gaussian intensity profile of the beam causes stronger change of the refractive index on the optical axis in the center of the crystal, and therefore self-focusing of the beam. Thus, Ti:sa lasers are passively mode-locked analogous to the saturable absorber mechanism: a stable resonator is achieved when the Kerr-lens is included in the cavity design. Consider a recurrent pulse which runs

around in such a Ti:sa oscillator. The temporal center undergoes less loss (because of self focusing) compared to the time wings. Stable cavity and spectrally broad beams are necessary conditions to generate short pulses. In a perturbative process a noise spike (for instance, by tapping one mirror mount in the cavity) can initiate the mode locking process.

The experiments were done with FEMTOLASERS sPro system which has been in use since 1999. The oscillator generates 4 nJ pulses at 800 nm with 12 fs duration, at a repetition rate of 75 MHz. It is pumped by A Verdi-5W laser. Pulses from the oscillator are stretched in time and selected at 500 Hz with a pockels cell. An 8-pass regenerative amplifier is pumped by a PHOTONICS INDUSTRIES DM15-527 laser. After compression with a prism pair and chirped mirrors, 30 fs pulses with 500 μJ energy are obtained. The pulse-to-pulse fluctuations are less than 2%. Pointing stability is achieved after a warm-up time of 2-3 hours.

3.3 Fluorescence up-conversion (based on own publication, Ref. [76].)

A setup for fluorescence up-conversion spectroscopy (FLUPS) was built which has 80 fs temporal response (fwhm) for emission in the spectral range 425 - 750 nm. Broadband phasematching had previously been achieved in this laboratory with a noncollinear geometry, with tilted gate pulses at 1340 nm.[77] But that design still showed strong background from harmonics of the gate pulse, which precluded the observation of fluorescence at $\lambda > 600$ nm. For the present work the background had to be removed, and therefore the sensitivity was increased significantly. Photometric calibration of the up-conversion process was performed, as usual, with a set of fluorescent dyes. The spectrograph was tested with Coumarin 153 in methanol, for which the peak position, band width, and asymmetry were measured depending on delay time.

3.3.1 Introduction

Time-resolved fluorescence up-conversion was first reported by Mahr and Hirsch in 1975.[13] A chromophore in solution is excited with short optical pulses, and its emission at wavelength λ_F is mixed with short gate pulses at λ_G in a nonlinear optical (NLO) crystal. Sum-frequency-generation occurs at a well-defined crystal orientation when phasematching conditions are met. In this case upconverted light at λ_U is generated and detected. By plotting the intensity $I_U(t)$ as function of time delay t between pump and gate pulses, a "kinetic trace" of the fluorescence at the chosen wavelength is obtained. This kind of measurement is well suited to measure short excited-state lifetimes. In step with advances in ultrafast laser technology, the accuracy improved steadily and the spectral scope widened. Representative examples and some milestones on this way are given in refs. [78-100]

Spectral evolution of the fluorescence may indicate a photochemical reaction or a photophysical process in the excited singlet state; examples are *cis/trans* isomerisation,[80, 93,100] proton-[84,96] or electron-transfer,[83,94,97] and dynamic solvation.[79,89,90,95,101] To understand such processes one must obtain not only an amplitude at various delay times t, but also the shape of the entire fluorescence quantum distribution $F(t,\lambda_F)$. This is usually achieved by recording 10 - 20 kinetic traces $I_U(t)$, corresponding to different λ_F which cover the emission region. The results are depicted schematically in Fig. 3.1. Because the crystal is rotated between recording kinetic traces, their relative amplitudes are usually not defined during measurement. Instead, amplitude scaling is performed afterwards with the help of additional information such as the steady-state emission spectrum of the compound under investigation. Spectral reconstruction then yields the desired transient emission spectra.[102, 103]

For photometric accuracy it is better to record the contiguous emission spectrum for any given delay time. The order of measurement should therefore be inverted. Whereas before, λ_F is kept fixed while t is scanned, now instead, for every

fixed delay the fluorescence wavelength is scanned. By this procedure, intensities for adjacent

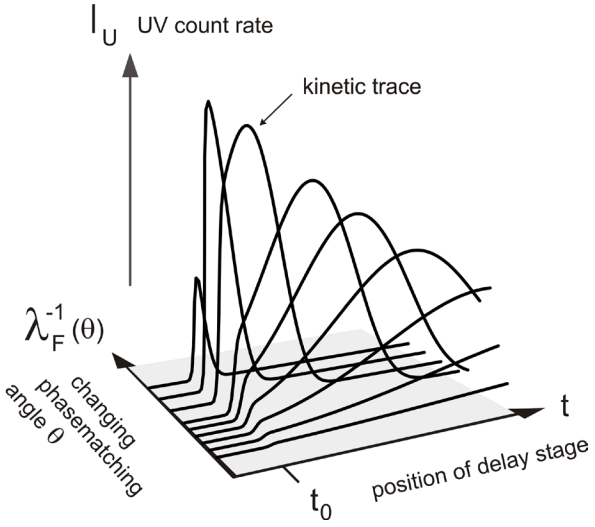

Fig. 3.1 With conventional fluorescence up-conversion, the emission wavelength λF is kept fixed while the time delay t is scanned, resulting in a kinetic trace. Relative amplitudes are obtained with the help of the stationary fluorescence spectrum. Transient spectra are constructed from 10-20 traces.

emission wavelengths are compared directly, allowing a more accurate correction of the apparatus response which may strongly depend on wavelength. Coverage of the fluorophore's emission region has been realized in various ways. The methods are (i) rotation of the NLO crystal while synchronously scanning the detection monochromator, [90,92, 104] (ii) wobbling the crystal while detecting with a spectrograph, [105] and (iii) simultaneous phasematching across a broad spectral range followed by multiplex detection. [106,107, 77]

Broadband fluorescence up-conversion spectroscopy (FLUPS), developed systematically in our laboratory along (iii),[106,107, 77] has similarities with ultrafast pulse generation by nonlinear-optical parametric amplification. Indeed, parametric amplification offers an alternative route to time-resolved fluorescence spectra, [108,109] but so far the bandshape could not be recorded accurately with this method. This renders FLUPS more promising. For gating we use near-infrared pulses at $\lambda_G \approx 1340\,\text{nm}$. Tilting of the gate pulses[77] turned out to be crucial to achieve a time resolution (fwhm of instrument response) of 85

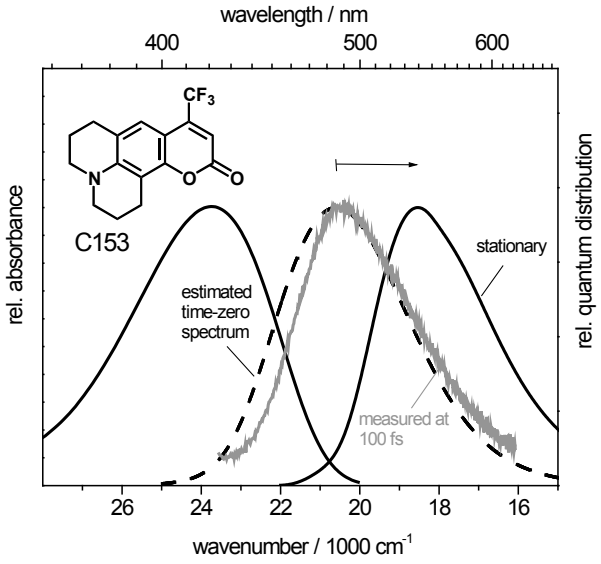

Fig. 3.2 Absorption and fluorescence spectra (quantum distributions over energy) of Coumarin 153 (inset) in methanol. *Dashed*: time-zero estimate [110], *gray:* transient fluorescence spectrum at 0.1 ps of this work. The time-dependent Stokes shift (TDSS) of fluorescence is indicated by a horizontal arrow.

fs. However two deficiencies remained: first, background due to direct fluorescence, and second, signal from the second-harmonic of the gate pulse which blocked the range $\lambda_F > 600$ nm. To overcome these drawbacks, we designed an improved setup which is easier to align, more sensitive and – most importantly - background free. This enables photometric correction of broadband sum-frequency for emission wavelengths $\lambda_F = 425\text{-}750$ nm.

In addition to instrument characterization, the increasing collaboration between laboratories triggers the need for a dynamic fluorescence standard. The dynamics of methanol is a case in point. For such measurements one observes the dynamic solvation of a polar molecular probe, for example Coumarin 153 (C153). Fig. 3.2 shows its absorption and stationary emission spectra. An estimate of the initial fluorescence band, after vibrational relaxation but before solvation,[110] is shown as a dashed line. The methanol dynamics is assumed to be reflected by the spectral position $\tilde{\nu}(t)$ of the fluorescence band (peak position or first moment) as a function of time. Polar solvation of C153 has been a subject for numerous experimental [90,101,77,110, 111, 112] and theoretical

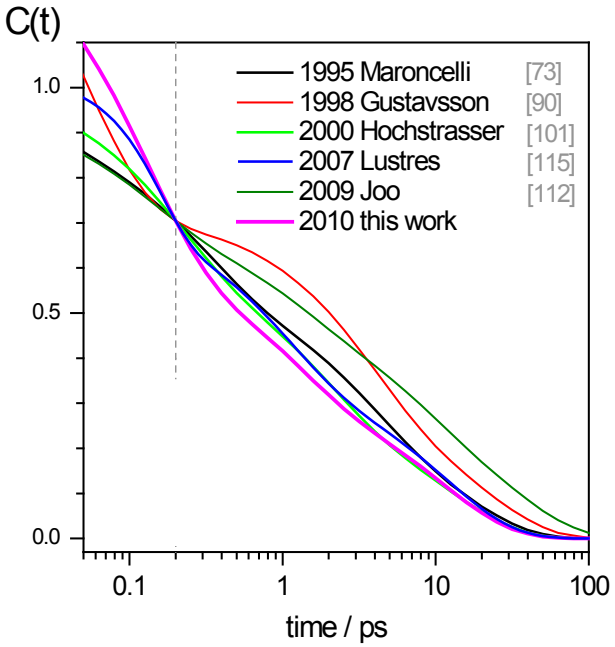

Fig. 3.3 Reports of the dynamic Stokes shift of C153 fluorescence in methanol: The "spectral relaxation functions" C(t) are set to a common value 0.704 at t=0.20 ps [84] when spectra were fully time-resolved. The relative variance at 10 ps, for example, is ~30%, limiting the accuracy of C(t) measurements. Reports of the time-dependent fluorescence bandwidth and asymmetry [84,108, 112] vary more strongly.

[113,114] studies. In Fig. 3.3 and Table 3.1 we compare the $\tilde{\nu}(t)$ curves for methanol reported by different groups.[90,101,112,115] To facilitate the comparison, curves $C(t) \propto \tilde{\nu}(t) - \tilde{\nu}(\infty)$ are shown that are scaled to a common value.[79] at t=0.20 ps. At this time the fluorescence spectrum should have been fully time-resolved in all cases. The variances between these results are notable, considering that C153 is the best-studied polarity probe. Similar discrepancies must be expected when results from different laboratories are combined to support a microscopic model for the spectral relaxation, thus limiting the significance of the model.

Why are the C(t) curves of Fig. 3.3 so different? When measurements of transient absorption are used [101,115] the main problem is the extraction of the band for stimulated emission. Conventional up-conversion methodology,[112] whereby spectra are reconstructed from kinetic traces, suffers from a lack of stationary calibration light on the blue side, in combination with (relatively) sparse spectral coverage. The latter problem is solved by synchronous wavelength scanning of the crystal angle and

detection monochromator, before the next delay time is accessed.[90] In this case geometrical instabilities might play a role.

Broadband up-conversion with a fixed crystal angle, by comparison, simultaneously monitors a range of frequencies and therefore needs less integration time to achieve the same signal/noise; also it allows better control of the geometry. Using this method, we quantify the C153 fluorescence in methanol in terms of peak position, band width, and asymmetry depending on delay time.

Table 3.1 Previous reports of C153 solvation dynamics in methanol: parameters for multiexponential description of C(t).

Ref.	Principal Investigator	λ_{pump} /nm	Method[a]	obsvd[b] $\tilde{\nu}$	a_1	τ_1/ps	a_2	τ_2/ps	a_3	τ_3/ps	a_4	τ_4/ps
73	Maroncelli,1995	385	upcon	avg	0.101	0.030	0.340	0.280	0.298	3.20	0.261	15.300
90	Gustavsson,1998	394	upcon	avg	0.546	0.050	0.262	3.360	0.191	20.13	-	-
101	Hochstrasser,2000	405	SE	peak	0.390	0.185	0.340	1.800	0.270	13.20	-	-
115	Lustres,2007	400	SE	peak	0.300[c]	0.110	0.360	0.980	0.340	12.00	-	-
112	Joo,2009	800[d]	upcon	avg	0.260	0.120	0.200	1.030	0.220	6.54	0.320	31.500
	This work	400	FLUPS	peak	0.535	0.098	0.201	0.774	0.107	5.15	0.157	14.06
				avg	0.497	0.091	0.193	0.737	-0.053	21.92	0.363	14.64

[a] upcon –up-conversion, SE – stimulated emission. Note that the curves apply only to the time-resolved part of the spectral evolution. [b] avg – average emission frequency.
[c] Gaussian initial term $a_1 e^{-t^2/(2\tau_1^2)}$. [d] two-photon excitation.

3.3.2 Sum frequency generation

Fluorescence up-conversion is formed via sum frequency of fluorescence and gate beams. The preliminary conditions are (a) conservation of energy

$$\hbar\omega_U = \hbar\omega_F + \hbar\omega_G \tag{3.1}$$

where $\omega_i = 2\pi c/\lambda_i$ denote the angular frequencies of upconverted (U), fluorescence (F) and gate (G) pulses and (b) phase matching between interacting wavevectors

$$\Delta\vec{k} = \vec{K}_U - (\vec{K}_G + \vec{K}_F) = 0. \tag{3.2}$$

Through relation between wavevectors and corresponding refractive indexes ($k_i = \omega_i n(\omega_i)/c$) phase matching condition can be written as

$$\omega_U n(\omega_U) = \omega_F n(\omega_F) + \omega_G n(\omega_G) \tag{3.3}$$

Refractive index of a birefringent crystal depends on the polarization of propagating light. In uniaxial crystals there is an axis which refractive index is independent of polarization which called optical axis. Polarizations perpendicular to the plane formed by optical axis and direction of propagation is termed ordinary waves and perpendicular polarization is termed extraordinary waves. Refractive index of extraordinary waves (n_e) depends on the angle between optical axis and its $\vec{k}$ vector.

$$n_e(\theta) = n_o \sqrt{\frac{1+\tan^2\theta}{1+(n_o/n_e)^2\tan^2\theta}} \tag{3.4}$$

Consider a negative uniaxial crystal in which $n_o > n_e$. For such crystal phase matching condition for sum frequency generation between fluorescence (400-800 nm) and gate (~1300 nm) beams can be satisfied by selecting n_{oF}, n_{eG} and n_{eU}. Such configuration of polarizations is known as type II phase matching.

3.3.3 Optimized optical setup for fs broadband fluorescence up-conversion

3.3.3.1 Experimental setup

The fs fluorometer is shown in Fig. 3.4. A Ti:sapphire laser (FEMTOLASERS *sPro*) provides 30fs, 500μJ pulses at 800nm (500 Hz repetition rate). This beam is split with a 6:1 ratio. 430 μJ pulses drive a traveling-wave optical parametric amplifier of superfluorescence (TOPAS, LIGHTCONVERSION) which delivers 60μJ, 1340 nm pulses in horizontal polarization, to be used for optical gating. The beam is widened and collimated

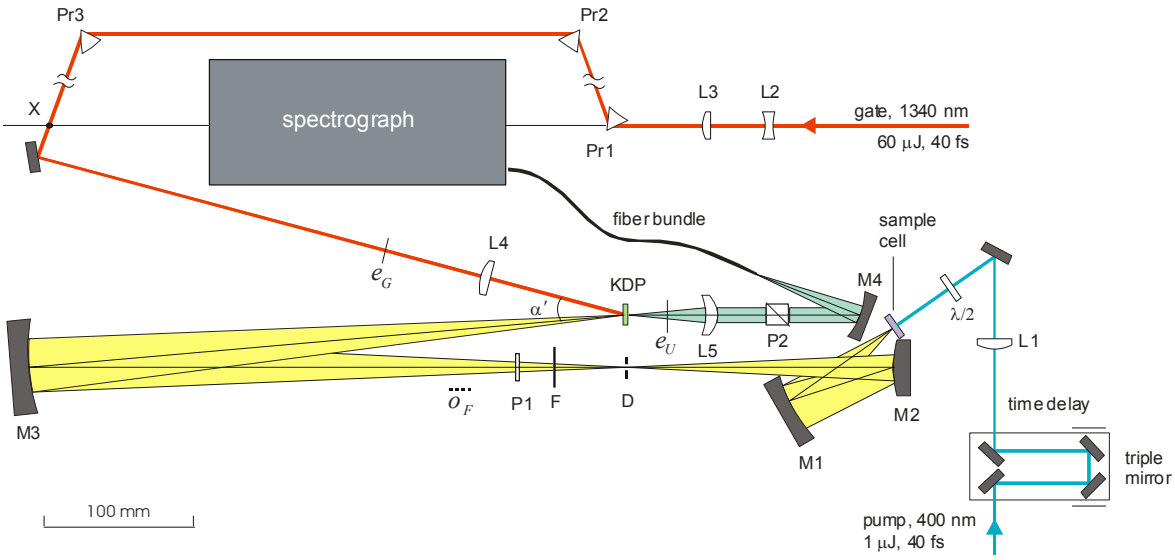

Fig. 3.4 Setup for broadband Fluorescence UP-conversion Spectroscopy (FLUPS). Pr - prisms; M_{1-4} - spherical mirrors; L - lenses; P - polarizers.

by a telescope L_2/L_3 with -50mm / +200mm lenses. All lenses in the gate path have antireflective coating at 1300 nm. For compression and subsequent tilting a combination of three prisms Pr_{1-3} (Schott SF50, apex angle 55.5°) is used. The forth prism of a normal compressor would be located at point X.[116] The tilt angle Φ=3.55° of the pulse front at X (due to the action of prism Pr_3) is calculated from equation 1 in ref. 77. X is imaged by a thin lens L_4 (f= 140 mm) onto the KDP crystal, whereby the tilt angle is leveraged to 20° at the crystal. Fine adjustment of the crystal-lens distance, and hence the tilt, is done simply by observing the generated sum frequency (from the pump laser) on a white piece of paper. When aligned properly, the upconverted light appears and disappears at the same location on the paper when the time difference between pump and gate pulses is varied, otherwise it moves across the wider up-conversion pattern.

3.3.3.2 Gate pulse tilting (mostly based on Ref. 77)

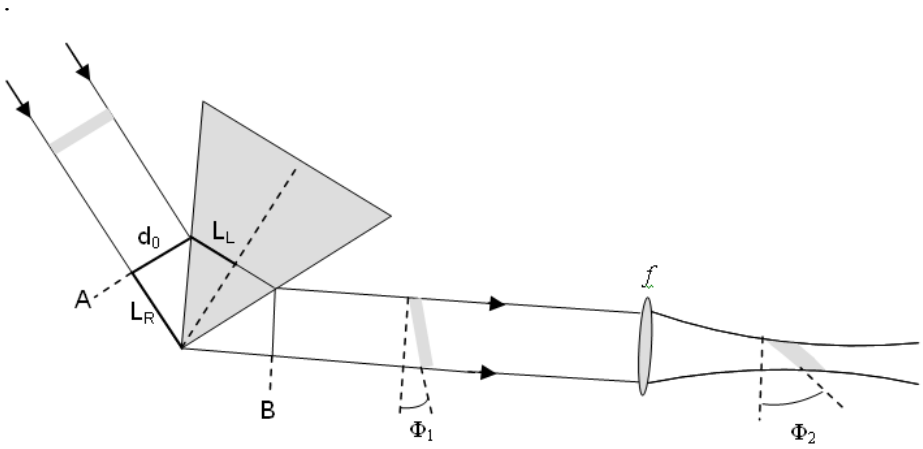

Fig. 3.5 Tilting the pulse front with a prism. And its magnification by a thin lens. Amount of tilting by introducing a prism can be calculated[77]

A large angle between gate and fluorescence beams ($a \approx 20°$) is inevitable for broad phase matching (see Fig. 3.7). As a consequence the two interacting beams cross in the crystal, where their diameter is relatively large (≈0.6 mm). This introduces a loss of time resolution for geometrical reasons (path difference at the two edges of spatial overlap). To regain the time resolution, a prism is introduced in the gate path to tilt the pulse front, to make it overlap the fluorescence pulse front optimally. As is shown in Fig. 3.5**,** the delay time between two sides of a beam (L_L and L_R) with diameter d_0 to pass the distance A-B is given by

$$\Delta\tau(\omega) = \tau_L - \tau_R = \frac{2L_L}{v_g(\omega)} - \frac{2L_R}{c} \tag{3.5}$$

here V_g is the group velocity of the beam inside the prism. Since two path lengths are connected ($L_L/V_{ph}=L_R/c$) one gets

$$\Delta\tau = \frac{2L_L}{v_{ph}}\left(\frac{V_{ph}(\omega)}{V_g(\omega)} - 1\right) \tag{3.6}$$

where V_{ph} is the phase velocity of the ray inside the prism. For a prism with apex angle γ and refractive index n in symmetrical configuration L_L is given by

$$L_L = \frac{d_0 \sin(\gamma/2)}{\sqrt{1 - n^2(\omega)\sin^2(\gamma/2)}} \tag{3.7}$$

$$\Phi_1=\arctan(\frac{c\,\Delta\tau}{d_0}). \quad (3.8)$$

Eq. (3.8) also implies that the tilt angle is independent of beam diameter and merely is a function of prism parameters. Further tilting can be done by a lens, whereby the apex of the prism is imaged onto the NLO crystal. In this case, Eq. (3.9) formulates the increase of tilting angle after a thin lens

$$\tan(\Phi_2)=(\frac{p-f}{f})\tan(\Phi_1) \quad (3.9)$$

where Φ_1 is the tilt angle after prism, P the distance between lens and prism, f the focal length of lens, and Φ_2 the tilt angle of the gate pulse in the image position. For tilting the beam by ~20° (3.55° after prism) we use f=140 mm thin positive lens with P=900 mm.

3.3.3.3 Fluorescence excitation, collection, and imaging

For optical pumping, the rest of the fundamental light is frequency doubled to 400 nm pulses which have 40 fs fwhm after compression. Their polarization is set with a λ/2 plate. After passing a triple mirror on a variable delay stage, attenuated pump pulses (~ 1 μJ) are focused by a thin lens L_1 (f = 200 mm, fused silica, *f.s.*) onto the sample cell, to a spot diameter ≤ 0.1 mm. To obtain an optical image with the subsequent collection optics, the cell is made as thin as possible for a given solution (*f.s.* windows, 0.2 mm thick, are typically spaced 0.2-0.3 mm apart). The sample solution is pumped through the cell which can also be oscillated perpendicular to the beam direction.

An off-axis Schwarzschild objective, Fig. 3.6, refocuses the generated fluorescence with seven-fold magnification at intermediate position D. This new arrangement provides more degrees-of-freedom to the sample cell compared to the axial geometry.[77] Fluorescence emitted from source A into the full angles 18° and 40° in horizontal and vertical planes, respectively, is collected by concave mirror M_1, consistent with the acceptance angles for sum-frequency generation. The effective waist diameter at D is 0.6 mm, allowing to select vertical polarization by a miniature Glan polarizer here.[117,118] For fluorescence wavelengths $\lambda_F \geq 420\,\text{nm}$ a wire-grid polarizer P_1 (Moxtec PPL04C, on 700μm of Corning 1737F glass) is used instead.

Pump scatter and low - frequency Raman signal are reduced with a long-pass edge filter (Schott GG420, 2mm). The fluorescence from D is relayed 1:1 onto the KDP crystal by concave mirror M_3 (R_3= -400 mm).

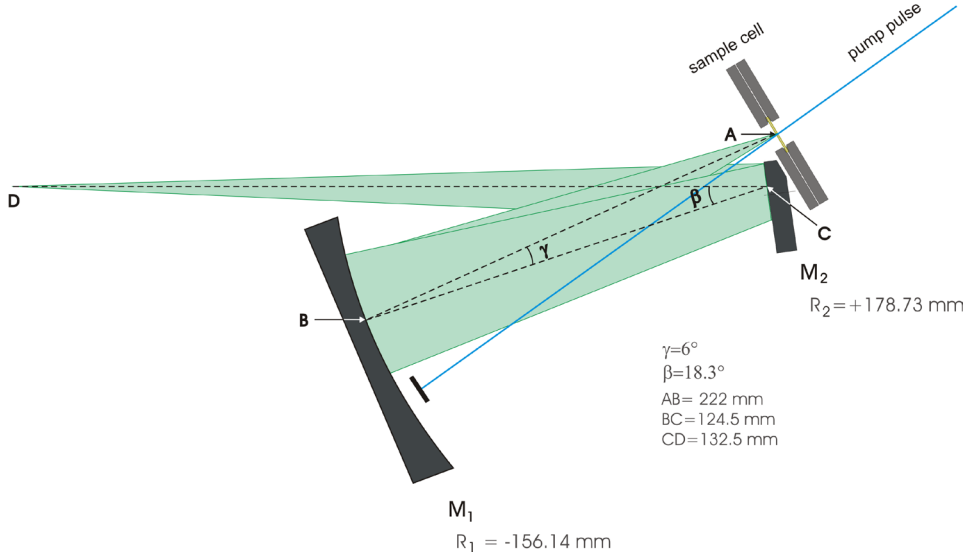

Fig. 3.6 Off-axis Schwarzschild objective for fluorescence collection, allowing to oscillate the sample cell perpendicular to the pump beam.

3.3.3.4 Up-conversion efficiency

For sum-frequency generation we use a KDP crystal cut at $\theta_N = 65°$ with the crystal axis in the horizontal plane. At first sight BBO might be considered superior due to its higher nonlinear susceptibility, but this advantage is more than cancelled by increased dispersion which limits broadband operation. The KDP crystal of thickness L=0.3 mm has antireflection (AR) coating at 520 nm and 1300 nm on the input face, and at 360 nm on the output face (EKSMA). The central rays of the fluorescence and the gate beam form an external gating angle $\alpha' \approx 20°$ at the crystal (internal angle $\alpha \approx 13°$). As it was mentioned Type II phasematching is chosen because it provides the broadest spectral window. Vertically polarized fluorescence at λ_F (*o – ordinary* in terms of crystal axes)

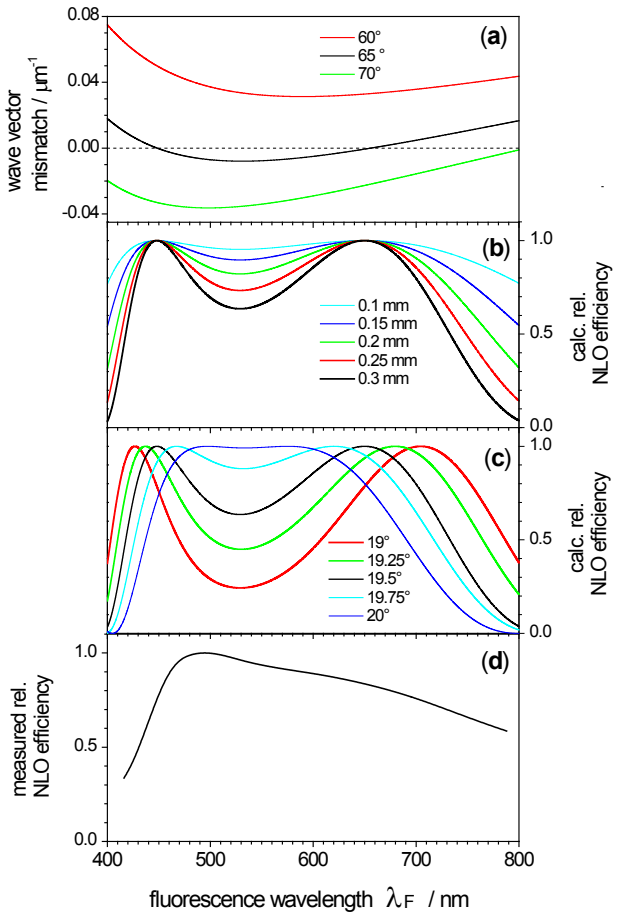

Fig. 3.7 (a) Phase matching curve for type II sum-frequency generation, for three cut angles θ_N of a KDP crystal with gate pulses at 1340 nm. Gate and fluorescence beams have external angle $\alpha' = 19.5°$ between them. (b) Relative conversion efficiency $\left[\frac{\sin(\Delta kL/2)}{\Delta kL/2}\right]^2 \cdot L^2$ for different crystal thicknesses (θ_N=65°, $\alpha' = 19.5°$). (c) Efficiency when varying the angle α', for a crystal of 0.3 mm thickness cut at 65°, with gate wavelength of 1340 nm. (d) Experimental NLO efficiency, i.e. $1/\bar{c}(p)$ of Fig. 3.9, divided by the quantum efficiency of the UV detection system.

interacts with horizontally polarized gate pulses at $\lambda_G = 1340$ nm ($e-extraordinary$), to generate horizontally polarized upconverted light at λ_U (e). Phasematching requires minimizing the wave vector mismatch $\Delta\vec{k} = \vec{k}_{eU}(\theta_U) - \left\{\vec{k}_{oF} + \vec{k}_{eG}(\theta_G)\right\}$ over a wide range of λ_F, for example 400-800 nm. The quantum efficiency of the up-conversion process is [119]

$$\eta_{NLO} = \frac{N_U(z=L)}{N_F(z=0)} = \frac{2^7\pi^3 I_G(z=0)}{c^3}\cdot\left[\frac{\omega_U\omega_F d_{eff}^2}{n_e(\omega_U)n_o(\omega_F)n_e(\omega_G)}\right]\cdot\left[\frac{\sin(\Delta kL/2)}{\Delta kL/2}\right]^2\cdot L^2 \quad (3.10)$$

here N is the photon flux, I_G the intensity of the gate light, L the crystal thickness, n_{eo} the pertinent refractive index, d_{eff} the effective nonlinear susceptibility, and ω_{FGU} are angular frequencies. Fig. 3.7 shows mismatch curves $\Delta\vec{k}(\lambda_F)$ for different cut angles θ_N The efficiency curve $\eta(\lambda_F)$ depends sensitively on thickness L (b) and external beam angle α' (c). A range of angles contributes to the upconverted signal, resulting in the measured efficiency curve (d) which was obtained upon photometric correction. Calculating the group velocity mismatch (between gate and fluorescence light, in the fluorescence direction) for these angles, we find that their passage times differ by < 20 fs.

3.3.3.5 UV collection, dispersion, and detection

The upconverted signal is collimated by a meniscus lens L_5 (f= +50 mm, *f.s.*, AR-coated for the UV). It is then passed through a Glan polarizer P_2 (10x10x10 mm^3, HALLE NACHFL.) to suppress direct fluorescence, pump scatter, and gate harmonics. The concave mirror M_4 (R_4= −70 mm) collects and focuses the signal light on the entrance of a fiber bundle. The bundle (CERAMOPTEC) consists of 30 *f.s.* fibers of 100 μm diameter, compacted into a round shape (0.6 mm diameter) at the input and into a slit (0.1×3.3 mm) at the spectrograph. This UV geometry allows suppressing the background signal which hampered the previous setup for $\lambda_F > 600$ nm, due to better use of the Glan polarizer. An important aspect of the geometry is the large input angle α'.

The spectrograph employs a ruled plane grating (NEWPORT *53-080R*) in a Czerny-Turner mount. Photon loss to unused orders is reduced and the UV efficiency maximized by the choice of blaze angle. The linear wavelength calibration $\lambda_U(p)$ as function of pixel number p is obtained with a mercury lamp. The spectral range $\lambda_U = 307\text{-}478$ nm (corresponding to $\lambda_F = 400 - 750$ nm) is mapped onto a spectrum 21 mm wide. It is recorded with a CCD camera (ANDOR DV420-BU, 25 μm pixel width). For example photons at $\lambda_U = 374$ nm ($\lambda_F = 522$ nm) are binned into a 14.5 cm^{-1} energy segment. The resolution of the spectrograph is 50 cm^{-1} (fwhm of spectral instrument response).

Using the dye C153 in methanol as described below, we measure a count rate of ~100 s^{-1} at long delay times. (The sensitivity is ~1.5-fold higher than in ref. 77 because of the new collection optics, but signal/noise is increased by a factor 3 because background has been removed.) The integration time is 1 s. For a time scan, the background is first recorded four times at negative delay, averaged, and smoothed. This background is subsequently subtracted from each recorded spectrum while the delay is scanned. Results from 16 time scans are individually corrected for cosmic spikes and then averaged.

3.3.4 Correction procedures

3.3.4.1 Photometric correction

The correction is performed with the "standard" dyes BBOT (2,5-bis[5-*tert*-butylbenzoxazolyl(2)]thiophene, CAS 7128-64-5), Coumarin 6H (58336-35-9), Coumarin 153 (53518-18-6) and DCM (51325-91-8) in methanol. The absorbance at the pump wavelength is set to 0.4 in order to limit the inner filter effect. The λ_F regions which were used to correct the spectral response of the setup are 425-630, 470-690, and 600-750 nm for the last three dyes.

Consider an up-conversion experiment with a standard dye whereby a total number $\Sigma^{(U)}$ of counts in the UV is registered. The time delay is chosen to be 250 ps so that nuclear relaxation in methanol has ceased. Actually one records the "technical" signal- or

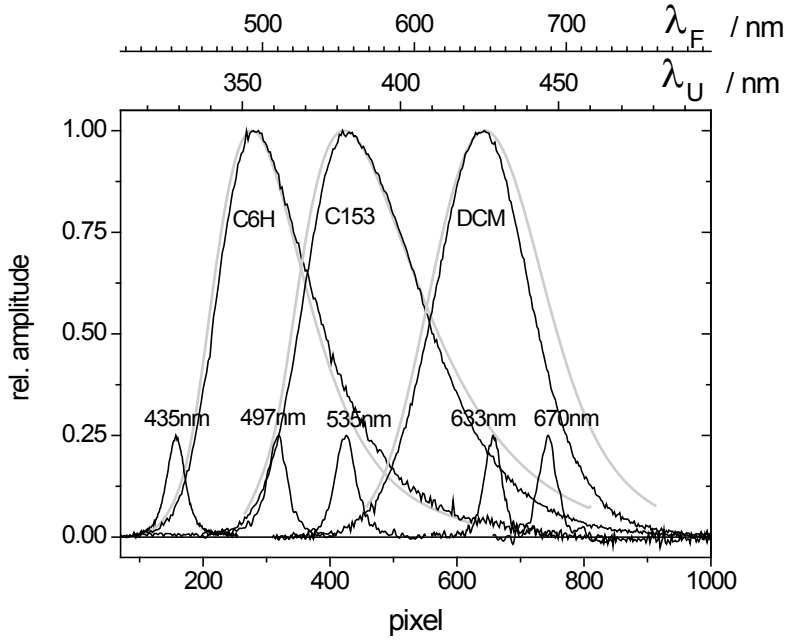

Fig. 3.8 Experimental *UV-count* distributions $s^{(U)}(p)$ over pixels (black lines) from fluorescence up-conversion measurements of the dyes C6H, C153 and DCM in methanol at 250 ps delay time (for BBOT see Fig. 3.11). Also shown are the count distributions when the fluorescence has been passed through interference filters which are centered at the indicated wavelengths. For comparison, the expected *UV-photon* distributions $f^{(U)}(p)$ (gray lines) were inferred from stationary fluorescence measurements.

count-distribution over pixels p, $s^{(U)}(p) \equiv \left(\frac{\partial \Sigma^{(U)}}{\partial p}\right)(p)$. This is to be compared with the "molecular" stationary distribution of $\Phi^{(F)}$ fluorescence photons over wavenumbers in the visible, $f^{(F)}(\tilde{\nu}_F) \equiv \left(\frac{\partial \Phi^{(F)}}{\partial \tilde{\nu}_F}\right)(\tilde{\nu}_F)$. The latter is conveniently provided as a sum of lognormal functions [120]

$$\log norm(\tilde{\nu}_F) = h \exp\left\{-\ln 2\left(\frac{\ln\left[1+2\gamma(\tilde{\nu}_F - \tilde{\nu}_0)/\Delta\right]}{\gamma}\right)^2\right\}. \qquad (3.11)$$

Table 3.2 Lognormal parameters (Eq. 2) for the fluorescence quantum distributions over wavenumbers, $f^{(F)}(\tilde{\nu}_F)$, in methanol.

	$\tilde{\nu}_0$ / cm^{-1}	Δ / cm^{-1}	γ	h
BBOT	24457	952	0.0303	0.4153
	23859	2126	0.001	0.1797
	22975	1517	0.0564	0.8736
	21532	1599	-0.3423	0.6292
	19826	1989	-0.567	0.1546
	18600	9937	-0.7929	0.0158
C6H	23200	886	0	0.0255
	21000	774	0.087	0.0203
	20717	2950	-0.308	0.9774
	15500	3186	0	0.0499
C153	20481	1601	-0.218	0.0724
	18519	2947	-0.402	0.9913
	16537	2884	-0.781	0.0904
DCM	15829	2388	-0.056	1.0000

Optimal values for peak wavenumber $\tilde{\nu}_0$ [cm^{-1}], width Δ [cm^{-1}], asymmetry γ [–], and amplitude h from conventional fluorescence measurements are collected in Table 3.2. In addition to the spectrograph calibration $\lambda_U(p)$ we also need the relationship

$$\lambda_F(p) = \frac{\lambda_G \cdot \lambda_U(p)}{\lambda_G - \lambda_U(p)} \tag{3.12}$$

which involves the gate wavelength λ_G. Fig. 3.8 shows several up-conversion spectra which are obtained when dye fluorescence is passed through narrow-band interference filters as indicated. For any such combination the peak wavelength λ_{Fmax} of the transmitted fluorescence light is known from stationary measurements, and the

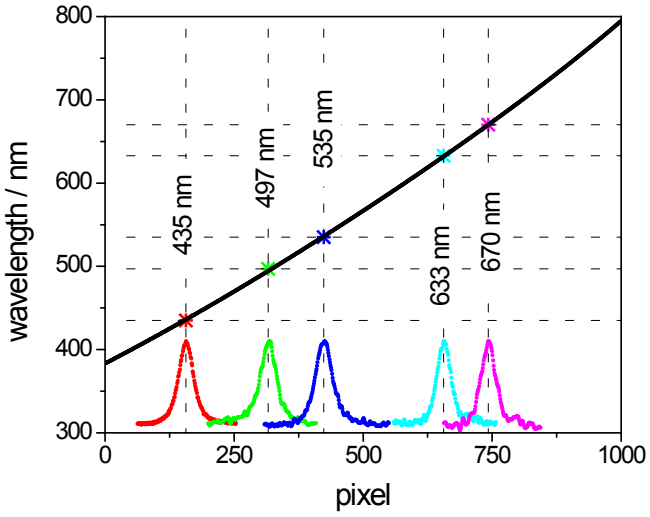

Fig. 3.9 Determination of the gate wavelength, by up-converting fluorescence which has been passed through interference filters centered at various λ_F.

corresponding pixel number p_{max} is obtained from the figure. Optimization gives $\lambda_G = 1340 \pm 4\,\text{nm}$, Fig. 3.9. Next, the stationary distribution $f^{(F)}(\tilde{\nu}_F)$ is transformed into an equivalent distribution of "upconverted" fluorescence photons over pixels,

$$f^{(U)}(p) \equiv \left(\frac{\partial \Phi^{(U)}}{\partial p}\right)(p) \propto \lambda_U^{-2} f^{(F)}(\tilde{\nu}_F) \cdot \left(\frac{\partial \lambda_U}{\partial p}\right) \quad \text{with } \lambda_U(p) \text{ and } \tilde{\nu}_F(p). \tag{3.13}$$

The two types of spectra, $s^{(U)}(p)$ and $f^{(U)}(p)$, are shown in Fig. 3.8 (black and gray lines, respectively) for each standard dye. The correction function is then

$$c(p) \propto f^{(U)}(p)/s^{(U)}(p). \tag{3.14}$$

Fig. 3.10 shows the c(p) segments which correspond to the dyes in Fig. 3.8. They are scaled so that their rms differences are minimized, and a smooth fit provides the final correction curve $\bar{c}(p)$. The correction function $\bar{c}(p)$ is used as follows. Pointwise multiplication of a measured, technical count distribution $s^{(U)}(p)$ with $\bar{c}(p)$ gives the distribution $f^{(U)}(p)$ of upconverted UV photons. To obtain the fluorescence distribution over fluorescence wavenumbers, $f^{(U)}(p)\,\lambda_U^2(p)$ is plotted against $10^7/\lambda_F(p)$. To obtain the fluorescence distribution over fluorescence wavelengths, $f^{(U)}(p)\,\lambda_U^2(p)/\lambda_F^2(p)$ is plotted against $\lambda_F(p)$. (Here it was assumed that λ_U is linear in p.)

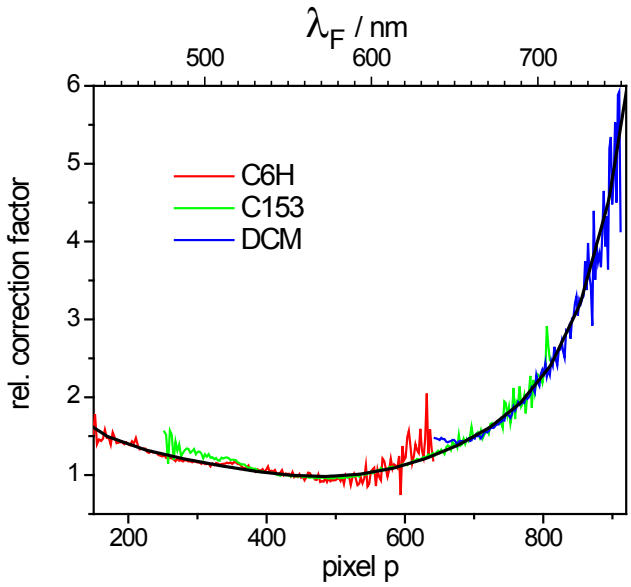

Fig. 3.10 Photometric correction curves $c_i(p)$ (see text for definition and use) obtained by comparing the count distributions in Fig. 3.8 with the expected photon distributions. The black line $\bar{c}(p)$ is a polynomial fit.

3.3.4.2 Group delay correction

Before gating, fluorescence passes the exit window of the sample cell, polarizer, and glass filter. These optical elements cause group velocity dispersion, which is measured by gating a white-light continuum. The latter is generated by focusing 10 µJ pump pulses with a thin lens (f=100 mm *f.s.*) into the cell containing pure methanol. For each pixel the transient signal is fitted with a temporal Gaussian

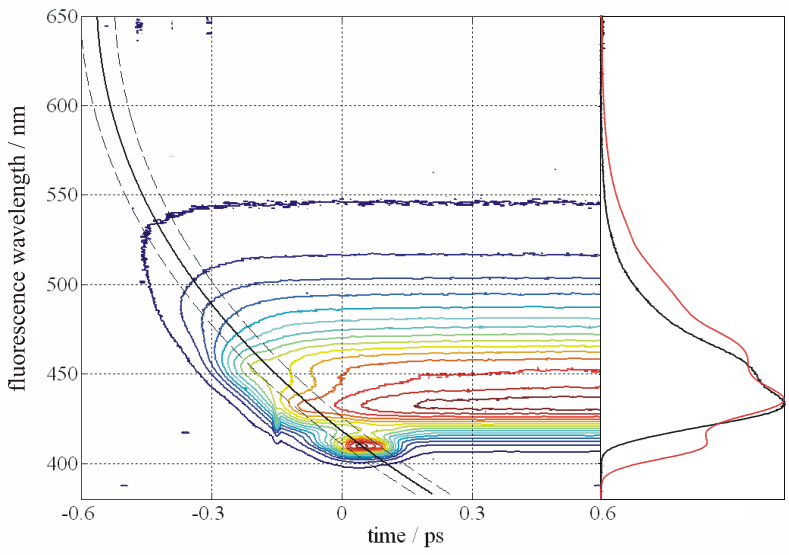

Fig. 3.11 *left:* The curve for time-zero as function of emission wavelength is plotted on top of the transient fluorescence of BBOT in methanol. The band ±40 fs indicates the width (fwhm) of the temporal apparatus function. Following red-edge excitation at 400 nm, spectral broadening is observed during the first 0.2 ps. *right:* The measured count distribution over wavelengths at late delay time (black line), compared to the stationary photon distribution (gray).

function, and the dispersion curve is obtained by taking the peak position of the fit as a function of pixel number. The temporal response is given by the fwhm≈80 fs of the Gaussian fits. To check the accuracy of the time correction obtained from continuum measurement, we measure the transient fluorescence of BBOT in methanol. The raw signal (λ_F, t) is shown as contour plot in Fig. 3.11, together with the time-zero function. With a time resolution of 80 fs, small changes of the vibronic fluorescence structure are observed before 200 fs. In the right panel the late raw signal (1 ps, black line) is compared to the fluorescence quantum distribution from stationary measurements (gray). Such comparisons were made above for photometric calibration. In the present case, the vibronic emission band of BBOT at 437 nm is reduced by the yellow glass filter.

3.3.5 C153 in methanol: a reference for transient fluorescence bandshape

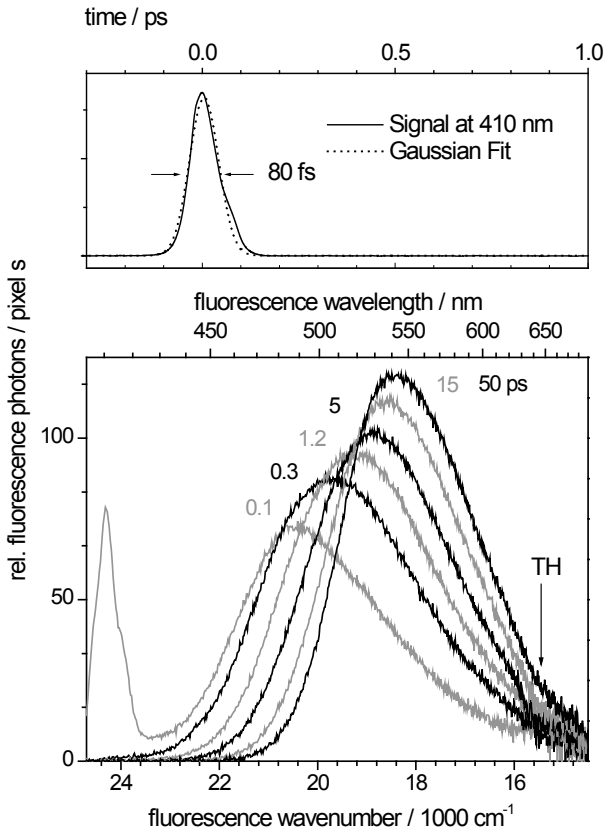

Fig. 3.12 Transient fluorescence spectra of C153 in methanol at 0.1, 0.3, 1.2, 5, 15, and 50 ps (*Bottom panel*). Shown are the relative quantum distributions over wavelength, *i.e.* after photometric and time corrections, for perpendicular polarization between gate pulse and fluorescence. The data were obtained by averaging over 16 scans. The sharp peak at blue side of the spectrum at 0.1 ps is the tail end of pump scatter. At TH, the third harmonic of the gate pulse rendered measurement impossible in previous designs.[77] *Top panel*: the time trace of residual pump scatter shows the instrument response function.

C153 has been studied extensively as a probe in time-resolved Stokes shift measurements[90,77,101, 110,111,112, 115] and has become a standard in this field. Sets of scans were taken from negative delays up to 4 ps in 20 fs steps, to 40 ps in 200 fs steps, and to 100 ps in 500 fs steps. Transient upconverted spectra corrected for group velocity dispersion and photometrically as discussed above, are shown in Fig. 3.12. Fluorescence polarized perpendicularly to the pump polarization is recorded in order to minimize contributions from Raman scattering of the solvent. As a consequence, the amplitude rises on the ps time scale due to electronic change and rotational diffusion of the emitting

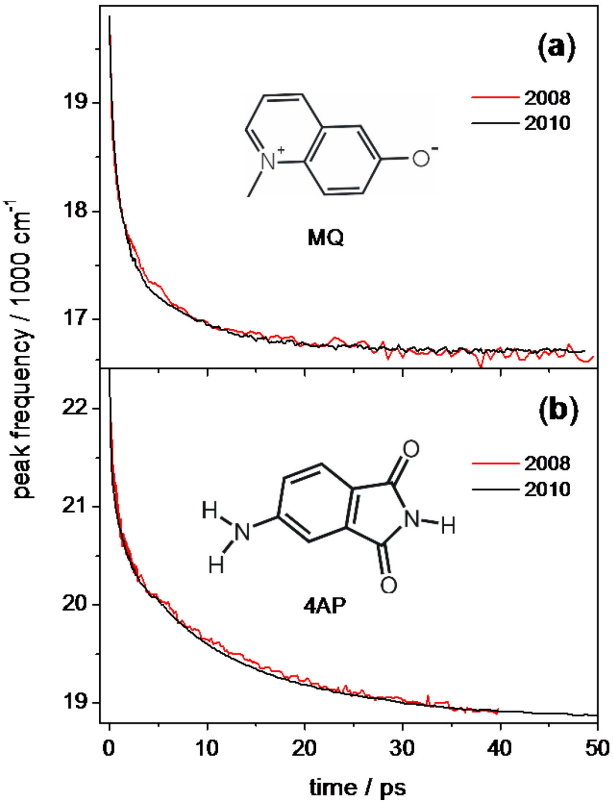

Fig. 3.13 The reproducibility of the up-conversion experiment is seen by measurements which were recorded two years apart. Shown is the peak frequency as function of time, for methyl quinolone (a) [121] and 4-aminophthalimide (b) [122] in methanol.

chromophore. We find biexponential behavior of the anisotropy decay, as in[123] but with faster initial component (0.3 ps, 38%). However the fact that the amplitude rises does not influence the determination of the spectral position and bandshape. The sharp peak near the blue edge of the spectrum at 100 fs is due to tailing pump scatter. After transformation to photon distributions over wavenumbers, the spectra are fitted with a lognormal function. Thus for every delay time *t*, we obtain the fit parameters together with their standard error (SE), comprising the final result.

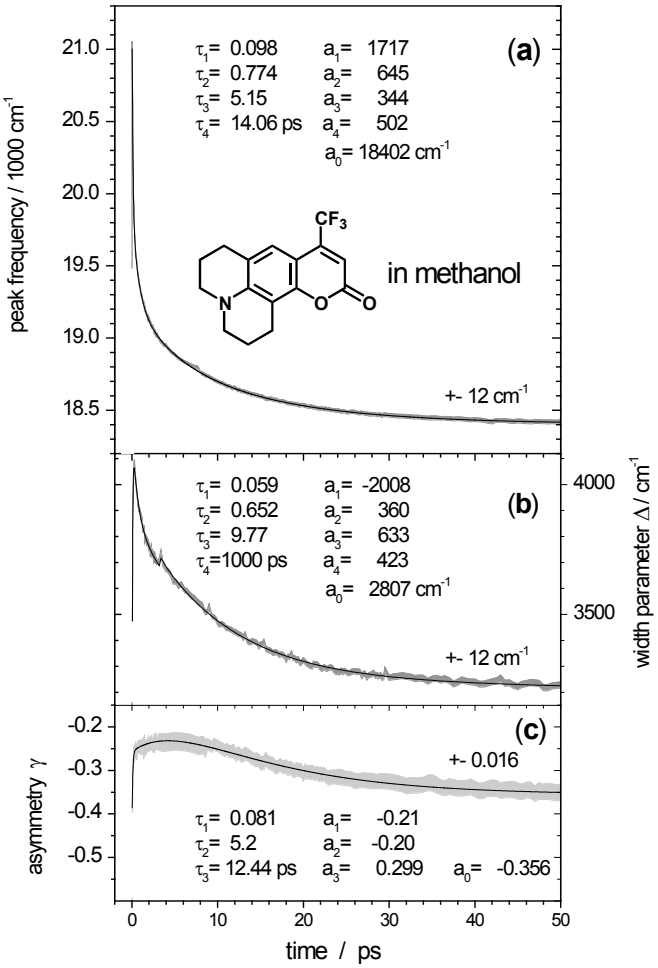

Fig. 3.14 Evolution of lognormal parameters (eq. 2) for the fluorescence distribution $f^{(F)}(\tilde{\nu}_F)$ from C153 in methanol. Gray bands outline the 95% confidence interval of the lognorm fits. For the time range 0.1-80 ps, the evolution is described by $\sum a_i \exp\{-t/\tau_i\} + a_0$ (black lines) with the parameters given as insets. A weak (2%) satellite pulse is responsible for a kink in (b) at 3.4 ps.

The reproducibility of dynamic fluorescence measurements with the new setup is demonstrated in Fig. 3.13. Here the evolution of peak frequency, in methanol, is shown for methyl quinolone (MQ, a) and for 4-aminophthalimide (4AP,b). The two measurements in each case were performed two years apart.

Let us return to C153 in methanol. Fig. 3.14 shows the evolution of peak position $\tilde{\nu}_0(t)$, band width parameter $\Delta(t)$, and asymmetry parameter $\gamma(t)$, in bands of ± 2 SE for 95% confidence. Here the confidence interval refers to the lognormal fit only and may be subject to other experimental problems. For example a weak satellite of the pump pulse is responsible for a sudden increase of bandwidth at 3.4 ps (panel

b). This perturbation can be removed by data analysis. Note that a multiexponential temporal fit of $\tilde{\nu}_0(t)$ may have different errors (slightly smaller in this case) because correlated changes over a large spectral range are measured. The Stokes shift from t=0.1 ps to time-infinity is determined as 2020 cm^{-1}. This value is smaller than the total shift (2190 cm^{-1}) from our stationary estimates[79] (see Fig. 3.2). We do not see the oscillations of $\tilde{\nu}(t)$ which were reported and analyzed recently.[112] Parameters for multiexponential fits (red lines) are given as insets. Such data could be used to develop this and other femtosecond fluorescence spectrometers consistently.

3.4 Kerr Shutter (to large extent based on Refs. 118, 124, and 125.)

Kerr gating is another method to record entire transient fluorescence spectra.[117,125,126,127] In the following a Kerr-shutter with 240 fs apparatus response is described. The Kerr-shutter was built to extend the spectral window into the UV. In the visible range broadband fluorescence up-conversion method is still preferred. Gating the fluorescence with tilted beam at λ= 1300 nm in a noncollinear geometry makes the signal free from gate scattering and minimizes the group velocity mismatch (GVM). As example, the fluorescence band shape of *cis*-stilbene is measured for the first time.

3.4.1 Introduction

In Kerr shutter a transient birefringence in an isotropic medium is created in response to an applied electric field. In the case of light induced birefringence, the change of refractive index is proportional to the intensity of the light [128]

$$\Delta n = \gamma I \tag{3.15}$$

where γ is Kerr constant. Induced phase difference between light component at wavelength λ (analogous to an optical retardation plates, polarization along fast and slow axes will have different speed) for a Kerr medium with thickness L is given by

$$\phi = 2\pi L\Delta n / \lambda \,. \tag{3.16}$$

If the Kerr medium is placed between two crossed polarizers and birefringence is created by a short laser pulse (gate pulse) the transmission is given by[124]

$$T = \sin^2(2\theta)\sin^2(\phi/2) \tag{3.17}$$

where θ is the angle between gate pulse polarization and the orientation of the first polarizer. Finally total transmission of the signal is given by

$$\mathrm{I}_{\text{gated signal}}(\mathrm{t}) = \int_{-\infty}^{t} T(t-t')I_{em}(t')dt' \tag{3.18}$$

Since in isotropic materials (with inversion symmetry) second order response is vanished, the Kerr phenomenon is formulated by third order of nonlinearity, χ^3. For short gate pulses, contributions to γ come from electronic response (in the range of femtosecond) or/and molecular orientational response (in the range of picosecond).

3.4.2 Experimental set up

Kerr gating is done by the setup shown in Fig. 3.4, with minor changes. Most importantly, the KDP crystal is replaced by the Kerr medium. To rotate the polarization of the gate pulse, a λ/2 plate is added to gate path. The Kerr-shutter is inherently broadband and phase matching is automatically fulfilled. But different from FLUPS, the gated fluorescence has the same spectrum as the original signal and appears as a large background to the gated fluorescence if the crossed polarizers P_1 and P_2 are not optimal. Ernsting et al have shown that this difficulty can be overcome with a pair of crossed Glan polarizers which provides a 10^{-6} extinction ratio.[117] The first polarizer P_1, placed in the intermediate focus at D (see Fig. 3.4), should be thin (about 2 mm) to minimize the chirp of the gated pulse.

3.4.2.1 Correction procedure

3.4.2.1.1 Photometric correction

Photometric correction was accomplished by comparing fluorescence spectra, *F(p)* measured over pixels, to the same spectra $f_{stat}(\lambda) = \frac{d\Phi_{stat}}{d\lambda}$ measured with a stationary fluorescence spectrometer. For the comparison, the latter quantity is converted to a fluorescence quantum distribution over pixels *p*, i.e. $f_{stat}(p) = \frac{d\Phi_{stat}}{dp}$. We have

$$f_{stat}(p) = f_{stat}(\lambda) \cdot \frac{d\lambda}{dp}, \qquad f_{stat}(\lambda) = f_{stat}(p) \cdot \frac{dp}{d\lambda}. \tag{3.19}$$

Then the correction function $\alpha(p)$ in pixel scale is

$$\alpha(p) = \frac{f_{stat}(p)}{F(p)} = \frac{f_{stat}(\lambda) \cdot \frac{d\lambda}{dp}}{F(p)}. \tag{3.20}$$

Similarly, the correction factor $\alpha(\lambda)$ can be written in wavelength scale

$$\alpha(\lambda) = \frac{f_{stat}(\lambda)}{F(\lambda)} = \frac{f_{stat}(\lambda)}{F(p) \cdot \frac{dp}{d\lambda}}. \tag{3.21}$$

By multiplying the measured spectra *F(p)* with $\alpha(p)$ in pixel scale, or $F(p) \cdot \frac{dp}{d\lambda}$ with $\alpha(\lambda)$ in wavelength scale one obtains photometrically corrected spectra. Fig. 3.15 shows the correction factor $\alpha(p)$ measured with trans-stilbene and BBOT dye.

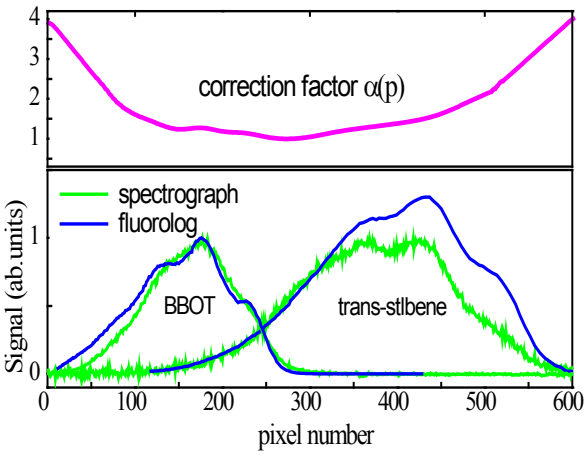

Fig. 3.15 Correction factor *α(p)* (magenta) obtained with *trans*-stilbene and BBOT dye. Green lines in lower panel: count distributions measured by Kerr gating, blue lines: photon quantum distributions from stationary measurements.

3.4.2.1.2 Time-correction and instrument response

Group velocity dispersion of the fluorescence light in the sample and Glan polarizer cause a wavelength-dependent delay between pump and gate. This was measured by gating a continuum generated in the sample cell, as represented by Fig. 3.17. A pump-gate cross-correlation time τ_{cc}, or instrument response fwhm, was derived from a biexponential fit of fluorescence kinetics convoluted with a Gaussian. With these fits we get τ_{cc}=240 fs for the UV observation range, as needed with stilbene.

3.4.3 Time-resolved fluorescence spectra of *cis*-stilbene in hexane and acetonitrile

As an example the time-resolved fluorescence band shape of *cis*-stilbene in solution, which have not been measured yet is presented. Photoinduced isomerisation of

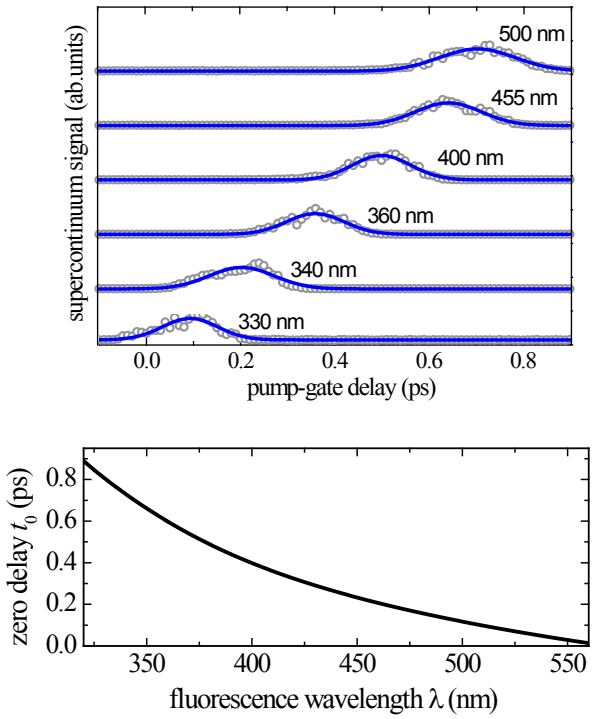

Fig. 3.16 Top: gated supercontinuum signal (symbols) and Gaussian fits (blue curves). Bottom: Time-zero dispersion curve $t_0(\lambda)$ from the peak position of the Gaussians.

cis-stilbene in solution has been extensively investigated[129] both with stationary[130] and ultrafast spectroscopies.[80,131,132,133,134,135,136,137] Transient absorption[132,133,134,136] and up-conversion [135,136] studies (performed at single probe wavelengths) report a monoexponential decay of the excited S_1 electronic state with characteristic times 0.4-1.5 ps depending on solvent.

In this experiment the sample solution is circulated in a flowing cell of 0.2 mm thickness and is excited at 283 or 267 nm (80 fs, 0.6 μJ, 500 Hz). Fluorescence is collected with an off-axis Schwarzschild objective, imaged to a 2 mm Glan polarizer (Glan 1) and focused to a microscope cover glass (Schott, hydrolytic class 3) used as Kerr medium. The gate beam (1300 nm, 80 fs, 60 μJ) is directed at $\alpha' \approx 20°$ relative to the fluorescence beam (see fig. 3.4) to minimize the group velocity mismatch with the fluorescence light. The gated fluorescence, after passing the Glan analyzer (Glan 2, 10^{-6}

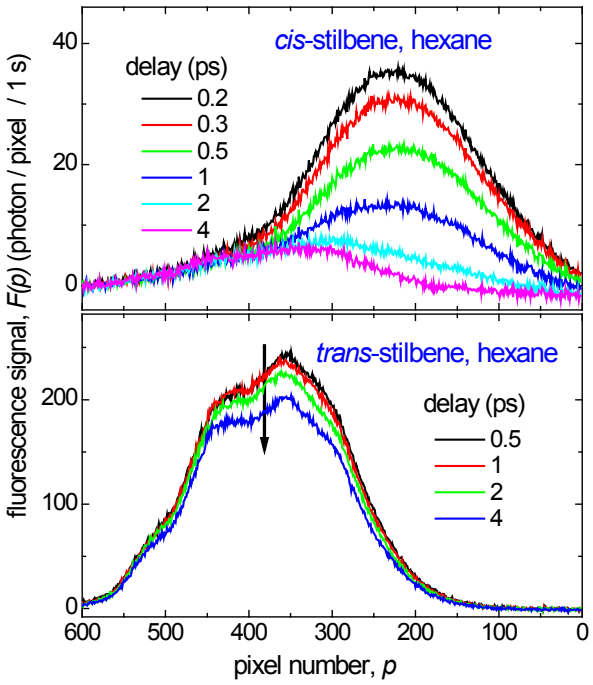

Fig. 3.17 Time-corrected *F(p)* fluorescence spectra from *cis*- (top) and *trans*-stilbene (bottom) in n-hexane upon 283 nm excitation before photometric correction. *Trans*-stilbene contribution to the *cis*-spectra is recognized at 4 ps (magenta) between 200-500 pixels. Arrows indicate signal evolution. Pump-gate polarization is parallel. A decay seen for *trans*-stilbene is mainly due to rotational diffusion which occurs with 14 ps.

extinction ratio), is sent to a spectrograph with a fiber and registered with a CCD camera (Andor Newton, DU970P-BV, 16 µm pixel width). To maximize the signal from *cis*-stilbene all measurements were done with parallel pump-gate polarization. Absorbance of the sample was kept 0.8 at the absorption peak, which corresponds to concentrations 0.3 g/L of *trans* and 0.9 g/L of *cis*. The normalized absorption spectra of *cis*- and *trans*-stilbene intersect about 283 nm, hence with this excitation the number of excited *cis*- and *trans*- molecules are approximately equal, which is necessary to correctly determine the radiative lifetime τ_{Rad} of *cis*-stilbene. The transient fluorescence spectra *F(p)* (*p* is the pixel number) were recorded in 20 fs steps with 1-2 s accumulation times. The spectra were averaged over 12-16 pump-gate scans and time-corrected for the chirp of gated fluorescence.

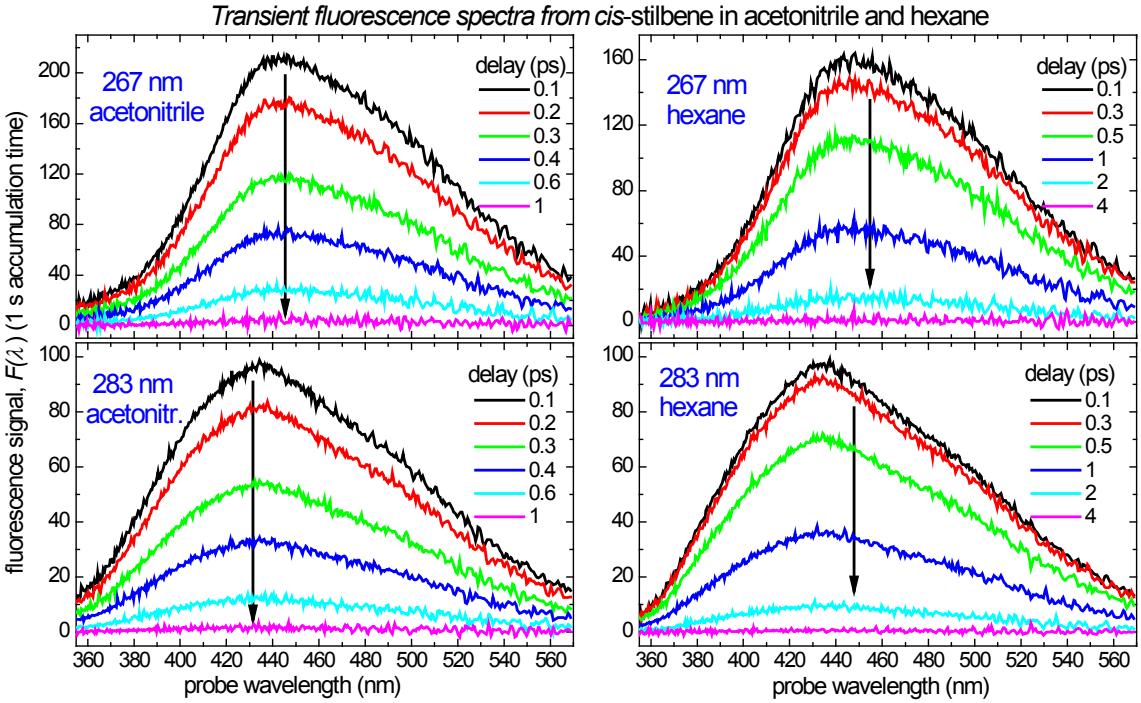

Fig. 3.18 Transient fluorescence spectra $F(\lambda,t)$ (at 21 C°) of *cis*-stilbene in acetonitrile (left) and n-hexane (rigth) upon 267 nm (top) and 283 nm excitation (bottom), after time- and photometric correction and upon subtracting the contribution from *trans*-stilbene. The signal decay is uniform; the spectra preserve their shape during the decay. A contribution from 4a,4b-dihydrophenanthrene (DHP) expected for λ>500 nm is apparently weak and cannot be recognized. The spectra upon 267 nm excitation, with higher excess energy, are red-shifted relative to those with 283 nm excitation.

Fig. 3.17 shows time-corrected *F(p)* spectra (upon 283 nm excitation) of *cis*- and *trans*-stilbene in hexane before photometric correction. In the *cis*-spectra (top), *trans*-stilbene contribution is recognized in the range 200-500 pixels at 4 ps (magenta). This contribution was subtracted by scaling the transient spectra from *trans*-stilbene (bottom) measured under the same experimental conditions. The apparent decay of *trans*-signal is mainly due to rotational diffusion which occurs with 14 ps in hexane. This decay, taking

place also for *cis*-stilbene, has a negligible effect on the subpicosecond time constants of the *cis*-evolution.

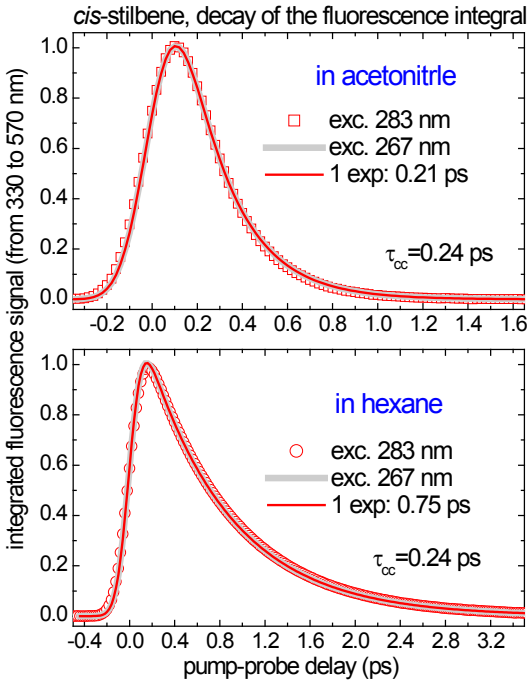

Fig. 3.19 The decay of the fluorescence integral, $\int f_{Kerr}(\lambda,t)d\lambda$ over the full fluorescence band, does not depend on the excitation wavelength. A monoexponential fit (red) gives 0.21 ps for acetonitrile and 0.75 ps for hexane. τ_{cc}=0.24 ps is the pump-gate cross-correlation.

The final time- and photometric-corrected spectra, $f_{Kerr}(\lambda,t)=\frac{d\Phi(t)}{d\lambda}$ (i.e. the fluorescence quantum distribution over wavelength interval) of *cis*-stilbene in hexane and acetonitrile are presented in Fig. 3.18. Top and low panels correspond to excitations at 267 and 283 nm, respectively. The spectra with 267 nm excitation, due to higher excess energy, are noticeably red-shifted relative to those with 283 nm excitation. Nonetheless, in both cases the spectra decay nearly uniformly preserving their shape. A contribution from 4a,4b-dihydrophenanthrene (DHP),[130] expected in the region λ>500 nm, is apparently weak and cannot be recognized. This is in agreement with the current view of DHP photochemistry, whereby DHP is produced in a non-fluorescing state. [129,138]

Fig. 3.19 shows the evolution of the fluorescence integral $\int f_{Kerr}(\lambda,t)d\lambda$ taken over the full fluorescence band. The behavior is independent on the excitation wavelength and well described with a monoexponential fit, giving for the decay time

0.21 ps in acetonitrile and 0.75 ps in n-hexane. Similar measurements on *trans*-stilbene (not shown) also result in monoexponential decays with 37 ps in acetonitrile and 79 ps in hexane.

3.5 Transient absorption

Experimental set up for transient absorption measurements is shown in Fig. 3.20. For this experiment, a Ti:sa laser (FEMTOLASERS s*Pro*) after amplification provides 30 femtosecond pulses at 800 nm with 500 μJ energy. Pulses are split with 6:1 ratio. A major part with ~420 μJ is sent to derive a parametric optical amplifier (LIGHT CONVERSION TOPAS) to generate pump beams at various wavelengths. The remainder of the fundamental is frequency-doubled in a 0.2 mm BBO crystal, θ=29°. After compression, 0.6 μJ of the 400 nm beam is used as the pump pulse and the rest is used to generate white light continuum (supercontinuum). This is done by focusing the ~20 μJ pulses (with an f=200 mm thin lens) onto a CaF_2 plate (1 mm). The generated light is spectrally filtered by a dye solution, to reduce a contribution at 400 nm from the exciting pulse and to prepare a spectrally smooth probe pulses. Probe pulses (270-700 nm with ability to extend up to 1000 nm) are split to generate sample and reference beams. These are imaged in to the entrance plane of two identical spectrographs. A probe spectrum is measured alternatively with the pump "on" and "off". Thus, pump induced optical density can be obtained

$$\Delta OD = -\log\left(\frac{I^{on}}{I^{off}}\right) \tag{3.22}$$

where I^{on} and I^{off} are transmitted probe registrations when pump is on and off, respectively. Transient absorption spectra are measured by changing the delay time between pump and probe pulses. Examples will be given in the next chapter.

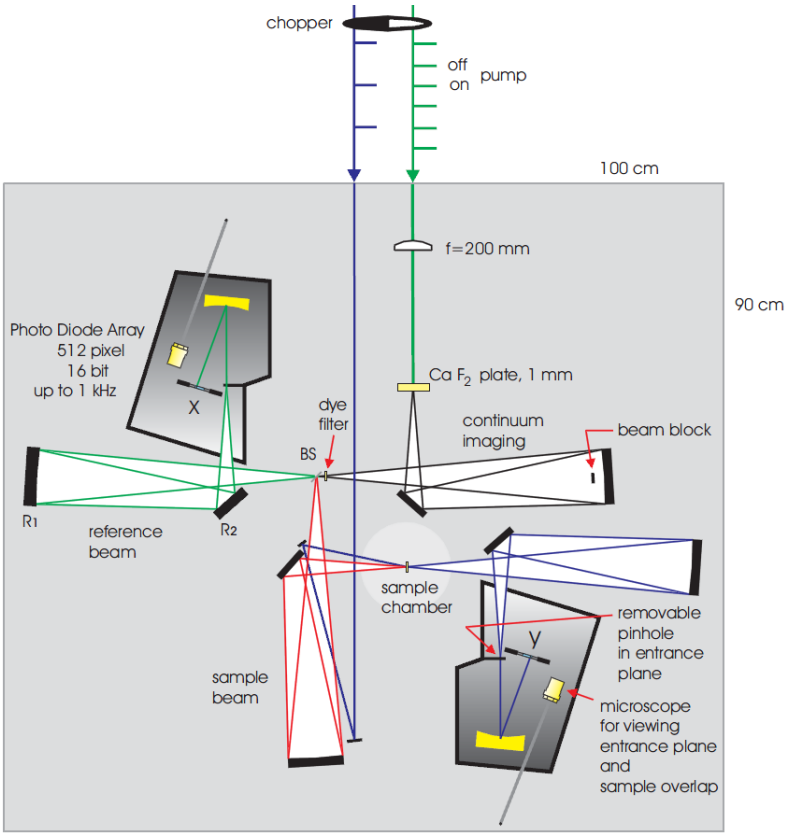

Fig. 3.20 Experimental setup for femtosecond transient absorption spectroscopy.

4 Solvation Dynamics of 4-Aminophthalimide in Methanol

4.1 Introduction (based on own publication Ref. 122.)

4-Aminophthalimide (4AP, inset to Fig. 4.1) and derivatives are widely used as fluorescent probes in complex media like cyclodextrins,[139] micelles,[140] ionic solutions,[141] ionic liquids,[142] and polymers[143] (citing examples where further references can be found). A long radiative lifetime,[144] large Stokes shift depending on solvent,[144,145] acceptable fluorescence quantum yield,[144] and absence of interfering excited states[110] render these probes useful for studying the polarity of the environment. In protic solvents the fluorescence lifetime decreases and the Stokes shift increases remarkably[146] compared to nonprotic solvents of the same polarity. The last point is illustrated in Fig. 4.1 where the peak position of the absorption and fluorescence lineshapes (see below) of 4AP are plotted against solvent polarity. The peaks in alcohols and water (black dots) stray below the regression lines for non-hydroxylic solvents[144] (colored dots) by ~1000 and 3000 cm^{-1} for absorption and emission, respectively. Since methanol is examined in this work, its deviations are marked especially by vertical lines. The large Stokes shift in protic solvents was attributed to differences in H-bonding between the S_1 and S_0 states, rather than to the difference between dipole moments.[144] Solvent-mediated proton transfer is another explanation,[147] supported by a comparison of photophysical properties in H_2O and D_2O.[148] A flash photolysis study showed that enhanced internal conversion is responsible for the decrease of fluorescence lifetime in protic solvents.[149]

The solvation dynamics of 4AP (and other dyes) in 1-propanol has been measured with 20 ps time resolution.[150] The spectral relaxation of the fluorescence band at 253 K was found to obey theories for nonspecific solvation despite the energetic importance of hydrogen bonding. For N-Methyl-4AP in n-butanol and n-decanol the relaxation dynamics at 298 K is roughly given by the longitudinal relaxation time of simple continuum theory.[151] Similar work on 3-AP in n-butanol

reached the same conclusion.[152] In complex media the solvation dynamics of 4AP is slower compared to pure solvents.[153,154,155]

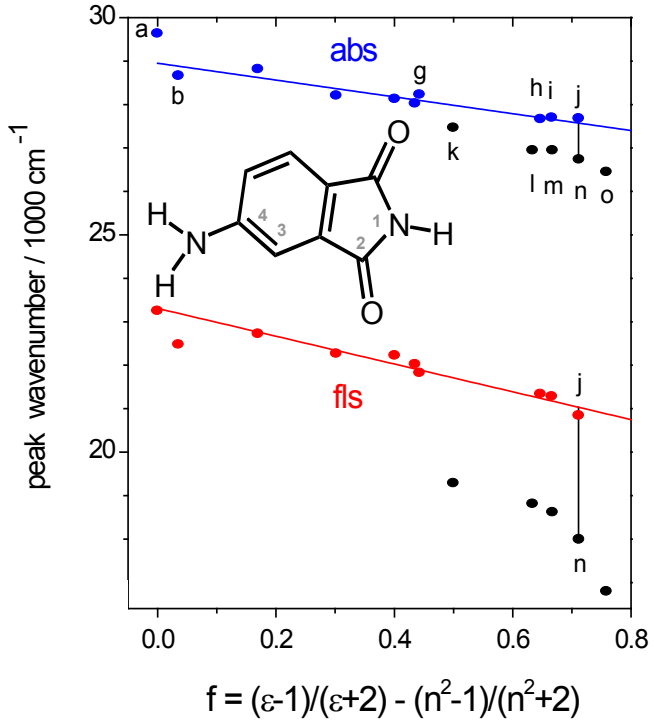

Fig. 4.1 Solvatochromism of 4AP: peak position of absorption and fluorescence lineshapes (corrected for dispersive shifts) against polarity f. *Colored, a-j:* cyclohexane, dioxane, dibutyl ether, diethyl ether, ethyl acetate, methyl acetate, thf, dmf, acetone, acetonitrile. *black, k-o:* n-octanol, n-propanol, ethanol, methanol, water. Vertical lines mark the deviation of 4AP in methanol from nonspecific polar behavior, represented by acetonitrile solutions.

Here we examine 4AP in methanol at room temperature. Broadband fluorescence up-conversion [106,107,77,156] enables higher temporal and photometric resolution than before,[73,90] and thus the question of molecularity is posed anew: can the reorganization of H-bonds be observed directly? We find that polar solvation based on simple continuum theory describes the temporal shape of $\tilde{\nu}(t)$ quantitatively. Extrapolation $\tilde{\nu}(t \to 0)$ points to an initial emission frequency which agrees with the time-zero result from stationary spectroscopy. Therefore an H-bond is not required *as dynamic variable* in the solvation process following optical excitation.

Transient absorption with supercontinuum probing [157,158] provides an alternative means for observing the dynamic Stokes shift of fluorescence. The band for stimulated emission is monitored in this case. The method is technically easier

than broadband up-conversion; it was used recently to characterize the early solvation dynamics in oligonucleotides.[10,159] But the measurements are less accurate to evaluate because the desired band for stimulated emission is overlaid by the induced spectra of ground-state bleaching and excited-state absorption, and their separation is not unique. Here, transient absorption spectra for 4AP in methanol are photometrically "calibrated" by comparison with the up-conversion results. An excited-state absorption spectrum, its relative amplitude and time evolution are obtained, and a prescription for the photometric correction in any solvent is given. The excited-state absorption spectrum is assigned with the help of time-dependent density-functional calculations.

The vibronic structure of the molecular probe, isolated at low temperature in a supersonic jet, is also relevant for solvation dynamics. Thus C153 was shown to have several conformations of the amino group.[160,161] The population flow between these conformations alters the shape of the emission band and thereby influences the dynamic Stokes shift. In an ideal probe the electronic chromophore should be rigid, *i.e.* the intramolecular reorganization energy after $S_1 \leftarrow S_0$ excitation should be small, confined to a few modes of a single isomer, and the modes should be identical in the S_1 and S_0 states. These conditions can be tested most directly by laser-induced fluorescence spectroscopy in a supersonic jet. Early work on N-Methyl-4APs showed that the vibrational levels in S_1 are organized in a few optically active modes only.[162,163] Microsolvation of isolated 4AP by one or two methanol molecules confirmed the strong coupling via H-bonds.[160] Here we examine isolated 4AP cooled in a supersonic jet. Optical-optical double resonance spectroscopy is used to determine 16 optically active modes. An intramolecular reorganization energy is inferred which is consistent with the value in 2-methylbutane.

4.2 Experimental

4.2.1 Materials

X-ray structure of 4AP were provided by A. Neugebauer and Dr. B. Ziemer.[i] 4AP (Acros) was sublimed; melting point 290.7°C. Crystals for X-ray diffraction were obtained from a solution in methanol upon slow evaporation, Scheme 4.1. Solvents were of spectroscopic quality (MERCK Uvasol). For fluorescence spectroscopy in 2-methylbutane, the solvent was degassed and dried over granulated sodium in a sealed vessel, previously dried under high vacuum, with a sample cell attached for optical measurements. All measurements were carried out at 21±0.5°C.

4.2.2 Absorption and emission spectra

Spectra were recorded on a CARY 300 spectrometer and a SPEX 212 fluorometer, respectively, with bandwidth ≤ 2 nm. Wavelengths were calibrated to ± 0.1 nm with a Holmium glass filter or a Hg lamp. Fluorescence was compared to the emission of a secondary standard lamp (GIGAHERTZ OPTIC Model BN9701), and background from the pure solvent was always subtracted. The absorption spectrum in 2-methylbutane is approximated by the excitation spectrum recorded with 420 nm detection. Excitation at 350 nm was used for the fluorescence spectrum in 2-methylbutane.

The experimental procedure for fluorescence up-conversion was described in Chapter 3.

[i] Chemistry Department, Humboldt Universität zu Berlin.

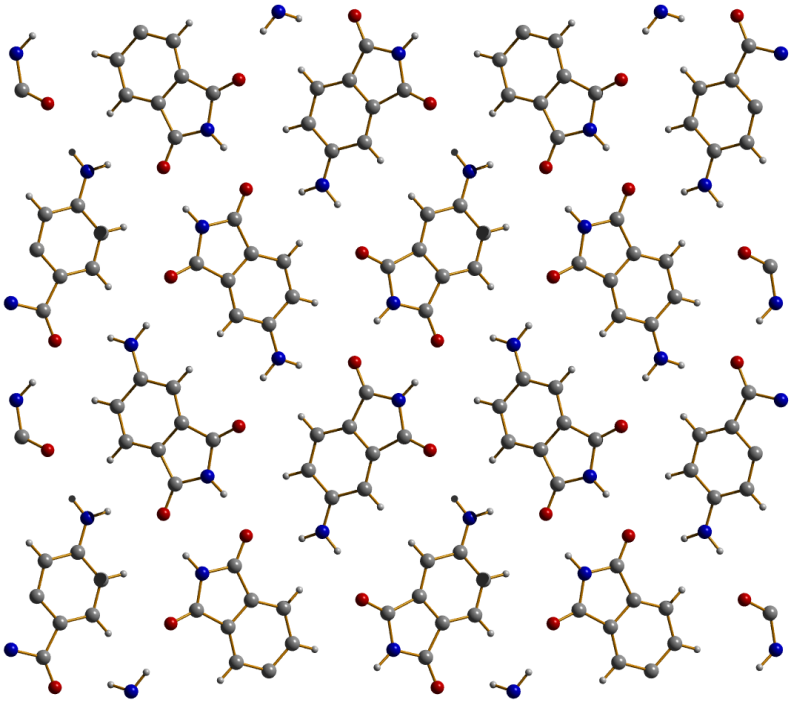

Scheme 4.1 Crystal unit cell of 4AP.

4.2.3 Transient absorption

Transient absorption spectra were provided by Dr. Sergey. A. Kovalenko.[ii] Transient absorption was measured by pump-supercontinuum probe spectroscopy in the setup of ref.15 with 0.6 μJ, 403 nm pump pulses. Single-shot absorption spectra were acquired at 250 Hz, and 50 such spectra were averaged for a recorded spectrum. The time resolution of this experiment was 65 fs (fwhm). Time steps were 6 fs and 100 fs, each with parallel, perpendicular, and magic-angle setting of the pump and probe polarizations. The corresponding time correction was obtained from measurements with pure methanol.[164] Finally, the results from 20 time scans were averaged.

[ii] Chemistry department, Humboldt Universität zu Berlin.

4.2.4 Fluorescence excitation in a supersonic jet

Supersonic jet spectra were provided by Thorsten Obernhuber and Prof. Bernhard Dick.[iii] The apparatus for the generation of supersonic beams was described elsewhere.[165] Experiments were performed with He carrier gas at a stagnation pressure of 2.0–2.5 bar. Fluorescence excitation and optical-optical double resonance (OODR) spectra were recorded with the laser setup described in ref. [166]. For OODR measurements, two dye-laser beams were arranged counter propagating, separated by 1.5 mm, crossing the supersonic jet ca. 6 mm downstream from the pulsed nozzle (GENERAL VALVE No. 9 operated at 204°C). Two photomultipliers were used, one on each side of the axis perpendicular to the plane spanned by the molecular beam and the laser beams. One collected the fluorescence produced by both laser beams, whereas the other detected only the fluorescence produced by the probe beam. Filters (SCHOTT GG 385) were used to suppress scattered laser light. Fluorescence signals were normalized to the pulse energy of the exciting laser.

4.2.5 Computational methods

Quantum calculations were conducted by Prof. Bernhard Dick.[iii] The geometry of the electronic ground state of 4AP was optimized with the density functional theory (DFT) method. The B3LYP functional and the GAMESS program[167] in the implementation for Windows[168] were used throughout. The result of this optimization was then taken as the reference point for the calculation of excitation energies by the TD-DFT method. Two basis sets, cc-pVDZ and aug-cc-pVDZ, were used to check for convergence. The optimized geometry and normal coordinates of the S_1 state were calculated with the CI-singles method.

[iii] Department of Physical and Theoretical Chemistry, Faculty for Chemistry and Pharmacy, University Regensburg, Germany.

Table 4.1 Lognormal parameters for 4AP spectra in Figs. 4.2 and 4.3.

4-Amino-Phthalimid	$\tilde{\nu}_P$ /cm^{-1}	Δ /cm^{-1}	γ	h
in 2-methylbutane (Fig. 4.2):				
~ absorption lineshape,	26119	1000	-0.0639	0.2218
(420 nm fluorescence excitation)	27487	3146	0.2498	0.9766
$\tilde{\nu} \leq 35000$ cm^{-1}	30068	3112	0.1204	0.2287
	33846	4277	0.2467	0.3410
~ emission lineshape	20195	3871	-0.4572	0.1040
(from 350 nm excitation)	23499	3605	-0.1257	0.8728
$\tilde{\nu} \leq 27700$ cm^{-1}	24471	5552	0.0010	0.1275
	24896	779	0.1288	0.0945
in methanol (Fig. 4.3)**:**				
~absorption cross section	27036	4939	0.2680	1.0000
$\tilde{\nu} \leq 35000$ cm^{-1}	32599	3633	0.6110	1.0250
~ t=0 fluorescence quantum distribution	18699	3935	-0.3418	0.0297
$\tilde{\nu} \leq 27500$ cm^{-1}	23132	4536	-0.0891	0.9994
	27128	2551	0.2087	0.0426
~ t=∞ fluorescence quantum	18550	3830	-0.1787	1.0000

4.3 Results

4.3.1 Stationary solution spectra and computational results

Intramolecular reorganization after $S_1 \leftarrow S_0$ excitation is studied in a nonpolar solvent. Fig. 4.2 shows the absorption and fluorescence bands of 4AP in 2-methylbutane. In order to expose mirror symmetry we present the distributions of the optical transition

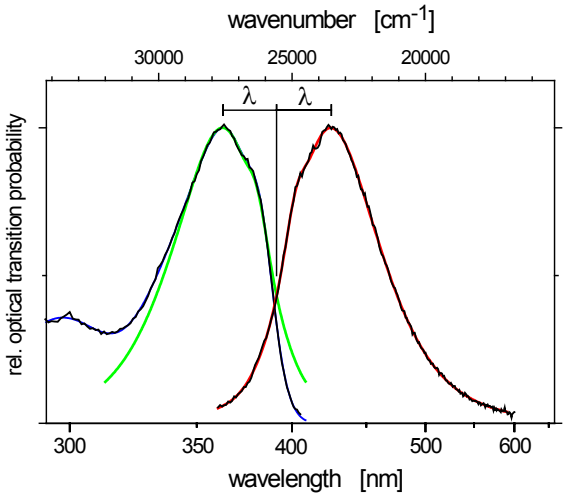

Fig. 4.2 Optical lineshapes of 4AP in 2-methylbutane, calculated from the fluorescence excitation and fluorescence spectra (see text). Blue and red lines indicate fits by lognormal functions; the green line was obtained by reflecting the emission band at 25580 cm^{-1}. The classical intramolecular reorganization energy is represented by $\tilde{\lambda} = 2025\,\mathrm{cm}^{-1}$.

probability, or lineshapes, $\propto \varepsilon(\tilde{\nu})/\tilde{\nu}$ and $\propto \mathrm{fqd}(\tilde{\nu})/\tilde{\nu}^3$. Here $\varepsilon(\tilde{\nu})$ is the molar extinction coefficient and $\mathrm{fqd}(\tilde{\nu})$ the fluorescence quantum distribution over energy.

Each lineshape is described by a sum of lognormal functions[169] (see Table 1). From that description one finds that vibrational structure is due to a mode of 1370-1400 cm^{-1}. By superimposing a reflected emission band onto the absorption band, the electronic origin $S_1(v'=0) \leftarrow S_0(v''=0)$ in 2-methylbutane is located at 25575±30 cm^{-1}. Referring to the peak positions, the intramolecular reorganization energy is $\tilde{\lambda}_{\mathrm{intra}} \approx 2025\,\mathrm{cm}^{-1}$.

The stationary absorption (a) and fluorescence (d) spectra of 4AP in methanol are shown in Fig. 4.3. Here and from now on, spectra are shown proportional to the extinction coefficient or the fluorescence quantum distribution over energy. The lowest absorption band peaks at 27040 cm^{-1} and the fluorescence at 18550 cm^{-1} (from lognormal[169] fits which are collected in the Table 4.1); the Stokes shift between them exceeds 8400 cm^{-1}. From a dynamic perspective, the reorganization process following ultrafast excitation can be envisaged in two stages: (i) intramolecular vibrational

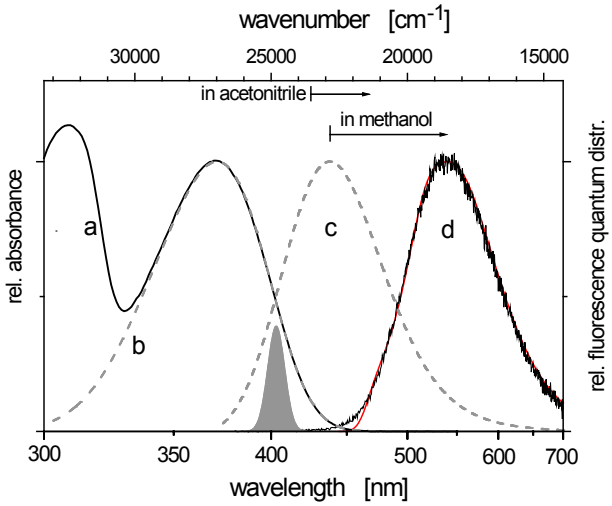

Fig. 4.3 Low-energy absorption spectrum (a) and fluorescence quantum distribution over energy (d) of 4AP in methanol. The $S_1 \leftarrow S_0$ band (b) and the fqd at time-zero (c) were obtained by comparison with the spectra in 2-methylbutane. Arrows indicate the dynamic Stokes shift following 40 fs excitation in methanol or acetonitrile.

redistribution such that the excited molecule attains thermal equilibrium internally, followed by (ii) solvent relaxation[110] and cooling. Note that the solvent must effectively be frozen during step (i). The "time-zero" emission band after (i) and before (ii) can be estimated by comparing with the spectra in 2-methylbutane.[110] By this method we obtain[170] the grey dashed line (c) which peaks at 22850 cm^{-1}. The "dynamic Stokes shift" consists of the spectral relaxation from here to the stationary fluorescence band; it is indicated in the figure by a horizontal arrow of 4300 cm^{-1} for methanol. Hydrogen-bonds are much less developed in acetonitrile,[171] which is why the dynamic Stokes shift amounts only to 2160 cm^{-1} in this solvent (small arrow).[172] — Finally for this part we return to the absorption spectrum in methanol. The two lowest bands are overlaid in the UV region, but it is possible to identify the $S_1 \leftarrow S_0$ absorption band (b) by comparison with the fluorescence excitation spectrum in 2-methylbutane. Calculated transitions from the electronic ground state are compared in Fig. 4.4 to the absorption spectrum in methanol. Absorptive transitions, indicated by a vertical bar representing oscillator strength, are specified in Table 4.2 together with the static dipole moment of the final

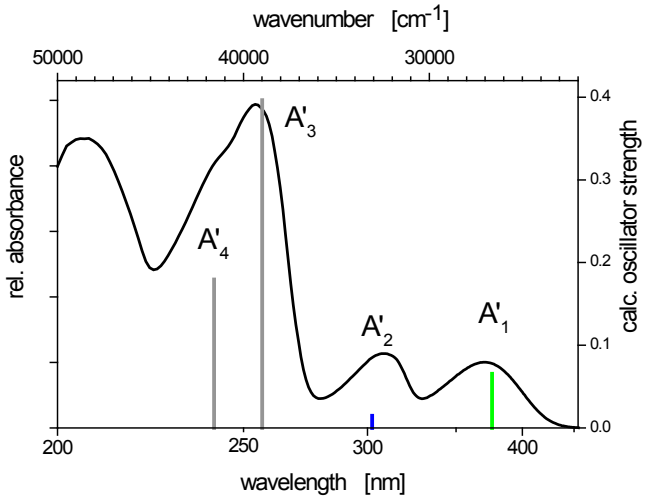

Fig. 4.4 Absorption spectrum in methanol, and oscillator strengths for transitions to excited states A'_i (vertical bars, see Table 4.2) from time-dependent density-functional theory. The calculated transition frequencies were reduced by 2000 cm^{-1} for the comparison.

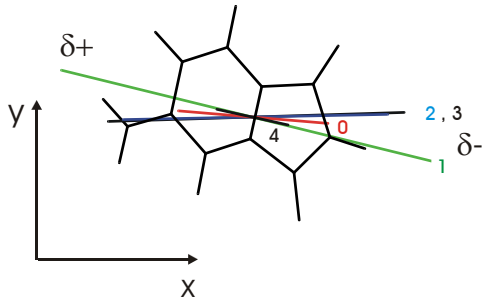

Scheme 4.2 Calculated coordinates and dipole moments of 4AP. Labels i=0-4 correspond to A'_i states in Fig. 4.4 and Table 4.2.

states. TD-DFT calculations predict 28630 cm^{-1} for the $S_1 \leftarrow S_0$ origin, which in the isolated molecule is found experimentally at 28968 cm^{-1} (see below). We conclude that calculated energies are accurate to within numerical precision; the dipole moments are overestimated.[173] The direction of dipole moments in the molecular frame is shown in Scheme 4.2. In solution, transition energies are modified by dispersive and polar interactions. To account for this effect, all calculated transition energies were reduced by

Table 4.2 Electronic states of 4AP constrained to planarity, in vacuo, from TD-DFT calculations (see text): transition frequency $\tilde{\nu}$ and oscillator strength f for optical transition from the ground state, and dipole moment μ. A' and A" refer to even or odd symmetry of the electronic wavefunction upon reflection in the molecular plane.

		$\tilde{\nu}$ [cm^{-1}]	f [-]	μ [D]
A'_0		0	—	5.52
A'_1		28630	0.0656	14.80
	A''_1	31060	0.0000	
A'_2		35080	0.0293	9.79
	A''_2	36250	0.0000	
	A''_3	38770	0.0022	
A'_3		41000	0.3963	10.96
	A''_4	42020	0.0000	
A'_4		43580	0.1795	2.65
	A''_5	44650	0.0015	
	A''_6	45720	0.0020	

2000 cm^{-1}, in which case excellent agreement with the absorption spectrum in methanol is obtained.

4.3.2 Time-resolved Stokes shift in methanol

The power spectrum of the 40 fs excitation pulse is also shown in Fig. 4.3. It intersects the absorption and time-zero emission bands and is thus centered on the electronic origin transition in methanol. Optical excitation should lead to minimal excess vibrational energy in S_1. The time evolution of the excited population is reflected in the basic experimental Figs. 4.5 and 4.8.

4.3.2.1 Broadband fluorescence up-conversion

Transient fluorescence spectra at 0.3, 1, 2.75, 10, and 40 ps are shown in Fig. 4.5. Observing entire spectra directly allows assessing the limits of the method, *i.e.* the factors which determine the accuracy of finding the peak or average emission frequency. The upconverted fluorescence at 0.3 ps is free of Raman signal due to a short (85 fs) apparatus function. A line at 407 nm belongs to a very weak satellite to the pump pulse. It hampers the analysis in the pump spectral region at early delay times but has practically no consequence for the population inversion. Remember that no filters were used, and the efficiency extends well across the 11000 cm^{-1} range shown.

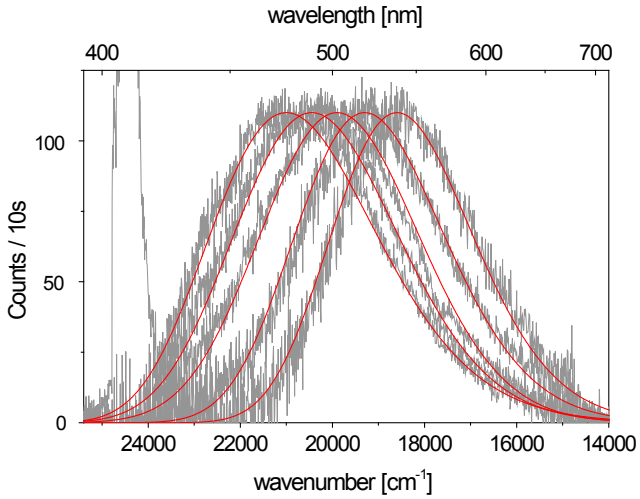

Fig. 4.5 Transient fluorescence spectra in methanol, from broadband up-conversion. Quantum distributions at t=0.3, 1, 2.75, 10 and 40 ps (grey lines) are averages of 8 measurements, each with 10 s integration time. Lognormal fits are indicated by red lines.

Transient fluorescence quantum distributions were fitted by a lognormal function[169] having peak frequency $\tilde{\nu}_p$, width parameter Δ, asymmetry parameter γ, and amplitude h. The resulting smooth spectra are shown as red lines in Fig. 4.5. Their peak frequencies $\tilde{\nu}_p(t)$ are entered as red points into Fig. 4.6, and the frequency relaxation is described by

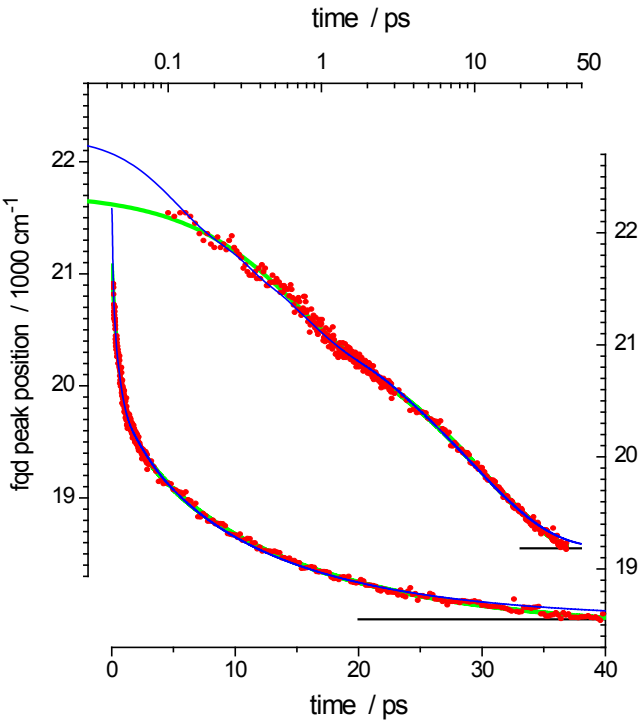

Fig. 4.6 Relaxation of the fluorescence (fqd) peak. Dots mark the peak of the red spectra in Fig. 4.5, and horizontal lines indicate the final frequency $\tilde{\nu}(\infty)$. Green lines – multiexponential fit; blue lines – dielectric relaxation according to continuum theory (α_1=18.2 Å^3; see discussion and compare Fig. 4.14).

a multiexponential fit to the data (green lines). A rms deviation of 40 cm^{-1} can be regarded as the precision of the measurement.[174] Horizontal lines mark the stationary state where $\tilde{\nu}_p(\infty) = 18550$ cm^{-1}. The first spectrum which can be analyzed with confidence has $\tilde{\nu}_P(100\,\text{fs}) = 21540$ cm^{-1}.

Fig. 4.7 shows the temporal behavior of the width and asymmetry parameters. For comparison, the frequency relaxation curve (red line) was copied from the previous figure. The amplitudes and decay times from all multiexponential fits are gathered in Table 4.3. Deconvolution of the transient fluorescence spectra with the apparatus function has no effect for $t \geq 150\,\text{fs}$.

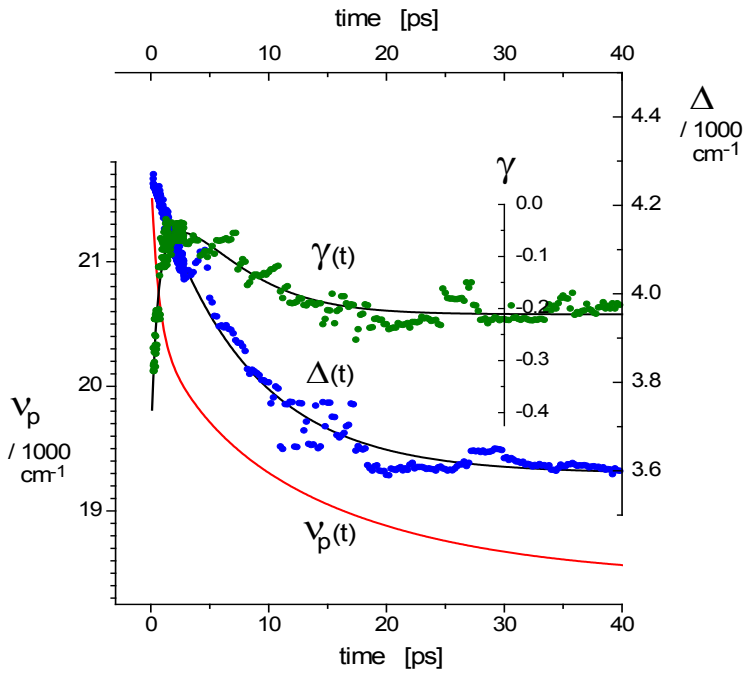

Fig. 4.7 Fluorescence width (Δ) and asymmetry (γ) parameters. Points represent measurement and black lines a multiexponential fit (Table 4.3). The $\tilde{\nu}_P$ relaxation curve from Fig. 4.6 is shown for comparison (red line).

Table 4.3 Time-dependence of the 4AP emission band in methanol, from transient absorption and fluorescence up-conversion.

		a_1 /cm^{-1}	a_2 /cm^{-1}	a_3 /cm^{-1}	a_4 /cm^{-1}	a_5 /cm^{-1}	τ_1 / ps	τ_2 / ps	τ_3 / ps	τ_4 / ps	τ_5 / ps	a_0 /cm^{-1}	$\langle\tau\rangle$ /ps
transient absorption	$\tilde{\nu}_P$	1922	1730	-3242	-	-	0.300	9.27	-532	-	-	21786	6.12
fluorescence up-conversion	$\tilde{\nu}_P$	1235	454	1579	-102	-	0.594	3.84	15.4	5000	-	18550	6.56
	Δ	882.4	-449	-	-	-	10.25	58.46	-	-	-	3830	-
	γ	-20.7	38.6	-18.9	5.07	-4.36	1.29	1.47	1.70	9.04	10.1	-0.179	-

Spectral parameters were fitted by $y = a_0 + \sum_{i=1}^{n} a_i \exp(-t/\tau_i)$, applicable to $0 \le t \le 50\,\text{ps}$.

The average solvation time is $\langle\tau\rangle = \left(y(0) - y(50\text{ps})\right)^{-1} \int_0^{50} \left(y(t) - y(50\text{ps})\right) dt$ for $y \equiv \tilde{\nu}_P$.

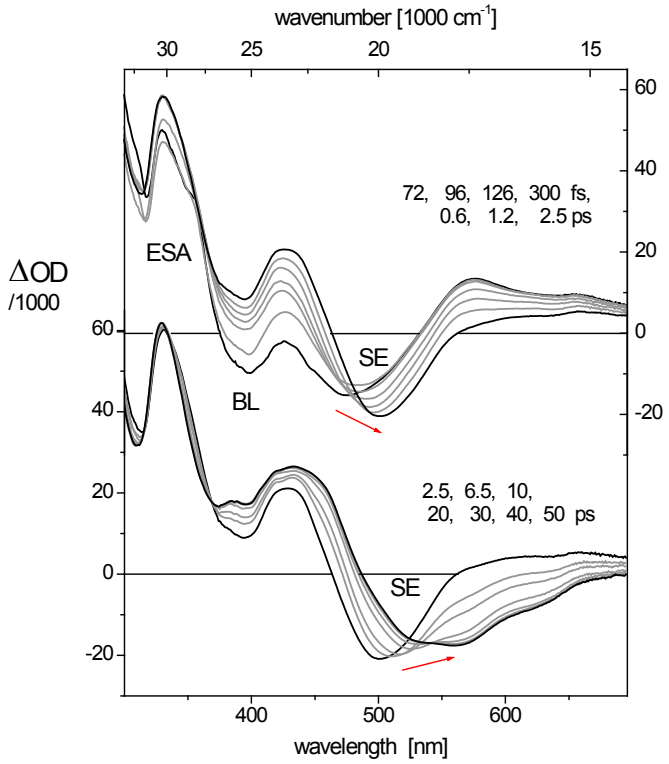

Fig. 4.8 Transient absorption spectra in methanol, following optical excitation at 403 nm. Negative induced optical density $\Delta OD < 0$ indicates bleach (BL) and stimulated emission (SE) in the absorption and fluorescence regions, respectively, while $\Delta OD > 0$ corresponds to excited state absorption (ESA). The rms noise of the raw data shown here is < 3 10^{-4}.

4.3.2.2 Transient absorption with supercontinuum probing

Transient absorption spectra are shown in Fig. 4.8. A wide spectral range, from 300 to 700 nm, is plotted against wavelength since this is how the spectra are registered in the experiment. Fluorescence now appears as stimulated emission (SE) in a band with negative induced optical density, $\Delta OD < 0$, around 500 nm. Bleach (BL) is recognized briefly as $\Delta OD < 0$ around 400 nm. Excited-state absorption (ESA) dominates the UV region and contributes a broad background in the red. The evolution of the characteristic features is indicated by arrows; it consists mainly of a redshift of the SE band and rise of ESA in the UV.

The results will be examined from two angles. First we see how accurately the dynamic Stokes shift in methanol can be extracted, using the fluorescence results for guidance. We also suggest a practical extraction procedure for use with any solvent.

In a second approach, the excited state absorption and its spectral evolution are determined for comparison with quantum-chemical calculations.

In order to extract the dynamic Stokes shift, the stimulated emission band in every transient spectrum must be estimated. The procedure, which has been described already,[157,158] is outlined here for consistency. We begin with the stationary absorption spectrum σ_{Abs} which is considered to be normalized at the peak of the $S_1 \leftarrow S_0$ band. A transition-dipole-squared, $M^2 = \int \sigma_{10} / \tilde{\nu} \, d\tilde{\nu}$, is determined where σ_{10} represents the $S_1 \leftarrow S_0$ band (Fig. 4.3, dashed line b). Then, from the stationary fluorescence, the band for stimulated emission at late time (symbolized by $t = \infty$) is derived, $\sigma_{SE}(\infty) \propto fqd(\tilde{\nu}) / \tilde{\nu}^2$, and normalized to the same M^2 also. We now possess a trial spectrum $\sigma_{AbsSE}(\infty) = \sigma_{Abs} + \sigma_{SE}(\infty)$. When $\alpha\sigma_{AbsSE}(\infty)$ is subtracted from a transient absorption spectrum measured at late time, the contribution $\Delta OD_{ESA}(\infty)$ should remain. The contribution due to bleaching is of course $\Delta OD_{BL} = \alpha\sigma_{Abs}$. The bleach amplitude α was not measured directly in our experiments. This parameter must be estimated, for example by the condition that $\Delta OD_{ESA}(\infty) \geq 0$ everywhere. For the moment let us assume that ΔOD_{BL} and $\Delta OD_{ESA}(\infty)$ are known. The next assumption concerns the evolution of excited-state absorption. For laser dyes such as 4AP the ESA contribution is relatively weak in the emission region and without prominent structure (see below). Under such conditions, subtraction of $\Delta OD_{BL} + \Delta OD_{ESA}(\infty)$ from a measured transient absorption spectrum should give the instantaneous stimulated emission band $\Delta OD_{SE}(t, \tilde{\nu}) \leq 0$. The spectral position $\tilde{\nu}(t)$ is determined from a quadratic fit of the band around its minimum.

Results are shown as dots in Fig. 4.9 for different estimates of the bleach amplitude α. The green line represents the evolution which is calculated (because bandshapes

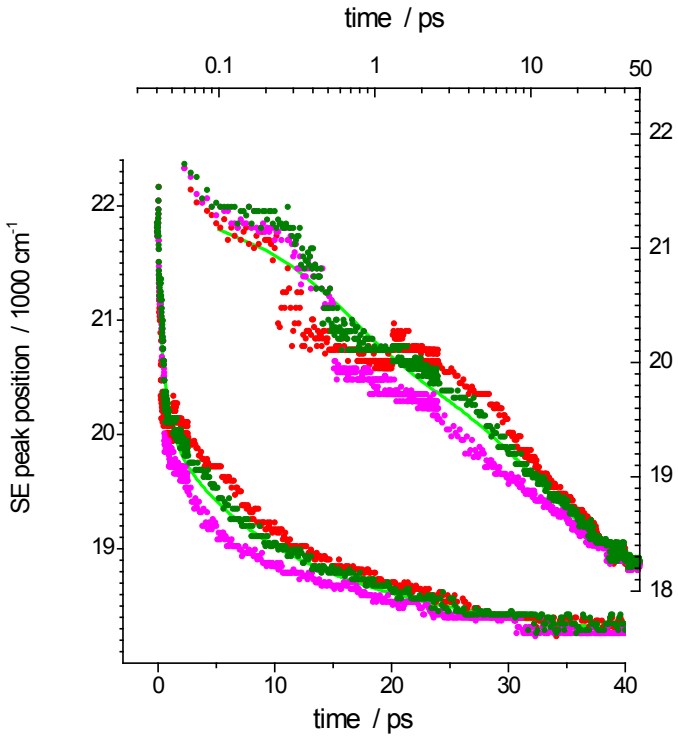

Fig. 4.9 Relaxation of the SE peak in Fig. 8, for different estimates of the bleach amplitude α (red – 29, olive – 34, magenta – 43 mOD). The green line represents the evolution which is calculated from the fluorescence up-conversion results (corresponding to the green line in Fig. 4.6).

differ) from the fluorescence up-conversion results; it is taken to represent the evolution of the emission band accurately for the purpose. The deviation between dots and line is lowest with α=34 10^{-3}, amounting to 110 cm^{-1} rms. However note that the minimal average error is unevenly distributed, with systematic deviations by +300 cm^{-1} (7% of the total dynamic shift) around 200 fs, and by -300 cm^{-1} around 0.6 ps. In principle, the residuals could indicate that an oscillatory solvation process is observed by transient absorption, due to its superior time resolution, which was not resolved by fluorescence up-conversion. But the excursions seen in Fig. 4.9 are not expected from model calculations (below) when the time resolution is increased; besides, they would be time-resolved by our fluorescence measurements. It follows that the residuals represent a systematic error of the method. A distinction of specific and nonspecific solvation processes can not be made by transient absorption measurements, even though the average solvation time is well determined (Table 4.3).

For any solvent, the previous comparison of 4AP transient absorption and fluorescence spectroscopies in methanol may serve to "calibrate" the amplitude of the trial spectrum $\sigma_{AbsSE}(\infty)$ which was defined earlier. Note that the optimal value of α is related to the ΔOD signal in the quasi-stationary state ($t = \infty$): 55% of the peak at 330 nm, or 194% of the broad minimum at 560 nm. A similar analysis with 4AP in acetonitrile (not shown) suggests that this relationship can be extended to nonprotic solvents. Tracing backwards one obtains the partial spectra $\Delta OD_{BL} + \Delta OD_{ESA}(\infty)$ and further, approximately, the time-dependent band for stimulated emission.

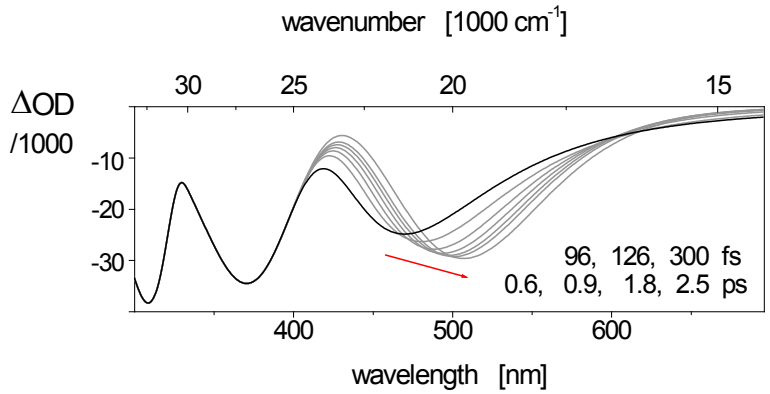

Fig. 4.10 Contributions to transient absorption (Fig. 4.8) due to bleach (BL) and stimulated emission (SE). The simulation uses stationary absorption and time-resolved fluorescence data, and β= 34 mOD.

Excited-state absorption in methanol may be obtained by combining transient absorption and fluorescence spectra more directly. Before only the stationary spontaneous emission spectrum was needed, but now we make use of every $fqd(t)$. From the latter one calculates $\sigma_{SE}(t)$ and reaches $\sigma_{AbsSE}(t) = \sigma_{Abs} + \sigma_{SE}(t)$, describing the shape of the joint contribution from bleach and stimulated emission at time t (remember that $\sigma_{AbsSE}(\infty)$ was introduced already). These time-dependent spectra are shown in Fig.

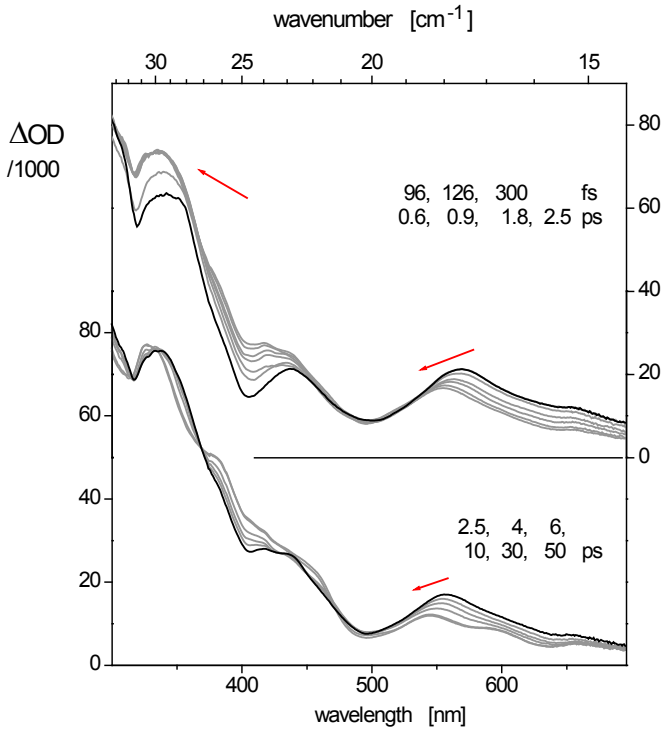

Fig. 4.11 Contribution to transient absorption from excited-state absorption, obtained by subtracting from measurement (Fig. 4.8) the corresponding bleach/stimulated emission spectrum (Fig. 4.10).

4.10, after scaling by some β. Subtraction from the measured data yields the transient ESA spectra which are shown in Fig. 4.11. An optimal bleach amplitude β may be found by monitoring spectro-temporal properties. For example consider the blueshift of the ESA band at 560 nm which seems to mirror the redshift of the emission band, probably because the corresponding $S_n \leftarrow S_1$ transition decreases the dipole moment.[157,158] By making the temporal shapes of the two opposing shifts agree, we find the same value which was used above. The excited-state absorption spectra in Fig. 4.11 will be assigned in the discussion.

4.3.2.3 Vibrational activity in the isolated molecule

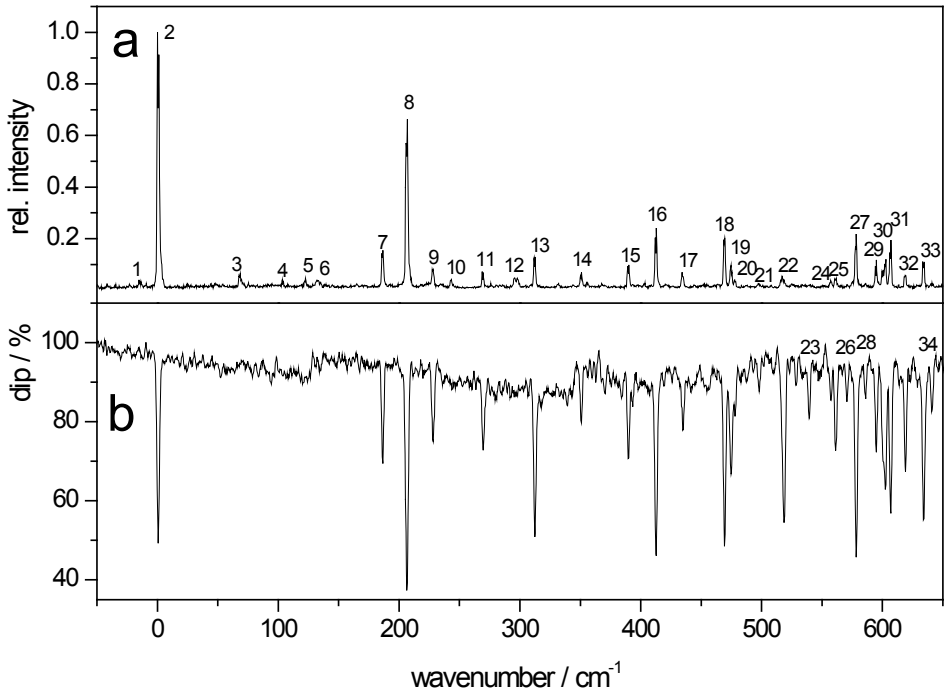

Fig. 4.12a Fluorescence excitation spectrum of isolated 4AP cooled in a supersonic expansion of helium (upper panel), and fluorescence dip in an optical-optical double resonance experiment (lower panel, see text. Line labels refer to Table 4.4).

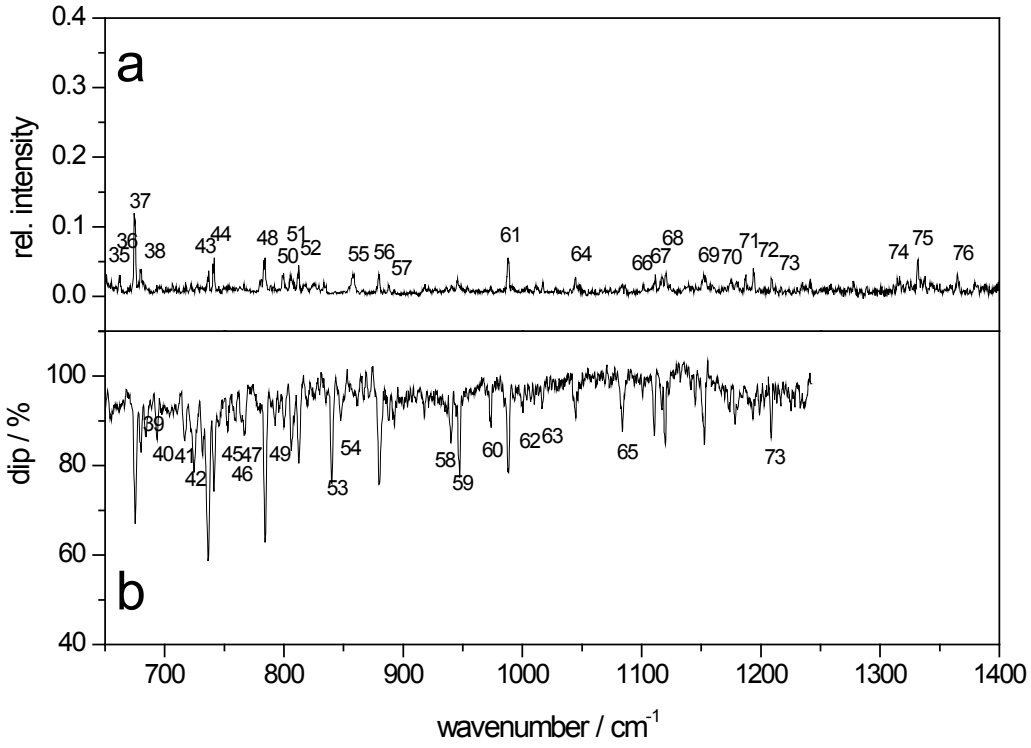

Fig. 4.12b (see Fig. 4.12a).

Gas phase spectra of 4AP were provided by Thorsten Obernhuberand Prof. Bernhard. Dick.[iv] The fluorescence excitation spectrum of 4AP seeded into a supersonic beam is shown in the upper parts of Figs. 4.12a,b. The electronic origin $S_1(v' = 0) \leftarrow S_0(v'' = 0)$ is observed at 28968.0 cm^{-1} and the excitation range extends 1400 cm^{-1} above. This spectrum was measured at high laser intensity so that some lines were partially saturated. With low laser intensity only the lines labeled 2, 8, 16, 18, and 27 were observed above the noise level up to an excess energy of 600 cm^{-1}.

Optical-optical double-resonance (OODR) spectroscopy was used to identify all lines that originate from the vibrationless ground state $v'' = 0$. In this experiment, a weak

probe laser drives the origin transition and the resulting fluorescence is collected. But ~500 ns before the probe pulse, a stronger "bleach" pulse interacts with the sample. When the bleaching laser is scanned, it will become resonant with other transitions which start from $v'' = 0$. In that case population is removed from the vibrationless ground state, registering as a fluorescence dip for the subsequent probe. The fluorescence dip spectrum is shown in the lower part of Figs. 4.12a,b. Several weak lines in the excitation spectrum do not show up in the OODR spectrum; these are assigned to impurities, which could be a complex with water molecules. Some lines in the OODR spectrum have no counterpart in the excitation spectrum, for example those labeled 23 and 53. These lines most likely lead to vibronic states that show fast internal conversion and hence do not result in significant fluorescence.

Table 4.4 lists the wavenumbers and relative intensities. Lines which appear in the OODR spectra are marked as (+) in the column "dip"; these can be assigned unequivocally to the vibrationless ground state of 4AP. Up to 1400 cm^{-1} above the origin, 16 fundamental frequencies are found which (by themselves and in combination) describe all of the observed "cold" lines.

[iv] Department of Physical and Theoretical Chemistry, Faculty for Chemistry and Pharmacy, University Regensburg, Germany.

Table 4.4 Transitions observed in a supersonic jet: Label in Fig. 4.11, shift Δν from the electronic origin at 28968 cm^{-1}, and relative LIF intensity. "Dip" marks whether the line also appears in the OODR spectrum (+) or not (-). All lines with Δν ≤ 1365 cm^{-1} are assigned to 16 fundamental frequencies (denoted a,b,c,…) and their combinations. Fundamental transitions are marked in bold face. The absorbance value for the dip signal (relative to an estimate for the 00-transition) is used to estimate the dimensionless shift of the mode, *i.e.* the displacement of the potential energy minima between S_0 and S_1 relative to the oscillation amplitude of the vibrationless state.[163]

Label	Δν	LIF intensity	dip	assignment	dip absorbance	dimensionless shift d
1	-15.3	0.04	-	-		
2	**0**	**2.28**	**+**	**origin**	**0.74[a]**	
3	68.5	0.07	-	-		
4	103.2	0.04	-	-		
5	122.7	0.05	-	-		
6	132.2	0.04	-	-		
7	**186.6**	**0.16**	**+**	**a**	**0.13**	**0.60**
8	**206.8**	**1.25**	**+**	**b**	**0.41**	**1.05**
9	**228.2**	**0.08**	**+**	**c**	**0.10**	**0.52**
10	243.4	0.04	-	-		
11	**268.9**	**0.07**	**+**	**d**	**0.10**	**0.51**
12	295.9	0.05	-	-		
13	**312.6**	**0.13**	**+**	**e**	**0.23**	**0.79**
14	**350.9**	**0.07**	**+**	**f**	**0.07**	**0.45**
15	**390.1**	**0.1**	**+**	**g**	**0.12**	**0.56**
16	412.9	0.24	+	2b		
17	434.2	0.07	+	b+c		
18	**469.5**	**0.2**	**+**	**h**	**0.27**	**0.85**
19	474.7	0.1	+	b+d		
20	477.7	0.04	+	-		
21	498.0	0.03	+	a+e		
22	516.8	0.06	+	b+e		
23	539.3	0	+	c+e		
24	557.2	0.04	+	b+f		
25	**561.7**	**0.05**	**+**	**i**	**0.11**	**0.55**
26	**571.1**	**0.02**	**+**	**j**	**0.05**	**0.35**
27	**578.3**	**0.22**	**+**	**k**	**0.31**	**0.92**
28	**586.3**	**0.03**	**+**	**l**	**0.04**	**0.33**
29	595.0	0.12	+	b+g		

30	602.9	0.12	+	2b+a		
31	**607.1**	**0.2**	**+**	**m**	**0.22**	**0.76**
32	618.9	0.06	+	3b		
33	**633.4**	**0.11**	**+**	**n**	**0.23**	**0.79**
34	641.0	0.03	+	2b+c		
35	651.3	0.03	-	-		
36	661.9	0.03	-	-		
37	674.5	0.12	+	b+h		
38	680.5	0.04	+	2b+d		
39	684.5	0	+	2a+e		
40	693.5	0.02	+	c+h		
41	**715.6**	**0.01**	**+**	**o**	**0.09**	**0.48**
42	724.5	0	+	a+2d, 2a+f, a+c+e		
43	737.0	0.04	+	d+h		
44	741.6	0.06	+	a+b+f, d+h, g+f		
45	752.7	0.01	+	a+i		
46	758.2	0	+	a+j		
47	766.6	0.02	+	3a+b, b+i, 2b+f		
48	784.1	0.06	+	b+k, 2g		
49	792.4	0.02	+	b+l, a+m		
50	799.8	0.03	+	b+g		
51	805.1	0.03	+	3b+a, c+k		
52	812.5	0.05	+	b+m		
53	840.3	0	+	a+d+g, d+j, a+h		
54	847.2	0	+	a+e+f, c+d+f, 2c+g, 2d+e		
55	857.9	0.03	-	-		
56	880.2	0.03	+	2b+h		
57	887.6	0.02	+	3b+d, e+k		
58	940.3	0.02	+	d+h, 2h, e+n		
59	945.6	0.03	+	e+n, b+d+h		
60	973.8	0.01	+	2b+i, 3b+f, a+b+k		
61	988.0	0.06	+	2b+k, b+e+h		
62	1000.4	0	+	a+b+e, a+c+l		
63	1017.3	0.02	+	2b+m, g+n, b+c+k		
64	1044.4	0.03	+	2b+n, h+k, b+c+m		
65	1083.9	0.02	+	b+d+m, 3b+h		
66	1101.7	0.02	+	h+n, b+e+k		
67	1111.5	0.03	+	b+d+n, a+e+m		
68	1120.5	0.03	+	b+e+m, 2h+a		

69	1151.9	0.03	+	2k, 2h+b		
70	1175.5	0.03	+	b+g+k, 4b+f, 3b+i		
71	1187.3	0.03	+	k+m,3b+j		
72	1193.6	0.04	+	3b+k, k+m		
73	1208.6	0.03	+	2m, k+n		
74	1316.3	0.03	?	b+h+n, d+h+k		
75	**1331.8**	**0.05**	**?**	**p**	**-**	**-**
76	1364.8	0.03	?	2k+b		

[a] Inferred from the value for mode b by using the ratio of LIF intensities.

The origin line is strongest in the spectrum. At low pump intensities the fluorescence excitation spectrum consists essentially of a progression in mode b (206.8 cm^{-1}) and of the fundamentals for modes h (469.5 cm^{-1}) and k (578.3 cm^{-1}). Note that the amplitudes of LIF lines are deceptive because internal conversion becomes significant at excess vibrational energy in S_1. The true amplitudes should be larger, as can be inferred from the OODR spectrum. Here lines no. 8 and 27, for example, have similar strength, whereas by LIF at low pump power their amplitude ratio is 6:1. The OODR dip signal is characterized by an absorbance value in Table 4.4.

4.4 Discussion

4.4.1 Dynamic Stokes shift

The extent of the 4AP Stokes shift is strongly affected by H-bonding.[141,145] For example, methanol and acetonitrile have almost the same solvent polarity, but the dynamic shifts amount to 4300 and 2160 cm^{-1}, respectively (Fig. 4.3). Half of the range in methanol may therefore be attributed to microscopic changes involving the carboxy, amino, and imide groups of 4AP. The question arises whether these changes can be recognized in the time behavior which was shown in Fig. 4.6.

Simple continuum theory ignores the shape of the chromophore, charge distribution, and specific solvent-solute interactions. The chromophore is treated as a point dipole at the center of a spherical cavity (radius r), and the surrounding solvent is replaced by a continuum with dielectric dispersion $\varepsilon(\tilde{\nu})$. One needs the dispersion including all fundamental modes; for liquid methanol this is provided in a convenient form in the supporting material. Optical excitation at t=0 increases the dipole moment of the solute instantly, causing the reaction field to change and follow in time.

The relevant calculations were outlined in chapter 1 and refs. [61,62]. They result in a normalized relaxation function $C(t)$ and thereby describe the instantaneous emission frequency $\tilde{\nu}(t)$ (approximated by the peak frequency $\tilde{\nu}_P(t)$ of the fluorescence band),

$$\tilde{\nu}(t) = \Delta\tilde{\nu} \cdot C(t) + \tilde{\nu}(\infty) \tag{4.1}$$

Here $\Delta\tilde{\nu} = 2\tilde{\lambda}_{solv} > 0$ is the spectral range over which the nuclear solvent reorganization is reported and $\tilde{\lambda}_{solv}$ the corresponding reorganization frequency. $\Delta\tilde{\nu}$ must be extracted from experimental results such as in Fig. 4.6, but it may also be calculated if only nonspecific solvation is present. The instantaneous emission frequency is governed by [175]

$$hc\,\tilde{\nu}(t) = hc\,\tilde{\nu}^{(np)} - \Delta\tilde{\mathbf{m}} \cdot \mathbf{R}(t) - \frac{1}{2}\Delta\tilde{\alpha} \cdot \mathbf{R}(t)^2 \tag{4.2}$$

where h Planck's constant, c the light velocity, and $\tilde{\nu}^{(np)}$ the emission frequency when only dispersion and induction forces are present. The second term on the r.h.s. is due to dipole/dipole interactions between solute and solvent.[175] In the present treatment the polarizability of 4AP in its ground and excited electronic states is also included; correspondingly, the third term in Eq. (4.2) is due to interaction of the induced solute dipole with solvent dipoles. $\Delta\tilde{\mathbf{m}} = f_1^{(el)}\mathbf{m}_1 - f_0^{(el)}\mathbf{m}_0$ is the difference of effective dipole moments in the S_1 and S_0 states of the solute, and similarly $\Delta\tilde{\alpha} = f_1^{(el)}\alpha_1 - f_0^{(el)}\alpha_0$ the difference of effective isotropic polarizabilities (note that $\mathbf{m}_i$ and α_i refer to the dipole moments and polarizabilities of the isolated solute in the gas phase). Self-consistency of the reaction field, to which the electronic (el) solvent polarization contributes, is achieved by the renormalization factors

$$f_i^{(el)} = \left[1 - 2\frac{n^2 - 1}{2n^2 + 1}\alpha_i \right]^{-1} \tag{4.3}$$

with solvent refractive index n. Following optical excitation, the instantaneous reaction field $\mathbf{R}(t)$ slides from $\mathbf{R}_0$ to $\mathbf{R}_1$ [48] which correspond to the equilibrium with the ground and excited state, respectively. Thus, the spectral range is given by

$$hc\,\Delta\tilde{\nu} = \Delta\tilde{\mathbf{m}} \cdot (\mathbf{R}_1 - \mathbf{R}_0) + \frac{1}{2}\Delta\tilde{\alpha} \cdot (\mathbf{R}_1^2 - \mathbf{R}_0^2). \tag{4.4}$$

The stationary reaction field is caused by the molecular dipole,

$$\mathbf{R}_i = 2\frac{1}{r^3}\left(\frac{\varepsilon - 1}{2\varepsilon + 1} - \frac{n^2 - 1}{2n^2 + 1} \right)\mathbf{m}_i\,, \tag{4.5}$$

with static dielectric constant ε of the solvent. For a test let us calculate the spectral range $\Delta\tilde{\nu}$ for solvation of 4AP in acetonitrile. Using the parameters m_0=4.5 D, m_1=7.1 D, $\alpha_0 = 16$ Å^3, $\alpha_1 = 18.4$ Å^3, r=3.3 Å [176,145] we obtain 1730+334 cm^{-1} for the dipole/dipole and induced-dipole/dipole terms of Eq. (4.4), in agreement with experiment (2160 cm^{-1}). Acetonitrile serves as non-hydroxylic reference solvent to methanol because their polarities are similar (Fig. 4.1).

The spectral dynamics $C(t)$ can be calculated from the autocorrelation function of the fluctuating reaction field $\mathbf{R}(t)$, denoted $\chi(t)$. First it is useful to consider the difference of the equilibrium reaction fields,

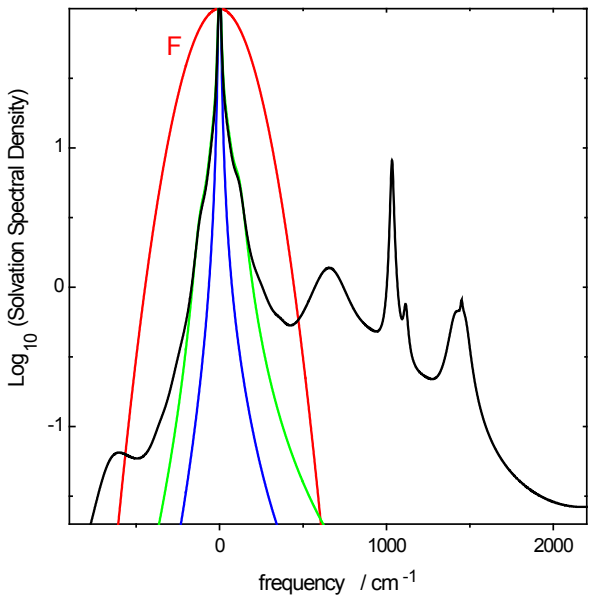

Fig. 4.13 Spectral density for dipole/dipole solvation, calculated by simple continuum theory (Eq. (4.6)) from the dielectric dispersion $\varepsilon(\tilde{\nu})$ of liquid methanol at 25°C (black line). Only the lower half of the needed frequency range is shown. The polarizability of 4AP in the excited state is $\alpha_1 = 18.2$ Å^3. The experimental time resolution (85 fs fwhm) leads to the Gaussian filter F (red). The spectral densities due to the "dielectric" modes and to the additional FIR modes up to 120 cm^{-1} are represented by the blue and green lines, respectively.

$$\mathbf{R}_1 - \mathbf{R}_0 = \frac{2}{r^3}\,\frac{\varepsilon - n^2}{2n^2+1}\left(\frac{n_1^2+2}{2\varepsilon+n_1^2}m_1 - \frac{n_0^2+2}{2\varepsilon+n_0^2}m_0\right)\mathbf{e}\,. \tag{4.6}$$

Here the dipole vectors $\mathbf{m}_i = m_i\mathbf{e}$ are taken to be parallel to a unit vector $\mathbf{e}$. The polarizabilities α_0 and α_1 of the solute have been expressed through the Clausius-Mossotti relation,

$$\frac{\alpha_i}{r^3} = \frac{n_i^2-1}{n_i^2+2}\,. \tag{4.7}$$

In effect, the cavity is considered homogeneously filled with a medium of refractive index n_i. Then Eq. (4.6) is extended into the frequency domain by $\varepsilon \to \varepsilon(\tilde{\nu})$. In this way a frequency-dependent susceptibility is obtained, and $\chi(t)$ can be reached.[175] Thus, the dynamics of the dipole/dipole contribution (second term in Eq. (4.2)) is described. Finally, from $\chi(t)$ the desired C(t) is calculated. The induced-dipole/dipole contribution (third term) slows down the initial part of the shift, but this effect is relatively small with 4AP.

Simulations should help establish the dielectric point of view. Specifically, we intend to show that the relaxation curve (Fig. 4.6) can be described completely with the set of parameters which reflects the current state of 4AP research.[176,145] Figure 4.13 shows the spectral density of dipolar solvation by methanol, extending to the Stokes ($\tilde{\nu} > 0$) and anti-Stokes sides (black line). Cosine Fourier transformation followed by normalization gives $C(t)$. In this context it is important to treat the limited time resolution correctly. The temporal apparatus function is represented in the frequency domain by a Gaussian filter which drops to 50% at 173 cm^{-1} (red line). An intermolecular mode of methanol, which in the FIR spectrum of the liquid[177] has a broad band at 116 cm^{-1}, is seen as a shoulder in the spectral density, and it is expected to be time-resolved by our fluorescence up-conversion measurement. Modes outside of the filter window, for example the sharp C-O or broad O-H stretching bands, can not be resolved. Instead they appear as an instantaneous drop from $C(0) = 1$ to an initial measurable value $C(0^+)$.[178] The latter is obtained as the integral over the filter-weighted spectral density, relative to the integral over the spectral density itself.

The measurement points $\tilde{\nu}(t)$ are now compared to the simulations by fitting them with Eq. (4.1). The parameters α_1 and $\Delta\tilde{\nu}$ are both allowed to adjust freely (the other parameter values above are kept) resulting in $\alpha_1 = 18.2 \pm 1.0$ $Å^3$ with correlated $\Delta\tilde{\nu} = 4410 \mp 290\,cm^{-1}$. Thus a value for α_1 is returned which is close to the previous estimate.[176] The optimal description is shown as blue lines in Fig. 4.6. The deviation of the measured points (49 cm^{-1} rms) is only marginally larger compared to the triexponential fit (green lines) which was mentioned in the Results section. The match by continuum theory extends over the entire time range 0.10-40 ps, and especially the exponential regime change around 1.3 ps is clearly expressed. Fig. 14 provides a decomposition of $C(t)$ into four Brownian oscillator modes, which may be associated

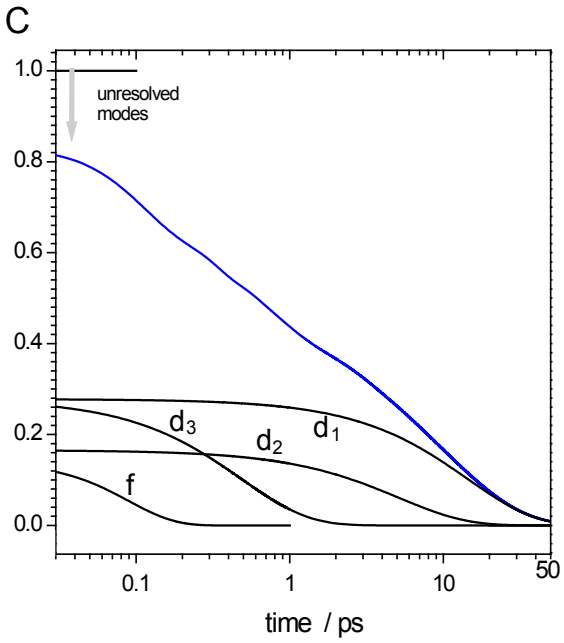

Fig. 4.14 Solvation relaxation function C(t) for 4AP, calculated from the dielectric dispersion of methanol with $\alpha_1 = 18.2$ Å^3. An initial drop is due to modes which can not be resolved at the given experimental resolution. On the logarithmic timescale, dielectric modes d_1 and d_2 known from microwave spectroscopy of the liquid can be distinguished from a fast dielectric mode d_3 and a FIR mode f at 116 cm^{-1} (black lines, Appendix A).

(see Appendix A) with three modes observed for dielectric relaxation[179] and the far-infrared band[177] at 116 cm^{-1} of pure methanol. These findings suggest that nonspecific polar solvation is being observed here. Not only the shape of the measured $\tilde{\nu}(t)$ data set agrees well with continuum theory, but also the extrapolation $t \to 0$ matches with the observations. It implies that polar solvation sets in an $\Delta\tilde{\nu} + \tilde{\nu}(\infty) = 22960$ cm^{-1}, in agreement with the value $\tilde{\nu}(0) = 22850$ cm^{-1} from the "spectroscopic time-zero analysis". There is no need to attribute part of the reorganization energy to H-bonding with specific dynamics, distinct from polar dynamics. (Contrast this with the multiexponential description of $\tilde{\nu}(t)$, Table 2, which upon extrapolation $t \to 0$ misses 1120 cm^{-1} of the dynamic Stokes shift;[150] Fig. 4.6.) It follows that fluorescing 4-Aminophthalimide reports polar solvation faithfully, at least in methanol, despite H-bonding.

4.4.2 Spectral broadening

Upon going from 2-methylbutane to methanol solution can also be explained by polar solvation. On one hand it is characterized through stationary spectroscopy, as convolution of the $S_1 \leftarrow S_0$ absorption lineshape in 2-methylbutane by a Gaussian $\sim\exp\left(-\tilde{\nu}^2 / 2\tilde{\delta}^2\right)$ with $\tilde{\delta}_{abs} = 1010\,cm^{-1}$ on the other hand it may be estimated from the dynamic reorganization frequency $\Delta\tilde{\nu}$ as[180]

$$\tilde{\delta}_{shift} = \sqrt{\Delta\tilde{\nu} \cdot k_B T / hc}\ . \qquad (4.8)$$

Here k_B is Boltzmann's and h Planck's constant and T is the temperature. Using the full dynamic shift $\Delta\tilde{\nu} = 4300\,cm^{-1}$ we find $\tilde{\delta}_{shift} = 940\,cm^{-1}$, *i.e.* 70 cm^{-1} below $\tilde{\delta}_{abs}$ at the limit of the confidence interval for time-zero analysis. For an explanation of this discrepancy let us compare the stationary emission spectra in 2-methylbutane and methanol also. When the emission lineshape in 2-methylbutane is properly shifted and then broadened by only $\tilde{\delta}_{fls} = 300\,cm^{-1}$, one obtains the simulated fluorescence quantum distribution which is shown as a red line in Fig. 4.3. The broadening diminishes as solvation by methanol proceeds, and this is reflected by the time-dependent width $\Delta(t)$ of the evolving fluorescence band (Fig. 4.7). Evidently, intramolecular modes are coupled to the solvent coordinate, but we can only speculate on the mechanisms: by nonlinear interaction with the reaction field,[113] or indeed specifically through H-bonds.[145] In either case a systematic difference is implied between $\tilde{\delta}_{abs}$ and $\tilde{\delta}_{shift}$.

Finally for this part the intramolecular reorganization energy in 2-methylbutane, $\tilde{\lambda}_{intra} \approx 2025$ cm^{-1}, is discussed. This value can be placed into the context of the jet spectroscopy above. There 16 modes $\tilde{\nu}_j$ (out of 48) were determined, and the dimensionless displacements d_j for 15 modes were estimated from the relative intensities of the OODR lines (Table 4.4). The classical intramolecular reorganization energy for these modes is $\sum_{j=1}^{15} \tilde{\nu}_j d_j^2 / 2 = 1440\,cm^{-1}$. Assuming that the mode at 1331.8 cm^{-1} is responsible for the remaining contribution $\tilde{\nu}_{16} d_{16}^2 / 2$ to $\tilde{\lambda}_{intra}$, we find

$d_{16} \approx 0.95$. In addition we simulated the absorption and emission lineshapes in 2-methylbutane with Brownian oscillators.[31,26] A high-frequency intramolecular mode of 1350-1400 cm^{-1} is again required, with dimensionless displacement 1.5-1.7 . Single-level fluorescence from 3AP in a supersonic jet showed activity in a mode at 1389 cm^{-1}, ascribed to a C=C stretching vibration, with an estimated displacement ≈ 1.[163] We conclude that the major part of the intramolecular reorganization can be represented by the modes collected in Table 4.4. An interesting aspect of the reorganization between the S_0 and S_1 states is a long progression in the fluorescence excitation spectrum with vibrational spacing of 206.8 cm^{-1}, mode b in Table 4.4. Our quantum-chemical calculations predict a planar S_1 state, whereas the amino group has a pyramidal conformation in the S_0 state (see Table 4.4). Correspondingly, mode b is assigned to out-of-plane motion of the amino group (rather than to in-plane wagging involving the >C=O groups[181]) and the progressional spacing to double quantum transitions.

4.4.3 The excited-state absorption spectrum

Excited state spectrum of 4AP in methanol (Fig. 4.11) was obtained as a side result in section 4.4.2. A blue-sift of the ESA band at 560 nm reflects a decrease of dipole moment upon excitation $S_n \leftarrow S_1$.[157,158] Since the band is neither sharp nor prominent, however, it can not be used to measure solvation dynamics as suggested for other probes.[158] It is interesting to discuss the ESA spectrum for other reasons instead.

The location of electronic states can be estimated in conjunction with quantum-chemical calculations. For this purpose the ESA spectrum is plotted on an energy scale in Fig. 4.15 (black lines, referring to $t = \infty$). The ground-state absorption spectrum is shown shifted by -23550 cm^{-1} (blue line). Before proceeding remember that the TD-DFT calculations were performed for the isolated molecule constrained to planarity. Disregarding the limitations of the method and of its implementation, the

calculations agree with experiments in that $S_2 \equiv A''(1)$ is well separated from $S_1 \equiv A'(1)$; only the

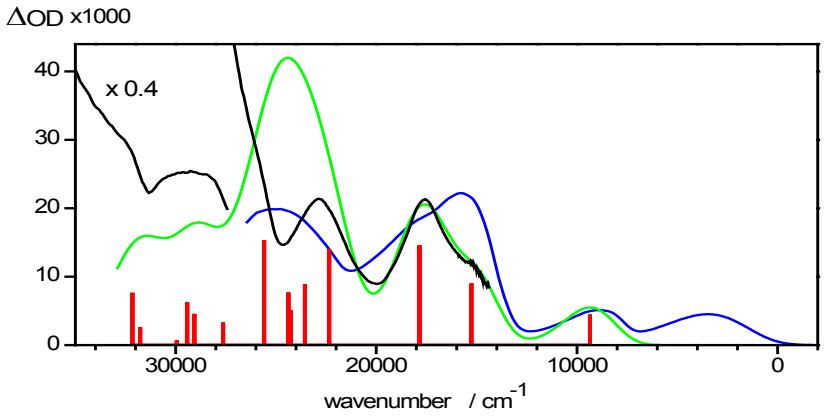

Fig. 4.15 Assignment of the ESA spectrum. Black – measurement at t=∞, blue – shifted ground-state absorption, green – spectrum from broadening the calculated A' transitions (vertical bars, see text).

latter is expected to be populated by excitation at 403 nm. Transition moments with sizable oscillator strength point essentially in the molecular plane, and this is why the ESA spectrum involves transitions only which can be classified $A'(i) \leftarrow A'(1)$. The higher states i=3,4 are readily identified by comparison with $A'(i) \leftarrow A'(0)$. The calculations predict a ratio of oscillator strengths $f_{40}/f_{30} \approx 0.45$ for ground-state absorption, which is inverted to $f_{41}/f_{31} \approx 1.62$ for excited-state absorption. With this knowledge the blue line in Fig. 4.15 was adjusted, thus locating the zero-point for the free energy axis (1260 cm^{-1} below the electronic origin in methanol). The calculated pattern of $A'(i) \leftarrow A'(1)$ transitions (vertical bars) and an associated absorption envelope are also shown in the figure (green line; lognormals with $\Delta = 1500\,cm^{-1}$, $\gamma = 0.16$). The calculated transition frequencies had to be increased by +2900 cm^{-1} for a match with experiment. The characteristic structure of the observed ESA spectrum, especially the minimum around 20000 cm^{-1}, is well represented by the calculations. We conclude that the states $A'(4)$ and $A'(3)$ are reasonably isolated from their neighbors. The peak of the $A'(4) \leftarrow A'(1)$ transition at 568 nm is convenient for time-resolved resonance Raman spectroscopy in the excited state.[182,183]. In that way one could follow the structural relaxation, including H-bonds, more directly.

4.5 Conclusion

We presented fs time-resolved emission and transient absorption spectra of the popular solvatochromic probe 4-aminophthalimide in methanol solution at room temperature. We also provided stationary spectra in a nonpolar reference solvent, results from supersonic jet spectroscopy, and calculations by density functional theory. Together they help to support the interpretation of the time-resolved data. The main conclusion of this work is that, despite the well-known fact that Stokes shifts of 4AP are nearly 2-fold larger in hydrogen bond donating solvents compared to polar aprotic solvents, the dynamic Stokes shift of 4AP in methanol is well described solely by non-specific solvation. This surprising result should be of interest to many researchers working in the area of solution-phase dynamics.

5 On the Molecularity of Solvation Dynamics

5.1 Introduction (partly based on own publication, Ref. 184)

In a solvation–dynamics measurement the charge distribution of a solvated dye molecule is suddenly changed by optical excitation $S_1 \leftarrow S_0$, and the band for fluorescence $S_1 \rightarrow S_0$ is subsequently observed in time. The peak or mean emission wavenumber $\tilde{\nu}(t)$ provides the time-dependent Stokes shift (TDSS) which, for a well–chosen probe, reflects the reorganizational dynamics of the solvent shells and bulk nearby. TDSS measurements are widely used to explore local dynamics in complex and biological systems.[5,6,7,8,9,10,11] In a ideal case the local THz spectrum can even be obtained.[121] Such applications require further investigations into the molecularity of the process, *i.e.* the dependence on the probe. TDSS measurements results are not easy to interpret since the environment of the solute comprises molecular groups which are dynamically active differently; hence, finding the dominant source of dynamics is highly debatable. Therefore, complementary measurements should be devised to help understand the results.

Picosecond studies established a close connection between the "tail" solvation time τ_{solv} (from an exponential fit of the TDSS) with the Debye time τ_D of dielectric relaxation in the microwave range, $\tau_{solv} \approx \tau_D \varepsilon_\infty / \varepsilon_0$. This formula is obtained by calculating $\tilde{\nu}(t)$ from simple continuum theory, *i.e.* from solvation of a point dipole in a spherical cavity surrounded by a dielectric. ε_∞ and ε_0 are the near-infrared and zero-frequency limits, respectively, of the complex dielectric permittivity $\varepsilon(\omega)$.

Dynamic solvation of a polar solute by water has been studied intensely (for example see [59,60,62,79] and references cited therein). Femtosecond resolution allowed searching for the water response before ≈100 fs where inertial solvent motion is expected.[60] Using the solvatochromic fluorophore *N*-methyl-6-oxyquinolinium betaine

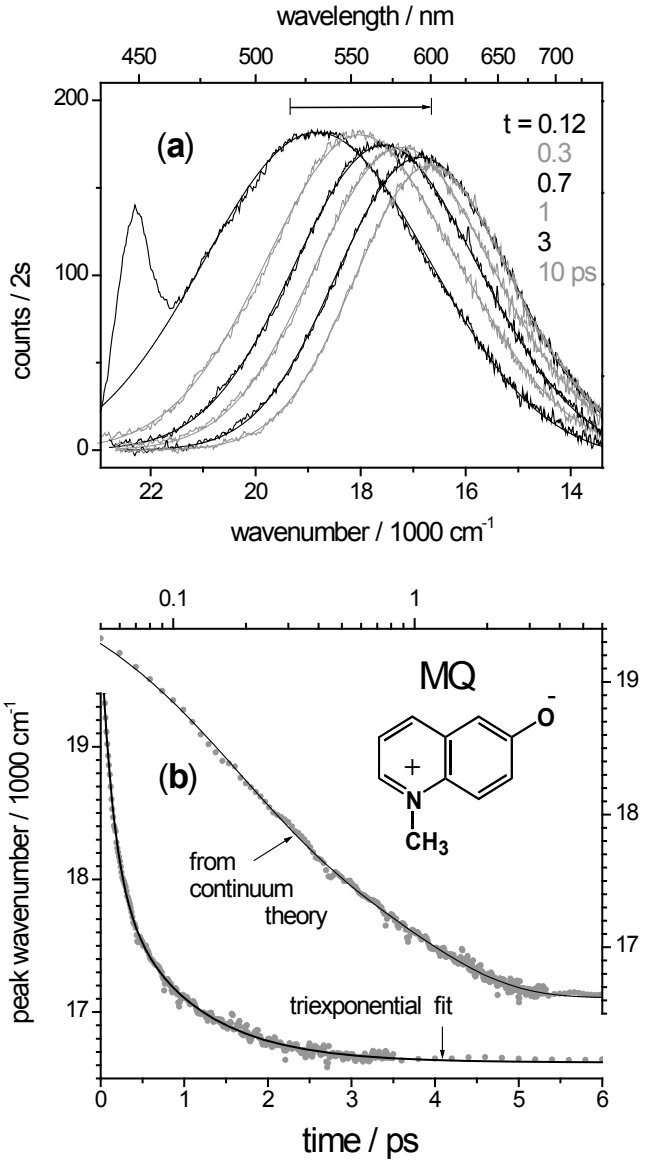

Fig. 5.1 (a) Transient fluorescence spectra of *N*-methyl-6-oxyquinolinium betaine (MQ) in water, and lognormal fits. Fluorescence was detected with parallel polarization to that of the pump in this case. The spike at 0.12 ps is due to scattered pump light, and the horizontal arrow indicates the total relaxation of the peak frequency. (b) A spectral relaxation function is constructed from the lognorm peak frequencies as function of delay time (gray dots). A multiexponential fit (for $t \geq 0.1$ ps) is used for empirical description. The behavior is well described by dipole solvation calculated with simple continuum theory (see text and ref. 62).

(MQ, inset to Fig. 5.1) Lustres et al showed quantitatively that the entire THz-FIR range of $\varepsilon(\omega)$ is involved and the polarizability of the solute is represented by an effective refractive index n_{cav} inside the cavity.[62] Results were corroborated and the accuracy improved by monitoring fluorescence instead of stimulated emission.[122] Especially for this purpose a broadband up-conversion spectrometer was

developed.[76,77,] Typical time-resolved fluorescence spectra in water (from the work below) are shown in Fig. 5.1. With $\varepsilon(\omega)$ of water and n_{cav}=1.3 we obtain a simulation curve (solid line in Fig. 5.1b) which matches the experimental result (gray dots) surprisingly well.

But the simplicity could be deceptive: structural effects may have been absorbed into the empirical fitting parameter n_{cav}.[185] With different probes it is conceivable that different n_{cav} values are obtained for the same solvent. This would indicate that n_{cav} no longer reflects the polarizability of the chromophore alone, but may also cover other effects like spatial variations. To expose dynamic differences which reflect the molecularity of solvation, here we use diverse chromophores in water and methanol (Fig. 5.3). As main result, polar solvation in water is found independent of the solutes used, in contrast to the methanol case. Excitation and temperature dependence of solvation dynamics are studied next. The former study reveals that in nonpolar and aprotic polar solvents upon exciting the molecular probes with significant amount of excess energy, in addition to the solvent contribution extra red shifts of the fluorescence bands are observed. The latter shifts are attributed to the intramolecular thermal effects of chromophores in their electronic excited state. Finally the temperature dependence of solvation dynamics in D_2O shows two activation energies, different from the other solvents where only single activation energy is found.

5.2 Experimental

5.2.1 Materials

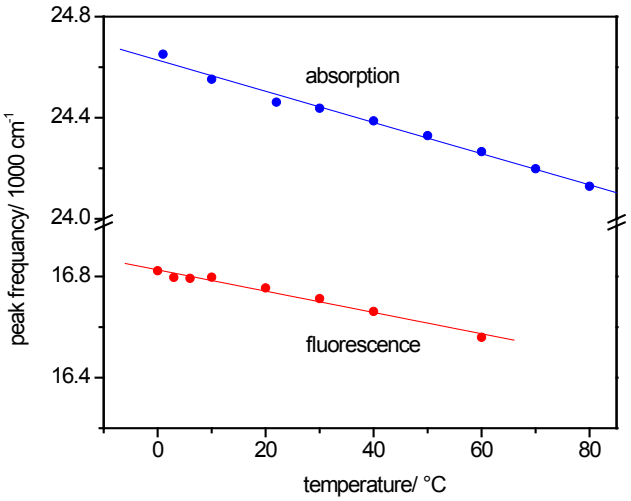

Fig. 5.2 Thermochromism of MQ in water. Absorption and fluorescence bands of MQ shift to the red when the temperature is increased. Since the dipole moment decreases 8 D ← 10 D upon excitation $S_1 \leftarrow S_0$, this red shift is consistent with the reverse solvatochromism of MQ.[62]

The chemical structures of the solutes in this study are shown in Fig. 5.3. Coumarins 153, 343 and 334 (C153, C343, C334) were obtained from RADIANT DYES, 7-(Dimethylamino)coumarin-4-acetic acid (DMACA) from MOLECULAR PROBES, 4-Dicyanomethylene-2-methyl-6-(p-dimethylaminostyryl)-4H-pyran (DCM) from LAMBDA PHYSIK, 3-Aminophthalimide (3AP) from ALDRICH, and 4-Aminophthalimide (4AP) from ACROS. The dyes were used as received. MQ and 4AP linked to 2´-deoxyribose (4AP-Ri, Fig. 5.3) were synthesized as described elsewhere.[62,186] To avoid protonation of zwitterionic MQ in water, the pH was adjusted to ≈9 with NaOH. Similarly the solubility of C343 in water was increased.

5.2.2 Stationary measurements

Stationary absorption and emission spectra were recorded with a CARY 300 spectrometer and a SPECTRONICS INSTRUMENTS 8100 spectrofluorometer, both with 1 nm resolution. The temperature dependence for MQ in water is shown in Fig. 5.2.

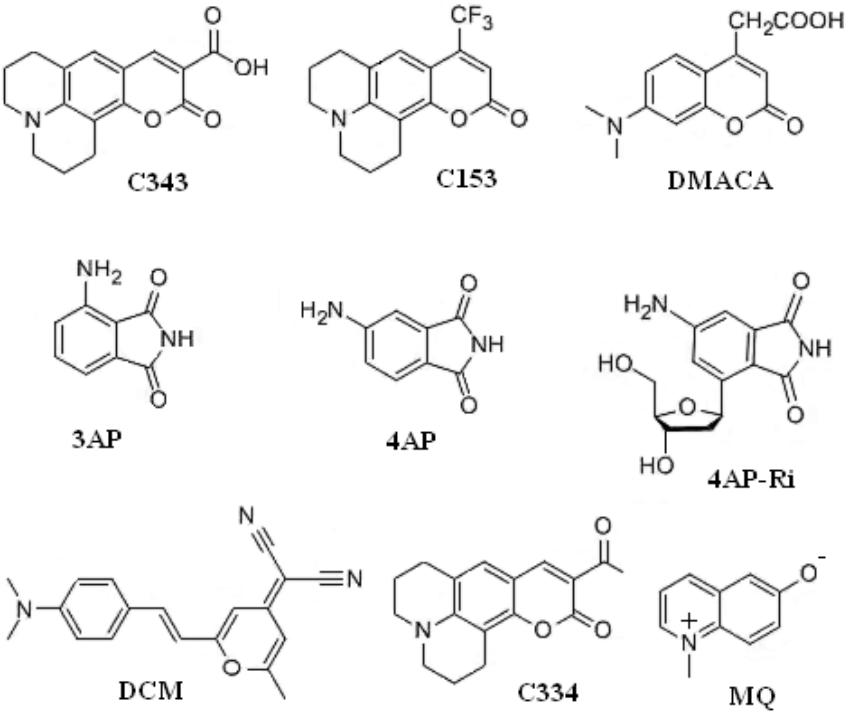

Fig. 5.3 Chemical structures of the molecular probes used in this study.

5.2.3 Time resolved measurements

Broadband fluorescence up-conversion was performed with the setup and procedures which was explained in chapter 3. To set the temperature for each measurement, the solution was passed through 150 mm of a stainless-steel tube with 1 mm internal diameter, embedded in a bath of controlled temperature. The tube feeds directly into the cell which is made of PEEK. A small PT100 sensor is located in the flowing solution prior to entering the cell. Windows were kept free of water

condensation by blowing with thermostatted dry air. The temperatures of entering and exiting flow differed by less than 1°.

Dyes were generally dissolved so that the optical density at the peak of the lowest absorption band, across the 0.4 mm sample cell, was $OD_{max} \leq 0.5$ (only with DCM was $OD_{max} \approx 1$). Optical excitation at 400 nm was achieved by focusing 1 μJ pulses (500 Hz) into the cell to a spot of 80 μm diameter. Transient fluorescence spectra of MQ and 4AP-Ri in water were measured with 2 s integration time, and of the other solutes with 1 s. The average of 16 time scans was then corrected for photometric and temporal instrument factors. In this way the (relative) fluorescence quantum distribution over wavenumbers was obtained as function of time. 85 fs (fwhm) time resolution is determined from the pump-gate cross-correlation between the gate and the pump pulses which have passed through the sample cell.

5.2.4 Anisotropy measurement

Anisotropy decay $r(t)=(I_{\parallel}-2I_{\perp})/(I_{\parallel}+2I_{\perp})$ was obtained from the lognorm amplitudes (see below) $I_{\parallel}(t)$ and $I_{\perp}(t)$, of transient spectra measured with vertical and horizontal pump polarizations (vertically polarized fluorescence is detected in our setup). These measurements were performed for room-temperature solutions only. Slightly different excitation pulse energies for the two time scans were corrected for by setting r(t)=0 at 5x the average anisotropy decay time. With DCM this late time could not be reached; in this case r(t) was also measured pointwise at t=100, 300, and 580 ps.

5.3 Results

Typical transient fluorescence spectra were already shown in Fig. 5.1a for MQ/water at room temperature (21°C). Shown are the relative quantum distributions over wavenumbers at pump-gate delays of 0.12, 0.3, 0.7, 1, 3 and 10 ps. The sharp peak on the blue side of spectrum, at 0.12 ps, is the tail of pump scatter. An evolution of bandwidth is also seen from the raw spectra. Every transient spectrum is fitted by a

lognormal function; the corresponding results are given as smooth lines in the figure. The spectral relaxation is taken to be the fitted peak wavenumber $\tilde{\upsilon}(t)$ as function of delay time, Fig. 5.1b**.** The first delay time for which the lognormal shape extends over most of the band,

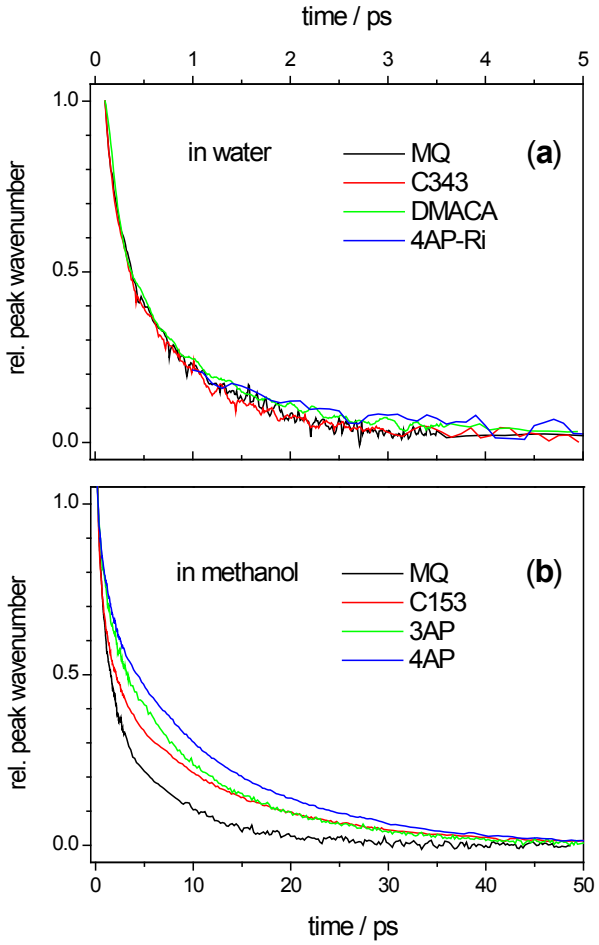

Fig. 5.4 Peak-frequency relaxation, normalized to 1 and 0 at t=0.10 ps and late time, respectively. In water (**a**) the dynamics of the probes are equal within experimental precision. In methanol (b) large differences are observed. Note the different time scales.

i.e. when $\tilde{\upsilon}(t)$ is reliable, is $t \approx 100\,\mathrm{fs}$. In water at room temperature, the fluorescence band of MQ relaxes from 18588 cm^{-1} at t=100 fs to 16730 cm^{-1} at t=20 ps.

Relaxation functions for different probes, at room-temperature, are compared in Fig. 5.4 where normalized values $s(t) = \left(\tilde{\nu}(t) - \tilde{\nu}(\infty)\right)/\left(\tilde{\nu}(100\mathrm{fs}) - \tilde{\nu}(\infty)\right)$ are shown. In water (a) the process is over by 5 ps, and the s(t) from the four water-soluble probes all appear to follow the same dynamics. The noise is different because of different

solubilities and hence, signal strengths (with MQ the standard error in s(t) is ±1.6%). In

Table 5.1 Peak frequency relaxations in methanol and water at 21°C: exponential fit parameters.

Solute / water	τ_1 /ps	τ_2 /ps	τ_3 /ps	b_1 %	b_2 %	b_3 %	a_0 /cm^{-1}	a_∞ /cm^{-1}	$\langle\tau\rangle$ /ps
MQ	0.112	0.30	1.45	43.3	33.5	23.2	19480	16730	0.48
C343	0.1	0.58	1.66	57	37	12	21400	20375	0.44
DMACA	0.1	0.72	3.48	65	29	5	22810	20745	0.47
4AP-ri	0.1	0.3	1.99	49	37	13	21100	17705	0.43

Solute / methanol	τ_1 /ps	τ_2 /ps	τ_3 /ps	b_1 %	b_2 %	b_3 %	a_0 /cm^{-1}	a_∞ /cm^{-1}	$\langle\tau\rangle$ /ps
MQ	0.23	1.15	6.81	21.5	47.8	30.7	19460	15940	2.69
C153	0.12	1.15	11.7	55.2	21.5	23.4	21475	18410	3.04
4AP	0.12	1.16	12.4	27.0	24.2	48.8	22390	18840	6.35
3AP	0.11	1.2	10.3	30.3	26.7	43.0	22765	20440	4.76
DCM	0.25	1.11	8.5	32.0	38.7	29.3	15650	14000	2.99

The fit $\tilde{\nu}(t) = (a_0 - a_\infty)\cdot C(t) + a_\infty$ with $C(t) = \sum b_i \exp(-t/\tau_1)$ is valid for delays $t \geq 0.1$ ps. The extrapolated value a_0 has no physical meaning. The average relaxation time is $\langle\tau\rangle = \sum_i b_i\tau_i$. The rms deviation between the measured MQ data and the fit is ±22 (18) cm^{-1} for solutions in water (methanol), or ±1.6 (0.6) %.

methanol (b) the process extends beyond 50 ps, and the s(t) of the various probes look qualitatively different. For an empirical description the $\tilde{\upsilon}(t)$ data points for $t \geq 100$ fs are fitted by a multiexponential time function (black line in Fig. 5.1b). Optimal fit parameters are collected in Tables 5.1. Anisotropy decay r(t) of several solutes in methanol is compared in Fig. 5.5a**,** and of DCM in methanol and dimethyl sulfoxide (dmso) in Fig. 5.5b. Here again, normalized curves are presented. Multiexponential fits to r(t) data for $t \geq 100$ fs are provided by

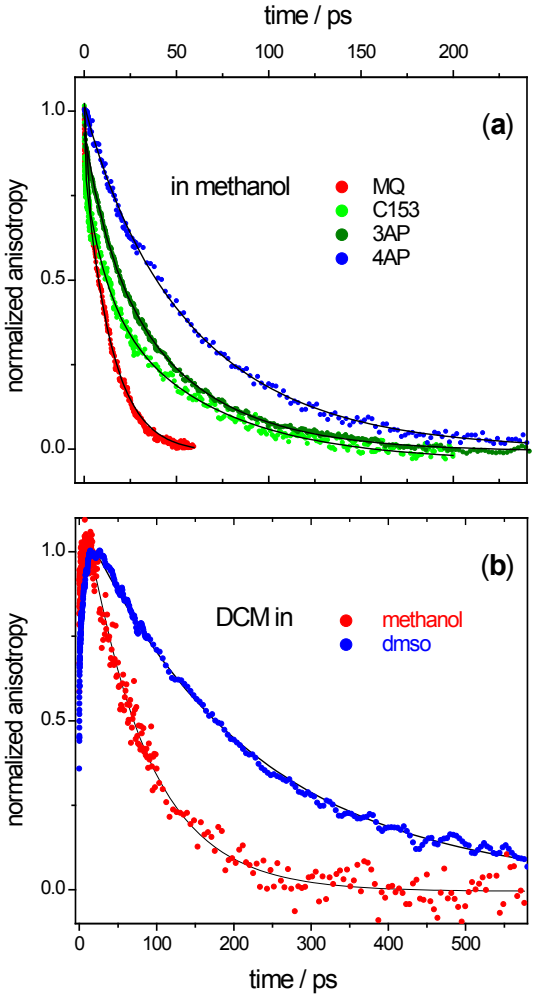

Fig. 5.5 Fluorescence anisotropy (a) for C153, 3AP, and 4AP in methanol, (b) for DCM in methanol (red) and DMSO (blue), showing a rise to a maximum at ≈10 ps. Initial or maximum anisotropies are > 0.34 with the exception of DCM in methanol.

Table 5.2. Note that for DCM/methanol (dmso) the anisotropy first rises to a value of 0.14 (0.36) around 10 ps, and then decays on a 100 ps time scale.

The excitation dependence of solvation dynamics in polar and non-polar solvents also is investigated. Instead of varying the excitation wavelength across entire absorption band, we use only two excitation energies but with diverse probes, in which, the same

Table 5.2 Anisotropy decays at 21°C: exponential fit parameters.

solute / solvent	τ_1 /ps	τ_2 /ps	τ_2 /ps	b_1 or a_1	b_2 or a_2	b_3	a_0
MQ / methanol	0.135	13.5	–	30%	70%	–	0.38
C153* / methanol	0.26	31	–	38%	62%	–	0.34
4AP / methanol	60	–	–	–	–	–	0.34
3AP / methanol	0.78	32.3	174	12.6%	79%	8%	0.36
DCM / methanol	6.1	78	–	-0.39	1.24	–	
DCM / dmso	5.9	189	–	-0.208	0.41	–	

Fits $r(t) = a_0 \cdot \sum b_i \exp(-t/\tau_i)$ or $r(t) = \sum a_i \exp(-t/\tau_i)$ are valid for delays $t \geq 0.1$ ps. * τ_1 =5.9 ps (23%) and τ_2 =44 ps with a_0=0.375 was reported by ref.123

Table. 5.3 Exponential fit parameters of peak frequency decay.

Solute /excitation	/solvent	τ_1 /ps	τ_2/ps	τ_3 /ps	a_1 /cm^{-1}	a_2 /cm^{-1}	a_3 /cm^{-1}	a_0 /cm^{-1}	<τ>*
C153/400nm	/acetonitrile	0.11	0.62	10.7	2052	649	-171	18930	0.232
C153/450nm	/acetonitrile	0.128	0.649	---	2361	530	---	18924	0.223
C343/400nm	/acetonitrile	0.13	0.69	12.7	748	365	-349	20385	0.314
C343/450nm	/acetonitrile	0.14	0.55	21.3	729	304	-31	20382	0.26
C334/400nm	/cyclohexane	0.085	----	10	255	----	-286	21658	----

* averaged over positive amplitudes

variation is achieved. Fig. 5.6 shows absorption spectra of MQ, DCM, C153, C343, and C334 in methanol, water, acetonitrile, and cyclohexane. Dashed lines at 400 nm and 450 nm indicate the excitation wavelengths. Relaxation functions in four selected solvents are shown in Fig. 5.7, and the exponential fit parameters are collected in Table 5.3. As seen from Fig. 5.7a and 5. 7b, relaxation in nonpolar and aprotic solvents shows a "retrograde" blue shift after a normal Stokes shift, if excess vibrational energy is given to the molecule

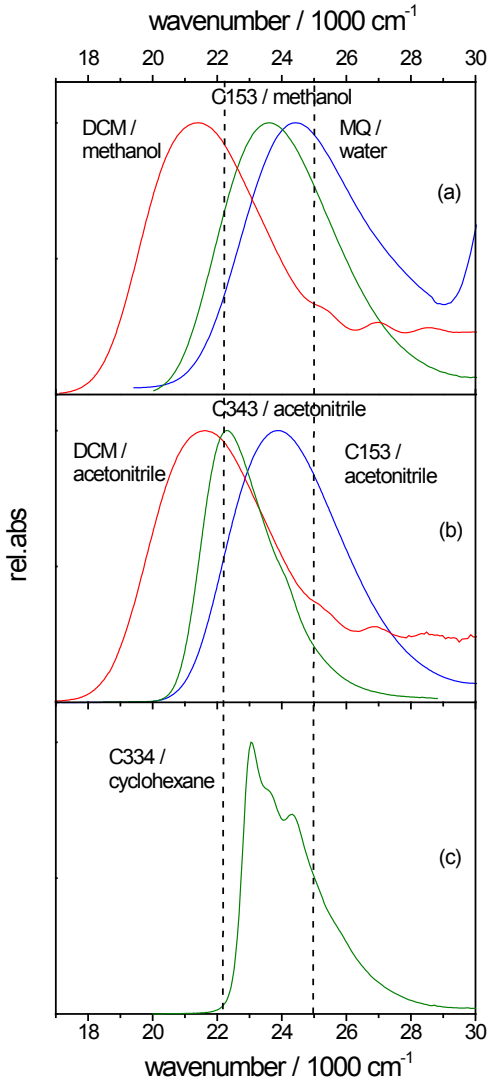

Fig. 5.6 Stationary absorption spectra of the dyes in (a) protic, (b) aprotic, and (c) nonpolar solvents. Dashed lines denote the excitation energies.

(see also Fig. 5.6). In another words, the probe chromophore undergoes an additional red shift in these cases, from which it recovers in the end. The amount of extra red shift is a function of excess energy. In protic solvents the retrograde shift is not observed. Fig. 5.7c shows the relaxation of MQ in water excited at 400 nm at blue flank of its absorption band.

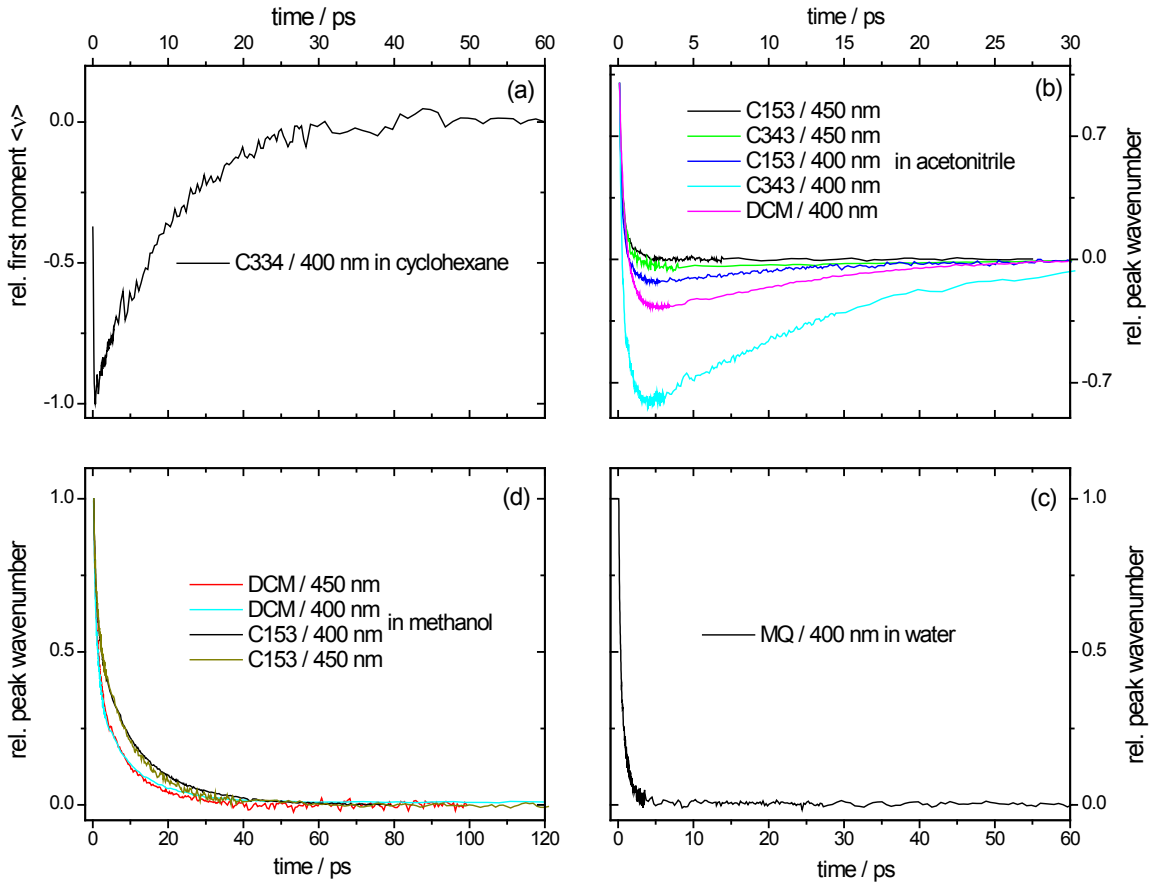

Fig. 5.7 Excitation dependence of spectral relaxation. (a) The fluorescence peak of C343 in cyclohexane shows a fast initial red-shifted upon 400 nm excitation. A part of that shift is resolved with 80 fs time resolution. Cooling take place with 8-10 ps time constant and is observed as a blue shift of spectra. (b) In acetonitrile the fluorescence band is also red-shifted upon blue edge excitation. Giving more excess energy to the molecule causes more red shift, and in turn, larger retrograde recovery. (c) In water, giving excess energy upon excitation to the solute does not change the normal spectral relaxation, i.e the retro effect is not seen. (d) In methanol also the spectral relaxation is independent of excitation energy.

Fig. 5.7d shows the shift dynamics of C153 and DCM with 400 nm and 450 nm excitation in methanol. Analogous to water, the relaxation is independent of excitation energy.

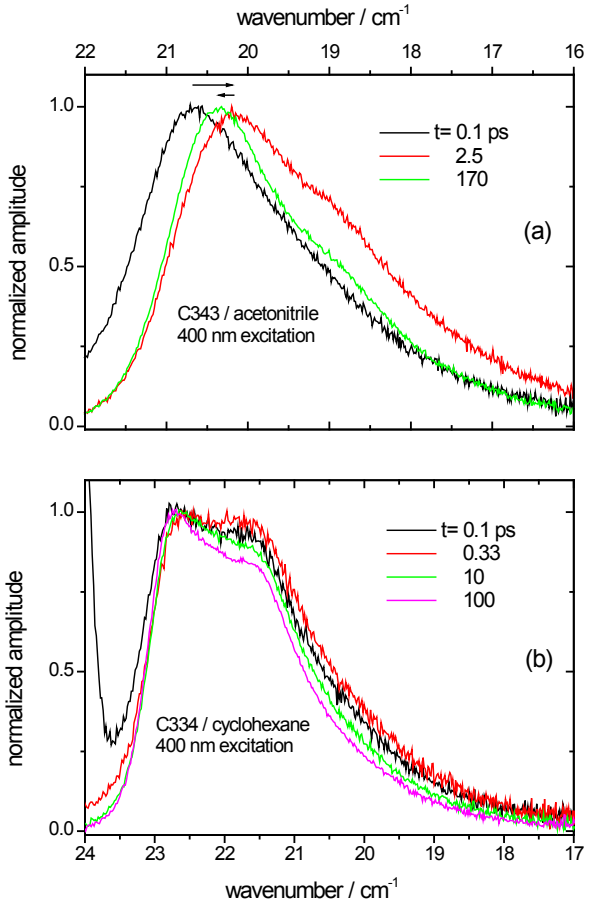

Fig. 5.8 (a) Transient fluorescence spectra of C343 in acetonitrile, upon 400 nm excitation. Note that spectrum at 170 ps is blue shifted compared to the spectrum at 2.5 ps. (b) Transient fluorescence spectra of C334 in cyclohexane, upon 400 nm excitation. Note the blue shift of spectra after a fast red shift.

In Fig. 5.7b a maximum retrograde shift is observed for C343 in acetonitrile upon 400 nm excitation. Fig. 5.8a shows transient fluorescence spectra of C343 in acetonitrile at 0.1, 2.5 and 170 ps. Clearly the spectrum at 2.5 ps is red shifted relative to the stationary state at 170 ps. Fig. 5.8b shows transient fluorescence spectra of C334 in cyclohexane at 0.1, 0.33, 10, and 100 ps. Transient spectra at early times (up to ~0.3 ps) are red shifted and afterwards blue shifted.

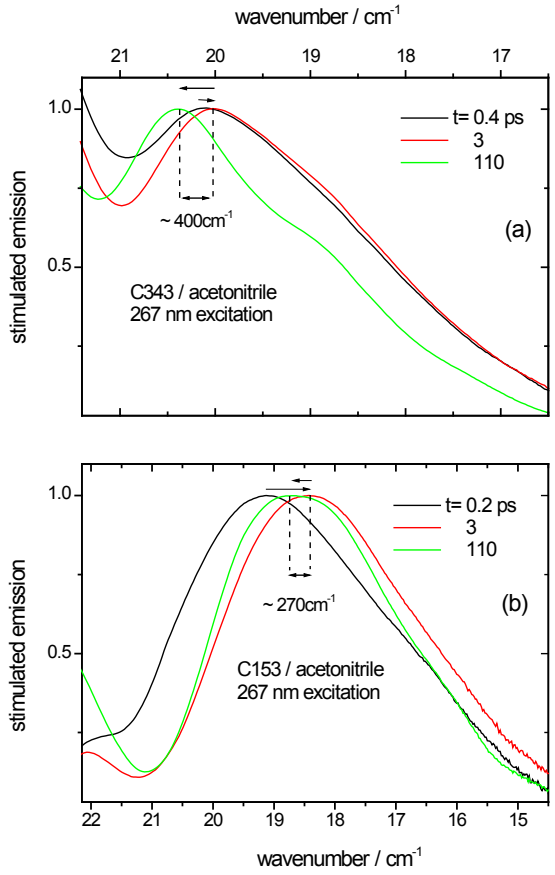

Fig. 5.9 (a) Transient stimulated emission of C343 in acetonitrile, upon 260 nm excitation. An additional red shift, when the excess energy to the molecule is increased, is estimated to be 400 cm^{-1}. (b) Transient stimulated emission of C153 in acetonitrile, upon 260 nm excitation. An additional red shift upon excess energy is estimated to be 270 cm^{-1}.

Transient absorption spectra of C343 and C153 in acetonitrile were measured to corroborate the accuracy of transient fluorescence results. Fig 5.9a shows the normalized stimulated emission of C334 in acetonitrile upon 260 nm excitation. The spectrum at 3 ps is ~ 400 cm^{-1} red shifted relative to the stationary spectrum at 110 ps. In C153 (Fig. 5.9b) also upon 260 nm excitation, a retrograde shift is observed. In this case the emission band at 3 ps is ~270 cm^{-1} red shifted relative to the quasistationary state at 110 ps.

5.4 Discussion

5.4.1 No solute dependence of water solvation dynamics

Four chromophores, MQ, C343, DMACA and 4AP-Ri (Fig. 5.3**)** were used to find a solute dependence of solvation in water. Zwitterionic MQ shows reverse solvatochromism and strong H-bonds in the S_0 state (Fig. 5.10). In water it has a well-defined first solvation shell of 3.6 H_2O molecules around phenolate oxygen on average, resembling the microsolvation of an anion. Upon $S_1 \leftarrow S_0$ excitation these bonds are weakened and one H_2O is ejected into the second shell.[187] By contrast, coumarins C343 and DMACA[79] become more polar upon excitation (normal solvatochromism). They differ in hydrophobicity/H-bonding ability as shown by solubilities. The effect of H-bonding on the optical spectra is stronger for 4AP which here, in addition, is tethered to 2′-deoxyribose to make it water soluble. But surprisingly, despite all of these molecular differences, the spectral relaxation of the four probes in water is not distinguishable and thus solute-independent. At our photometric resolution, relaxation can always be constructed from $\varepsilon(\omega)$. In this sense there is no evidence for molecularity.

5.4.2 Solute dependence of methanol solvation dynamics

For methanol a similar set of probes is composed of MQ, C153, 4AP and 3AP. Their spectral dynamics, Fig. 5.4b, now *do* show differences; for example the average shift time increases more than twofold in going from MQ to 4AP. Dielectric simulation can describe the 4AP shift dynamics almost to experimental noise, but with n_{cav}=2.6.[188] It fails to describe MQ dynamics even qualitatively for any n_{cav} (Fig. 5.11).

To find a microscopic reason why the solutes show different spectral relaxation in the course of solvation, consider the anisotropy decays in methanol, Fig. 5.5a and Table 5.2. The difference between 4AP (slow) and MQ (fast) is striking and,

in view of the discussion above, suggests a connection between rotational diffusion of the probe and its

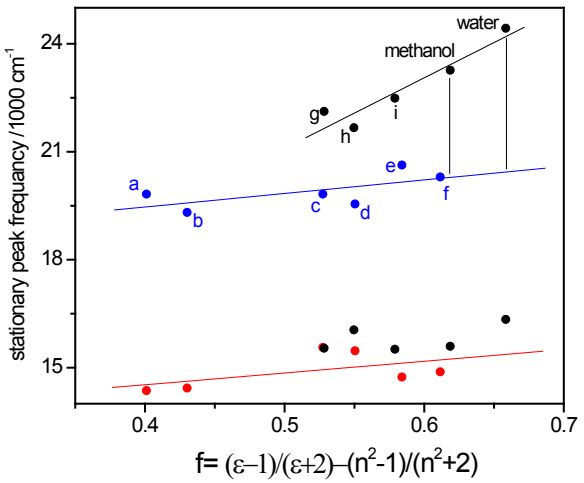

Fig. 5.10 Solvatochromism of MQ: peak position of absorption and fluorescence line shapes against polarity *f*. a-i: ethylacetate, methylacetate, dimethyl sulfoxide, dimethyl formamide, propionitrile, acetonitrile, n-butanol, n-propanol, and ethanol. Regression lines for subsets are also shown. Vertical lines mark the deviation of MQ in methanol and water from regression line for nonspecific polar behavior.

spectral relaxation. The common solvent methanol sets the time scale by its longest Debye time, $\tau_D = 52$ ps,[189] associated with CH_3OH orientational diffusion in the hydrogen–bonded network.[190] Rotational diffusion of 4AP is slightly slower, τ_{rot}=60 ps from anisotropy decay (66 ps was reported in ref 191), but MQ with $<\tau_{rot}> \approx$ 9.5 ps ps is much faster. These two extreme cases represent immobile and mobile solutes, respectively, for rotating CH_3OH molecules. Although solvation dynamics does not reflect a single molecular orientational correlation,[55] rapid solute motion may accelerate the solvation relaxation in the same way as two rotating dipoles affect their energy correlation. Interestingly, as discussed above, water shows no solute dependence. This observation may be explained by a separation of time scales: (i) the anisotropy of MQ in water decays with τ_{rot}=16 ps and C343, DMACA and 4AP-Ri are expected to be slower, and (ii) the dielectric relaxation of water has longest Debye time $\tau_D \approx$ 9 ps[192] (note that comparison could instead be made by τ_{solv}). In other words, solvation in water is faster than rotational diffusion of all our solutes. The molecularity therefore escapes detection.

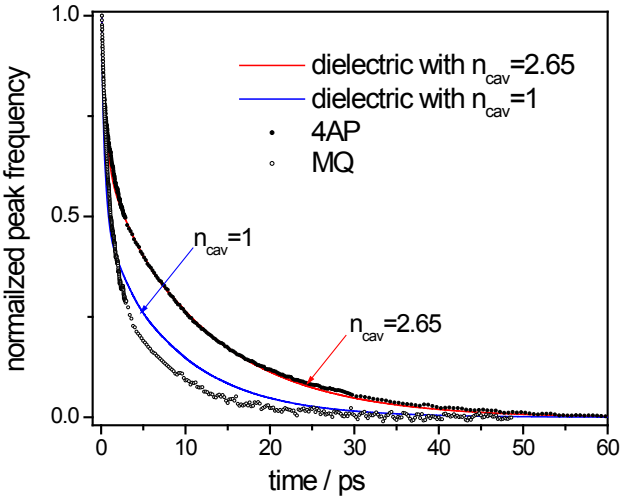

Fig. 5.11 The dielectric prediction of solvation in methanol (see text) with n_{cav}=2.65 (red line) matches the observed spectral relaxation function of 4AP in methanol (circles). The same kind of calculation, for example with n_{cav}=1 (blue line), differs for MQ in methanol (open circles, T=22°C).

At this point remember that the subsets of solutes for water and methanol measurements are not identical. However, looking at Fig. 5.3, we see that the chromophores are shared for the two solvents, and MQ as the rotationally fastest chromophore is measured in both solvents. Therefore it is unlikely that our argument depends on the structural differences between the subsets.

In the literature only one theoretical work addresses the effect of solute rotational motion on solvation,[51] to the best of our knowledge. Using molecular–dynamics simulations, Kumar and Maroncelli showed that for a solute like benzene, its rotation has significant influence on solvation dynamics, but that the effect is negligible for a solute like C153 in methanol and acetonitrile.[71] Rotation of the probe was taken into account by multiplying the solvation correlation function C(t) of an immobile probe with the rotational correlation function of the probe dipole:

$$C_{mobile}(t) = C_{immobile}(t) \times [r(t)]^{\alpha}. \qquad (5.1)$$

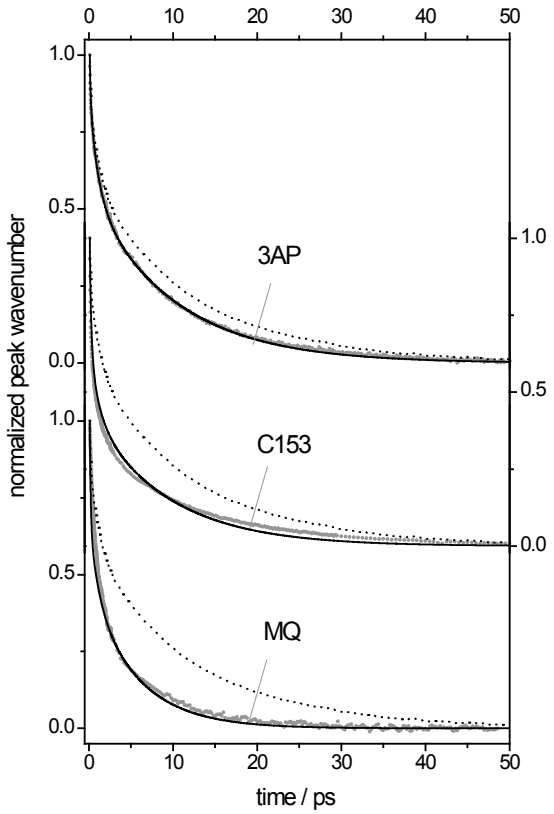

Fig. 5.12 Transfer of the TDSS in methanol, of 4AP (dashed black lines) which is assumed to be immobile, to the spectral relaxation of mobile solutes (gray dots), by taking into account the rotational diffusion of the solute.

here *r(t)* is the normalized anisotropy decay of the solute and α an empirical power coefficient. Taking 4AP as immobile reference, we show in Fig. 5.12 that Eq. (5.1) applies quite well. For 3AP and C153, optimal coefficients are α=0.6 and α=0.85, reduced from unity as expected for scaling from tensor to vector correlation (ideally α=1/3). For MQ the solvation is sped up by more than the anisotropy decay, α=1.4. Fast rotational diffusion of MQ could be related to the reverse solvatochromism and shedding of H-bonds after excitation, which was mentioned earlier.

Several experimental papers deal with probe dependence in the context of dynamic solvation. Su *et al* [193] compared the solvation of C153, (diethylamino)benzonitrile, and (dimethylamino)benzonitrile in 1-propanol, and found that it becomes faster in order of decreasing size. Jarzeba *et al* [194] examined C153 and C152 in protic and aprotic solvents and came to the analogous conclusion. These experimental results could not be explained by molecular theories where the size ratio of spherical solute and solvent molecules play a role.[46,56 ,57, 48]

In an extensive study, Maroncelli and coworkers[150] measured the Stokes shift of 16 solutes in 1-propanol with 20 ps time resolution. Instead of categorizing the solutes by size, the authors found that solutes which have more than one hydrogen bond with the surrounding solvent show at least twofold slower solvation, compared to small aromatic amines having a single H-bond. Comparing the present work with refs 193 and 194, we see here that smaller solutes show faster solvation provided that specific interactions with the solvent are negligible. Hydrogen bonding to the solvent means more rotational friction for the solute,[150] and therefore slower spectral relaxation upon solvation. Interestingly, the anisotropy decay of 4AP is almost twofold slower than that of 3AP where the amino group has an intramolecular H-bond to neighboring carbonyl oxygen, reducing the interaction with the solvent.

Solute dependence of solvation dynamics in methanol also was studied by T. Fonseca et al. in an MD simulation.[195] Using a diatomic solute, the authors found that the inertial and librational components, before 200 fs, relax faster for the larger solute or when the charge distribution is reversed. At later time the relaxation curves look identical. Our argument is effectively based on comparing average times or even the tails of solvation. Therefore their finding does not contradict our conclusion. On the other hand, even before 200 fs we do not observe solvent dependence in the small time window from 80 fs (our time resolution). This could indicate that the relative differences between our probes are not as large as for the diatomic model solutes.

Fig. 5.13 shows the dynamic shift of DCM in methanol (solvation time 2.99 ps, Table 5.1) which is almost as fast as that of MQ (2.69 ps), but much faster than 4AP (6.35 ps). Fast evolution of DCM was first reported by Gustavsson et al [104], and diverse spectroscopic methods [196,197,198,199] have been used to explore its photophysics. DCM is the largest solute in Fig. 5.3. This is consistent with a slow decay of fluorescence anisotropy in methanol, $\tau_{rot} = 80\,\mathrm{ps}$, which makes DCM an immobile solute. So why is the TDSS so fast? A possible explanation may be intramolecular flexibility in the excited

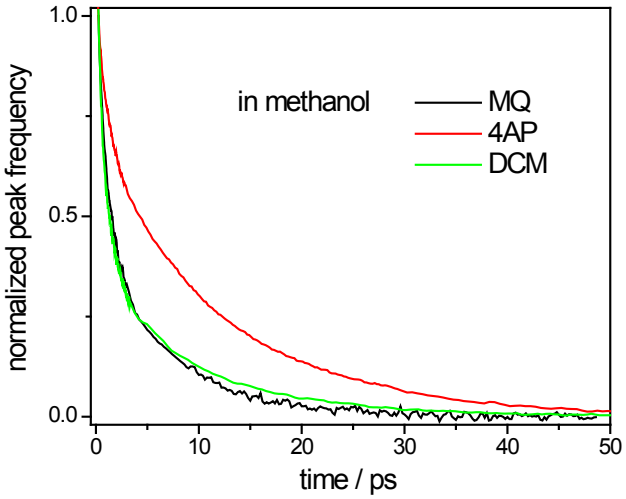

Fig. 5.13 Normalized peak frequency evolution of DCM (green), MQ (black) and 4AP (red) in methanol (T=22°C). Normalization as in Fig. 5.10.

state, which was reviewed by VanTassle *et al.*[200] An additional indication is provided by our anisotropy measures r(t) which show a 6 ps rise both in methanol and dmso, Fig. 5.5b. Abnormality in r(t) may indicate intramolecular rotation of the DCM transition dipole moment in the excited state. The anisotropy of DCM in dmso is also shown. An initial rise, of 6 ps, demonstrates the significance of the effect. This may be of interest for DCM photophysics which is under debate.[200]

5.4.3 Excitation dependence of solvation dynamics

A retrograde blue shift was observed in nonpolar and aprotic polar solvents (at relatively late time) which is absent in protic solvents. To understand the reasons, consider the stationary absorption of anthracene in the gas phase, Fig. 5.14, for the

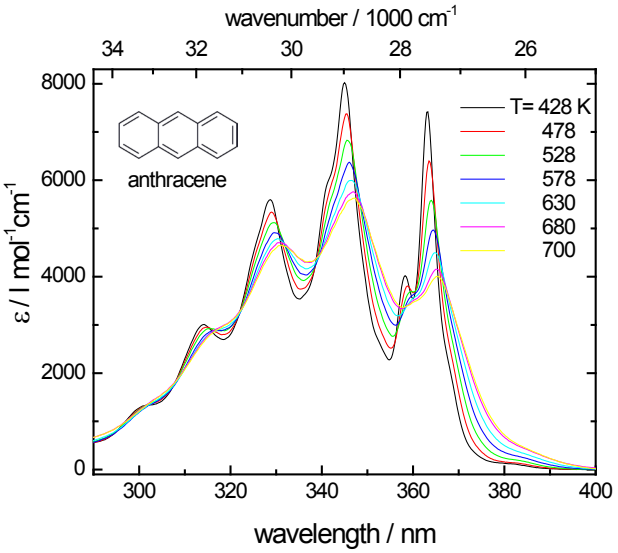

Fig. 5.14 Gas phase absorption spectra of anthracene red shifted by increasing temperature.

temperature range 428-700 K.[v] Heating causes a red shift in the spectral position of vibronic bands.[201] Thus we may infer an analogous effect in solution. Femtosecond excitation of a molecule with excess energy prepares a hot molecule in its excited state, and consequently the spectra appear red shifted, in addition to the Stokes shift caused by the solvent. The hot molecule in the excited state can releases its excess energy to the solvent bath, and finally cools down. Therefore, in transient fluorescence measurements cooling of the molecule is observed as the blue shift of spectral relaxations after the first extra red shift.

In protic solvents (Fig. 5.7c,d) solvation dynamics is independent of excitation energy. It is plausible to attribute this effect to the H-bonding between solute and solvent molecules such that excess energy is dissipated very quickly through the bonds.[202] The lack of such bonds in aprotic polar solvents and nonpolar solvents slows down the dissipation of excess energy. Here two points should be emphasized. First, as the fit parameters of Table 5.3 show, apart from the third exponential component with negative amplitude (blue shift), the first two exponential terms are identical for the two excitation energies (C153 and C343 in acetonitrile with 400 nm and 450 nm excitations). One may conclude that solvation dynamics -in cases when it is much faster than cooling- can be extracted from TDSS despite intramolecular evolution.

[v] Spectra were provided by Prof. Dr. Dirk Schwarzer, Max-Planck-Institut für Biophysikalische Chemie, Am Fassberg, Göttingen, Germany.

However in slower aprotic solvents, cooling dynamics may be covered by solvation dynamics and both evolutions are not readily separable; therefore correct dynamics can only be obtained by red edge excitation. Second, a part of intramolecular relaxation (hot molecule in the excited state) is observed in dynamic evolution of C334 in cyclohexane. A component with ~ 80 fs (limit of our apparatus response) is seen in the relaxation.

5.4.4 Temperature dependence

The temperature dependence was studied for MQ in methanol, H_2O, and D_2O (Table 5.4) and for C153 in benzonitrile (Table 5.5). The data were generally fit with a tri-exponential function from t=0.1 ps until 10/40/60 ps in the case of (heavy) water/methanol/benzonitrile, respectively. In all four solvents we find a fast component $\tau_1 \approx 100$ fs which has almost 50% amplitude in water and heavy water, and 20% in methanol and benzonitrile. Its amplitude does not depend on temperature in methanol/water/heavy water, but a small monotonic change of both amplitude and time constant is seen in benzonitrile. The lower panel of Fig. 5.16 shows the tail rate $1/\tau_3$ for the methanol and benzonitrile solutions, plotted on a log scale against reciprocal temperature. In these cases the three time constants are well separated. From the slope, the activation energy $E^{\#}_{solv}$ of the slowest solvation process is found to be $E^{\#}_{solv} \approx 8.8 \pm 0.8$ kJ/mol in methanol. Remember that the slow process is associated with the principal resonance of dielectric relaxation, which for methanol has an estimated activation energy of $E^{\#}_{Debye} \approx 10.9 \pm 0.6$ kJ/mol.[203] This agrees with our result and also with the activation energy of viscosity, 9.1 kJ/mol.[204] In benzonitrile the solvation activation energy $E^{\#}_{solv} \approx 14$ kJ/mol is not far from the activation energy of viscosity, 11 kJ/mol.[204]

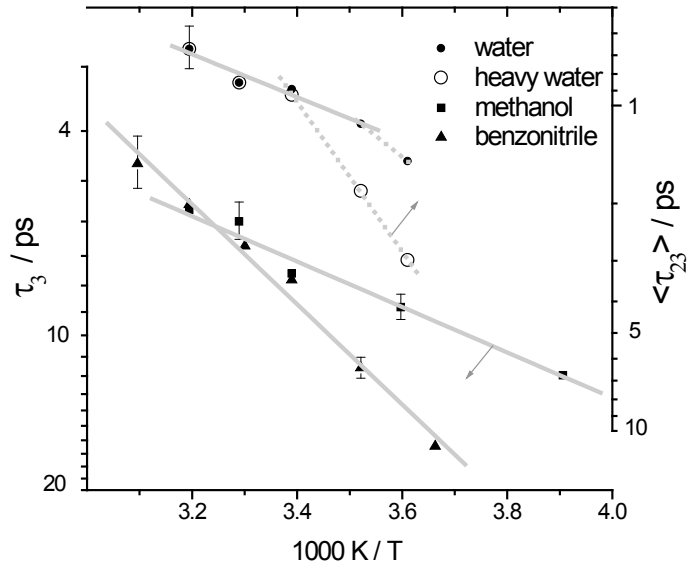

Fig. 5.16 Temperature dependence of the tale rates, from the peak-wavenumber evolution of MQ in methanol, water and heavy water, and C153 in benzonitrile. Lines are fits to the experimental results (see text).

Water or heavy water, on the other hand, do not possess well-separated spectral relaxations, as can be seen from Table 5.4. Using the notation in the Table, we determine the average relaxation time for the slower processes, $\langle \tau_{2,3} \rangle = (b_2\tau_2 + b_3\tau_3)/(b_2 + b_3)$. From the corresponding plot in the upper panel of Fig. 5.16, one obtains an experimental activation energy of 15.5±3 kJ/mol for relaxation in water. Comparison with dielectrics is facilitated by $\varepsilon(T,\omega)$ in ref. 205. For all temperatures T used in the experiment, the solvation relaxation function C(t) is calculated (with n_{cav}=1.3), the part $t \geq 0.1\,\mathrm{ps}$ is fitted biexponentially, and the average solvation time is calculated from the fit parameters. Activation energy is obtained to be 17 kJ/mole. reasonably close to the experimental one. Also it agrees with the activation energy of viscosity, 16.5 kJ/mol.[204]

With simulations, solvation in liquid H_2O and D_2O was compared by Bagchi and coworkers.[206] Relaxation curves calculated for 25°C show significant differences at their tails. We find a divergence only below 20 °C, as seen from Fig. 5.17. Note that the points

Table 5.4 Temperature dependence of peak-frequency relaxation, of MQ in methanol and water: exponential fit parameters.

Solvent	T /°C	τ_1 /ps	τ_2 /ps	τ_3 /ps	b_1 %	b_2 %	b_3 %	a_0 /cm^{-1}	a_∞ /cm^{-1}	$\langle\tau\rangle$ /ps
	-15	0.101	1.17	11.9	20.5	43.0	36.5	19550	16110	4.88
	5	0.124	1.15	8.8	22.5	41.1	36.4	19590	16030	3.71
methanol	22	0.270	1.44	7.6	26.1	48.3	25.6	19460	15940	2.71
	30	0.075	0.74	6	24.2	42.4	33.4	19790	15860	2.34
	40	0.118	1.04	5.7	27.9	49.3	22.8	19810	15780	1.94
	4	0.121	0.85	3.2	54.3	33.4	12.3	19850	16760	0.75
	11	0.121	0.81	1.9	55	31	14	20150	16770	0.58
H_2O	22	0.112	0.30	1.45	43.3	33.5	23.2	19480	16730	0.48
	30	0.151	–	0.82	59.5	–	40.5	19640	16680	0.42
	40	0.12	–	0.67	61	–	39	18780	16660	0.33
	4	0.170	0.98	6.4	41.9	36.6	21.5	19755	16800	1.81
	11	0.161	0.79	3.77	47.9	33.9	18.2	19735	16780	1.05
D_2O	22	0.129	0.45	1.4	45.3	31.8	22.9	20550	16760	0.53
	30	0.142	–	0.81	59	–	41	19530	16720	0.416
	40	0.14	–	0.72	64.7	–	35.3	19100	16700	0.34

Notations and conditions as in Table 5.1.

of maximum density (11.6 °C for D_2O and 4 °C for water) and freezing (3.85 °C for D_2O) reflect large changes of the H-bonding network. In this temperature range the measured activation energy of D_2O differs significantly from that above 20 °C. Thus, for D_2O solvation we see two activation processes but for H_2O solvation only one. This observation could help in the study of biological systems.[207] Here the contribution of water to the solvation of an attached or embedded chromophore is being discussed controversially. We suggest that the temperature behavior of such systems should be studied in water and heavy water, in order to recognize the water contribution.

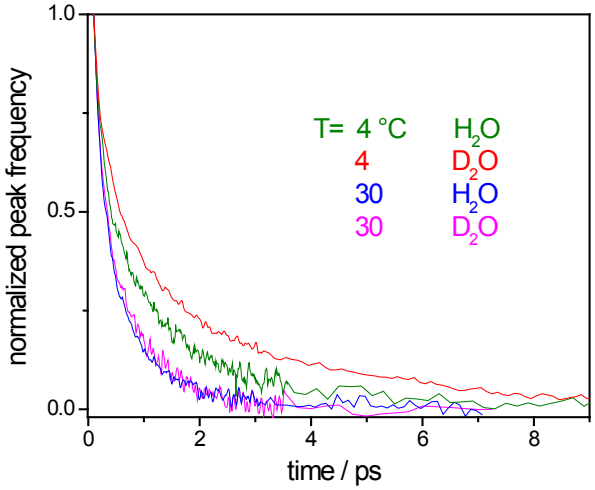

Fig. 5.17 Peak frequency evolution of MQ in H_2O and D_2O at 30°C and 4°C. Data were set to 1 and 0 at 100 fs and 10 ps, respectively.

Table 5.5 Temperature dependence of peak-frequency relaxation, of C153 in benzonitrile: exponential fit parameters.

T /°C	τ_1 /ps	τ_2 /ps	τ_3 /ps	b_1 %	b_2 %	b_3 %	a_0 /cm^{-1}	a_∞ /cm^{-1}	$\langle\tau\rangle$ /ps
0	0.273	3.16	16.4	28.4	39.5	32.1	19620	18550	6.60
10	0.188	2.14	11.6	24.6	37.6	37.8	19660	18565	5.22
20	0.169	1.36	7.8	22.3	34.9	42.8	19565	18580	3.85
30	0.159	1.01	6.5	24.9	29.8	45.3	19600	18600	3.28
40	0.142	1.18	5.6	19.4	33.3	47.3	19640	18615	3.06
50	0.115	0.88	4.6	19.2	35.5	45.3	19700	18630	2.43

Notations and conditions as in Table 1.

5.5 Conclusion

Time-dependent Stokes shifts (TDSS) were measured for diverse polarity probes in water, heavy water, methanol, acetonitrile, benzonitrile, and cyclohexane by broadband fluorescence up-conversion with 85 fs time resolution. In water the spectral dynamics is solute–independent and quantitatively described by simple dielectric continuum theory of solvation. In methanol the slower part of the TDSS is solute-dependent. A correlation with anisotropy decay suggests that methanol

solvation dynamics is modulated by orientational solute diffusion. An empirical power law which links the solvation relaxation function of a mobile solute to that of an immobile solute is experimentally verified. In nonpolar and aprotic solvents spectral relaxation dynamics depends on excitation energy and shows a retrograde blue shift with exciting the molecule with excess energy. However, in protic solvents, spectral relaxation is independent of amount of excess energy given to the molecule, likely because of H-bonding. Activation energies for the average relaxation rate are also given. Solvation dynamics in H_2O and D_2O are identical at and above 20°C but diverge below. Finally, we may conclude, local THz-FIR spectroscopy of aqueous solutions may therefore be performed faithfully with molecular probes, preferentially with red edge excitation. Other environments should be measured with a linked or immobilized probe.

6 Local THz Spectroscopy of Trehalose/Water Mixture

6.1 Introduction (partly based on own publication Ref. 121.)

Some organism can recover their biological activity even after long periods of dehydration. To survive such harsh conditions they synthesize a large amount of carbohydrates, especially the disaccharide trehalose.[208] Trehalose has remarkable thermodynamical features. In the dehydrated state, water molecules are replaced by trehalose and so the structure is protected from collapsing. Also by destructuring the hydrogen bonding network of water, trehalose lowers the freezing temperature of water.[209] Concentrated aqueous solutions have high viscosity and glass transition temperature.[210] The molecular model for the protection mechanism is still fairly open however. Early discussions centered on structural perturbations which a sugar molecule induces in water.[211] Recent molecular dynamics (MD) [212,213] and spectroscopic [214,215] investigations examine how sugar solutes influence H_2O hydrogen-bonding and the collective dynamics.

In dielectric measurements of aqueous solutions, Mashimo et al[214] found an additional Debye term at the low-frequency side of the dominant water relaxation mode, but only with maltotriose or larger saccharides. The additional term was assigned to the rotational relaxation of the sugar. The authors concluded that smaller solutes, like glucose, fit into the hexagonal ice structure of water so that their relaxation behavior is similar to that of water clusters. More recent measurements by Weingärtner et al[216] as well as Kaatze and coworker [217] discovered the corresponding feature with glucose solutions also. It was corroborated with depolarized Rayleigh scattering by Fioretto et al.[215] Dynamical studies of water in sugar mixtures [212,218,213,219] showed that a sugar solute alters the tetrahedral configuration of water molecules, and that the dynamics of the solution differs from that of pure water. Trehalose was found to particularly effective.

Protein dynamics experiments suggest that trehalose forms a stabilizer shell around biomolecules. Using flash-photolysis, Eaton and coworkers [220] observed that

part of the protein motion is inhibited in a trehalose glass. Optical absorption and Mössbauer spectroscopy by Cordone et al[221] showed that the contribution of non-harmonic protein modes at high temperature is reduced in trehalose solution. The latter seems to dampen protein modes severely, as concluded by Gottfried et al[222] from their time-resolved resonance Raman and fluorescence measurements. These results are supported by vibrational echo experiments of Fayer and coworkers[223,224,225] who demonstrated that the rate of dynamical dephasing of the CO stretching mode is reduced in proteins in a trehalose solution, relative to other viscous solvents.

Far-infrared absorption between 2-3 THz was examined Havenith and coworkers. [226] These authors measured the absorbance of aqueous solutions as function of sugar concentration ranging up to saturation. From the non-ideal behavior and with the help of MD simulations, a dynamical hydration shell was deduced which extends well beyond the first static hydration layer. THz time-domain spectroscopy was used by Tanaka and coworkers[227] to measure the complex reflection index of sugar mixtures. Signal quality is improved in their attenuated reflection setup because the detrimental effect of water absorption is minimized. Even though, the precise analysis of concentration dependence remains a field which has barely been touched.

Trehalose slows down the translational and rotational motion of nearby water molecules.[212] Collective intermolecular motion in pure water is reflected by the dielectric dispersion below 1000 cm^{-1}, which may be described by Debye terms τ_1 and τ_2, an O…O stretching band ν_S, and a librational band ν_L.[228] Intermolecular modes are overdamped or just underdamped, and therefore the corresponding bands are broad compared to intramolecular bands. When a trehalose solution is formed and further concentrated to a trehalose/water mixture, new bands are expected (for example due to reorientational motion of the solute as mentioned above) and existing water bands may shift or alter shape. If a mode description is desired, such subtle changes have to be measured across the entire "intermolecular" range which encompasses the microwave, THz, far-infrared and infrared regions. The wavelengths which must be employed differ by four orders of magnitude and every range has its characteristic method (relaxation or

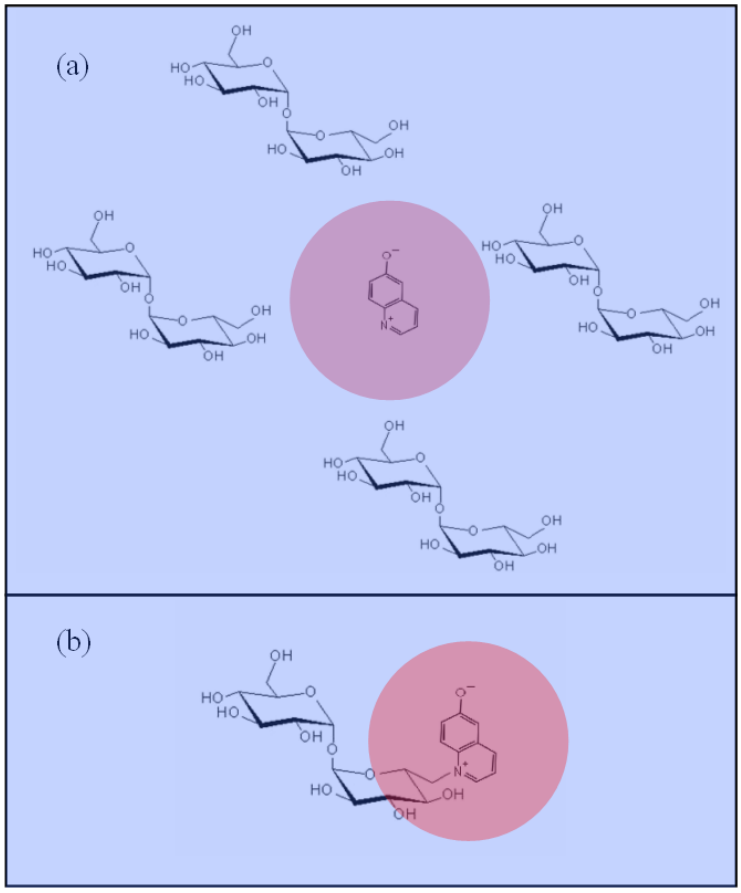

Fig. 6.1 MQ as a local spectrometer (a) Free in trehalose/ water mixture and (b) covalently bound to trehalose in bulk water.

response, time- or frequency-domain). A practical problem is represented with strong THz-FIR absorbers such as water or acetonitrile, because thin sample cells are needed which cause interference. Also the window material contributes substantially to the measured signal. It would be helpful to combine a broad spectral range with a general scheme by which the electric field is applied directly in the sample, avoiding window contributions. Both requirements can be met by exploiting the local field around a solvatochromic probe, as will be explained next.

As a proof of principle, the spectral relaxations of N-Methyl-6-Quinolone (MQ) as the local spectrometer, either free in trehalose/water mixture (Fig. 6.1a) or covalently bound to trehalose in water (Fig. 6.1b), are measured. In the former, local IR-THz spectra

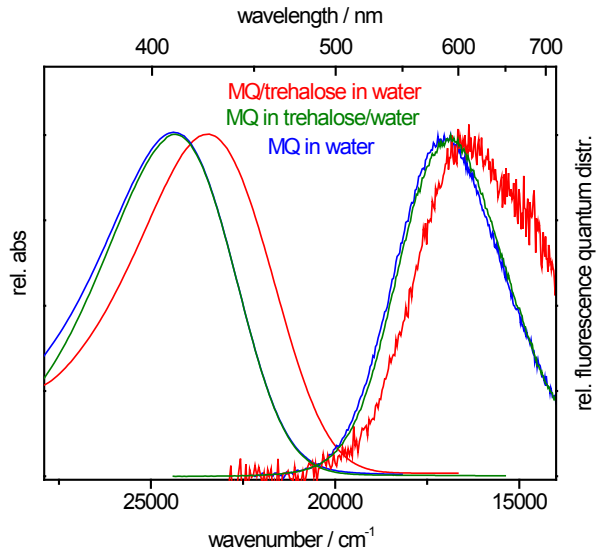

Fig. 6.2 Absorption and fluorescence spectra (quantum distribution over energy) of MQ in water (blue), in a 1.0 M solution of aqueous trehalose (olive), also in a dilute solution with MQ covalently linked to trehalose (red).

of the solution in different concentration of the sugar is obtained. In the latter case, the thickness of the hydration layer in proximity to the trehalose moiety is estimated.

6.2 Materials

Trehalose was purchased from Sigma and used without further purification. Solutions in deionized water were prepared by sonification of the appropriate amount of trehalose in about 90% of the final volume of water for one hour at 21°C, followed by the addition of water until the final volume was reached. Identical solutions were used in the microwave and femtosecond work. For fs spectroscopy the dye was dissolved in the mixture such that the optical density in the 0.3 mm sample cell was 0.6 at 400 nm. The synthesis of covalently linked MQ to trehalose also was described elsewhere.[229]

6.3 Stationary absorption and emission

Stationary spectra were recorded with a CARY 300 spectrometer and a SPEX 212 fluorometer, both with 1 nm wavelength resolution. Fluorescence was compared to the emission from a secondary standard lamp (GIGAHERTZ OPTIC). Spectra in water and 1.0 molar aqueous trehalose and MQ covalently linked to trehalose are compared in Fig. 6.2. In 1 M solution of trehalose, both the absorption and fluorescence of MQ are slightly red shifted compared to pure aqueous solution. For the linked moiety a large red shift is observed.

6.4 Broadband dielectric spectroscopy

Broadband dielectric spectra were provided by Yathrib Ajaj and Prof. Hermann Weingärtner.[vi] The real part (dielectric dispersion) and imaginary part (dielectric absorption or loss) of the frequency-dependent complex dielectric permittivity $\varepsilon(\omega) = \varepsilon'(\omega) - i\,\varepsilon''(\omega)$ of the solutions were measured as a function of frequency $\nu = \omega/2\pi$ with a coaxial reflection method as described elsewhere.[230] In preliminary experiments two experimental setups operating at 0.3 MHz $< \nu <$ 1.3 GHz and 100 MHz $< \nu <$ 20 GHz were used. In agreement with observations for other saccharides in water[216,217,231] the dispersion/absorption regimes occurred at frequencies ν well above 100 MHz, so that the final measurements were conducted with the setup for 100 MHz $< \nu <$ 20 GHz. We focused on the real part of the complex permittivity which decays from the static permittivity ("dielectric constant") ε_0 of the solution to a high-frequency limit ε_∞, comprising processes beyond the microwave regime. Fig. 6.3 shows some dispersion curves.

It is known that the dispersion/loss regimes of saccharide solutions extend over a broader frequency range than rationalized by the Lorentzian line shape of a Debye-type exponential relaxation process.[216,217,231] A more accurate representation of the results for saccharides by Kaatze and coworkers expressed the permittivity in terms of the Cole-Cole distribution of relaxation times[232,233] which assumes a

[vi] Physical Chemistry II, Faculty of Chemistry and Biochemistry, Ruhr University Bochum, Germany.

symmetrical relaxation time distribution, characterized by the central relaxation time τ_{CC} and a width parameter $0 \le \alpha < 1$. For $\alpha = 0$ this function transcribes into the Debye model for purely exponential relaxation. At high concentrations a good representation of the spectra required however an additional term, for simplicity chosen as a Debye term

$$\varepsilon(\omega) = \varepsilon_0 + \frac{\varepsilon_0 - \varepsilon_m}{1 + (i\omega\tau_{cc})^{1-\alpha}} + \frac{\varepsilon_m - \varepsilon_\infty}{1 + i\omega\tau_d}. \tag{6.1}$$

Table. 6.1 Fit parameters of the dielectric spectra (Eq. (6.1)) for different concentration of aqueous trehalose.

conc / M	τ_d /ps	τ_{cc} /ps	ε_∞	ε_m	ε_0	α
0.05	6.39	11.63	2.35	28.56	77.56	0.010
0.10	6.40	12.22	3.00	29.74	77.52	0.043
0.25	8.13	13.42	4.00	18.41	76.66	0.115
0.50	8.16	24.99	3.77	16.07	74.70	0.126
0.75	10.77	26.20	5.00	15.50	72.55	0.217
1.00	12.75	30.12	2.01	14.00	70.79	0.254
1.25	18.69	38.72	4.99	13.96	69.55	0.284
1.50	25.55	49.96	4.79	11.86	67.77	0.296

Table 6.1 summarizes the parameters of the fit. Note that this representation is empirical and was only used for a compact representation. The parameters reproduce the experimental dispersion curves within the uncertainty of each data point (the size of the symbols). This is shown in Fig. 6.3 for a representative solution.

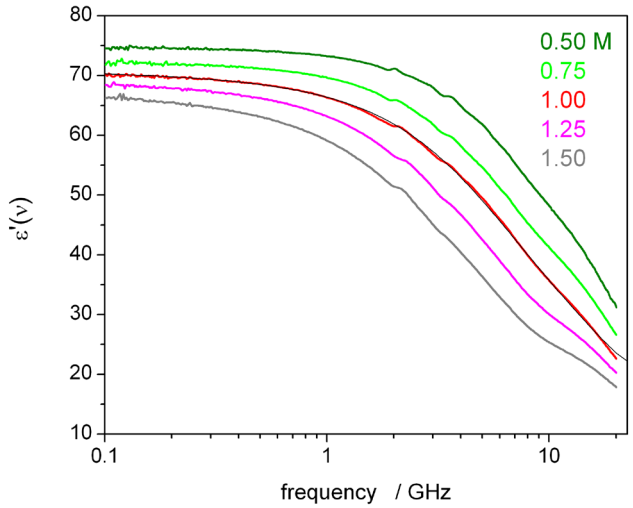

Fig. 6.3 Microwave measurements of $\varepsilon(\omega)$. The real part $\varepsilon'(\omega)$, shown here, could be determined more accurately than the imaginary part. The stationary value $\varepsilon'(0)$ was used as a fixed parameter when fitting the fluorescence relaxation curve.

6.5 Quantum calculation of dipole moments and polarizabilities

Quantum-chemical calculation was performed by Ilya Ioffe[vii]. Dipole polarizability calculations were carried out with the PC GAMESS/Firefly QC package[234] which is partially based on the GAMESS (US)[235] source code. Initially the ground state was optimized at the CASSCF(12,11) level of theory, *i.e.* with all pi-electrons and pi-orbitals included in the active space, with the aug-cc-pVTZ basis set[236] on the highly negatively charged oxygen atom and cc-pVTZ[237] basis sets on the other atoms. Further computation of excitation energy, dipole moments of S_0 and S_1, and their static dipole polarizabilities via numerical differentiation of energy with respect to the electric field were performed at the XMCQDPT2 level of theory[238] with a CASSCF(12,11) reference (state-averaged over S_0 and S_1 for more symmetric treatment thereof) and five lowest singlet states included in the model space.

[vii] Department of Chemistry, Lomonosov Moscow State University, Russian Federation.

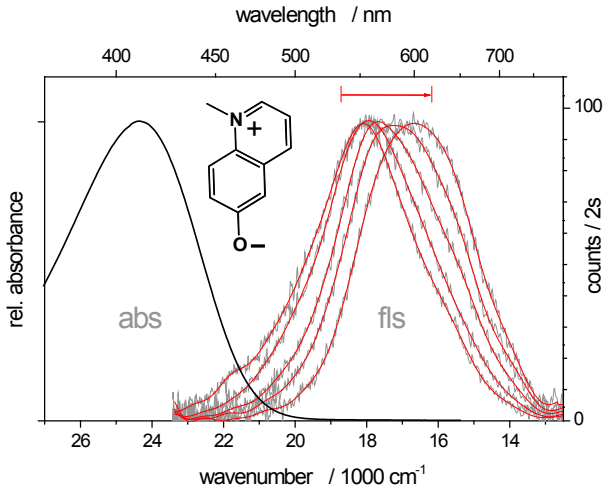

Fig. 6.4 Absorption (abs) and fluorescence (fls) spectra of the polarity probe MQ (inset) in 1 M aqueous trehalose. After 40 fs excitation at 400 nm, the evolving emission was time-gated by broadband up-conversion. Shown are the fluorescence quantum distributions at 0.11, 0.20, 0.4, 5.0 ps. Time resolution was 85 fs (fwhm), and the red arrow indicates the observed range of the dynamic Stokes shift.

The vertical $S_1 \leftarrow S_0$ transition energy *in vacuo* was thus calculated to be 2.0 eV, the respective oscillator strength (length gauge) being 0.07 (experimental: 0.061). The dipole moments *in vacuo* are found to be 10.5 D for S_0 and 5.8 D for S_1, and the isotropic dipole polarizability values 21.19 $Å^3$ and 19.12 $Å^3$, respectively.

6.6 Results

The femtosecond experiment consists of optical excitation of MQ at 400 nm, followed by broadband fluorescence up-conversion[77,122] (see also chapter 3) with 85 fs time resolution (fwhm). Fig. 6.4 shows the absorption spectrum and several time-gated fluorescence spectra ($\propto$ quantum distribution over wavenumbers). The average emission wavenumber $\langle\tilde{\nu}\rangle$ as function of time constitutes the spectral relaxation function R(t) which is determined by solvation completely.[62]

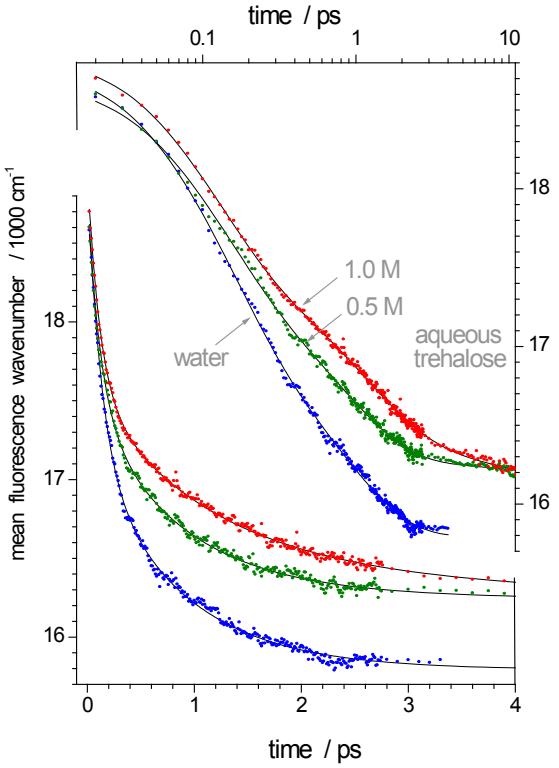

Fig. 6.5 Mean fluorescence wavenumber relaxes on several time scales after femtosecond optical excitation (blue dots: water, red and olive: trehalose/water mixtures). Fits by continuum theory (black lines) yield ε(ω) for each solution.

Experimental spectral relaxations are shown in Fig. 6.5 for 0.0, 0.5 and 1.0 M trehalose solutions. As it is clear from the figure by increasing concentration of sugar relaxation slows down.

In Fig. 6.6 we compare the spectral relaxation of MQ in water, in 1.0 M solution of aqueous trehalose and MQ covalently bound to trehalose in water. Surprisingly, we find that spectral relaxations of both systems, free and linked probes, are analogous. From here one may infer the thickness of hydration layer (see discussion).

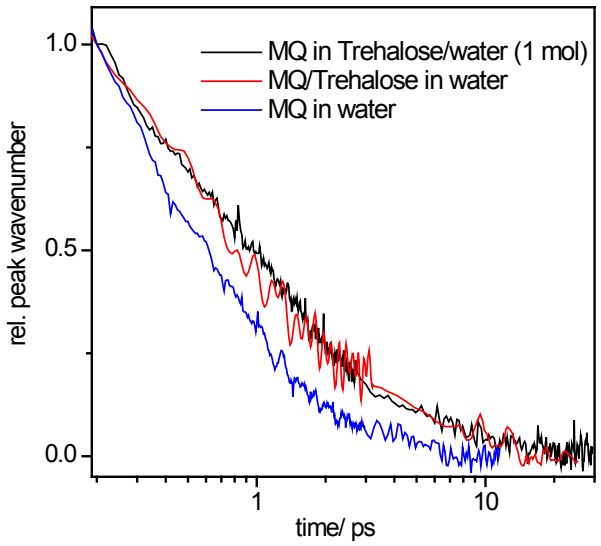

Fig. 6.6 Spectral relaxations of MQ in water (blue), MQ in 1 molar solution of trehalose (black) and MQ covalently linked to the trehalose in water (red). Relaxations are normalized between frequencies at time = 0.2 ps and in the quasi-stationary state.

6.7 Discussion

Water is important for the structure, stability, and function of biomolecules. It can simplify the energy landscape for molecular recognition or protein folding and often controls the native stability.[239,240] Proton transfer through local water networks requires correlated movement of H-bonds,[241] and conformational changes of proteins appear to be slaved to the dynamics of bulk and hydration water.[242] To understand such processes the vibrational absorption spectrum of the biomolecule/water interface must be observed. The underlying dynamics are widely distributed in time, from fast vibrational modes to slow diffusive reorientation. In low-viscosity liquids, such as water, the diffusive regime comprises processes on the picosecond-to-nanosecond time scale (corresponding to wavenumbers $\tilde{\nu} < 1.5$ cm^{-1}) which are captured by microwave dielectric spectroscopy. On the high-frequency side (in neat water > 1000 cm^{-1}) *intra*molecular vibrations are routinely observed by infrared absorption spectroscopy. What is usually lacking is information on the *inter*molecular vibrational and librational dynamics which are reflected in the intermediate segment of the spectrum, in the THz (≤ 30 cm^{-1}) and far-infrared (FIR, 30-250 cm^{-1}) regions. It is just

this intermediate regime where processes associated with H-bond dynamics are expected. Unfortunately the generation and detection of light is difficult here. Furthermore the response of the biomolecule/water interface is generally not so different from that of bulk water. There is thus a clear need to develop local spectroscopic schemes which avoid contributions from the bulk and confine absorption measurements to the interfacial region.

6.7.1 Free molecular probe

Using the polarity probe N-Methyl-6-Quinolone (MQ, inset to Fig. 6.4), it was shown recently that the time-resolved Stokes shift (TRSS) of fluorescence reflects the infrared spectrum of the surrounding liquid.[62] The effective distance for the interaction ranges up to ca. 15 Å;[243] spatial resolution of this size may therefore be achieved by linking the probe to the supramolecular structure of interest. Thus MQ excellently fulfils the requirements for a local probe. What was missing so far is the inversion: how to extract the (unknown) dielectric properties from a measured TRSS curve. This key step is provided here and tested with aqueous trehalose solutions

To illustrate the kind of spectrum which must be recorded, Fig. 6.7 shows the dielectric loss $\varepsilon''(\omega)$ of bulk water up to infrared frequencies.[228,244,245,246] This spectrum represents the background against which changes induced by the biomolecule have to be seen, therefore we describe it in a useful digression. $\varepsilon''(\omega)$ is essentially the oscillator strength distribution $\alpha(\omega)/\omega$, obtainable from the light attenuation coefficient $\alpha(\omega)$.[247,37] More generally, the dielectric absorption or loss $\varepsilon''(\omega)$ is the imaginary part of a frequency-dependent complex dielectric permittivity $\varepsilon(\omega) = \varepsilon'(\omega) - i\varepsilon''(\omega)$. The real part $\varepsilon'(\omega)$, which reflects the deceleration of the electromagnetic wave (dielectric dispersion), is related to the imaginary part by the so-called Kramer-Kronig condition.[37] Thus $\varepsilon''(\omega)$ determines $\varepsilon(\omega)$ completely. — The spectrum can be described by several

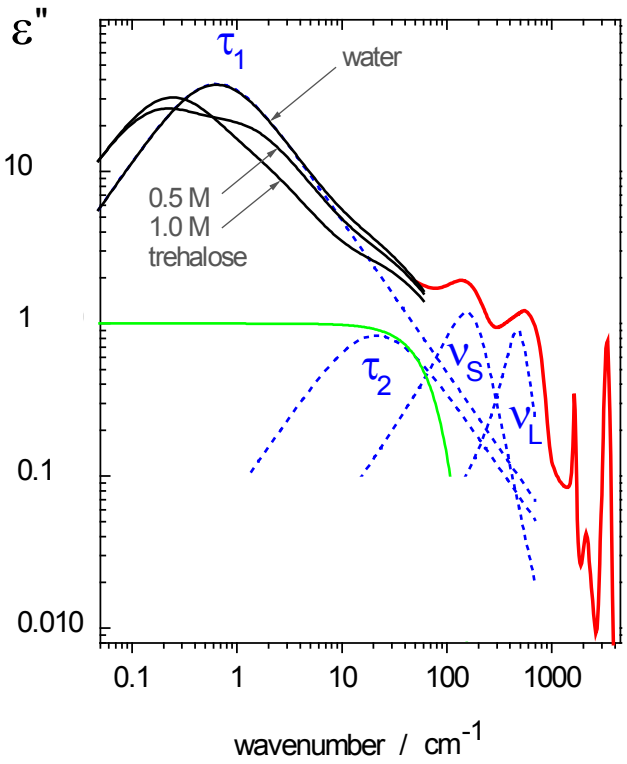

Fig. 6.7 Dielectric loss of pure water (red and corresponding black line) is modified by the addition of trehalose (inset). *Inter*molecular modes D_1, D_2, ν_T, ν_L of pure water are separately shown as blue dashed lines. Mode S is assigned to rotational diffusion of the hydrated sugar. Black curves were determined from the time-resolved fluorescence Stokes shift of added 6-Methyl-Quinolone. The observation window (green) is determined by the effective time resolution.

bands.[246] The weak FIR band ν_T at 200 cm^{-1} actually has substantial oscillator strength; it corresponds to translational vibration of the OH···O network.[246] Rotational diffusion is observed at lowest frequencies, in the microwave region around 20 GHz, and contributes a dominant Debye term D_1 together with a small Debye contribution D_2[228,244] to $\varepsilon(\omega)$. Librational water motion is observed in a band ν_L around 500 cm^{-1}.[244,245,246] All of these bands are broad (relative to the peak frequency) because *inter*molecular motion is easily perturbed, and thus the coherence strongly damped, compared to *intra*molecular oscillations which are seen as narrow lines above 1000 cm^{-1}.

By the addition of trehalose, spectral changes should be induced throughout, including the THz regime (1 THz = 33 cm^{-1}) of major interest here. In fact, as the concentration of trehalose is increased to 1 M, the attenuation at 80 cm^{-1} decreases by almost 20%.[226] Here we observe how the water bands in Fig. 6.7 are modified and

which new bands appear, using MQ dissolved in the bulk solution as a "molecular spectrometer". In practice, we assume a realistic expression for $\varepsilon(\omega)$ and analytically derive R(t), the relaxation function which describes the time-resolved Stokes shift of fluorescence. This new kind of TRSS spectroscopy will be explained next.

The probe functions as a microscopic THz light source when its charge distribution is suddenly altered by femtosecond optical excitation **(**Fig. 6.8a**).**[5,248,249] In case of MQ, $S_0 \rightarrow S_1$ excitation at 400 nm reduces the dipole moment from 10.8 D to 5.8 D; in this way the local electric field is switched down instantaneously. As the new field acts on nearby groups with partial charges, these reorient and collectively create the reaction field R(t) (Fig. 6.8b). The latter is reported by the polar probe molecule through an emission frequency which depends on R(t). The probe is therefore not only light source but also detector. Compare this with classical dielectric relaxation measurements (Fig. 6.8c), in which a capacitor containing the bulk liquid is suddenly discharged. The original polarization then relaxes with characteristic time-behavior P(t) (Fig. 6.8d). By forming the time derivative one obtains the response function to a δ-shaped pulse (Fig. 6.8e); the response can also be measured by THz time-domain spectroscopy (THz-TDS) more directly.[228] $\varepsilon(\omega)$ is reached by Laplace transformation.

A bridge from dielectric relaxation to solvation of a dipolar probe is provided by[232]

$$\chi_{dip}(\omega) \propto \frac{\varepsilon(\omega)-1}{2\varepsilon(\omega)+n_{cav}^2} - \frac{n_\infty^2-1}{2n_\infty^2+n_{cav}^2}. \qquad (6.2)$$

here $\chi_{dip}(\omega)$ is the susceptibility of the dipole reaction field R(t), n_∞ the refractive index of the medium at optical frequencies, and n_{cav} represents the polarizability of the solute.[61,232] Eq. (6.2) is based on simple continuum theory which was shown to be valid, empirically, for MQ.[62] Regarding the complex permittivity $\varepsilon(\omega)$, for water up to 100 cm^{-1} it can be described by two Debye terms (see Fig 6.1).[228] To allow for spectral changes

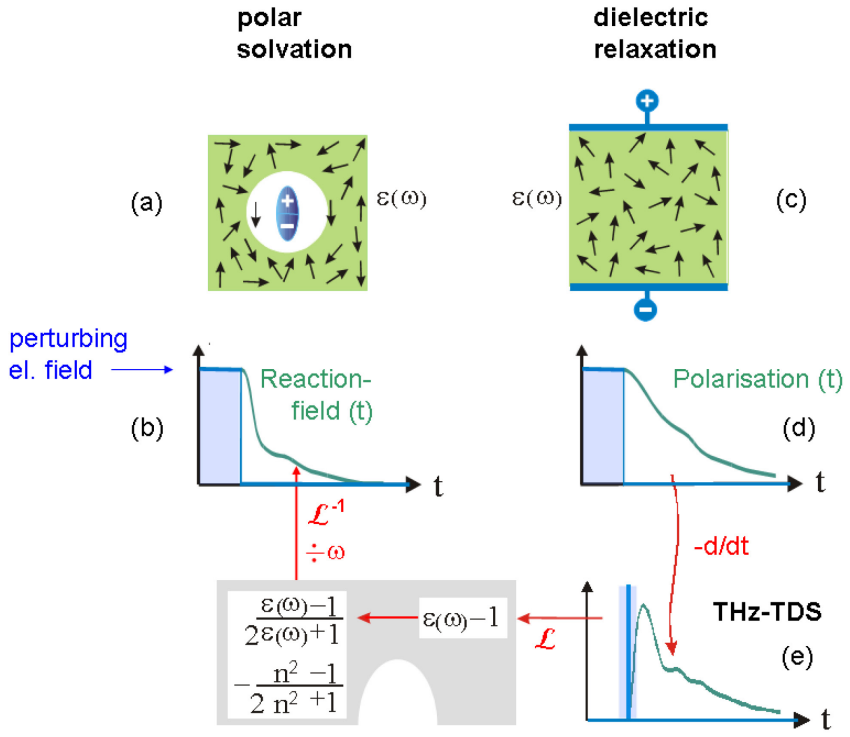

Fig. 6.8 Bridge between spectroscopies. With a suitable molecular probe, polar solvation (a) may be described by continuum theory. A key quantity is the frequency-dependent permittivity $\varepsilon(\omega)$ of the medium. It is usually measured by dielectric relaxation (c) or THz time-domain spectroscopy (e). In the present work we measure the fs solvation dynamics of 6-Methyl-Quinolone (b) and find the corresponding $\varepsilon(\omega)$ quantitatively. The far-infrared absorption spectrum is given by $\omega\,\varepsilon''(\omega)$: the probe works as a "molecular spectrometer". (L is the Laplace transformation, and for simplicity $n_{cav} = 1$ has been assumed; see text.)

upon addition of trehalose we write generally for this range a triple-Debye ansatz plus a background correction $\varepsilon_\infty \cong n_\infty^2$ for electronic displacement polarizations in the optical regime:

$$\varepsilon(\omega) = \frac{\varepsilon_0 - \varepsilon_1}{1 + i\omega\tau_1} + \frac{\varepsilon_1 - \varepsilon_2}{1 + i\omega\tau_2} + \frac{\varepsilon_2 - \varepsilon_\infty}{1 + i\omega\tau_3} + \varepsilon_\infty . \qquad (6.3)$$

Each mode is characterized by a Debye relaxation time τ_k and an amplitude $\Delta\varepsilon_k = \varepsilon_{k-1} - \varepsilon_k$. Note that by forming the zero-frequency limit, the conventional static dielectric constant ε_0 is recovered.

After passage through eq. (6.3) and division by $s \equiv i\omega$ (equivalent to time integration, *cf*. Fig. 6.8) the inverse Laplace transform L^{-1} is carried out analytically. The parameters which enter the calculation are τ_1, τ_2, τ_3, and $\varepsilon_0, \varepsilon_1, \varepsilon_2, \varepsilon_\infty$ and n_{cav}. They determine a triple-exponential form for reaction field R(t) as outlined in Appendix B.[viii]

These key data are fitted by optimizing $\varepsilon(\omega)$, resulting in the black interpolation lines in Fig. 6.5. The low-frequency behavior is obtained from separate microwave measurements[230] (see also section 6.4). For fitting, the input parameters $\varepsilon_1, \varepsilon_2, \varepsilon_\infty, \tau_1, \tau_2, \tau_3$ are allowed to vary, while ε_0 is fixed to the microwave value. This link with microwave data will no longer be needed when R(t) becomes more precise in the long-time region.

The cavity refractive index n_{cav} is governed by the effective polarizability of the probe and the cavity volume;[232] at this exploratory stage it must be treated specially as follows. For pure water the known dielectric dispersion $\varepsilon(\omega)$ is used to find n_{cav}=2.3 from the time-resolved Stokes shift of MQ. Also the THz absorption spectrum of pure water is calculated for reference. Regarding the sugar solutions, note that the dielectric permittivity curve which is extracted from the fs measurements depends on the value which was assumed for n_{cav}, and so does the attenuation coefficient $\alpha(\omega)$ which is derived.[247] That dependence can be used to obtain n_{cav} from absorption measurements at a fixed frequency. Havenith and coworkers[226] found that 0.5 M (1.0 M) trehalose reduces the absorption coefficient of water around 80 cm^{-1} by 7.2 (16.4) %. To reproduce this observation with the present data we need to change n_{cav} slightly to 2.26 (2.0), which implies that the cavity volume increases with sugar concentration.

The resulting $\varepsilon(\omega)$ curves are shown in Fig. 6.7 as black lines. They connect smoothly with the microwave results and obey the known far-infrared absorbance at 80 cm^{-1}. When the trehalose concentration is raised to 0.5 M and 1.0 M, characteristic changes are observed:

(i) A new relaxational mode S appears at 7.1 GHz on the low-frequency side of the dominant water mode D_1 (19 GHz). It is assigned to rotational relaxation of the hydrated trehalose solute, by analogy to results from dielectric relaxation of

[viii] A Matlab code is given in Appendix C to fit spectral relaxation with an unlimited trial $\varepsilon(\omega)$.

maltotriose[214] and glucose[216,217] solutions which were confirmed by depolarized Rayleigh scattering.[215]

(ii) The dynamics of the solution differs from that of pure water. The rotational water mode D_1 looses amplitude and is blue-shifted (becomes faster) as the trehalose concentration reaches 0.5 M, and is strongly reduced when the concentration is raised further to 1.0 M. The water mode D_2 at higher frequency (≈0.14 THz or 5 cm^{-1}) seems less affected. Our observation agrees with dynamical studies[212,213,10,218,219] which showed that a sugar solute alters the tetrahedral configuration of water molecules.

(iii) Between D_2 and ν_L no further distinct processes are observed. No new information is obtained for the single point at 2.5 THz, since here the far-infrared results from Havenith and coworkers[226] were used. These authors measured the absorbance of aqueous solutions as function of sugar concentration ranging up to saturation. Non-ideal quadratic behavior with increasing trehalose concentration was attributed to overlap of dynamical hydration shells. The dissolved polarity probe MQ should reside increasingly in such overlap regions, which explains why its cavity volume changes similarly with sugar concentration.

6.7.2 Covalently bound probe

In Fig. 6.6 normalized spectral relaxations of MQ covalently bound to trehalose in water, in 1 M solution of aqueous trehalose, and also free in water were compared. The fact that spectral relaxations in both solutions of trehalose show similar dynamics, indicate that both environments have similar responses. In another words, the dynamical behavior of both local environments is practically the same. From this similarity one may obtain the thickness of hydration layer around trehalose in a way that is explained next.

If the volume of water for each trehalose molecule in 1M solution is calculated (which presumably is the only dynamically active species), then the thickness of the hydration layer is obtained. The total volume is divided between trehalose with partial molar volume equal to 243.75 cm^3mol^{-1} [250] and water molecules. Also we assume that each trehalose has a spherical shape with concentric water shells, Fig. 6.9. In this way for 1 M solution of aqueous trehalose the thickness of hydration layer accessible to

each trehalose is 7.35 Å. This thickness is in a good agreement with the one obtained by Havenith and coworkers, 6.5 ± 0.9 Å.[226]

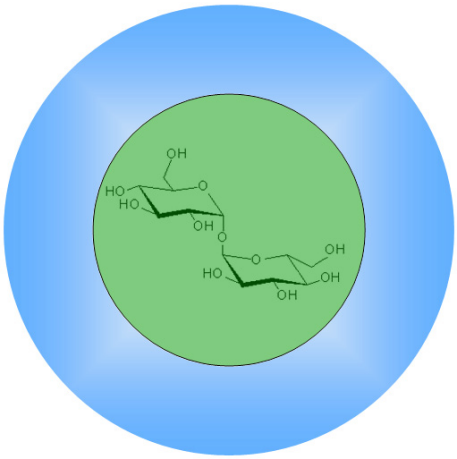

Fig. 6.9 Trehalose is assumed as a spherical cavity (green) surrounded by concentric hydration shells.

6.8 Conclusion

Using a molecular probe N-methyl-6-quinolone (MQ) in trehalose/water mixture it is shown that spectral relaxation of the fluorescence can be implemented to obtain local IR-THz absorption spectra up to about 100 cm^{-1}. Measurements with bulk trehalose/water solutions serve to establish and test the method. Its unique feature is locality, *i.e.* the possibility to measure $\varepsilon(\omega)$ around a supramolecular structure with a covalently connected or embedded probe. Measuring the spectral relaxation of MQ covalently bound to trehalose in water, we showed that spectral relaxation of the latter system and 1 M aqueous trehalose are identical. From this observation the thickness of hydration layer is obtained to be 7.35 Å.

7 Oscillations in Coordinate of DNA Biomolecular Recognition- Observable on Stokes Shift of Ligand Fluorescence

7.1 Introduction (based on own publication, Ref. 281)

Low-frequency structural vibrations of proteins and DNA are important for their physiological functions, and these motions are altered when biomolecules interact with each other and with small molecules. As a model we examine the DNA duplex $d(CGCAAATTTGCG)_2$ together with the bis-benzimidazole dye Hoechst 33258 (H33258), which recognizes and binds to A:T-rich regions in the minor groove.[251,252] Dynamical aspects of recognition are increasingly seen to be essential for inter- and intracellular signaling networks,[253] enzyme catalysis,[254] and allosteric regulation.[255] Improved strategies for drug discovery also consider the flexibility of the biomolecular target.[256] But despite its importance, vibrational motion of ligand dye binding was not yet observed because (i) infrared spectroscopy is not selective for the binding coordinate and (ii) stationary Raman spectroscopy at low frequencies (~THz or 30 cm^{-1}) is dominated by Rayleigh scattering. Here we show that binding oscillations can be seen with the help of ligand fluorescence. Frequency modulation of the time-dependent Stokes shift (TDSS) may reflect coherent in/out motion of the ligand, synchronous with breathing[257] of the minor groove. The observation method is spatially selective and sensitive, compared to THz absorption measurements, and may become useful through advances in fluorescence gating.[108,109]

Fig. 7.1 shows the X-ray structure of the DNA:H33258 complex.[251] The imido HN1 and HN3 groups of the H33258 ligand form bifurcated hydrogen bonds with nucleobase edges T O2 and A N3 in the groove floor, and they play an important role in biomolecular recognition.[251,252] We excite the ligand with short optical pulses and

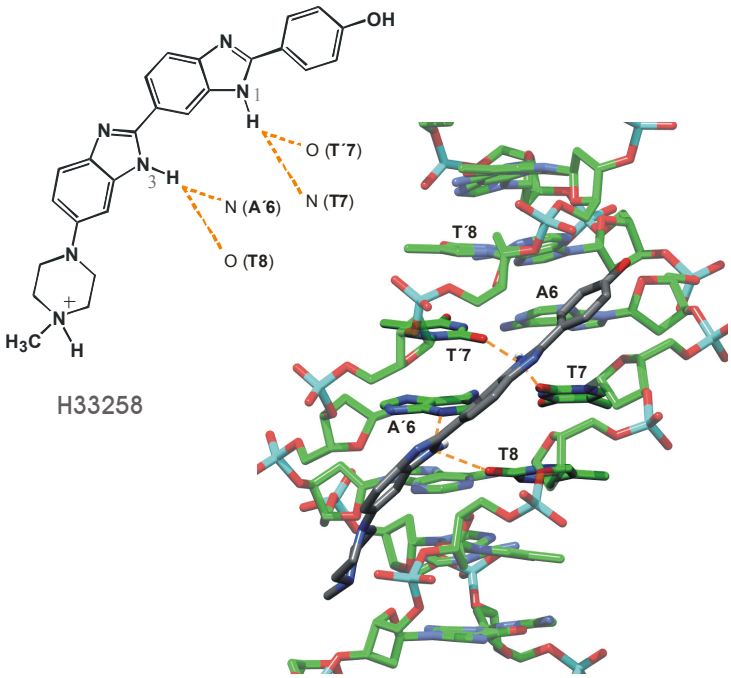

Fig. 7.1 Central view of H33258 bound to d(CGCAAATTTGCG)$_2$, looking onto the minor groove. The ligand (black) extends bifurcated hydrogen bonds (dashed lines) from its two imido groups to nucleobase edges in the groove floor. We show that these hydrogen-bond distances and the groove width oscillate coherently when the chromophore is optically excited. This movement is observed through fluorescence, as frequency-modulation of the time-dependent Stokes shift.

monitor the entire fluorescence band as it evolves over several picoseconds. For this purpose the emission is time-gated by broadband up-conversion with 85 fs resolution.[76] In general the TDSS reflects the response of the local environment to a sudden electrostatic perturbation, induced by the electronic excitation of a molecular probe. For an oxyquinolinium betain dye in various solvents it has been shown that oscillations in the TDSS encode not only intramolecular probe vibrations but also coherent motion of the solvent.[62] If the fluorescent probe is a specifically–binding ligand, even its distance to the substrate could – conceivably – be seen as oscillating. But in all previous studies of proteins and natural DNA, only multiexponential or similar Stokes shifts were observed, corresponding to diffusive reorganization of the environment.[10,89,101, 258,259,260,261,262,263,264] The debate has therefore focussed on the time scales 10 ps– 100 ns, and to which extent the biomolecule or water are responsible for the diffusive reorganization.[11,207,265,266] Meanwhile experimental

methods were improved and an oscillatory TDSS contribution has been found, albeit with unnatural DNA in which nucleobases had been replaced and where a ligand coordinate is not defined.[267] Here we report such oscillations for DNA:H33258 whose interpretation, in terms of specific and coupled motions, is guided by molecular dynamics (MD) simulations.[268,269,270]

7.2 Experimental

Single-stranded DNA was synthesized and purified by reverse-phase HPLC (Biotez). After annealing, the duplex DNA was desalted with a Sephadex PD-10 column. Samples were prepared in two different buffer solutions, an aqueous Tris buffer (0.01 M Tris / 0.05 M NaCl) at pH 7.4 and in ethylene glycol with 1 % water (0.01 M Tris / 0.05 M NaCl / 0.009 M HCl). DNA:H33258 (CAS 233491-45-4, Sigma-Aldrich) complexes were prepared by mixing buffer solutions of duplex and dye 5:4. Transient absorption experiments were performed as in ref.16 and femtosecond fluorescence measurements as in chapter 2. In ethylene glycol, hybridization of 21mer oligonucleotides has been shown at reduced temperature.[32] Our association studies in ethylene glycol (Fig. 7.2) show sharp change at 23°C, both for ligand absorption and hyperchromism of natural bases, indicating that an ordered DNA:H33258 complex exists below this temperature.

7.3 Results

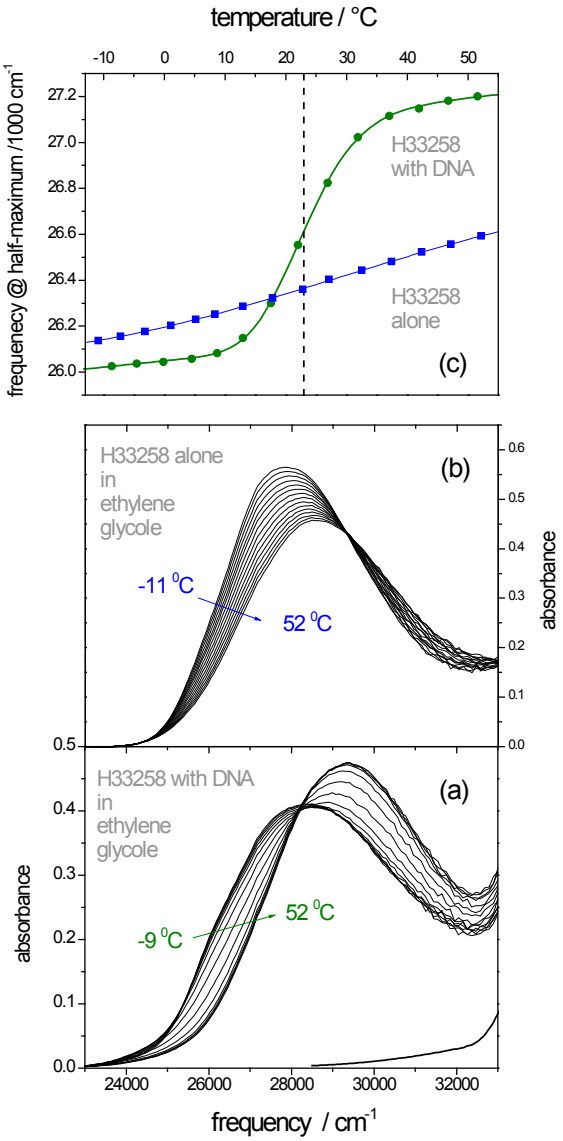

Fig. 7.2 Absorption spectra of H33258 in ethylene glycol (EG, a) in the presence of excess DNA (ss concentration 20 μM) and (b) alone, as function of increasing temperature. Even at 52 °C the spectra in (a) and (b) differ, showing that the dye remains associated with ssDNA.[271] (c) position of the dye absorption in EG (half-point) as function of temperature. Sigmoidal behavior (dashed line) around 23 °C shows melting of the DNA:H33258 complex.

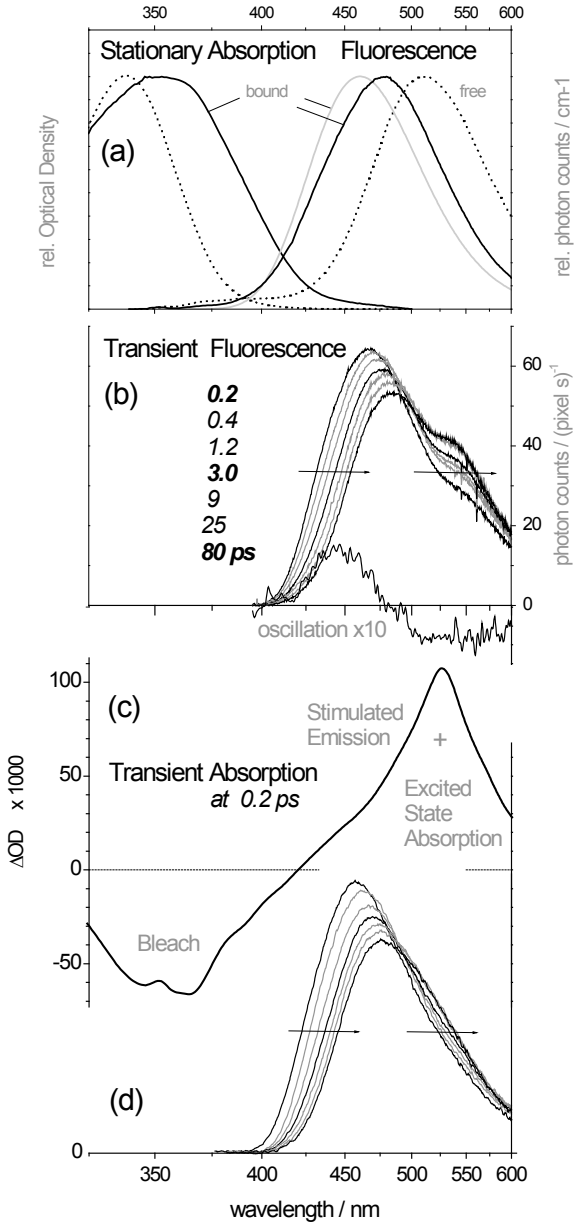

Fig. 7.3 Optical spectra of the DNA:H33258 complex in water (pH 7.4). (a) Stationary absorption and fluorescence at 20°C. *Gray line*: fluorescence at low concentration. *Black solid lines*: at duplex concentration 0.7 mM, upon excitation at 400 nm. (b) Transient fluorescence of in Fig. 7.5d after femtosecond (fs) laser excitation at 400 nm, 1°C, 0.7 mM, with 85 fs time resolution (fwhm instrument response function). Shown are the recorded spectra directly after photometric correction by comparison to standard dyes. The spectrum of a frequency-modulation, with recurrences at 0.6 and 1.2 ps, is also shown (see text). (c) Transient absorption after fs excitation.[16] Excited-state absorption at 530 nm is responsible for a dip in the recorded transient fluorescence spectra ("inner filter effect"). (d) Transient fluorescence spectra at 1 °C, obtained from (b) after smoothing over 3 pixels and correction for the inner filter effect. The dynamic red-shift of the band (arrows) is measured by the peak frequency ν_p or average emission frequency $\overline{\nu}$ as functions of time.

Steady-state spectra of H33258 are shown in Fig. 7.3a. Upon binding to the duplex the absorption band shifts to the red and broadens compared to aqueous solution. For technical reasons we use a relatively high concentration (0.7 mM) of the complex. In this case the stationary emission band is red-shifted from the position at

low concentration because of heterogeneity (dye loading) and self-absorption.[272] But regardless of these complications, femtosecond optical pumping at the red absorption edge (400 nm) promotes a bound H33258 chromophore to the first excited singlet state S_1. Following this, we are interested in the first few picoseconds of spectral relaxation.

The time-resolved fluorescence spectra $S_1 \rightarrow S_0$, as measured, are shown in Fig. 7.3b. The emission was monitored simultaneously at all relevant wavelengths and compared to that of standard dyes, to give photon distributions over fluorescence frequency directly. A dip at 530 nm is caused by strong excited-state absorption.[16] This kind of "inner filter effect" can be corrected by knowledge of its shape (Fig. 7.3c) and amplitude (from comparison with steady-state at late time). Similarly the inner filter effect of ground-state absorption is estimated. After corresponding corrections we obtain the "true" molecular quantum distributions which are shown.

7.3.1 Determination of the spectral relaxation function

The quality of the spectral relaxation function is crucial for the observations and conclusions which may be drawn from it. A discussion of statistical errors and possible systematic errors is therefore an integral part of such measurements. Here we look at the problems which are encountered with the transient fluorescence spectra in Fig. 7.3d and with the relaxation functions in Fig. 7.5. As example the 20 °C data are discussed.

The spectra as in Fig. 7.3d represent the fluorescence quantum distributions over frequency ν [cm^{-1}]. They were fitted by a lognormal function[73] for the range 17000–23700 cm^{-1} (588–421 nm):

$$\log\mathrm{norm}(\nu) = h \exp\left\{ -\ln 2 \left(\frac{\ln\left[1 + 2\gamma\,(\nu - \nu_P)/\Delta\right]}{\gamma} \right)^2 \right\} \qquad (7.1)$$

with peak frequency ν_P [cm^{-1}], width Δ [cm^{-1}], asymmetry γ [–], and amplitude h [–]. To the blue of the fitting range ($\lambda < 422\,\mathrm{nm}$), the use of a long-pass edge filter (Schott GG420) in the fluorescence path results in systematic uncertainties which

should not be tolerated. Similarly to the red ($\lambda > 588\,\mathrm{nm}$), the efficiency of broadband up-conversion decreases and thus impedes the photometric accuracy. From the fit one can also calculate the average frequency

$$\bar{\nu} = \int \nu \ \log \mathrm{norm}(\nu) \ d\nu \Big/ \int \log \mathrm{norm}(\nu) \ d\nu . \tag{7.2}$$

Both measures are compared in Fig. 7.4. They are seen to be almost identical, apart from a constant offset which is due to the asymmetry of the fluorescence spectra. This suggests that the average frequency may be taken for that of the peak in determining the relaxation dynamics. The average frequency can be calculated directly so that spectral fits (and their uncertainties) are avoided. Actually both measures are equally eligible for that purpose.[73]

Next we inquire whether the "raw" spectra of Fig. 7.3b can be used to obtain the dynamics. The corresponding $\bar{\nu}(t)$ data are entered as black points in Fig. 7.4. Again an offset is applied to make the two measures $\bar{\nu}$ (from "raw" and corrected spectra) agree at late times. The range of the "raw" shift is seen to be smaller than that of the true (*i.e.*, corrected) shift, with nearly constant scaling between the two curves. The reason for this behaviour is given by ground-state absorption. Note that comparatively high concentration was used to have sufficient absorbance (0.4 across 0.5 mm) at the excitation wavelength, where DNA:H33248 has an estimated extinction coefficient of $\varepsilon_{400\,\mathrm{nm}} \approx 13480$ ltr mole^{-1} cm^{-1}. We conclude that $\bar{\nu}$ from "raw" spectra (as in Fig. 7.3b) may be used to compare the relaxation behaviour of DNA:H33258, for example between 20°C and 1°C and over relatively small time intervals (0.1-10 ps) as shown in Fig. 7.5b.

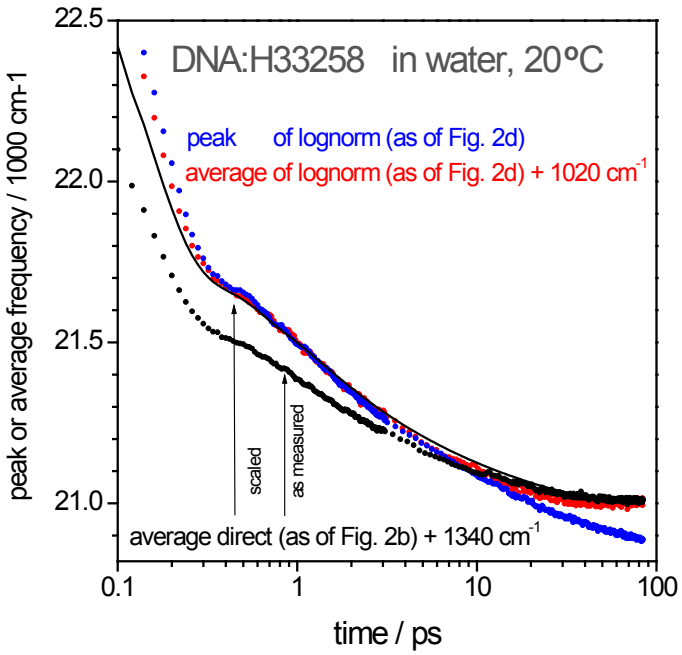

Fig. 7.4 Measures for the position of the evolving fluorescence band. The black line represents a fit to the black points, but scaled such that the red points are reached optimally.

7.3.2 Multiexponential fit of the spectral relaxation function

Let us return to the $\nu_P(t)$ curve in Fig. 7.5a, obtained from transient spectra which may be assumed to reflect the true molecular emission for the system under investigation (*i.e.,* DNA:H33258 at high concentration). Again only the curve at 20 °C is considered (gray line). As initial point, t=0.1 ps is considered acceptable in view of the time resolution (85 fs fwhm) and by inspection of the corresponding spectrum. The curve is best described by a Gaussian $\exp\left(-t^2/2\tau_0^2\right)$ with 1368 cm^{-1} amplitude and τ_0 = 0.111 ps, plus three exponentials with time constants [ps] (amplitudes [cm^{-1}]) of 0.969 (514), 6.61 (279), 34.8 (217) and $\nu_P(\infty) = 20867$ cm^{-1}. In this case the residuals are centered at zero for all time intervals, with standard error σ = 4 cm^{-1}. The simpler description $a_0 \exp\left(-t^2/2\tau_0^2\right) + a_1 \exp\left(-t/\tau_1\right) + a_2 \exp\left(-t/\tau_2\right)$ for the entire time range 0.1-84 ps

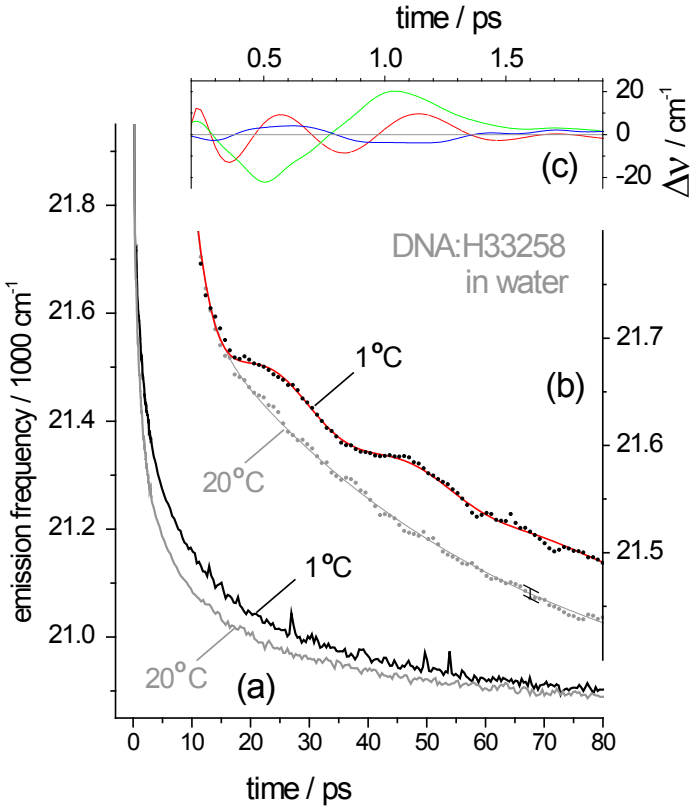

Fig. 7.5 Time-dependent Stokes shift (TDSS) of DNA:H33258 in water (0.7 mM). (a) Peak frequency ν_p, from fitting a spectral lognorm shape to the fluorescence bands as in Fig. 7.3d. Note that noise is smaller before 10 ps due to better statistics. (b) Average frequency $\overline{\nu}$ (points) calculated directly, avoiding spectral fits, from the raw spectra as in Fig. 7.3b. A constant was added to align with ν_p. On lowering temperature to 1 °C, weak oscillations appear on a diffusive spectral relaxation curve. $\overline{\nu}$ curves calculated from a global (t,ν) fit of the transient spectra are also shown (lines), and the confidence interval is indicated. (c) Residuals of the red curve in (b) to a triexponential fit (*red line*). Also shown are residuals for simulated time-correlation functions $C_{DNA}(t)$ (*green*) and $C_{water}(t)$ (*blue*). They are scaled by the observed Stokes shift to indicate the oscillation amplitudes which are expected from the two relaxation channels. Multi-exponential fits were restricted to t=0.1–10 ps. For (c), the ordinate scale of (b) was expanded 2x.

gives the optimal parameters τ_0=0.115 ps, a_0=1376 cm^{-1}, τ_1=1.32 ps, a_1=575 cm^{-1}, τ_2=16.9 ps, a_2=363 cm^{-1}. It results in residuals whose center just leaves the 98% confidence interval $\pm 2\sigma$ for some time ranges. When multiexponential fits are restricted to smaller time windows, such systematic deviations are avoided.

For example the 1 °C curve in Fig. 7.5b was fitted for t=0.1–10 ps, to obtain the residuals which are shown (until 1.9 ps only) in Fig. 7.5c. Note that the resolution of the UV spectrograph was 50 cm^{-1} (fwhm of apparatus function). The precision of

determining ν_P is significantly better because, essentially, correlated changes over a large spectral range (≈1900 cm^{-1}) are measured.

7.3.3 Comparison with previous work

The TDSS of DNA:H33258 was first studied by Zewail and coworkers[89] who used a solution of about 70 μM duplex concentration. A standard femtosecond fluorescence up-conversion setup was employed and the data were analyzed by conventional solvation methodology.[73] Using 352 nm excitation at the peak of the absorption band, the authors reported a total Stokes shift of 1304 cm^{-1} (from t=0 onward) with time constants of 1.4 ps and 19 ps (64% and 36%, respectively). Components below 100 fs were not resolved. Their final value for the peak frequency is $\nu_P(\infty)$=21650 cm^{-1} (taken from a fit to the published spectrum at 100 ps). Our final value $\nu_P(\infty)$=20870 cm^{-1} is lower because of red-edge excitation and spectral selection of a loaded system, as already mentioned. The peak of the stationary fluorescence quantum distribution in Fig. 7.3a is located (from a fit of two lognorm functions to the black solid line) at ν_P(stationary)=20930 cm^{-1}. The difference between our $\nu_P(\infty)$ and ν_P(stationary) is partly due to an uncertainty of the gate frequency used for up-conversion. It may also reflect slow spectral changes after 85 ps, the last time point here, on the nanosecond time scale.[273] We note in passing that the above-mentioned fit of our $\nu_P(t)$ data by a Gaussian plus two exponential time functions has time constants close to those reported in ref. 20, with a similar amplitude ratio.

We observe a decay of fluorescence rate (integrated transient spectra in Fig. 7.3d) with time constants of 0.87 ps (21%) and 27.8 ps (24%) to a final 100% level. This could be due to electron transfer and/or twisting of excited H33258,[272,274] possibly with heterogeneity. No further explanation can be given at this point.

7.3.4 Frequency modulation of spectral relaxation

The fluorescence frequency as function of time is shown in Fig. 7.5. Panel (a) shows the peak position $\nu_P(t)$ for 20 °C and 1 °C (from lognorm fits of spectra as in Fig. 7.3d). Similarly the average position $\overline{\nu}(t)$ could be used; there is no reason why one should be preferred. With red-edge excitation the two measures yield the same dynamics. The $\nu_P(t)$ curve for 20 °C is described by a Gaussian plus exponential time functions in Fig. 7.4. This result agrees qualitatively with up-conversion data on the (different) diluted system.[89]

Discovery of frequency modulation (FM) during the first few picoseconds is at the center of this work. For this purpose we prefer to calculate the average position $\overline{\nu}(t)$ directly from the measured transient spectra (as in Fig. 7.3b). The early behavior is shown in Fig. 7.5b. Upon lowering temperature from 20 to 1 °C, oscillations appear on a diffusive relaxation curve (because friction is reduced for coherent nuclear motion which is responsible, see below). Comparison of the two curves shows that the oscillations at 1 °C are significant. The spectral change beneath $\overline{\nu}(t)$ is found with a global fit, *i.e.* for all wavelengths, by one Gaussian plus 3 exponentials. To model the oscillatory part at 1 °C we add (after some trials) the function $s(t) = \xi\ \mathrm{Exp}[-\gamma_1 t]\mathrm{Cos}[\omega_1 t] + \mathrm{Exp}[-\gamma_2 t]\mathrm{Cos}[\omega_2 t]$. Optimal values are ξ=0.2, ω_1=5.4 ps^{-1}, γ_1=0.85, $\omega_2 \approx 2\omega_1$, γ_2= 1.71 ps^{-1}. We also tried a single frequency, but in this case the observed damping can not be described nor the behavior in ethylene glycol (see below). The spectrum associated with s(t) is also shown in Fig. 7.3b; it has a dispersive form passing through zero near the fluorescence peak, as expected for FM. Very likely the oscillations reflect coherent supramolecular motion, as will be argued in the remainder of this work.

7.3.5 Observation of oscillations also with lower dye load

Transient absorption spectra were provided by Dr. Sergey Kovalenko.[ix] The TDSS is usually measured by time-gating the spontaneous fluorescence. Here we use femtosecond transient absorption of a white-light probe pulse, which is equivalent because the band for stimulated emission from excited H33258 is strictly related to that of fluorescence. The concentration of the duplex was 0.7 mM as before. Since our transient absorption setup is highly sensitive[16] and optical excitation was technically possible at the dye absorption peak, significantly lower dye concentration (≈1/3) could be used. We find an oscillation pattern on the time-dependent Stokes shift of stimulated emission which is quite similar to what was observed by fluorescence (Fig. 7.5c). The results which are reported below were, however, produced with a slightly different biopolymer, namely the duplex d(GCGTTTAAACGC)$_2$. Inadvertently the direction of the self-complementary ss sequences had been reversed. The resulting duplex will be called DNA´ in the following. With this substrate the oscillations are significant even at room temperature, and the early (≤0.6 ps) $\Delta\nu_p(t)$ peaks are more pronounced relative to the 1.1 ps maximum. This fascinating observation is currently the subject of further work. Here we only intend to prove that the characteristic oscillation pattern does not disappear upon lowering the dye load.

For excitation, 0.6μJ/40fs pulses at 360 nm were focused on a sample flow cell to a spot size of 100–120 μm diameter. Induced spectral changes were probed with a delayed white-light continuum in a dual-beam arrangement.[16] Transient absorption spectra are shown in Fig. 7.6b for the early period 180-720 fs. Pump-induced absorbance

[ix] Chemistry Department, Humboldt-Universität zu Berlin.

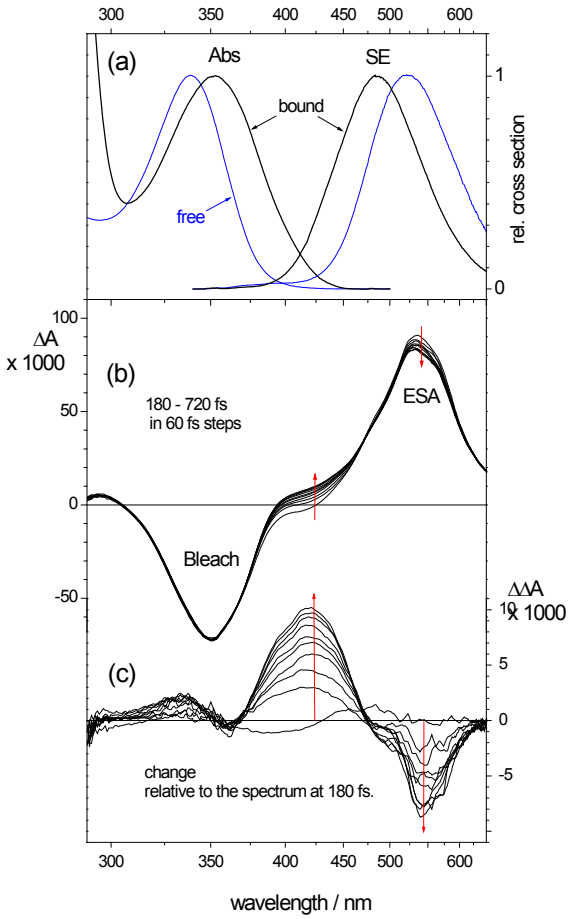

Fig. 7.6 (a) Stationary optical absorption (Abs) and stimulated emission band (SE) of the DNA´:H33258 complex, (b) early transient absorption spectra after femtosecond excitation of the ligand at 360 nm, and (c) change relative to the spectrum at 180 fs. The evolution in (b and c) reflects stimulated emission which shifts to the red.

changes $\Delta A(\lambda)$ are presented in steps of 60 fs. Negative ΔA in a well-defined band around 350 nm is recognized as bleached ground-state absorption, and positive signal around 550 nm is due to excited-state absorption (ESA). Stimulated emission by itself should have $\Delta A < 0$ in the fluorescence region; indeed this is briefly observed in the earliest spectrum around 400 nm. With increasing delay time, however, the only change is increase of signal in the range 370–469 nm and equivalent decrease in the adjacent range 469–650 nm. The change $\Delta\Delta A$ from the earliest spectrum is expanded in Fig. 7.6c. It has a dispersive shape with an isosbestic point at 469 nm. Such behavior indicates a band which shifts to the red, and which may be identified with stimulated emission. The negative lobe with extremum at 540 nm is noisier than the positive lobe with extremum at 425 nm because the white-light continuum was

weaker in the red. The same behavior is observed for the period 1–9 ps, after which bleach and ESA bands decay without change of shape.

The time-dependent Stokes shift of the emission band can be extracted from the spectral evolution in Figs. 7.6b,c. The induced absorbance $\Delta A(t)$ at 425 nm, Fig. 7.7a, measures the shift with highest sensitivity; here the slope $\partial\sigma/\partial\lambda$ on the blue side of the emission band $\sigma(\lambda)$ must be largest. The lower part of the figure contains the behavior until 9 ps which is well described by a triexponential fit (red). Traces from two different measurements – to demonstrate reproducibility – are shown in the upper part on an expanded time scale. The right ordinate gives the relative peak position of the band for stimulated emission. In the expanded time window, oscillations can be discerned which are more evident after the triexponential fit has been subtracted, Fig. 7.7b. Crests are observed at 0.30 and 0.48 ps, and a broad maximum around 1.1 ps also appears to be significant.

7.3.6 Molecular dynamics simulations

MD simulations were provided by Dr. Kristina E. Furse and Prof. Steven A. Corcelli[x] and were predominantly taken from their earlier work,[269,274] including seven 1.3 ns equilibrium trajectories for H33258 free in solution and bound to DNA, and 5000 2.56 ps nonequilibrium trajectories of the complex, all with coordinates saved at 10 fs intervals. The equilibrium trajectories were used for the Fourier analysis described below. For the analysis of the minor groove width we used seven 1.5 ns equilibrium trajectories of the DNA:H33258 complex, along with a new 105 ns control simulation of the dodecamer duplex with no probe bound; coordinates were saved every 100 fs. All simulation used

[x] Department of Chemistry and Biochemistry, University of Notre Dame, Notre Dame, Indiana 46556, U.S.A.

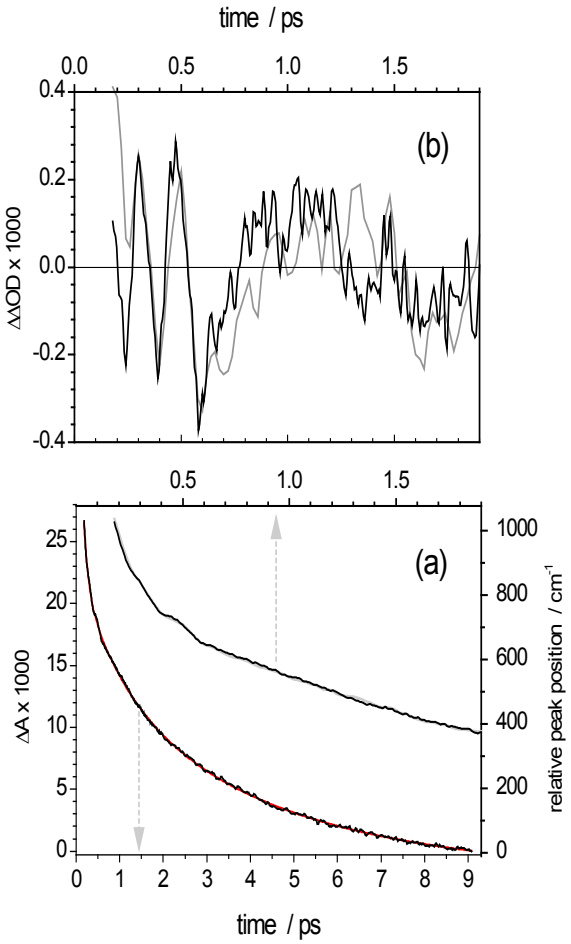

Fig. 7.7 (a) Transient absorbance at 425 nm where change is maximal (left ordinate, lower time scale) is used to determine the relative peak position of the stimulated emission band (right ordinate). Black and gray curves: different measurements, red curve: triexponential fit. (b) Oscillations of the time-dependent Stokes shift (TDSS) of DNA´:H33258, visible directly in the curves in (a), are shown as residuals from a triexponential fit. Black and gray curves represent different measurements. Oscillation peaks are observed at 0.30 and 0.48 ps, and a broad maximum at approximately 1.1 ps is also significant.

AMBER 9.0 [275] with the ff99 [276] force field and the SPC/E [277] water model. The trajectories were post-processed to obtain $\Delta E(t)$, the difference in solvation energy between the excited and ground electronic states of H33258. The TDSS response, $S(t)$, was computed using the expression

$$S(t) = \frac{\overline{\Delta E(t)} - \left\langle \Delta E(\infty) \right\rangle_1}{\left\langle \Delta E(0) \right\rangle_0 - \left\langle \Delta E(\infty) \right\rangle_1}, \tag{7.3}$$

where the overbar represents a nonequilibrium average, and $\left\langle \cdots \right\rangle_{0(1)}$ denotes an equilibrium average with the solute in its ground and excited electronic states. Within

linear response theory, $S(t)$ is equal to the equilibrium time correlation function of the fluctuations in $\Delta E(t)$, [278,279]

$$S(t) = C(t) = \frac{\left\langle \delta\Delta E(0)\delta\Delta E(t)\right\rangle_0}{\left\langle \left|\delta\Delta E\right|^2\right\rangle_0}, \tag{7.4}$$

where $\delta\Delta E(t) = \Delta E(t) - \left\langle \Delta E\right\rangle_0$. Power spectra were obtained by direct analysis of the individual fluctuating components, $\Delta E_\alpha(t)$, of the solvation energy:

$$I_\alpha(\omega) \propto \left[\left\langle \left| \int_{-\tau/2}^{\tau/2} e^{-i\omega t}\Delta E_\alpha(t)dt \right|^2 \right\rangle_0\right]^{1/2}, \tag{7.5}$$

where the subscript α represents the components that contribute to $\Delta E(t)$: DNA, water, counterions, and intramolecular conformation, and τ is the length of the trajectory. Each computed power spectrum (Fig. 7.8) was smoothed with a running average of 10 cm^{-1}. Normal modes for H33258 were calculated with the NMODE module of AMBER. The width of the minor groove was defined as the distance between phosphorous atoms at positions *i* and *j+4* on opposite strands, where *i* and *j* represent a base pair. Ignoring the terminal base pairs, this analysis provides 6 measurements for the dodecamer studied here: A6–C11', T7–G10', T8–T9'. T9–T8', G10–T7', and C11–A6'. Since this dodecamer is a palindrome, the two strands are identical; primes in the base numbering indicate the equivalent position on the opposite strand.

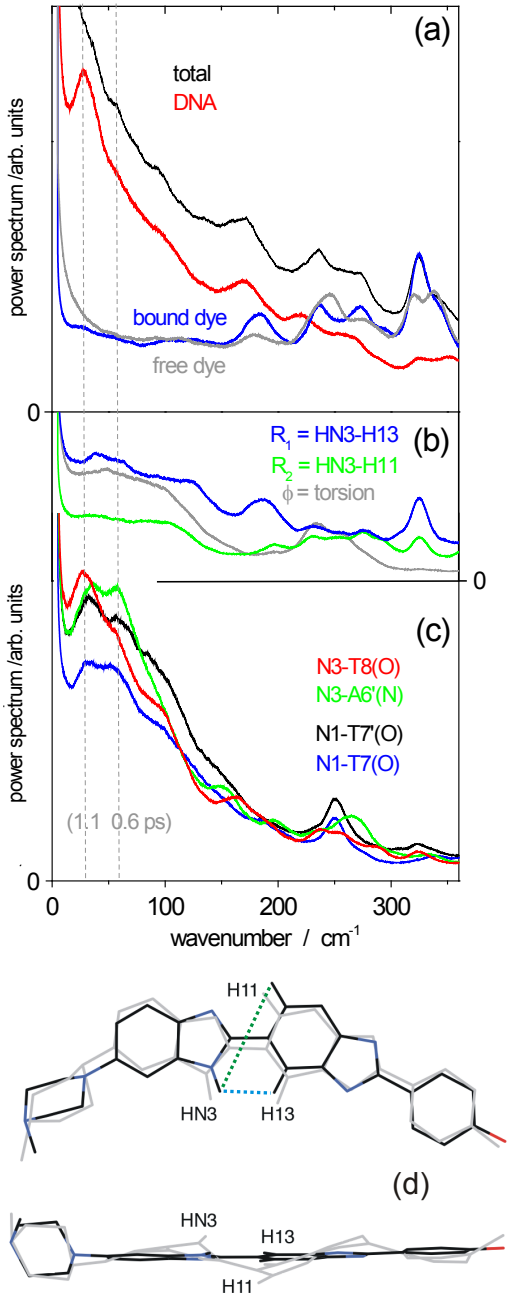

Fig. 7.8 Power spectrum analysis of the simulated fluctuations in the solvation energy and its components: (a) total and partial solvation energies (counterion component has been omitted for clarity), (b,d) H33258 internal distances and central torsion angle, (c) distances between H33258 nitrogen atoms to acceptors on the minor groove edge (see Fig. 7.1). Observed frequency-modulations of the TDSS response (dashed lines) can thereby be assigned and localized.

7.4 Discussion

Molecular dynamics simulations have been used by some of us[268,269,270] to decompose the calculated solvation relaxation function of DNA:H33258, C(t), into contributions from the environment (DNA, water, ions) and from the intramolecular conformation of the H33258 solute: $C(t) = C_{DNA}(t) + C_{water}(t) + C_{ions}(t) + C_{conf}(t)$. High-frequency oscillations of the partial $C_i(t)$ are caused by intramolecular motion (Fig. 7.9). The underlying slow behavior for $C_{DNA}(t)$ shows a local maximum around 1.05 ps. For $C_{water}(t)$ the slow behavior has a very weak shoulder around 0.6 ps. Oscillations are seen better when a multiexponential fit is subtracted from each smoothed curve and the resulting $\Delta C_i(t)$ are scaled to match the experiment, Fig. 7.5c. Modulation of the fluorescence frequency is predicted for solvation by DNA (green line) and, to a lesser extent, by water (blue). The ion contribution is featureless for the time range of interest and the conformational contribution is too small to be observed.

Comparison with experiment (black points and red lines in Fig. 7.5b,c) shows that amplitude and time scale of the simulated frequency modulation (FM) agree reasonably with the observed FM. The qualitative features appear to be captured by MD even though the exact simulation results depend on the force field. More specifically, the DNA contribution is predicted to be of the same size or larger than that of water, and its recurrence at 1.05 ps matches the experimental recurrence at 1.1 ps. When H33258 is simulated free in water, no oscillations are found. Thus the wave $\mathrm{Exp}[-\gamma_1 t]\mathrm{Cos}[\omega_1 t]$ should reflect coherence in a 29 cm^{-1} structural mode of the complex.

Looking into the set of coordinates we find that the “docking” distances of the two bifurcating H-bonds also oscillate with a 1.05 ps period. It makes sense to associate this motion with the oscillation in the calculated $C_{DNA}(t)$ curve (and therefore with the observed frequency modulation) because the emission of the chromophore shifts upon binding (Fig. 7.3a). Similarly the width of the minor groove (Fig. 7.10) could be involved. It is defined as the distance between phosphorous atoms

at positions four base pairs away on the opposite strand. Ignoring the terminal base pairs, there are 6 minor–

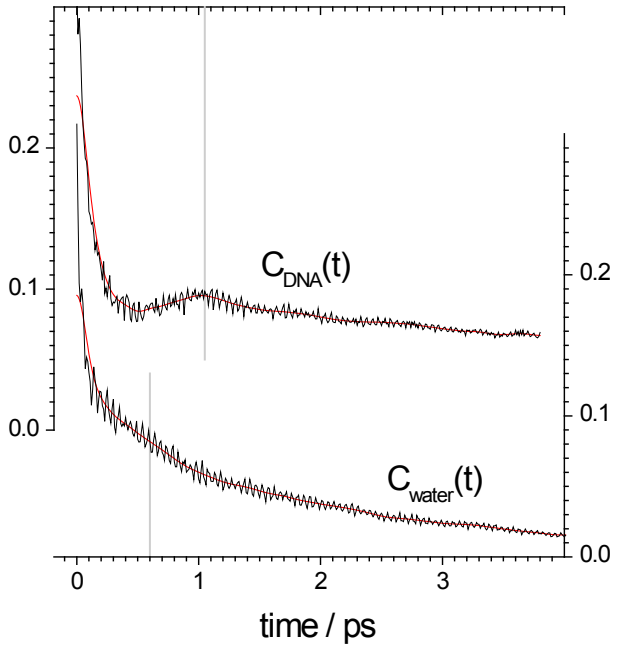

Fig. 7.9 Partial time-correlation-functions from Molecular Dynamics simulations, of equilibrium fluctuations in the H33258 interaction energy with the DNA substrate and with surrounding water (black lines). High frequency oscillations are due to intramolecular motion. After filtering (red lines) a weak oscillation shoulder emerges for C_{water} at t≈0.6 ps; a clear maximum is produced for $C_{DNA}(t)$ at t=1.05 ps.

–groove widths for the dodecamer studied: A6 – C11', T7 – G10', T8 – T9', T9 – T8', G10 – T7', and C11 – A6'. Their time correlation functions (TCFs, Fig. 7.10) exhibit a recurrence near 1 ps, implying coherent motion across the entire binding region close to the frequency which is observed experimentally. A comparison of the groove-width TCFs with and without the dye molecule attached to DNA reveals several distinct differences. Most notably, the recurrence at approximately 1 ps is absent from the TCFs when the dye is not bound. Moreover, the TCFs decay more rapidly when the dye is bound to DNA, which suggests the intrinsic flexibility of DNA is changed upon formation of the complex. Taken together, we may conclude that the observed oscillatory motion is essentially that of biomolecular recognition.

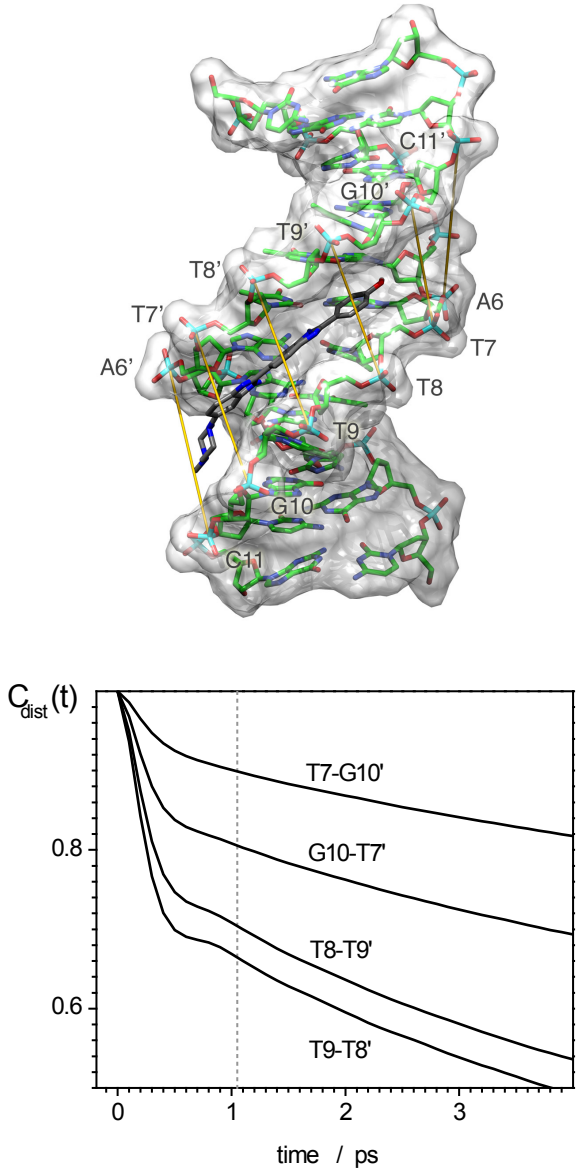

Fig. 7.10 *Left*: Minor groove width, measured between phosphorous atoms of positions separated by four bases on opposite DNA strands. *Right*: Time correlation functions of fluctuations in minor groove width for 15 ns simulations of the DNA:H33258 complex (100 fs resolution). The recurrence around 1 ps is not found for the uncomplexed duplex.

The MD simulations suggest that the 0.6 ps recurrence is due to water. One may object that the calculated amplitude is too small, compared to that of the DNA contribution, for both to add up to the double-peak structure of Fig. 7.5c (red lines). But the imbalance could be due to inadequacies in the simulation force fields or in the approximations necessary to compute the response.[270] Also the experimental curve

could be inaccurate since it was taken from a strongly sloping background (*cf.* Fig. 7.5b). Thus coherent, collective, water motion remains a viable explanation which will be discussed below. First an alternative interpretation: that the 0.6 ps feature is an overtone of the DNA fundamental, will be explored with the help of Fig. 7.11.

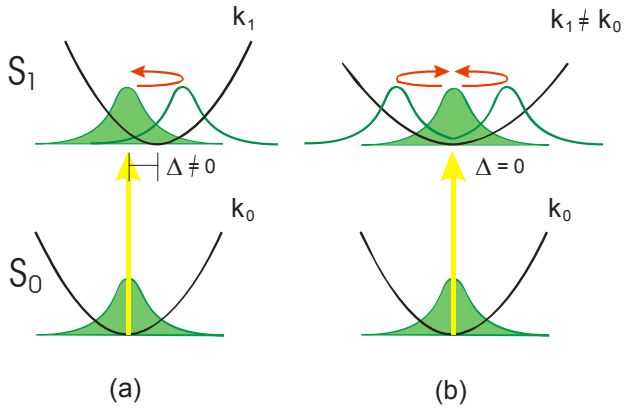

Fig. 7.11 Modulations of the emission frequency, expected from coherence (red arrows) in the 29 cm^{-1} "recognition" mode. (a) When the structure is changed upon optical excitation, a single wavepacket is generated, leading to modulation at the fundamental frequency. (b) When the structure remains (displacement Δ=0) but the force constant is changed instead, the wavepacket becomes bimodal, leading to a modulation at twice the fundamental frequency.

Optical excitation $S_1 \leftarrow S_0$ of the H33258 ligand is generally accompanied by a change of equilibrium structure for the entire complex. The change along the 29 cm^{-1} "recognition" coordinate is measured by displacement Δ of the potential energy minima. If the mode is displaced upon excitation ($\Delta \neq 0$, Fig. 7.11a) then a simple wavepacket is launched on S_1, leading to modulation of the $S_1 \rightarrow S_0$ emission energy at the fundamental frequency ω_1. Another situation is sketched in Fig. 7.11b. Here the mode is not displaced upon excitation (Δ=0) but the force constant is changed instead. The initial Gaussian distribution in the excited state S_1 evolves into a bimodal distribution and back, causing a modulation of the emission energy at the overtone $2\omega_1$, which could also explain the 0.6 ps recurrence.

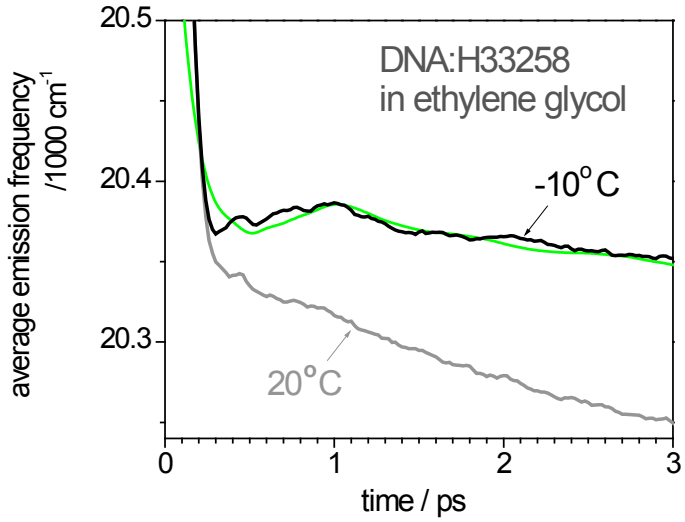

Fig. 7.12 Stokes shift of DNA:H33258 fluorescence in ethylene glycol (average of spectra as in Fig. 7.5b). At -10°C the chromophore, bound to the duplex, shows a broad oscillation peak at 1.2 ps. The curve strongly resembles simulated $C_{DNA}(t)$ which, after scaling, is represented by the green line. At 20 °C the complex is partly dissociated.

With a final experiment we explore the other hypothesis: that water is behind the 0.6 ps recurrence of the time-resolved emission frequency. Would this feature disappear if water is removed? As it was mentioned DNA:H33258 complex in ethylene glycol has stable structure in the temperatures below room temperature, therefore one may replace water with ethylene glycol and perform the measurement at low temperature. The spectral relaxation curve of the complex in ethylene glycol at -10 °C (black line in Fig. 7.12**)** has a broad local maximum around 1 ps, almost identical to simulated $C_{DNA}(t)$ (green line in Fig. 7.12**,** scaled from Fig. 7.9). The significance of the oscillation is again seen by comparison with the curve for 20 °C. (In this case not only friction is larger, as before, but also the complex is partly dissociated.)

In summary for the 58 cm^{-1} FM, there are two interpretations: (i) water is involved directly, by coherent collective motion which affects the ligand; (ii) water acts indirectly, by reducing a structural change for biomolecular recognition upon electronic excitation. Simulations by mixed quantum-mechanics/molecular-mechanics, for example, would resolve which mechanism is responsible for the 0.6 ps

recurrence. Also the groove width coordinates should be correlated with the solvation energy of the ligand.

Most importantly, the dynamics of biomolecular recognition appears to be reflected in a 29 cm^{-1} (1.1 ps) frequency modulation of the fluorescence band, due to coherent oscillation of the ligand-substrate distance and groove breathing. The molecular mechanics of ligand-substrate binding may thus be observed directly, with the potential to become ultra sensitive.[108,109]

7.5 Conclusion

Structural vibration on local structure of DNA is observed via femtosecond Stokes shift measurement of a chromophore bound into the A-T rich regions in the minor groove of DNA duplex $d(CGCAAATTTGCG)_2$. Spectral relaxation of the ligand, bis-benzimidazole dye Hoechst 33258 (H33258), is modulated with an oscillation at 30 cm^{-1}. MD simulation attributes this oscillation to the in/out motion of the ligand, synchronous with breathing of the minor groove.

8 Summary and Outlook

Throughout this work the idea of a molecular THz spectrometer was followed and developed further.

We started from a practical and well-studied solvent, methanol. The transient Stokes shift of a solvatochromic dye, 4-aminophthalimed in methanol, was measured. The latter was compared with predictions of simple continuum theory (using the entire dielectric dispersion of the solvent). Perfect agreement between experiment and theory was achieved. This achievement could, however, be the result of fitting only; it could hide the true physical effects of solvation.

Molecularity aspects of solvation dynamics were therefore studied next. We found that rotation of solutes can accelerate the observed spectral relaxation. Energy relaxation of a molecular probe which is rotationally rapid (compared to rotation of the solvent), N-Methyl-6-Quinolone (MQ), is two-fold faster than that of 4-aminoththalimide. We also learned that in water, as the fastest solvent known, solvation dynamics is independent of the solute since the rotational diffusion of any probe is slower. The influence of excitation energy on solvation dynamics was also studied. It was shown that in nonpolar and aprotic polar solvents, giving excess energy to the molecule shifts the fluorescence band to the red, and in the tail of the relaxation a “retrograde” or blue shift is observed. This was interpreted as a result of cooling. Therefore, to obtain correct solvation dynamics (to be interpreted with simple theories) the probe should be immobile and should be excited at the red edge.

“Local spectroscopy” was tested by measuring the transient Stokes shift of MQ in an aqueous trehalose solution. As a result, the local THz absorption spectrum of the solution up to ~ 3 THz was obtained. In another system MQ is covalently bound to trehalose. Comparing to free-probe solvation, the thickness of the hydration layer could be estimated.

By increasing the accuracy and improving the S/N ratio of fluorescence up-conversion signals, a small oscillation was found in the spectral relaxation of a bis-benzimidazole dye (Hoechst 33258), bound in minor groove of DNA. In this measurement the rmsd of energy relaxation was about 3 cm^{-1}, which enabled us to observe an oscillation of about 10 cm^{-1}. Simulations show that this oscillation reflects an in/out motion of the ligand, synchronous with breathing of the minor groove.

Finally let us discuss in which direction this work might be continued. Different directions are considered:

- Spatial dependence
- Molecularity
- Increase of S/N
- Complementary experiments
- Higher-order effects

Spatial dependence. In the simple continuum model, the polarizability of the solute enters as a parameter (through refractive index of solute cavity, n_{cav}) into the susceptibility of the reaction field. Unreasonably large value of n_{cav} may come from spatial heterogeneity of the solvent in the vicinity of the solute. Likely the dielectric dispersion $\varepsilon(\omega)$ obtained from solvation dynamics measurement indeed depends on space, $\varepsilon(\omega, k)$. If this hypothesis is well established, local THz spectroscopy can be extended to give directly the local structural information in addition to the local dynamics. As the starting point, solvation relaxations of a molecular probe in polyethylene glycol with different chain length can be compared with simple continuum prediction (accurate $\varepsilon(\omega)$ of the solvents up to ~300 cm^{-1} are needed). If solvation dynamics follows $\varepsilon(\omega, k)$ rather than $\varepsilon(\omega)$, deviation from simple continuum prediction is expected for larger chains lengths. In this way it might be possible to formulate the functionality of $\varepsilon(\omega)$ on wavevector, k.

Molecularity. A more precise description of the molecularity aspects of solvation dynamics is urgently needed. In this work the effects of solute rotation and also excitation energy on solvation dynamics were discussed. Other aspects of

molecularity, like translational motion of the solutes and solute polarizability, are highly important to know. The former could influence the solvation relaxation rate of solutes in confined environments[8] and ionic liquids.[142]

Increase of S/N. On the experimental side, increase of S/N ratio and efficiency of the transient signals may be achieved by amplification of the fluorescence and/or using other nonlinear crystals with higher effective non-linearity in broad band up-conversion. Observing small amplitude oscillations modulating the TDSS requires very high rmsd in the spectral relaxation curve. Such tiny but important information is usually hidden under the noise of the measurements.

Complementary experiments. For biological systems, the interpretation of the solvation relaxation process is under intense debate.[207] Since the measured spectral relaxation is a cooperative result of diverse molecular groups, finding the dominant contributor is difficult. Complementary experiments could be devised in order to get more insight into the nature of the process. In chapter 5, temperature dependence of solvation dynamics was suggested as such complementary experiments. This can be tested, and even better methods can be found.

Higher-order effects. In the THz domain, coherent motions of the solute surrounding, which are rarely observed in TDSS measurements, are rich sources of dynamical information. Such motions might be even thought as the fingerprint of intramolecular vibrations. Since the latter motions tend to be overdamped modes, solvation relaxation measurements may fail to catch them. In order to observe such contributions in solvation relaxation curve, it might be possible to enhance them by devising two dimensional solvation dynamics measurements. The second dimension would be externally or internally generated THz pulse. The 2D solvation dynamics experiment may work as follows. Normal solvation relaxation of the solute is measured when the THz pulse comes at a specific delay time. If the delay time of THz pulse matches the coherent motion of the solvent, it could be enhanced. THz pulses can be generated internally by exciting second solute in the vicinity of the main one, whose spectral relaxation is being measured.

Appendix A Description of C(t) by Brownian Oscillators

It is useful to describe the spectral fluorescence dynamics C(t) (calculated from $\varepsilon(\tilde{\nu})$, as for Fig. 4.14, with α_1=18.2 Å^3) by the multimode Brownian oscillator (MBO) model. For this purpose we expand

$$\Delta\tilde{\nu}\cdot C(t) = 2\left(\sum_{k=1}^{3}\tilde{\lambda}_k^{(so)}\,S_k^{(so)}(t) + \tilde{\lambda}^{(ud)}S^{(ud)}(t)\right). \qquad (A1)$$

The relaxation function of an underdamped Brownian oscillator with angular frequency ω and damping constant $\gamma < 2\omega$ is

$$S^{(ud)}(t) = \exp(-\gamma\, t/2)\left[\cos\omega_1 t + \frac{\gamma}{2\omega_1}\sin\omega_1 t\right] \qquad (A2)$$

where $\omega_1 = \sqrt{\omega^2 - \gamma^2/4}$. For strongly overdamped oscillators

$$S_k^{(so)}(t) = \exp(-\Lambda_k t)\ . \qquad (A3)$$

The fit parameters are: $\tilde{\lambda}_1^{(od)} = 628.7\,\mathrm{cm}^{-1}$, $\Lambda_1 = 0.069\,\mathrm{ps}^{-1}$; $\tilde{\lambda}_2^{(od)} = 364.6\,\mathrm{cm}^{-1}$, $\Lambda_2 = 0.195\,\mathrm{ps}^{-1}$; $\tilde{\lambda}_3^{(od)} = 612.4\,\mathrm{cm}^{-1}$, $\Lambda_3 = 2.063\,\mathrm{ps}^{-1}$; and $\tilde{\lambda}^{(ud)} = 303.5\,\mathrm{cm}^{-1}$, $\omega/hc = 116.2\,\mathrm{cm}^{-1}$, $\gamma/hc = 196.0\,\mathrm{cm}^{-1}$. (Note that $2\sum\tilde{\lambda} < \Delta\tilde{\nu}$ because of the unresolved initial drop). The four polar solvation modes (d_1, d_2, d_3 and f in Fig. 4.14) correspond to the dielectric modes with Debye relaxation times 51.5, 7.09, 1.12 ps and to the broad FIR band centered at 116 cm^{-1}.

Appendix B Extracting dielectric dispersion from solvation relaxation

Here we use $\varepsilon(\omega)$ with 3 Debye terms (Eq. (5.1)) to describe the dielectric of trehalose/water mixture. Optimizing the parameters in $\varepsilon(\omega)$ we are able to fit solvation relaxation of the molecular probe in corresponding mixture.

Only ε_0 was used from microwave work. Therefore the $\varepsilon(\omega)$ curves from solvation and microwave data can become different as frequency increases to 20 GHz. Remember that only the dispersion $\varepsilon'(\omega)$ was measured by dielectric spectroscopy; the loss $\varepsilon''(\omega)$ was derived by fitting the real part with Eq. (5.1). Figs. C1-C3 show the frequency-dependent permittivity which was obtained by the two methods. The Naperian attenuation coefficient α was calculated according to

$$\alpha = \sqrt{8}\pi\tilde{\nu}\sqrt{\sqrt{\varepsilon'^2 + \varepsilon''^2} - \varepsilon'} \tag{B1}$$

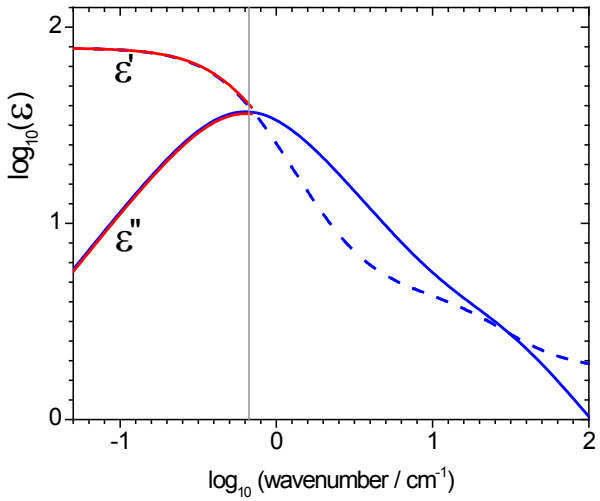

Fig. B1 Dielectric dispersion of pure water, as determined from time-resolved MQ fluorescence (blue lines). Microwave data for the same mixture are shown for comparison (red, up to 0.66 cm^{-1} or 20 GHz corresponding to the vertical grey line)**.**

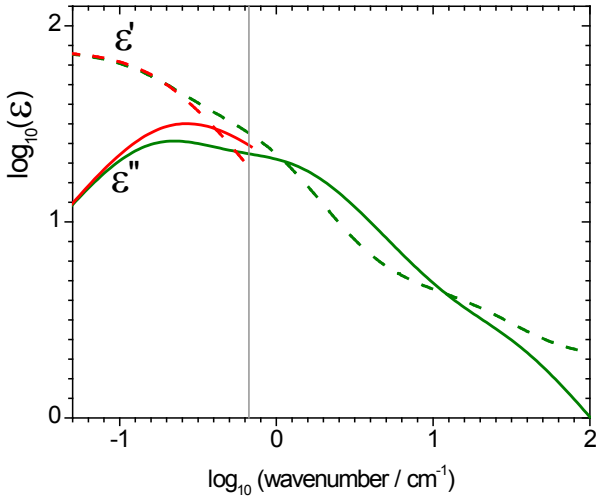

Fig. B2 Dielectric dispersion of the 0.5 M trehalose/water mixture, as in Fig. S3 (olive lines). Microwave data are shown as red lines. Remember that only the dielectric dispersion $\varepsilon'(\omega)$ was measured by broadband dielectric relaxation.

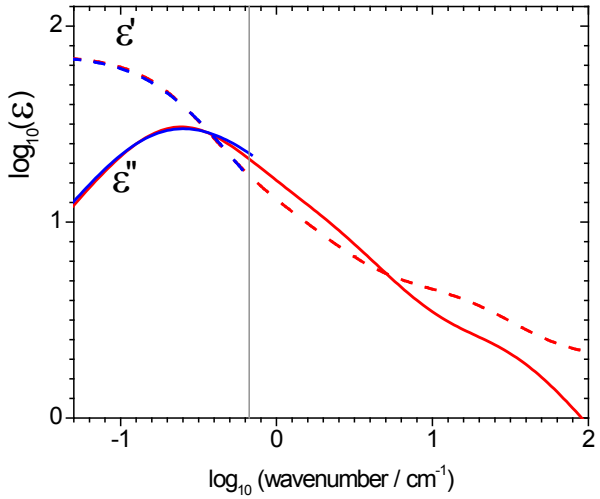

Fig. B3 Dielectric dispersion of the 1.0 M trehalose/water mixture, as determined from time-resolved MQ fluorescence (red lines). Microwave data are shown as blue lines up to the measurement limit of 20 GHz (vertical line)**.**

The calculation of the solvation relaxation function R(t) is specified next. We consider the functional

$$G(\omega) = \frac{\varepsilon(\omega) - 1}{2\varepsilon(\omega) + n_{cav}^2} - \frac{n_\infty^2 - 1}{2n_\infty^2 + n_{cav}^2}. \qquad \text{(B21)}$$

and seek $\hat{R}(t) = 2^{-1}\,[G(s)/s]$ where $s \equiv i\omega$ and L^{-1} is the inverse Laplace transform. For input it is convenient to specify $\varepsilon_0, \varepsilon_\infty$, and amplitude fractions x_2, x_3. The other

parameters which are needed – and must be optimized – are: Debye times τ_1, τ_2, τ_3, and the cavity refractive index squared, n_{cav}^2. We set the dielectric amplitudes

$$\delta_1 = (1 - x_2 - x_3)(\varepsilon_0 - \varepsilon_\infty), \quad \delta_2 = x_2(\varepsilon_0 - \varepsilon_\infty), \quad \delta_3 = x_3(\varepsilon_0 - \varepsilon_\infty). \tag{B3}$$

The frequency-dependent permittivity $\varepsilon(\omega)$ is written as a sum of three Debye terms

$$\varepsilon(\omega) = \frac{\delta_1}{1 + s\tau_1} + \frac{\delta_2}{1 + s\tau_2} + \frac{\delta_3}{1 + s\tau_3} + \varepsilon_\infty . \tag{B4}$$

We obtain G(s) as a rational polynomial,

$$G(s) = f\,\frac{n_0 + n_1 s + n_2 s^2}{g_0 + g_1 s + g_2 s^2 + g_3 s^3}, \tag{B5}$$

where the following abbreviations are used:

$$f = \frac{2 + n_{cav}^2}{2\varepsilon_\infty + n_{cav}^2} \tag{B6}$$

$$\begin{aligned} n_0 &= \delta_1 + \delta_2 + \delta_3 \\ n_1 &= (\delta_2 + \delta_3)\tau_1 + (\delta_1 + \delta_3)\tau_2 + (\delta_1 + \delta_2)\tau_3 \\ n_2 &= \delta_3\tau_1\tau_2 + \delta_2\tau_1\tau_3 + \delta_1\tau_2\tau_3 \end{aligned} \tag{B7}$$

$$\begin{aligned} g_0 &= 2\delta_1 + 2\delta_2 + 2\delta_3 + 2\varepsilon_\infty + n_{cav}^2 \\ g_1 &= (2\delta_2 + 2\delta_3 + 2\varepsilon_\infty + n_{cav}^2)\tau_1 + (2\delta_1 + 2\delta_3 + 2\varepsilon_\infty + n_{cav}^2)\tau_2 + (2\delta_1 + 2\delta_2 + 2\varepsilon_\infty + n_{cav}^2)\tau_3 \\ g_2 &= (2\delta_3 + 2\varepsilon_\infty + n_{cav}^2)\tau_1\tau_2 + (2\delta_2 + 2\varepsilon_\infty + n_{cav}^2)\tau_1\tau_3 + (2\delta_1 + 2\varepsilon_\infty + n_{cav}^2)\tau_2\tau_3 \\ g_3 &= (2\varepsilon_\infty + n_{cav}^2)\tau_1\tau_2\tau_3 \end{aligned} \tag{B8}$$

It is convenient to divide the numerator and the denominator by g_3 to obtain

$$G(s) = f\,\frac{p + qs + rs^2}{a + bs + cs^2 + s^3} \tag{B9}$$

where

$$\begin{aligned} a &= g_0 / g_3, \quad b = g_1 / g_3, \quad c = g_2 / g_3 \\ p &= n_0 / g_3, \quad q = n_1 / g_3, \quad r = n_2 / g_3 \end{aligned} . \tag{B10}$$

In order to facilitate the inverse Laplace transform of $G(s)/s$ we have to find the roots of the equation

$$a + bs + cs^2 + s^3 = 0 . \tag{B11}$$

For physically meaningful parameter values there exist three real roots u,v,w which are all <0 (with x_1=0, τ_1>0 the scheme works also). The inverse Laplace transform of $G(s)/s$ represents the desired relaxation function (not normalized; an offset due to integration has been removed and the sign changed to obtain $0 \le \hat{R}(t) \to 0$ as $t \to \infty$).

$$\begin{aligned}\hat{R}(t) = &-f\frac{p+qu+ru^2}{u(u-v)(u-w)}\ \exp\{ut\}\\ &-f\frac{p+qv+rv^2}{v(v-u)(v-w)}\ \exp\{vt\}\\ &-f\frac{p+qw+rw^2}{w(w-u)(w-v)}\ \exp\{wt\}\end{aligned} \tag{B12}$$

The characteristic solvation times are given by

$$\tau_{solv1} = -1/u, \quad \tau_{solv2} = -1/v, \quad \tau_{solv3} = -1/w. \tag{B13}$$

To account for limited time resolution, the exponentials $\exp\{ut\}$... must be replaced by capped relaxation functions $S[u,t]$.. which, at times longer than the time resolution t_{fwhm}, approach and then merge with the original exponential function

$$S[u,t] = \exp\{ut\} - u^2\sigma^2 \exp\{t/(u\sigma^2)\}, \tag{B14}$$

$$\sigma = t_{fwhm}/\sqrt{8\ln 2}. \tag{B15}$$

The form of the experimental curves in Fig. 5.7 is therefore described by

$$\begin{aligned}\tilde{R}(t) = &-f\frac{p+qu+ru^2}{u(u-v)(u-w)}\ S[u,t]\\ &-f\frac{p+qv+rv^2}{v(v-u)(v-w)}\ S[v,t]\\ &-f\frac{p+qw+rw^2}{w(w-u)(w-v)}\ S[w,t]\end{aligned} \tag{B16}$$

The measured time-dependent mean emission wavenumber is then fitted by

$$\langle\tilde{\nu}\rangle(t) = \gamma\tilde{R}(t) + \langle\tilde{\nu}\rangle_\infty. \tag{B17}$$

Here $\langle\tilde{\nu}\rangle_\infty$, which is fixed, is obtained from the stationary emission spectrum. Once (dimensionless) $\tilde{R}(t)$ is calculated according to Eq. (B.16) for a given set of input parameters, the unique scaling factor γ is determined which minimizes the rms deviation between the data points in Fig. 5.7 and the points calculated with Eq. (B.17). This optimal rms deviation Δ depends on ε_0, τ_1, x_2, τ_2, x_3, τ_3, ε_∞, n_{cav}^2. Their variation to minimize Δ constitutes the fitting routine.

For the calculations we used t_{fwhm}=0.090 ps. Remember that ε_0 was always taken from the microwave experiment. The data needed to calculate the relaxation

functions of Fig. 5.7 are given in the Table below. The total (deconvoluted) Stokes shift can be estimated by back-extrapolation of $\hat{R}(t)$, Eq. B. 12,

$$\text{shift} = \gamma\hat{R}(0) \tag{B18}$$

mode:		S		D_1		D_2					
conc/ M	ε_0	δ_1	τ_1 /ps	δ_2	τ_2 /ps	δ_3	τ_3 /ps	ε_∞	n_{cav}^2	shift/ $^{-1}$	$\langle\tilde{\nu}\rangle_\infty$ /
0.0	*78.32*[a]	—	—	(73.93)	*8.38*[a]	2.59	0.232	1.80	*5.29*[b]	3130	15790[e]
0.5	*74.70*[c]	(43.15)	29.46	27.12	4.30	2.43	0.201	*2.0*	*5.10*[d]	2930	16160[e]
1.0	*70.79*[c]	(59.34)	22.35	6.84	2.89	2.61	0.200	*2.0*	*3.98*[d]	2820	16180[e]

Independent fitting parameters are indicated by shading. However, values in italics were kept fixed during fitting: *(a)* ref. [280], *(b)* ref. [62], *(c)* from microwave measurements above, *(d)* adjusted to obey the relative absorbance at 80 cm^{-1} [226] , *(e)* from steady-state measurements. Data in parentheses depend on the other parameters and were therefore not fitted. Parameters are grouped into modes D_1 and D_2 as in water, and mode S which is associated with rotational diffusion of the hydrated sugar solute. When the appropriate parameter values are used in Eqs.B.6 - B.11, then Eq. B.16 reproduces the form of the measured relaxation function, while the scaling factor γ can be recovered with the help of Eq. B.18.

In order to assess the relative error of the measurement, consider the spectral relaxation curve of MQ fluorescence in pure water, *i.e.* the corresponding black line in Fig. 1. It drops from the first measurement point, 18510 cm^{-1} at t=0.030 ps, to 15790 cm^{-1} at t=∞, *i.e.* the observed (not deconvoluted) Stokes shift is 2720 cm^{-1}. The rms deviation of the measured values $\langle\tilde{\nu}\rangle(t)$ is 29 cm^{-1} ; the relative error is ≈1%. The deconvoluted fluorescence shift in water is determined to be 3130 cm^{-1}, in line with the value of 3050±200 cm^{-1} which was found by transient absorption.[62]

Appendix C Program for optimizing ε(ω) to fit spectral relaxation

This code was written in Matlab. Input data are multiexponential fit parameters, from a fit to the spectral relaxation obtained from measurement. Any form of dielectric function can be given as the tail model for ε(ω). In this example the dielectric dispersion is given by three Debye terms plus two high-frequency terms. Spectral relaxation is taken from MQ in methanol experiment (see chapter 5). Output is the optimized coefficients of the trial ε(ω).

```
function fitDielectricn
close all
clc
%%%%%%%%%%%%%%%%%%%%%%%%%%%%%%%%%%%%%%%%%%%%%%%%%%%%%%%%%%%%%%%%%%%%%%%%%%%%
%%
start=19;    % correspond to 100fs
endd=9000;   % correspond to 10000fs
%----------------------
%speed of light
c=2.997925e-2;% in ps scale
ps=1;  %new scale
%THz=1e12;
THz=1; %new scale%
hb=1.0540e-34;%hbar
kB=1.38e-23;%Boltzmann's constant
step=0.05; cm=[-3000:step:3000]; cm=cm'; w=cm*(2*pi*c); wvn=cm;
T = 273.15 +30;
%%%%%%%%%%%%%%%%%%%%%%%%%%%%%%%%%%%%%%%%%%%%%%%%%%%%%%%%%%%%%%%%%%%%%%%%%%%%
%%

% just to have time axis consistant with simulation
dee=74; ta= 20*ps; e1= dee./(1 + 1i*w*ta); eps=e1 ;

% omega=2*pi*c*wvn;
er=real (eps);
ei=imag (-eps);
e=er-1i*ei;

% Fluctuation-Dissipation factors
factor=(1+coth (hb.*pi.*c.*wvn/(kB*T)));
nc=1; n2=1 ;
   ec=(e-1)./(2*e+nc^2)-(n2-1)/(2*n2+nc^2);
   eci=imag (ec);
   % Weighted susceptibility
   tmp2=eci.*factor;    tmp4=-tmp2;
   ll=length (tmp4);    llm=(length (tmp4)-1)/2;
   jjo=find (wvn==0);
   % input ('value for tmp4 at zero frequency');
   tmp4 (jjo)=-(tmp4 (jjo-1)+tmp4 (jjo+1))/2;

% Fourier transform
```

```
  tmp4fft=[tmp4((llm+1):2*llm+1,1);tmp4(1:llm,1)];
  trial=fft (tmp4fft);

  % time axis
  deltat=1/(length (tmp4fft)*0.05*c);
  tfft=(0:deltat:(length (trial)-1)*deltat);
  timeax=tfft';   %  new scale

%%%%%%%%%%%%%%%%%%%%%%%%%%%%%%%%%%%%%%%%%%%%%%%%%%%%%%%%%%%%%%%%%%%%%%%%%%%%%%%
%%
% spectral relaxation of MQ in methanol as input data
a1=8398.805440; a2=1573.963081; a3=1525.948316;
t1=0.027537140;  t2=0.708080073; t3=4.796366650;

peak=a1*exp(-timeax/t1)+a2*exp(-timeax/t2)+a3*exp(-timeax/t3);

% normalizing the spectral relaxation between 0.1 and 100 ps
 peak=peak-peak(endd); peak=peak/peak(start);

 DATA=[timeax(start:endd) peak(start:endd)];
 plot(timeax(start:endd), peak(start:endd))

figure(1)
 semilogx(DATA(:,1), DATA(:,2),'r');grid;set(gca,'NextPlot','add')
 HPlothandle(1) = semilogx(DATA(:,1), DATA(:,2),'b-
','EraseMode','xor'); %FIT

% gaussian filter to the dielectric
tfwhm=120*1e-3;   % new scale
cs=c;
nue=cs*wvn;
tsig=tfwhm/sqrt(8*log(2));
nuesig=1/(2*pi*tsig);
Gaus=exp(-0.5*(nue./nuesig).^2);
%%%%%%%%%%%%%%%%%%%%%%%%%%%%%%%%%%%%%%%%%%%%%%%%%%%%%%%%%%%%%%%%%%%%%%%%%%%%%%%
%%
% initial parameters
de11=25; tau11=22.5*ps; de12=1.27; tau12=8.23*ps; de13=1.93;
tau13=1.05*ps; As=0.98*(2.68*THz)^2;   Al=0.15*(3.63*THz)^2;
ws=2.68*THz; wl= 3.63*THz; gs=(7.04*THz)/2*pi;
gl=(2.11*THz)/2*pi;
einf=1.82;
ncc=2.2; % n cavity

X0=[de11; de12; de13; tau11; tau12; tau13; ws; wl; As; Al; gs; gl];

% lower limit
lb=[de11; 0.5*de12; 0.5*de13; 0.1*tau11; 0.1*tau12; 0.1*tau13;
0.5*ws; 0.5*wl; 0.1*As; 0.1*Al; 0.1*gs; 0.1*gl];

% uper limit
ub=[4*de11; 1.5*de12; 1.5*de13; 4*tau11; 4*tau12; 4*tau13; 2*ws;
2*wl;     2*As; 2*Al; 2*gs; 4*gl];

%%%%%%%%%%%%%%%%%%%%%%%%%%%%%%%%%%%%%%%%%%%%%%%%%%%%%%%%%%%%%%%%%%%%%%%%%%%%%%%
%%
OPTIONS = optimset('lsqnonlin');
OPTIONS = optimset('TolX',1e-8);
OPTIONS = optimset(OPTIONS,'TolFun',1e-12);
```

```
vx=lsqnonlin('lsqDielec',X0,lb,ub,OPTIONS,DATA,start,endd,w,Gaus,ncc,
einf,T,HPlothandle);

[err,FIT,Amp] =
funDielec(vx,DATA,start,endd,w,Gaus,ncc,einf,T,HPlothandle);

RES1=FIT; RES2=vx; RES3=Amp;

%%%%%%%%%%%%%%%%%%%%%%%%%%%%%%%%%%%%%%%%%%%%%%%%%%%%%%%%%%%%%%%%%%%%%%%%
%%
save('D:\My_thesis\PAR.dat','RES2','-ascii')



% function 1


function err =
lsqDielec(VarPar,Data,start,endd,w,Gaus,ncc,einf,T,HPlothandle)

y=Data(:,2);
%=====================================================================
=%
   de1  = VarPar(1); de2  = VarPar(2); de3  = VarPar(3);
   tau1 = VarPar(4); tau2 = VarPar(5); tau3 = VarPar(6);
   ws   = VarPar(7);   wl  = VarPar(8);
   As   = VarPar(9);   Al  = VarPar(10);
   gs   = VarPar(11);  gl  = VarPar(12);

%=====================================================================
=%
A=funepsn(w,Gaus,start,endd,ncc,de1,de2,de3,tau1,tau2,tau3,As,Al,gs,g
l,ws,wl,einf,T);   %MeOH

c1=A\y;  z = A*c1; err=(z-y);

%ERR=norm(err)
%%%%%%%%%%%%%%%%%%%%%%%%%%%%%%%%%%%%%%%%%%%%%%%%
set(HPlothandle( 1),'ydata',z)      % FIT
%=========================================%
drawnow
%=========================================%


% function 2

function [err,z,c1] =
funDielec(VarPar,Data,start,endd,w,Gaus,ncc,einf,T,HPlothandle)

y=Data (:,2);
%=====================================================================
=%
   de1  = VarPar(1); de2  = VarPar(2); de3  = VarPar(3);
   tau1 = VarPar(4); tau2 = VarPar(5); tau3 = VarPar(6);
   ws   = VarPar(7);   wl  = VarPar(8);
   As   = VarPar(9);   Al  = VarPar(10);
   gs   = VarPar(11);  gl  = VarPar(12);
```

```
%=====================================================================
=%
A=funepsn(w,Gaus,start,endd,ncc,de1,de2,de3,tau1,tau2,tau3,As,Al,gs,g
l,ws,wl,einf,T);

c1=A\y;  z = A*c1; err=norm (z-y);
% ERR=norm (err)
%%%%%%%%%%%%%%%%%%%%%%%%%%%%%%%%%%%%%%%%%%%%%%%%
 set (HPlothandle (1),'ydata',z)      % FIT
%=========================================%
 drawnow
%=========================================%

% function 3

function
epsil=funepsn(w,Gaus,start,endd,ncc,de1,de2,de3,tau1,tau2,tau3,As,Al,
gs,gl,ws,wl,einf,T)

%c=3e10;%speed of light
c=2.997925e-2;% in ps scale %  (* cm/ps *);
ps=1;  %new scale
THz=1; %new scale%
wvn=w/(2*pi*c);

hb=1.0540e-34;% hbar
kB=1.38e-23;% Boltzmann's constant

e1 = de1./(1 + 1i*w*tau1); e2 = de2./(1 + 1i*w*tau2); e3 = de3./(1 +
1i*w*tau3);
es = As./(ws^2 - w.^2 + 1i*w*gs); el = Al./(wl^2 - w.^2 + 1i*w*gl);
eps=e1+e2+e3+es+el+einf;
er=real (eps); ei=imag (-eps); e=er-1i*ei;

%%%%%%%%%%%%%%%%%%%%%%%%%%%%%%%%%%%%%%%%%%%%%%%%%%%%%%%%%%%%%%%%%%%%%%%
%%
% Fluctuation-Dissipation factors
factor=(1+coth (hb.*pi.*c.*wvn/(kB*T)));
nc=ncc;% refractive index in the cavity  at first 2.3

   ec=(e-1)./(2*e+nc^2);
   eci=imag(ec);

   % Weighted susceptibility

   tmp2=eci.*factor;
   tmp4=-tmp2;
   ll=length (tmp4);
   llm=(length (tmp4)-1)/2;

   jjo=find (wvn==0);
   % input ('value for tmp4 at zero frequency');
   tmp4 (jjo)=(tmp4 (jjo-4)+tmp4 (jjo-3)+tmp4 (jjo-2)+tmp4 (jjo-
1)+tmp4 (jjo+1)+tmp4 (jjo+2)+tmp4 (jjo+3)+tmp4 (jjo+4))/8;
   % Filter function G
   tmp4=tmp4.*Gaus;
   % Fourier transform
```

```
    tmp4fft=[tmp4((llm+1):2*llm+1,1);tmp4(1:llm,1)];
    trial=fft (tmp4fft);

      trial=real(trial)-real(trial(endd));
      A=abs ((real (trial))./((real (trial (start)))));
      B=A(start:endd);          %&&&&  important

epsil=B;
```

Acknowledgement

I would like to thank all people contributing to shape up my scientific vision and future during the course of my PhD thesis. Without their supports I would have not been able to finish this work. This work was done under the supervision of *Prof. Dr. Nikolaus P. Ernsting* in the Chemistry Department and of *Prof. Dr. Jürgen P. Rabe* in the Physics Department of the Humboldt-Universität zu Berlin.

In the first place, I would like to thank *Prof. Nikolaus P. Ernsting* for giving me this great opportunity to enter the femtosecond world. His continued support, careful supervision, and encouragements gave me enough confidence to solve the difficulties of the work.

I would like to thank *Prof. Dr. Jürgen P. Rabe* to accept the supervision of my PhD thesis in Physics Department and allowing me to participate in his group seminars. I learned a lot from the discussions in his group.

I would like to acknowledge the contribution of following people in this work:

Dr. Sergey Kovalenko for fruitful discussions, criticisms and comments. Also I thank his transient absorption measurements of 4-aminophthalimide, Coumarin 343, and H33258/DNA.

Dr. Alexander Dobryakov for Codes in Matlab and useful discussions. *Prof. Mark Maroncelli*, for invaluable discussions on the solute dependence of solvation dynamics.

I thank *Yathrib Ajaj* and *Prof. Dr. Hermann Weingätner* for measuring dielectric dispersion of aqueous trehalose, *Prof. Dr. Bernhard Dick* for density-functional calculations and jet spectra of 4-aminophthalimide (4AP), *A. Neugebauer* and *Dr. B. Ziemer* for the X-ray structure of 4AP, *Falko Berndt* and *Prof. Dr. Rainer Mahrwald*

for binding N-Methyl-6-Quinolone (MQ) to trehalose, *Dr. Ilya Ioffe* for quantum calculations of MQ, *Dr. Uter Resch-Genger* for letting me use their fluorescence spectrometer, *Dr. Kristina E. Furse* and *Prof. Steven A. Corcelli* for their MD simulations of H33258/DNA complex ,and *Lars Dahmel* for DNA sample preparation.

I would like to thank my colleagues *Dr. Horst Hennig*, *Heiderose Steingräber*, *Dr. Alexander Weigel*, *Dr. Luis Perez-Lustres, Iris Suter*, *Sabrina Penn*, *Xinxing Zhang* for their help and support during my PhD work.

At this point, I have to be not only thankful but grateful to my wife, Fatemeh for her help, patience, understanding, endless encouragement and love. Without her love and endurance it would have not been possible to complete the long journey of time for this doctorate work.

References

[1] M. Maroncelli, J. Mol. Liquids, 57, 1, 1993.

[2] R. M. Stratt, M. Maroncelli, J. Phys. Chem., 100, 12981, 1996.

[3] P. J. Rossky, J. D. Simon, Nature, 370, 263, 1994.

[4] B. Bagchi, Annu. Rev. Phys. Chem., 40, 115, 1989.

[5] S. M. Bhattacharyya, Z. G. Wang and A. H. Zewail, J. Phys. Chem. B, 107, 13218, 2003.

[6] B. Bagchi, Chem. Rev, 105, 3197, 2005.

[7] N. Nandi, K. Bhattacharyya and B. bagchi, Chem. Rev., 100, 2013, 2000.

[8] K. Bhattachryya, Account of Chemical research, 36, 95, 2003.

[9] P. Jurkiewicz, A. Olzù yn´ska, M. Langner and Martin Hof, Langmuir, 22, 8741, 2006.

[10] D. Andreatta, J. L. P. Lustres, S. A. Kovalenko, N. P. Ernsting C. J. Murphy, R. S. Coleman, M. A. Berg, J. Am. Chem. Soc., 127, 7270, 2005.

[11] L. Nilsson, B. Halle, Proc. Natl. Acad. Sci. USA, 102, 13867, 2005.

[12] J. R. Lakowicz, *Principles of fluorescence spectroscopy*, 2nd ed, Pelenum publisher, New York, 1999.

[13] H. Mahr, M. D. Hirsch, Opt. Comm., 13, 96, 1975.

[14] S.Kinoshita, H.Ozawa, Y.Kanematsu, I.Tanaka, N.Sugimoto and S.Fujiwara, Rev. sci. instr., 71, 3317, 2000.

[15] A. L. Dobryakov, N. P. Ernsting, *Analysis and Control of Ultrafast Photoinduced Reactions*, O. Kühn, L. Wöste, Eds, Springer Series in Chemical Physics, Vol. 87, Springer, Heidelberg, Germany, 2007.

[16] A. L. Dobryakov, S. A. Kovalenko, A. Weigel, J. L. P. Lustres, J. Lange, A. Müller, N. P. Ernsting, Rev. Sci. Instrum., 81, 113106, 2010.

[17] M. Chergui, A. H. Zewail, Chem.Phys.Chem, 10, 28, 2009.

[18] U. Heugen, G. Schwaab, E. Bruendermann, M. Heyden, M. X. Yu, D. M. Leitner, M. Havenith, Proc. Natl. Acad. Sci., 103, 12301, 2006.

[19] E. T. J. Nibbering, H. Fidder, E. Pines, Ann. Rev. Phys. Chem., 56, 337, 2005.

[20] P. Kukura, D. W. McCamant, and R. A. Mathies, Ann. Rev. Phys. Cem., 58, 461, 2007.

[21] J. D. Jackson, *Classical Electrodynamics* (3rd ed.). New York: Wiley, 1998.

[22] P. N. Butcher, D. Cotter, The elements of nonlinear optics, New York: Cambridge University Press, 1990.

[23] R. Kubo, M. Toda, N. Hashitsume, *Statistical physics II. Non-equilibrium Statistical Mechanics*, Berlin: Springer, 1985.

[24] J.G. Saven, J. L. Skinner, J.Chem. Phys., 99, 4391, 1993.

[25] D. A. McQuarrie, *Statistical mechanics*, Harper Collins Publishers, New York, 1976.

[26] S. Mukamel, *Principles of Nonlinear optical Spectroscopy*, Oxford University, New York, 1995.

[27] Y. Yan, R. E. Gillilan, R. M. Whitnell, K. Wilson, S. Mukamel, J. Phys. Chem., 97, 2320, 1993.

[28] Y.J. Yan, S. Mukamel, J. Phys. Chem., 89, 5160, 1988.

[29] B. Li, A. E. Johnson, S. Mukamel, A. B. Myers, J. Am. Chem. Soc., 116, 11039, 1994.

[30] Y.J. Yan, S. Mukamel, Phys. Rev. A, 41, 6485, 1990.

[31] E. T. J. Nibbering, D. A. Wiersma, K. Duppen, Chem. Phys., 183, 167, 1994.

[32] R. Kubo, J. Phys. Soc. Jap., 12, 570, 1957.

[33] C. H. Wang, *Spectroscopy of condensed media*, dynamics of molecular interactions, Academic Press, INC, London, 1985.

[34] Merzbakher, *Quantum mechanics*, 2nd ed, Wiley, New York, 1970.

[35] R. Zwanzig, Ann. Rev. Phys. Chem., 16, 67, 1965.

[36] C. F. Mazenko, *Non-equilibrium statistical mechanics*, Wiley-VCH, Weinheim, 2006.

[37] Böttcher, C. J. F.; *Theory of Electric Polarization*, Elsevier Science, 2nd Ed, 1993.

[38] C. Reichardt, T. Welton, *Solvents and solvent effects in organic chemistry*, 4nd ed, Wiley-VCH publisher, Weinheim, 1988.

[39] L. Onsager, J. Am. Chem. Soc., 58, 1486, 1936.

[40] Y. Ooshika, J. Phys. Soc. Jap., 9, 594, 1954.

[41] N. S. Bayliss, E. G. McRae, J. Phys. Chem., 58, 1002, 1954.

[42] E. lippert, Z. Naturforsch, 10a, 541, 1955.

[43] E. G. McRae, J. Phys. Chem., 61, 562, 1957.

[44] R. A. Marcus, J. Chem. Phys., 38, 1858, 1963.

[45] G. Van der Zwan, J. Hynes, J. Phys. Chem., 89, 4181, 1985.

[46] P. G. Wolynes., J. Chem. Phys., 86, 5133, 1987.

[47] I. Rips, J. Klafter, J. Jortner, J. Chem. Phys., 88, 4288, 1988.

[48] M. Maroncelli, G. R. Fleming, J. Chem. Phys., 89, 875, 1988.

[49] B. Bagchi, E. W. Castner, G. R. Fleming, J. Mol. Struc. Theor. Chem, 194, 171, 1989.

[50] F. O. Raineri, Y. Zhou, H. L. Friedman, Chem. Phys., 152, 201, 1991.

[51] B. Bagchi, D.W. Oxtoby, G. R. Fleming, Chem. Phys., 86, 257, 1984.

[52] M. Maroncelli, G. R. Fleming, J. Chem. Phys., 86, 6221, 1987.

[53] Yu T. Mazurenko, Opt. Spectrosc., 36, 283, 1974.

[54] E. W. Castner, Jr., B. Bagchi, G. R. Fleming, Chem. Phys. Lett., 143, 270, 1988.

[55] M. Maroncelli, J. MaciInnis, G. R. Fleming, Science, 243, 1674, 1989.

[56] I. Rips, J. Klafter, J. Jortner, J. Chem. Phys., 88, 3246, 1988.

[57] A. L. Nichols, D. F. Calef, J. Chem. Phys., 89, 3783,1988.

[58] M. A. Kahlow, W. Jarzeba, T. J. Kang, P. F. Barbara, J. Chem. Phys., 90, 151, 1989.

[59] C-Ping Hsu, X. Song, R. A. Marcus, J. Phys. Chem., 101, 2546, 1997.

[60] R. Jimenez, G. R. Fleming, P. V. Kumar, M. Maroncelli, Nature, 369, 471, 1994.

[61] J. Ruthmann, S. A. Kovalenko, N. P. Ernsting, J. Chem. Phys., 109, 5466, 1998.

[62] J. L. P. Lustres, S. A. Kovalenko, M. Mosquera, T. Senyushkina, W. Flasche, N. P. Ernsting, Angew. Chem. Int. Ed. 44, 5635, 2005.

[63] M. Marroncelli, J. Chem. Phys., 94, 2084, 1991.

[64] E. W. Castner, G. R. Fleming, B. Bagchi,, M. Maroncelli, J. Chem. Phys., 89, 3519, 1988.

[65] R. F. Loring, S. Mukamel, J. Chem. Phys., 87, 1272, 1987.

[66] B. Bagchi, A. Chandra, J. Chem. Phys., 90, 7338, 1989.

[67] A. A. Kornyshev, A. M. Kuznetsov, D. K. Phelps, M. J. Weaver, J. Chem. Phys., 91, 7159, 1989.

[68] R. Biswas, B. Bagchi, J. Phys. Chem. A, 103, 2495, 1999.

[69] M. Maroncelli, G. R. Fleming, J. Chem. Phys., 89, 5044, 1988.

[70] J. S. Bader, D. Chandler, Chem. Phys. Lett., 157, 501, 1989.

[71] P. V. Kumar, M. Maroncelli, J. Chem. Phys., 103, 3038, 1995.

[72] B. M. Ladanyi, R. M. Stratt, J. Phys. Chem., 99, 2502, 1995.

[73] M. L. Horng, J. A. Gardecki, A. Papazyan, M. Maroncelli, J. Phys. Chem., 99, 17311, 1995.

[74] M. Maroncelli, P. V. Kumar, A. Papazyan, M. L. Horng, S. J. Rosenthal, G. R.Fleming, "Studies of the Inertial Component of Polar Solvation Dynamics," in Ultrafast Reaction Dynamics and Solvent Effects, Y. Gauduel, P. J. Rossky. (American Institute of Physics, 1994), 310.

[75] W. P. de Boeij, PhD thesis, Rijksuniversiteit Groningen, Netherlands, 1997.

[76] X.-X. Zhang, C. Würth, L. Zhao, U. Resch-Genger, N. P. Ernsting .M. Sajadi, Rev. Sci. Instrum., 82, 063108, 2011.

[77] L. Zhao, J. L. Perez Lustres, V. Farztdinov, N. P. Ernsting, Phys. Chem. Chem. Phys., 7, 1716, 2005.

[78] M. A. Kahlow, W. Jarzeba, T. P. DuBruil, P. F. Barbara, Rev. Sci. Instr., 59, 1098, 1988.

[79] W. Jarzeba, G. C. Walker, A. E. Johnson, M. A. Kahlow, P. F. Barbara, J. Phys. Chem., 92, 7039, 1988.

[80] D. C. Todd, J. M. Jean, S. J. Rosenthal, A. J. Ruggiero, D. Yang, G. R. Fleming, J. Chem. Phys., 93, 8658, 1990.

[81] S. E. Bradforth, R. Jimenez, F. V. Mourik, R. V. Grondelle, G. R. Fleming, J. Phys. Chem., 99, 16179, 1995.

[82] B. P. Krueger, G. D. Scholes, R. Jimenez, G. R. Fleming, J. Phys. Chem. B, 102, 2284, 1998.

[83] I. V. Rubtsov, K. Yoshihara, J. Phys. Chem. A, 103, 10202, 1999.

[84] D. Marks, P. Prosposito, H. Zhang, M. Glasbeek, Chem. Phys. Lett., 289, 535 1998.

[85] M. Chattoraj, B. A. King, G. U. Bublitz, S. G. Boxer, Proc. Natl. Acad. Sci., 93, 8362, 1996.

[86] X. H. Shi, P. Abbyad, X. K. Shu, K. Kallio, P. Kanchanawong, W. Childs, S. J. Remington, S. G. Boxer, Biochemistry, 46, 12014, 2007.

[87] S. Takeuchi, T. Tahara, J. Phys. Chem. A, 102, 7740, 1998.

[88] S. K. Pal, J. Peon, A. H. Zewail, Chem. Phys. Lett., 363, 57, 2002.

[89] S. K. Pal, L. Zhang, A. H. Zewail, Proc. Natt. Acad. Sci. USA, 100, 8113, 2003.

[90] T. Gustavsson, L. Cassara, V. Gulbinas, G. Gurzadyan, J.-C, Mialocq, S. Pommeret, M. Sorgius, P. V. D. Meulen, J. Phys. Chem. A, 102, 4229, 1998.

[91] T. Gustavsson, N. Sarkar, E. Lazzarotto, D. Markovitsi, R. Improta, Chem. Phys. Lett., 429, 551, 2006.

[92] H. S. Cho, H. Rhee, J. K. Song, C-K. Min, M. Takase, N. Aratani, S. Cho, A. Osuka, T. Joo, D. Kim, J. Am. Chem. Soc., 125, 5849, 2003.

[93] A. Fürstenberg, M. D. Julliard, T. G. Deligeorgiev, N. I. Gadjev, A. A. Vasilev, E. Vauthey, J. Am. Chem .Soc., 128, 7661, 2006.

[94] Y.-T. Kao, C. Saxena, T.-F. He, L. J. Guo, L. J. Wang, A. Sancar, D. P. Zhong, J. Am. Chem. Soc., 130, 13132, 2008.

[95] L. Y. Zhang, Y. Yang, Y.-T. Kao, L. J. Wang, D. P. Zhong, J. Am. Chem. Soc., 131, 10677, 2009.

[96] P.-T. Chou, Y.-C. Chen, W.-C. Chen, W.-S. Yu, Y.-H. Chou, C.-Y. Wei, Y.-M. Cheng, J. Phys. Chem. A, 105, 1731, 2001.

[97] C.-Y. Chen, C.-T. Cheng, J.-K. Yu, S.-C. Pu, Y.-M. Cheng, P.-T. Chou, J. Phys. Chem. B, 108, 10687, 2004.

[98] T. Pancur, N. K. Schwalb, F. Renth, F. Temps, Chem. Phys., 313, 199, 2005.

[99] N. K. Schwalb F. Temps, Phys. Chem. Chem. Phys., 8, 5229, 2006.

[100] G. Zgrablić, S. Haacke, M. Chergui, J. Phys. Chem. B, 113, 4384, 2009.

[101] P. Changenet-Barret, C. T. Choma, E. F. Gooding, W. F. DeGrado, R. M. Hochstrasser, J. Phys. Chem. B, 104, 9322, 2000.

[102] D. V. O'Connor, D. Phillips, Time-Correlated Single Photon Counting, 1st ed. (Academic, London, 1984).

[103] J. A. Gardecki, M. Maroncelli, J. Phys. Chem. A, 103, 1187, 1999.

[104] T. Gustavsson, G. Baldcchino, J.-C. Mialocq, S. Pommeret, Chem. Phys. Lett., 236, 587, 1995.

[105] A. Cannizzo, O. Bräm, G. Zgrablic, A. Tortschanoff, A. Ajdarzadeh-Oskouei, F. van Mourik, M. Chergui, Opt. Lett., 32, 3555, 2007.

[106] R. Schanz, S. A. Kovalenko, V. Kharlanov, N. P. Ernsting, Appl. Phys. Lett. 79, 566, 2001.

[107] S. A. Kovalenko, R. Schanz, T. Senyushkina, N. P. Ernsting, Phys. Chem. Chem. Phys., 4, 703, 2002.

[108] P. Fita, Y. Stepanenko, C. Radzewicz, Appl. Phys. Lett., 86, 021909, 2005.

[109] X-F. Han, X-H. Chen, Y-X. Weng, J-Y. Zhang, J. Opt. Soc. Am. B, 24, 1633, 2007.

[110] R. S. Fee, M. Maroncelli, Chem. Phys., 183, 235, 1994.

[111] S. J. Rosenthal, R. Jimenez, G. R. Fleming, P. V. Kumar, M. Maroncelli, J. Mol. Liq., 60, 25, 1994.

[112] I. Eom, T. Joo, J. Chem. Phys. 131, 244507, 2009.

[113] D. V. Matyushov, M. D. Newton, J. Phys. Chem. A, 105, 8516, 2001.

[114] R. Improta, V. Barone, F. Santoro, J. Phys. Chem. B, 111, 14080, 2007.

[115] J. L. Perez-Lustres, F. Rodriguez-Prieto, M. Mosquera, T. A. Senyushkina, N. P. Ernsting, S. A. Kovalenko, J. Am. Chem. Soc., 129, 5408, 2007.

[116] Y. Nabekawa, K. Midorikawa, Opt. Express, 11, 324, 2003.

[117] N. P. Ernsting, J. Breffke, D. Y. Vorobyev, D. A. Duncan, I. Pfeffer, Phys. Chem. Chem. Phys., 10, 2043, 2008.

[118] M. Sajadi, A. L. Dobryakov, E. Garbin, N. P. Ernsting, S. A. Kovalenko, Chem. Phys. Lett., 489, 44, 2010.

[119] F. Zernike, J. E. Midwinter, *Applied Nonlinear Optics,* Wiley, New York, 1973.

[120] E. L. Crow, K. Schimizu, *Lognormal Distributions: Theory and Applications*, New York, Dekker, 1988.

[121] M. Sajadi, Y. Ajaj, I. Ioffe, H. Weingärtner, N. P. Ernsting, Angew. Chem. Int. Ed., 49, 454, 2009.

[122] M. Sajadi, T. Obernhuber, S. A. Kovalenko, M. Mosquera, B. Dick, N. P. Ernsting, J. Phys. Chem. A, 113, 44, 2008.

[123] M. L. Horng, J. A. Gardecki, M. Maroncelli, J. Phys. Chem. A, 101, 1030, 1997.

[124] S. Arzhantsev, M. Maroncelli, Appl. Spectroscopy, 59, 206, 2005.

[125] B. Schmidt, S. Laimgruber, W. Zinth, P. Gilch, Appl. Phys. B, 76, 809, 2003.

[126] S. Arzhantsev, K. Zahariasse, M. Maroncelli, J. Phys. Chem. A, 110, 3545, 2006.

[127] S. Arzhantsev, H. Jin, G. A. Baker, M. Maroncelli, J. Phys. Chem. B, 111, 4978, 2007.

[128] R. W. Boyd, *Nonlinear Optics*, Academic Press, San Deigo, 1992

[129] D. H. Waldeck, Chem. Rev., 91, 415, 1991.

[130] J. Saltiel, A.S. Waller, D.F. Sears, J. Photochem. Photobiol. A, 65, 29, 1992; J. Am. Chem. Soc., 115, 2453, 1993.

[131] S. Abrash, S. Repinec, R. M. Hochstrasser, J. Chem. Phys., 93, 1041, 1990.

[132] R.J. Sension, S.T. Repinec, A.Z. Szarka, R.M. Hochstrasser, J. Chem. Phys., 98, 6291, 1993.

[133] S. T. Repinec, R.S. Sension, A.Z. Szarka, R.M. Hochstrasser, J. Phys. Chem., 95, 10380, 1991.

[134] L. Nikowa, D. Schwarzer, J. Troe, J. Scroeder, J. Chem. Phys., 97, 4827, 1992.

[135] D. Todd, G.R. Fleming, J. Chem. Phys., 98, 269, 1993.

[136] K. Ishii, S. Takeuchi, T. Tahara, Chem. Phys. Lett., 398, 400, 2004.

[137] S. Takeuchi, S. Ruhman, T. Tsuneda, M. Chiba, T. Taketsugo, T. Tahara, Science, 322, 1073, 2008.

[138] H. Petek, Y. Fujiwara, D. Kim, K. Yoshihara, J. Am. Chem. Soc., 110, 6269, 1988; J. H. Frederick, Y. Fujiwara, J. H. Penn, K. Yoshihara, H. Petek, J. Phys. Chem., 95, 2845, 1991.

[139] T. Soujanya, T. S. R. Krishma, A. Samanta, J. Phys. Chem. 96, 8544, 1992.

[140] G. Saroja, B. Ramachandram, S. Saha, A. Samanta, J. Phys. Chem. B, 103, 2906, 1999.

[141] C. F. Chapman, M. Maroncelli, J. Phys. Chem., 95, 9095, 1991.

[142] A. Paul, A. Samanta, J. Phys. Chem. B, 111, 4724, 2007.

[143] B. C. Barja, C. Chesta, T. D. Z. Atvars, P. Aramendia, J. Phys. Chem. B, 109, 16180, 2005.

[144] D. Noukakis, P. Suppan, J. Lumin., 47, 285, 1991.

[145] K. Dobek, Photochem. Photobiol. Sci., 7, 361, 2008.

[146] E. Krystkowiak, K. Dobek, A. Maciejewski, J. Photochemistry & Photobiology A- Chemistry, 184, 250, 2006.

[147] T. Harju, A. H. Huizer, C. A. G. O. Varma, Chem. Phys., 200, 215, 1995.

[148] S. Das, A. Datta, K. Bhattacharyya, J. Phys. Chem. A, 101, 3, 1997.

[149] B. Bhattacharya, A. Samanta, Chem. Phys. Lett., 442, 316, 2007.

[150] C. F. Chapman, R. S. Fee, M. Maroncelli, J. Phys. Chem., 99, 4811, 1995.

[151] E. Laitinen, K. Salonen, T. Harju, J. Chem. Phys., 104, 6138, 1996.

[152] E. Laitinen, K. Salonen, T. Harju, J. Chem Phys., 105, 9771, 1996.

[153] A. Datta, D. Mandal, S. K. Pal, S. Das, K. Bhattacharyya, J. Mol. Liqu., 77, 121, 1998.

[154] D. Mandal, A. Datta, S. K. Pal, K. Bhattacharyya, J. Phys. Chem. B, 102, 9070, 1998.

[155] S. K. Mondal, D. Roy, K. Sahu, P. Sen, R. Karmakar, K. Bhattacharyya, J. Photochem & Photobio A- Chemistry, 173, 334, 2005.

[156] S. Haacke, R. A. Taylor, I. Bar-Joseph, M. J. S. P. Brasil, M. Hartig, B. Deveaud, J. Opt. Soc. Am. B, 15, 1410, 1998.

[157] S. A. Kovalenko, J. Ruthmann, N. P. Ernsting, Chem. Phys. Lett., 271, 40, 1997.

[158] V. Karunakaran, M. Pfaffe, I. Ioffe, T. Senyushkina, S. A. Kovalenko, R. Mahrwald, V. Farztdinov, H. Sklenar, N. P. Ernsting, J. Phys. Chem., 112, 4294, 2008.

[159] D. Andreatta, S. Sen, J. L. P. Lustres, S. A. Kovalenko, N. P. Ernsting, C. J. Murphy, R. S. Coleman, M. A. Berg, J. Am. Chem. Soc., 128, 6885, 2006.

[160] B. A. Pryor, P. M. Palmer, Yu. Chen, M. R. Topp, Chem. Phys. Lett., 299, 536, 1999.

[161] A. Mühlpfordt, R. Schanz, N. P. Ernsing, V. Fartzdinov, S. Grimme, Phys. Chem. Chem. Phys., 1, 3209, 1999.

[162] M. Asimov, N. P. Ernsting, J. Lumin., 28, 119, 1983.

[163] I. M. Gulis, A. I. Komyak, K. A. Saechnikov, V. A. Tsvirko, Zhurnal Prikladnoi Spektroskopi, 50, 385, 1989.

[164] S. A. Kovalenko, A. L. Dobryakov, J. Ruthmann, N. P. Ernsting, Phys. Rev. A, 59, 2369, 1999.

[165] A. Kessler, A. Slenczka, R. Seiler, B. Dick, Phys. Chem. Chem. Phys., 3, 2819, 2001.

[166] R. Seiler, U. Kensy, B. Dick, Phys. Chem. Chem. Phys., 3, 5373, 2001.

[167] M. W. Schmidt, K. K. Baldridge, J. A. Boatz, S. T. Elbert, M. S. Gordon, J. H. Jensen, S. Koseki, N. Matsunaga, K. A. Nguyen, S. J. Su, T. L. Windus, M. Dupuis, J. A. Montgomery, J. Comput. Chem., 14, 1347, 1993. M. S. Gordon, M. W. Schmidt *Theory and Applications of Computational Chemistry, the first forty years*. C. E. Dykstra, G. Frenking, K. S. Kim, G. E. Scuseria, Elsevier, Amsterdam, 2005.

[168] A. A. Granovsky, PC GAMESS version 7.0, http://classic.chem.msu.su/gran/gamess/index.html; A. V. Nemukhin, B. L. Grigorenko, A. A. Granovsky, Moscow University Chemistry Bulletin 2004, 45, 75.

[169] D. B. Siano, D. E. Metzler, J. Chem. Phys., 51, 1856, 1969.

[170] Since excitation pulse is short eq. (3) of ref. 87 must be integrated over $\tilde{\nu}_{exc}$ also.

[171] Y. Marcus, M. J. Kamlet, R. W. Taft, J. Phys. Chem., 92, 3613, 1988.

[172] Regarding the spectral position of the pump pulse on the red edge of the absorption band, excitation of 4AP in acetonitrile centered at 388 nm is equivalent to excitation in methanol centered at 403 nm. The former leads to a time-zero fqd which peaks at 23550 cm-1. The peak of the stationary fqd in acetonitrile is observed at 21390 cm^{-1}.

[173] A. Dreuw, M. Head-Gordon, Chem. Rev., 105, 4009, 2005.

[174] Since nonexponentiality is expected at early time, the triexponential fit should properly be restricted to t > 1 ps. The same rmsd of 40 cm^{-1} is found for the restricted time interval.

[175] D. V. Matyushov, J. Chem. Phys., 115, 8933, 2001.

[176] N. G. Bakshiev, Optika i Spektroskopiya, 91, 721, 2001.

[177] J. E. Bertie, S. L. Zhang, H. H. Eysel, S. Baluja, M. K. Ahmed, Appl. Spectrosc., 47, 1100, 1993.

[178] At the given time resolution, the emission frequency $\tilde{\nu}(0^+) = \Delta\tilde{\nu}\, C(0^+) + \tilde{\nu}(\infty)$ would be measured at delay time t=0 if solvent Raman signal were absent. In practice, only at t=100 fs did the solvent Raman signal become small enough so that the peak frequency can be determined reliably.

[179] J. Barthel, K. Bachhuber, R. Buchner, H. Hetzenauer, Chem. Phys. Lett., 165, 369, 1990.

[180] R. A. Marcus. J. Chem. Phys., 43, 1261, 1965.

[181] Y. Chen, M. R. Topp, Chem. Phys. Lett., 355, 270, 2002.

[182] M. Yoshizawa, M. Kurosawa, Phys. Rev. A, 61, 013808, 1999.

[183] P. Kukura, S. Yoon, R. A. Mathies, Anal. Chem., 78, 5952, 2006.

[184] M. Sajadi, M. Weinberger, H-A. Wagenknecht, N. P. Ernsting, Phys. Chem. Chem. Phys., 13, 17768, 2011.

[185] for example, our previous value ncav=2.3 may have accommodated the systematic difference between the spectral relaxation observed by stimulated-emission and by spontaneous fluorescence.

[186] M. Weinberger, H.-A. Wagenknecht, *in preparation*.

[187] N. Rega, private communication.

[188] Relatively large n_{cav} may come from uncertainty of methanol dielectric data in the THz range.

[189] T. Fukasawa, T. Sato, J. Watanabe, Y. Hama, W. Kunz, R. Buchner, Phys. Rev. Lett., 95, 197802, 2005.

[190] S. K. Garg, C. P. Smyth, J. Phys. Chem., 69, 1294, 1965.

[191] J. A. Ingram, R. S. Moog, N. Ito, R. Biswas, M. Maroncelli, J. Phys. Chem. B, 107, 5926, 2003.

[192] H. Yada, M. Nagai, K. Tanaka, Chem. Phys. Lett., 464, 166, 2008.

[193] S.-G. Su, J. D. Simon, J. Phys. Chem., 93, 753,1989.

[194] W. Jarzeba, G. C. Walker, A. E. Johnson, P. F. Barbara, Chem. Phys., 152, 57, 1991.

[195] T. Fonseca, B. M. Ladanya, J. Molecular Liquids, 60, 1, 1994.

[196] M. Yoshizawa, M. Kubo, M. Kurosawa, J. Lumin., 87, 739, 2000.

[197] M. Meyer, J. C. Mialocq, B. Perly, J. Phys. Chem., 94, 98, 1990.

[198] R. Lapouyade, A. Kuhn, J.-F. Letard, W. Rettig, Chem. Phys. Lett., 208, 48, 1993.

[199] S. Marguet, J. C. Mialocq, P. Millie, G. Berthier, F. Momicchioli, Chem. Phys., 160, 265 1992.

[200] A. J. VanTassle, M. A. Prantil, G. R. Fleming, J. Phys. Chem. B, 110, 18989, 2006.

[201] A. Thöny, M. Rossi, J. Photochem. Photobiol. A: Chem, 104, 25, 1997.

[202] S. A. Kovalenko, R. Schanz, H. Hennig, N. P. Ernsting, J. Chem. Phys., 115, 3215, 2000.

[203] H. Pickl, PhD thesis, Regensburg university, Regensburg, Germany, 1997.

[204] Y. Marcus, *The properties of solvents*, Wiley: New York, 1998.

[205] W. J. Ellison, J. Phys. Chem., 36, 1, 2007.

[206] N. Nandi, S. Roy, B. Bagchi, J. Chem. Phys., 102, 1390, 1995.

[207] D. Zhong, S. K. Pal, A. H. Zewail, Chem. Phys. Lett., 503, 1, 2011.

[208] J. H. Crowe, L. M .Crowe, Science, 223, 701, 1984.

[209] G. M. Beattie, J. H. Crowe, A. D. Lopez, V. Cirulli, C. Ricordi, A. Hayek, Diabetes, 46, 519, 1997.

[210] J. L. Green, A. Angell, J. Phys. Chem., 93, 2880, 1989.

[211] M. C. Donnamaria, E. L. Howard, J. R. Grigera, J. Chem. Soc. Fraday Trans., 90, 2731, 1994.

[212] S. Magazu, V. Villari, P. Migliardo, G. Maisano, M. T. F. Telling, J. Phys. Chem. B, 105, 1851, 2001.

[213] M. E. Gallina, P. Sassi, M. Paolantoni, A. Morresi, R. S. Cataliotti, J. Phys. Chem. B, 110, 8856, 2006.

[214] S. Mashimo, N. Miura, T. Umehara, J. Chem. Phys., 97, 6759, 1992.

[215] D. Fioretto, L. Comez, M. E. Gallina, A. Morresi, L. Palmieri, M. Paolantoni, P. Sassi, F. Scarponi, Chem. Phys. Lett., 441, 232, 2007.

[216] H. Weingärtner, A. Knocks, S. Boresch, P. Höchtl, O. Steinhauser, J. Chem. Phys., 115, 1463, 2001.

[217] K. Fuchs, U. Kaatze, J. Chem. Phys., 116, 7137, 2002., R. Behrends, U. Kaatze, Chem. Phys. Chem., 6, 1133, 2005.

[218] C. Branca, S. Magazu, G. Maisano, P. Migliardo, J. Chem. Phys., 111, 281, 1999.

[219] M. Paolantoni, P. Sassi, A. Morresi, S. Santini, J. Chem. Phys., 127, 024504-1, 2007.

[220] S. J. Hagen, J. Hofrichter, W. A. Eaton, J. Phys. Chem., 100, 12008, 1996.

[221] L. Cordone, P. Galajda, E. Vitrano, A. Gassmann, A. Ostermann, F. Parak, Eur. Biophys. J., 27, 173, 1998.

[222] D. S. Gottfried, E. S. Peterson, A. G. Sheikh, J. Wang, M. Yang, J. M. Friedman, J. Phys. Chem., 100, 12304, 1996.

[223] K. D. Rector, J. R. Engholm, C. W. Rella, J. R. Hill, D. D. Dlott, M. D. Fayer, J. Phys. Chem. A., 103, 2381, 1999.

[224] K. D. Rector, J. Jiang, M. Berg, M. D. Fayer, J. Phys. Chem. B., 105, 1081, 2001.

[225] A. M. Massari, L. J. Finkelstein, B. L. McClain, A. Goj, X. Wen, K. L. Bren, R. F. Loring, M. D. Fayer, J. Am. Chem. Soc., 127, 14279, 2005.

[226] M. Heyden, E. Bründermann, U. Heugen, G. Niehues, D. M. Leitner, M. Havenith, J. Am. Chem. Soc., 130, 5773, 2008.

[227] T. Arikawa, M. Nagai, K. Tanaka, Chem. phys. lett., 457, 12, 2008.

[228] C. Rønne, S. R. Keiding, J. Mol. Liquids, 101, 199, 2002.

[229] F. Berndt, M. Sajadi, N. P. Ernsting, R. Mahrwald, Carbohydrate Research, 346, 2960, 2011.

[230] A. Oleinikova, P. Sasisanker, H. Weingärtner, J. Phys. Chem. B, 108, 8467, 2004.

[231] M. J. Tait, A. Suggett, F. Franks, S. Abbett, P. A. Quickeneden, J. Solution Chem., 1, 131, 1972.

[232] C. J. F. Böttcher, P. Bordewijk, Theory of Dielectric Polarization, Elsevier, Amsterdam, 1978.

[233] K. S. Cole, R. H. Cole, J. Chem. Phys., 9, 341, 1941.

[234] A. A. Granovsky, PC GAMESS/Firefly version 7.1.F, http://classic.chem.msu.su/gran/gamess/index.html

[235] M. W. Schmidt, K. K. Baldridge, J. A. Boatz, S. T. Elbert, M. S. Gordon, J. H. Jensen, S. Koseki, N. Matsunaga, K. A. Nguyen, S. Su, T. L. Windus, M. Dupuis, J. A. Montgomery, J. Comput. Chem., 14, 1347, 1993.

[236] R. A. Kendall, T. H. Dunning, R. J. Harrison, J. Chem. Phys., 96, 6796, 1992.

[237] T. H. Dunning, J. Chem. Phys., 90, 1007, 1989.

[238] http://classic.chem.msu.su/gran/gamess/xmcqdpt.pdf, paper in preparation

[239] Y. Levy, J. N. Onuchic, Annu. Rev. Biophys. Biomol. Struct., 35, 389, 2006.

[240] P. Auffinger, Y. Hashem, Curr. Op. Struct. Biol., 17, 325, 2007.

[241] D. Marx, *Chem. Phys. Chem.*, 7, 1848, 2006 ; G. Mathias, D. Marx, Proc. Natl. Acad. Sci. USA., 104, 6980, 2007.

[242] H. Frauenfelder, G. Chena, J. Berendzena, P. W. Fenimore, H. Janssonb, B. H. McMahon, I. R. Stroec, J. Swensond, R. D. Young, Proc. Natl. Acad. Sci. USA., 106, 5129, 2009.

[243] S. Sen, D. Andreatta, S. Y. Ponomarev, D. L. Beveridge, M. A. Berg, J. Am. Chem. Soc., 131, 1724, 2009.

[244] T. J. Kindt, C. A. Schmuttenmaer, J. Phys. Chem., 100, 10373, 1996.

[245] J. E. Bertie, Z. Lan, Appl. Spectroscopy., 50, 1047, 1996.

[246] A. Y. Zasetsky, V. I. Gaiduk, J. Phys. Chem. A, 111, 5599, 2007.

[247] J. B. Bircks, *Photophysics of aromatic molecules*, Wiley Interscience, New York 1970.

[248] G. I. Groma, J. Hebling, I. Z. Kozma, G.Varo, J. Hauer, J. Kuhl, E. Riedle, Proc. Natl. Acad. Sci. USA., 105, 6888, 2008.

[249] J. Léonarda, E. Portuondo-Campab, A. Cannizzob, F. van Mourikb, G. van der Zwan, J. Tittord, S. Haacke, M. Chergui, Proc. Natl. Acad. Sci. USA., 106, 7718, 2009.

[250] P. K. Banipal, T. S. Banipal, B. S. Lark, J. C. Ahluwalia, J. Chem. Soc., Faraday Trans., 93, 81, 1997.

[251] M. C. Vega, I. G. Saez, J. Aymami, R. Eritja, G. A. Vandermarel, J. H. Vanboom, A. Rich, M. Coll, Eur. J. Biochem., 222, 721, 1994.

[252] C. E. Bostock-Smith, S. A. Harris, C. A. Laughton, M. S. Searle, Nucleic Acids Res., 29, 693, 2001.

[253] R. G. Smock, L. M. Gierasch, Science, 324, 198, 2009.

[254] S. Hammes-Schiffer, S. J. Benkovic, Annu. Rev. Biochem., 75, 519, 2006.

[255] G. M. Lee, C. S. Craik, Science, 324, 213, 2009.

[256] R. V. Mauldin, M. J. Carroll, A. L. Lee, Structure, 17, 386, 2009.

[257] T. Ambjörnsson, S. K. Banik, O. Krichevsky, R. Metzler, Biophys. J., 92, 2674, 2007.

[258] P. Abbyad, X. H. Shi, W. Childs, T. B. McAnaney, B. E. Cohen, S. G. Boxer, J. Phys. Chem. B, 111, 8269, 2007.

[259] E. B. Brauns, M. L. Madaras, R. S. Coleman, C. J. Murphy, M. A. Berg, J. Am. Chem. Soc., 121, 11644, 1999.

[260] E. B. Brauns, M. L. Madaras, R. S. Coleman, C. J. Murphy, M. A. Berg, Phys. Rev. Lett., 88, 158101, 2002.

[261] X. J. Jordanides, M. J. Lang, X. Y. Song, G. R. Fleming, J. Phys. Chem. B, 103, 7995, 1999.

[262] T. P. Li, A. A. P. Hassanali, Y. T. Kao, D. P. Zhong, S. J. Singer, J. Am. Chem. Soc., 129, 3376, 2007.

[263] S. K. Pal, J. Peon, A. H. Zewail, Proc. Natl. Acad. Sci. USA., 99, 1763, 2002.

[264] L. Y. Zhang, Y. T. Kao, W. H. Qiu, L. J. Wang, D. P. Zhong, J. Phys. Chem. B, 110, 18097, 2006.

[265] B. Halle, L. Nilsson, J. Phys. Chem. B, 113, 8210, 2009.

[266] S. K. Pal, A. H. Zewail, Chem. Rev., 104, 2099, 2004.

[267] A. Dallmann, M. Pfaffe, C. Mügge, R. Mahrwald, S. A. Kovalenko, N. P. Ernsting, J. Phys. Chem. B, 113, 15619, 2009.

[268] K. E. Furse, S. A. Corcelli, J. Phys. Chem. Lett., 1, 1813, 2010.

[269] K. E. Furse, S. A. Corcelli, J. Am. Chem. Soc., 130, 13103, 2008.

[270] K. E. Furse, S. A. Corcelli, J. Chem. Theory Comp., 5, 1959, 2009.

[271] D. Banerjee, S. K. Pal, J. Phys. Chem. B, 111, 10833, 2007.

[272] G. Cosa, K. -S. Focsaneanu, J. R. N. McLean, J. P. McNamee, J. C. Scaiano, Photochem. Photobiol., 73, 585, 2001.

[273] D. Banerjee, S. K. Pal, J. Phys. Chem. B, 111, 10833, 2007.

[274] K. E. Furse, B. A. Lindquist, S. A. Corcelli, J. Phys. Chem. B, 112, 3231, 2008.

[275] D. A. Case, T. A. Darden, T. E. Cheatham, C. L. Simmerling, J. Wang, R. E. Duke, R. Luo, K. M. Merz, D. A. Pearlman, M. Crowley, R. C. Walker, W. Zhang, B. Wang, S. Hayik, A. Roitberg, G. Seabra, K. F. Wong, F. Paesani, X. Wu, S. Brozell, V. Tsui, H. Gohlke, L. Yang, C. Tan, J. Mongan, V. Hornak, G. Cui, P. Beroza, D. H. Mathews, C. Schafmeister, W. S. Ross, P. A. Kollman, AMBER 9; University of California, San Francisco, 2006.

[276] J. M. Wang, P. Cieplak, P. A. Kollman, J. Comput. Chem., 21, 1049, 2000.

[277] H. J. C. Berendsen, J. R. Grigera, T. P. Straatsma, J. Phys. Chem., 91, 6269, 1987.

[278] B. B. Laird, W. H. Thompson, J. Chem. Phys., 126, 211104, 2007.

[279] E. A. Carter, J. T. Hynes, J. Chem. Phys., 94, 5961, 1991.

[280] R. Buchner, J. Bathel, J. Stauber, Chem. Phys. Lett., 306, 57, 1999.

[281] M. Sajadi, K. E. Furse, X.-X. Zhang, L. Dehmel, S. A. Kovalenko, S. A. Corcelli, N. P. Ernsting, Angewandte Chemie Int. Ed., 123, 6973, 2011.

List of Publications

M. Sajadi, M. Weinberger, H-A. Wagenknecht, N. P. Ernsting, Polar solvation dynamics in water and methanol: search for molecularity., *Phys. Chem. Chem. Phys*., accepted.

M. Sajadi, K. E. Furse, X.-X. Zhang, L. Dehmel, S. A. Kovalenko, S. A. Corcelli, N. P. Ernsting, Detection of DNA-ligand binding oscillations by Stokes-shift measurements., *Angewandte Chemie Int. Ed*., accepted

X.-X. Zhang, C. Würth, L. Zhao, U. Resch-Genger, N. P. Ernsting, **M. Sajadi**, Femtosecond Broadband Fluorescence Upconversion Spectroscopy: Improved Setup and Photometric Correction., *Rev. Sci. Instrum., 82, 063108 (2011)*

M. Sajadi, A. L. Dobryakov, E. Garbin, N. P. Ernsting, and S. A. Kovalenko, Time-resolved fluorescence spectra of *cis*-stilbene in hexane and acetonitrile., *Chem. Phys. Lett., 489, 44 (2010)*

M. Sajadi, Y. Ajaj, I. Ioffe, H. Weingärtner, N. P. Ernsting, THz Absorption Spectroscopy of a Liquid via a Polarity Probe. A Case Study of Trehalose/Water Mixtures., *Angewandte Chemie Int. Ed., 49, 454 (2009)*

M. Sajadi, T. Obernhuber, S. A. Kovalenko, M. Mosquera, B. Dick, N. P. Ernsting, Dynamic polar solvation is reported by fluorescing 4-Aminophthalimide faithfully despite H-bonding., *J. Phys. Chem. A 113, 44 (2008)*

Selbständigkeitserklärung

Ich erkläre, dass ich die vorliegende Arbeit selbständig und nur unter Verwendung der angegebenen Literatur und Hilfsmittel angefertigt habe.

Ich habe mich anderweitig nicht um einen Doktorgrad beworben und besitze keinen entsprechenden Doktorgrad.

Berlin, den 26.08.2011 Mohsen Sajadi Hezaveh